universität wien

DISSERTATION

Titel der Dissertation

Long Period Variables: Period Luminosity Relations and Classification in the Gaia Mission

Verfasserin:

Mag. Denise Lorenz

angestrebter akademischer Grad

Doktorin der Naturwissenschaften (Dr. rer. nat.)

Wien, 2011

Studienkennzahl lt. Studienblatt:	A 091 413
Dissertationsgebiet lt. Studienblatt:	Astronomie
Betreuer:	Doz. Dr. Thomas Lebzelter

Contents

English

Long period variables (LPVs) are found among highly evolved stars on the Asymptotic Giant Branch (AGB). Their initial masses range from 0.8 to about 10 $M_\odot$, hence, they belong to the so called intermediate-age population with ages of 1 to 10 Gyr. Variable stars are in general very useful diagnostics since their pulsational behaviour can help to gain further information (e.g. internal structure, distances, evolution). Up to now LPVs were classified into three subclasses – Mira variables, semiregular variables, and irregular variables. But the evolutionary relation between those subclasses is not clear, and several attempts to reclassify this type of variable have been made. A very promising solution to this problem was the discovery of several almost parallel sequences of LPVs of the Large Magellanic Cloud LMC in a period-luminosity diagram (PLD). This distribution of LPVs was also found in other stellar systems, both for single and multiple stellar populations, respectively. Consequently, LPVs can be reclassified according to their location within a PLD. Furthermore, the question arose if a period-luminosity relation (PLR) for LPVs can be found and, therefore, serve as additional tool to measure distances (as, e.g., the PLR of Cepheids). Owing to the intrinsic brightness of AGB stars their PLR could serve as additional rung in the so called distance ladder (reaching even beyond the Local Group). Hence, studying AGB stars, and especially LPVs, is a critical issue not only for stellar but also for galactic and extragalactic astrophysics. In the first part of this thesis I, therefore, attempt to give an overview of stellar evolution with a focus on AGB stars, and how stars can be used as indicators for age and distance.

Currently the European Space Agency (ESA) is building the Gaia satellite which will be launched in spring 2013. It is the follow up mission of the successful Hipparcos satellite. Like Hipparcos Gaia will measure the position, distance, and brightness of stars. But owing to the improved equipment, Gaia will be able to observe stars down to 20 mag (in the visual). Furthermore, the satellite will obtain spectrophotometry in two channels (blue and red) and radial velocities with an accuracy of about 5 km/s (for the brighter objects). This ambitious mission aims to carry out measurements (e.g., distances, brightness, colour) of about one billion stars with an unprecedented precision, covering a big part of our galaxy. Approximately 250 000 of these stars are expected to be LPVs, for which the author of this thesis is developing a software package suited for their detection and classification (according to their position in a PLD as mentioned above). The huge amount of detected LPVs will allow the construction of a very precise PLD of the Milky Way and its various parts. Our software package is still under development and will be finalised once the first Gaia data are available. The second part of this thesis reports on the current status of this software and describes the single modules in detail.

In the last part of this thesis I will present a search for LPVs in the two dwarf galaxies NGC 147 and NGC 185. By comparing the results of both galaxies with each other and with the literature, I discuss the implications for various scientific topics like distance determination or star formation history. Photometric monitoring allowed the detection of 213 LPVs in NGC 147 and 513 LPVs in NGC 185. Both galaxies show signs of more than one sequence of LPVs in the PLD. The slopes of the resulting PLRs are not only close to each other but also to those published for other stellar systems. This finding is very encouraging concerning the universality of a PLR of LPVs (at least for fundamental mode pulsators). However, there is obviously a difference in the zero point for NGC 185 compared to the reference relation of the LMC, whereas the PLR of NGC 147 is in excellent agreement with the expected location. A simple, but not necessarily final explanation for this difference would be an error in the distance modulus of NGC 185. Another interesting feature is the lack of first overtone pulsators in the PLD of NGC 147. In the case of NGC 185 roughly 10% of all LPVs can be attributed to this sequence, while only less than 3% in NGC 147. This discrepancy could result from a difference in the mass distribution among the LPVs in the two galaxies, which again could be interpreted in terms of a difference in the star formation history.

Deutsch

Lang-periodisch Veränderliche (LPVs) sind weit entwickelte Sterne, die sich auf dem Asymptotischen Riesenast (AGB) befinden. Ihre ursprünglichen Massen liegen in einem Bereich von 0.8 bis circa 10 $M_{\odot}$, womit sie (im Sinne der Sternentstehungsgeschichte von Galaxien) mit einem Alter von 1 bis 10 Mrd Jahren zur Population mittleren Alters zählen. Veränderliche Sterne sind allgemein sehr hilfreich, um weitere physikalische Informationen der Sterne zu erhalten (z.B. interne Struktur, Entfernung, Entwicklung). Bislang wurden LPVs in drei Klassen unterteilt – Mira Sterne, halbregelmäig Veränderliche und unregelmäig Vernderliche. Der evolutionäre Zusammenhang der einzelnen Untergruppen von LPVs jedoch ist unklar, weshalb mehrere Versuche einer Neuklassifizierung unternommen wurden. Die Entdeckung von einigen, beinahe parallelen Sequenzen in einem Perioden-Leuchtkraft Diagramm (PLD) von LPVs der Groen Magellanschen Wolke (GMW), eröffnete einen neuen Weg der Klassifizierung, und zwar abhängig von der Position eines LPV in einem PLD. Somit drängte sich auch die Frage auf, ob man (wie bereits für Cepheiden) Perioden-Leuchtkraft-Relationen (PLRs) finden könne, die als zusätzliches Werkzeug zur Entfernungsbestimmung dienen. Aufgrund der gröeren Leuchtkraft von AGB Sternen (im Vergleich zu Cepheiden), könnte man mit deren PLRs Entfernungen zu noch weiter gelegenen Objekten messen (sogar auerhalb der Lokalen Gruppe). Aus diesem Grund ist es von groer Bedeutung, sowohl fr die galaktische als auch die extragalaktische Astronomie, AGB Sterne und insbesondere LPVs zu studieren. Der erste Teil dieser Arbeit soll daher einen Überblick über die Sternentwicklung mit Fokus auf AGB Sterne geben als auch über die Möglichkeit, Sterne als Indikatoren zur Alters- und Entfernungsbestimmung zu nutzen.

Momentan fertigt die Europäische Weltraum Agentur (ESA) den Gaia Satelliten an, der im Frühlung 2013 gestartet werden soll. Gaia ist der Nachfolger des berümten Hipparcos-Satelliten und wird wie dieser die Positionen, Entfernungen und Helligkeiten von etwa einer Milliarde Sternen messen. Allerdings werden dank der Instrumente an Bord von Gaia, Sterne mit einer Helligkeit bis zu 20 mag (im Visuellen) detektiert. Des Weiteren werden niedrig aufgelöste Spektren in zwei Kanälen (blau und rot) zu photometrischen Zwecken genutzt, und ein Spektrometer höherer Auflösung dient zur Ermittlung von Radialgeschwindigkeiten (mit einer Genauigkeit von etwa 5 km/s für hellere Objekte). Das ehrgeizige Ziel dieser Mission ist es Messungen (wie z.B. Entfernungen, Helligkeiten, Farben) von etwa einer Milliarde Sternen mit bislang unerreichter Genauigkeit durchzuführen, welche einen beträchtlichen Teil unserer Galaxie abdecken. Ungefähr 250 000 dieser Sterne werden voraussichtlich LPVs sein, deren Erkennung und Klassifizierung (je nach deren Lage innerhalb eines PLD, wie bereits oben erwähnt) mit einem von der Autorin dieser Arbeit erstellten Software Paket gehandhabt wird. Diese groe Anzahl an LPVs wird es ermöglichen, ein sehr genaues PLD der Milchstrae zu konstruieren. Das Software Paket befindet sich noch in der Entwicklung und wird mit den ersten Daten, die von Gaia erhalten werden, finalisiert. Der zweite Teil dieser Arbeit berichtet daher über den derzeitigen Status dieser Software und beschreibt die einzelnen Module im Detail.

Im letzten Teil dieser Arbeit werden die Ergebnisse neu entdeckter LPVs in den Zwerggalaxien NGC 147 und NGC 185 präsentiert. Durch Vergleichen der Resultate dieser Sternsysteme mit Werten aus der Literatur, untersucht die Autorin deren Anwendung auf wissenschftliche Themen wie Entfernungsbestimmung und Sternentstehungsgeschichte. Photometrische Langzeitbeobachtung ermöglichte die Entdeckung von insgesamt 213 LPVs in NGC 147 und 513 LPVs in NGC 185. Im PLD beider Galaxien gibt es Hinweise auf die Existenz mehrerer Sequenzen von LPVs. Die Steigungen der resultierenden PLRs beider Galaxien weisen ähnlich Werte auf und sind auch vergleichbar mit jenen von anderen Systemen (zumindest jene, die in der Fundamentalschwingung pulsieren). Dies lät das Vorhandensein von universal gültigen PLRs von LPVs vermuten, welche dann als zusätzliches Werkzeug zur Entfernungsbestimmung dienen könnten. Der Nullpunkt der PLR von NGC 147 entspricht dem erwarteten Vergleichswert der GMW (nach Anpassung des Distanzmoduls), doch jener von NGC 185 weicht deutlich vom Vergleichswert ab. Eine mögliche aber nicht unbedingt endgültige Erklärung für diesen Unterschied, wäre ein Fehler des zuvor angenommen Distanzmoduls von NGC 185. Ein weiterer Unterschied, der bei einem Vergleich der PLDs beider Galaxien ins Auge sticht, ist das Fehlen von LPVs in erster Überschwingung in NGC 147. Weniger als 3% der detektierten LPVs in NGC 147 können dieser Sequenz zugeordnet werden, in NGC 185 sind es immerhin etwa 10% der LPVs. Diese Abweichung könnte aus einer unterschiedlichen Massenverteilung von LPVs in diesen Galaxien resultieren und somit auch auf verschiedene Sternentstehungsgeschichten dieser Galaxien hinweisen.

Part I

Introduction

1 Stellar Evolution

Where do we come from? What are we made of? How were the elements that we are made of formed after the Big Bang? Fundamental questions of crucial importance to all of us!

The answers to these questions are found in stars. Their interiors are the main production sites of elements. Generations of stars have been formed and released their matter via mass-loss processes or explosions to the interstellar medium. This chemically enriched matter provides the building blocks of new stellar systems, planets, and even live itself. The main fraction of elements that our body is made of, consists of carbon (C), oxygen (O), and nitrogen (N) – all these elements are produced in stars via nuclear fusion reactions.

The theory of stellar evolution, therefore, serves as essential tool to study stellar populations (e.g., star clusters, galaxies) and their formation histories, and to understand the chemical evolution of the present universe. In addition, it also provides methods for distance determinations and kinematic investigations of the universe.

This chapter intends to give a short overview of the physics of stellar interiors and its impact on stellar structure and evolution. The focus is laid on stars, which evolve to asymptotic giant branch (AGB) stars. The chapter is based on various review papers and lecture notes on this subject. In particular, the reader is referred to the lecture notes of O. Pols[1], and the reviews of this subject given by Iben & Renzini (1983), Salaris & Cassini (2006), Herwig (2005), Habing & Olofsson (2003) and Chiosi (1992, 1997) and references therein.

1.1 The Hertzsprung-Russell Diagram

The Hertzsprung-Russell Diagram (HRD) is a very powerful tool in astronomy. It enables us to study stars in different astrophysical environments (e.g., solar neighbourhood, star clusters, galaxies) and investigate their formation history. Assuming that star clusters consist in first approximation of one population only (small spread in age and chemical composition), the cluster members mainly vary in mass and can therefore be used as testbed for stellar evolution models to which stellar evolution models are compared. The HRD displays the distribution of effective temperature versus the luminosity of stars (see Fig. 1.1).

According to the Stefan-Boltzmann law, the energy (F) that is radiated per second per unit surface area of a blackbody (an idealised physical body that absorbs all incoming radiation)

[1] see: http://www.astro.uu.nl/ pols/education/stev/

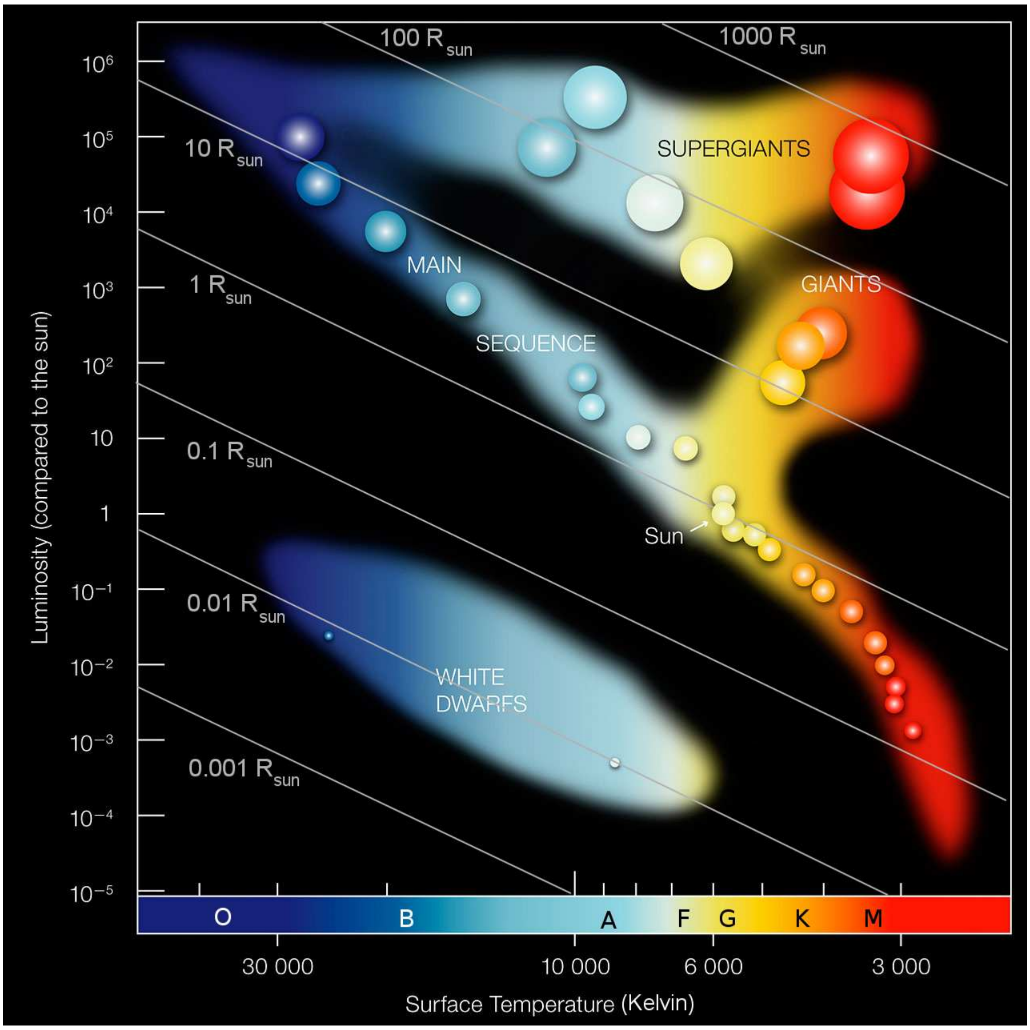

Figure 1.1: The schematic Hertzsprung-Russell diagram of stars detected in the solar neighbourhood (T_{eff} in logarithmic scale vs $L/L_{\odot}$). The letters at the bottom indicate the regions of the corresponding spectral type of the stars. The location of the main sequence as well as for red giants, super giants, and white dwarfs are given. Inserted lines of constant radii are shown which are increasing from the lower left to the upper right corner. Stars with low initial masses are at the lower end of the main sequence and those with high initial masses at the bright top of the main sequence. This figure was taken from ESO (www.eso.org/public/images/eso0728c/) and has been adapted by the author.

is proportional to the fourth power of the effective temperature (T_{eff}).

$$F_{bol} = \sigma T_{eff}^4 \tag{1.1}$$

where σ is the Stefan-Boltzmann constant. For reasons of simplification, stars are approximately considered as blackbody radiators in astrophysics. The Planck law describes the spectral distribution of a blackbody at a certain temperature, and Wien's displacement law gives the wavelength at which the Planck law has the maximum intensity. This perfectly explains why we observe stars of different colours (see planck curves in Fig. 1.2).

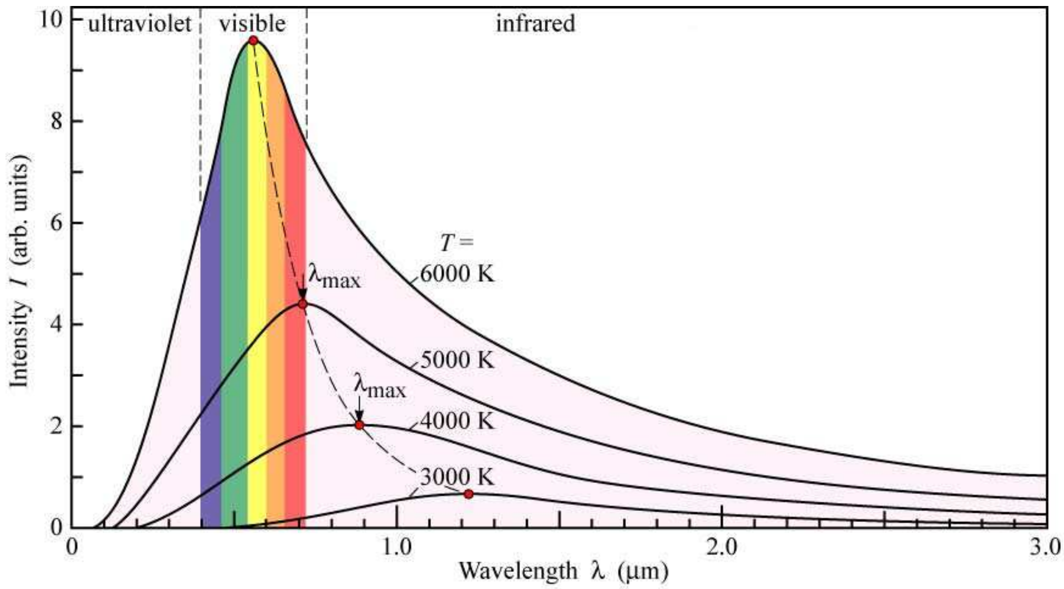

Figure 1.2: The spectral energy distribution of blackbody radiators as a function of wavelength. Planck curves of different temperatures are drawn as black lines, red dots indicate the maximum intensity of that curve. This figure was taken from E. F. Schubert (2006).

Since the stellar surface brightness is given as

$$F = \frac{L}{4\pi R^2} \tag{1.2}$$

where F is the flux density of an illuminated surface area of a sphere with radius R, the stellar luminosity can be written as

$$L = 4\pi R^2 \sigma T_{eff}^4. \tag{1.3}$$

The continuous lines in Fig. 1.1 stem from the estimated radii, given in solar units, of equation 1.3. Following this simple relation nicely illustrates that small objects are found at the lower left corner of the HRD, and large objects at the upper right corner. It has been predicted from stellar evolution models and approved by observations (of binary stars) that stars along the main sequence (MS) follow the so-called mass-luminosity relation (see e.g., Weigert & Wendker 1996):

$$L \sim M^{3.5} \tag{1.4}$$

Consequently, massive stars are located at the upper left end of the MS, whereas low mass stars are on lower right end of the MS. All the parameters explained above are pieces of information that are summarised in a HRD, which stresses the importance of this tool for astrophysics.

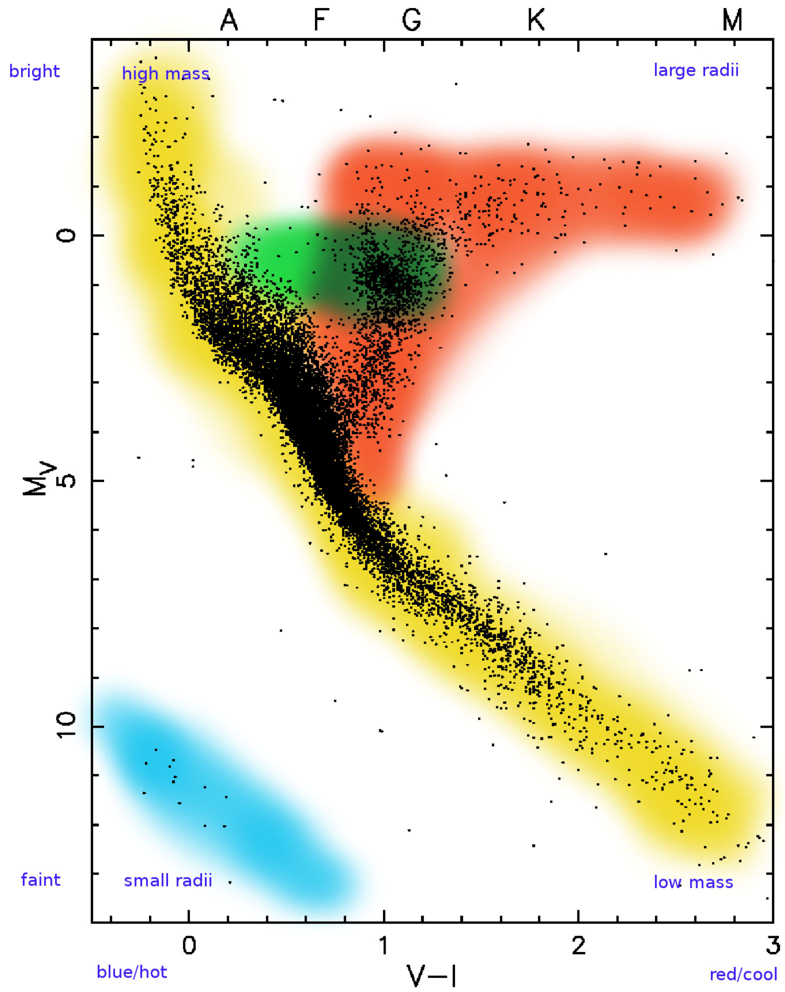

Figure 1.3: Colour-magnitude diagram (M_V vs $V - I$) of the solar neighbourhood with distances measured by the Hipparcos satellite within 10% accuracy. The letters at the top indicate the regions of the corresponding spectral type of the stars. The yellow region shows the location of the MS, the location of red giant branch and the asymptotic giant branch are labelled in red, the horizontal branch and red clump are coloured in green, and the region of white dwarfs in blue. The figure was taken form the lecture note of O. Pols (see http://www.astro.uu.nl/ pols/education/stev/).

In order to compare the observations with stellar evolution models, the absolute visual magnitude M_V is used as a measure of the luminosity and a colour index (e.g., $B - V$ or $V - I$) as a measure for the effective temperature. One example for such a colour-magnitude diagram (CMD) can be seen in Fig. 1.3, which shows the stars in the vicinity of the sun with accurate distances ($\sigma < 10\%$) obtained from the Hipparcos satellite. Most of the stars in this figure are located along a densely populated sequence, the MS. However, a significant fraction of stars in this CMD are giants that form a branch towards low temperatures and high luminosities.

The importance of the HRD, or rather the CMD, to stellar evolution studies becomes more evident, when comparing two different stellar systems: an open cluster and a globular cluster. The left panel of Fig. 1.4 illustrates the CMD of the Pleiades – an open cluster that consists of young stars. The right panel shows the CMD of M3 – a well known globular cluster, that is made up of old stars.

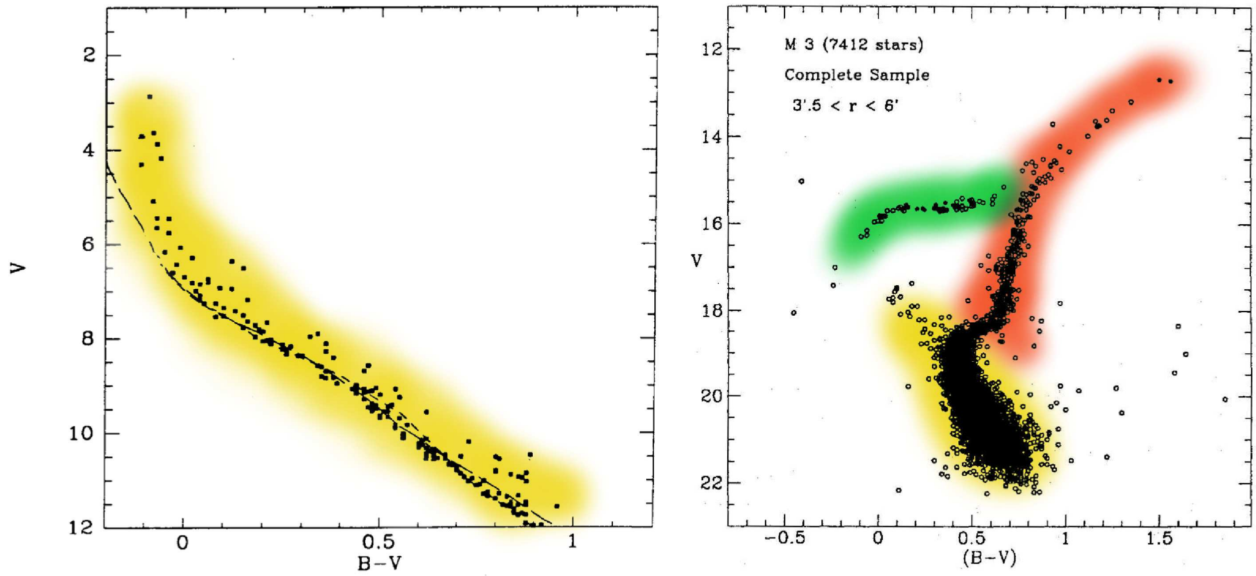

Figure 1.4: Colour-magnitude diagram of the open cluster M45 (Pleiades, left panel) and the globular cluster M3 (right panel). Both figures were taken form the lecture note of O. Pols (see http://www.astro.uu.nl/ pols/education/stev/).

As the cluster age increases, the most luminous (and therefore more massive) MS-stars (labelled in yellow in Fig. 1.4) start to disappear, and a red giant branch (RGB, labelled in red in Fig. 1.4) and eventually a horizontal branch (HB, labelled in green Fig. 1.4) become visible. At a certain luminosity in a CMD of globular clusters, a bend in the distribution of stars towards red colours is seen. This so-called turn-off point (TO) from the MS can be used as an age indicator (see chapter 5 for more information), owing to the well known duration of time that stars of a certain mass spend on the MS. This time is increasing with decreasing mass (see following section for more details).

1.2 Stellar Evolution: Star Formation to Main Sequence

Our understanding of the star formation process is mainly based on observations, which indicate that stars are formed out of giant **molecular clouds** with masses of about $10^{5-6} M_{\odot}$, typical dimensions of ≈ 10 parsec, and temperatures of 10-100 K (see e.g., Ehrenfreund & Menten, 2001; Williams et al., 2000). These clouds are in hydrostatic equilibrium with the surrounding interstellar medium, and their densities of 10-300 molecules cm^{-3} are increasing with decreasing temperatures. A fraction of about 1% of the cloud mass consists of dust, which makes them difficult to observe at visual wavelengths. If the equilibrium of a molecular cloud (or parts of it) is disturbed, it can become gravitationally unstable and start to collapse. This process can last for several millions of years (dynamical timescale $\tau_{dyn} \propto \rho^{-1/2}$) due to the low densities (ρ) involved. The Jeans mass of the cloud gives the maximum mass to fulfil the stability criterion. Since the Jeans mass decreases with increasing density, smaller fragments of the cloud are formed and, therefore, clumps of different mass form stars of different initial masses. If the density during the collapse exceeds a certain limit, radiation will be trapped within the central part of the cloud/fragment which leads to heating and an increase in gas pressure.

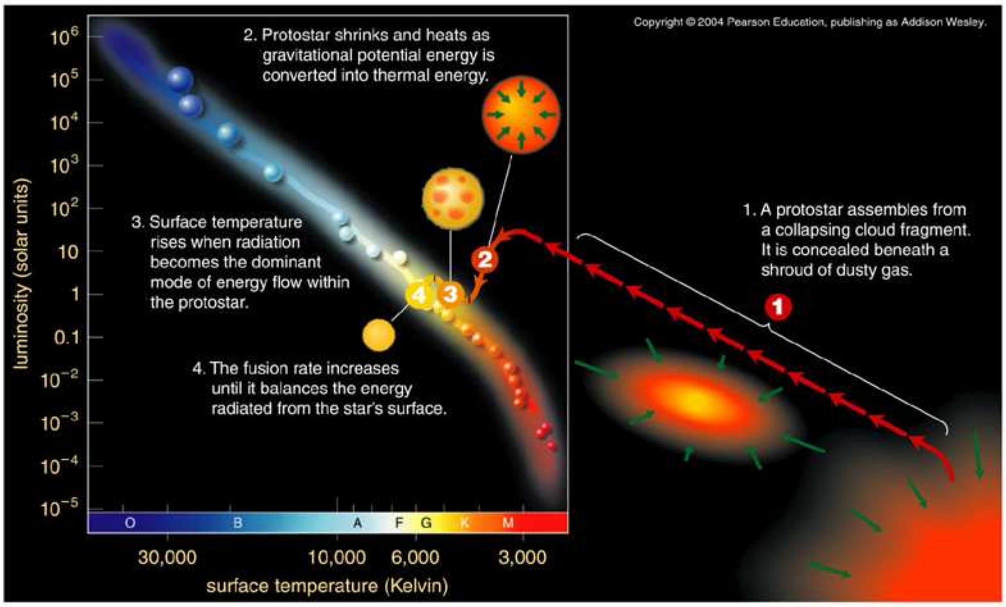

Figure 1.5: Schematic documentation of pre-main sequence evolution of stars with initial masses of about $1 M_{\odot}$. Near the abscissa of the HRD the colour scale for different spectral classes is given. Image credit: Pearson Education Inc. (2004), publishing as Addison Wesley.

As soon as the collapse slows down and the cloud core reaches hydrostatic equilibrium, it is called a **protostar** (see step 1 in Fig. 1.5). The rest of the cloud material keeps falling onto the protostar which forms an accretion disk that surrounds the protostar. One part of this energy goes into accretion goes into further heating of the core where at ≈ 2000 K molecular hydrogen starts to dissociate. As a consequence, the specific heat increases and another collapse follows until hydrogen is fully dissociated into atomic hydrogen (H). The hydrostatic equilibrium is restored and the temperature continues to rise. At $\approx 10^4$ K, H and helium (He) are ionized and the protostar further contracts until the ionization is complete, and the protostar is again in hydrostatic equilibrium. The surface cools and a temperature gradient builds up, transporting energy outwards.

In the **pre-main sequence phase** the accretion has finally slowed down (probably stopped) and the star settles on the Hayashi line appropriate for its mass (see step 2 in Fig. 1.5). The Hayashi line is an almost vertical line in the HRD (at $T \approx 3500$ K) which would represent fully convective stars in hydrostatic equilibrium. Hence, the region to the right of the Hayashi line is the so called forbidden region. Stars at higher temperatures can not be fully convective, at least a part of their interior must be in radiative equilibrium. Since the temperature in a pre-main sequence star is still too low for nuclear burning, it is evolving along the Hayashi line towards lower luminosities. If the central parts of the star decrease in opacity due to increasing temperature, a radiative core develops, and the star evolves away from the Hayashi line towards higher effective temperatures whereby the luminosity slightly increases (see step 3 in Fig. 1.5). Now, the luminosity is mainly determined by the mass of the protostar and the contraction continues until the central temperature becomes high enough to start H-burning (see step 4 in Fig. 1.5). Some time after the ignition, the energy release from the nuclear fusion in the centre stops the contraction, and the star settles on the zero-age main sequence (ZAMS). The time it takes for the protostar to reach the ZAMS is again dependent on its mass (massive protostars reach the ZAMS earlier than low-mass stars). Note that this picture of stellar evolution is very simplified, since effects of processes like e.g., rotation and magnetic fields were neglected in this scenario.

Stars on the **ZAMS** are in hydrostatic and thermal equilibrium with an almost homogeneous composition (mainly hydrogen). Most of their lifetime they will spend on the MS converting H into He and, depending on their initial mass, evolve slowly to cooler temperatures and/or higher luminosities. The evolutionary path of an object of a given stellar mass in the HRD (see Fig. 1.6) results from structural changes in the stellar interior as a consequence of its chemical evolution.

As can be seen from Fig. 1.6 the initial mass of a star is strongly correlated with its luminosity along the MS (see equation 1.4) as well as with its evolutionary history and final fate. Accordingly, the stars can be classified into three categories:

low-mass stars:	$0.8 \lesssim M/M_\odot \lesssim 2$
intermediate mass stars:	$2 \lesssim M/M_\odot \lesssim 8$
massive stars:	$M \gtrsim 8\ M_\odot$.

The mass limit for low-mass stars depends on the development of an electron-degenerate He-core after the MS phase (see lecture notes of O. Pols, 2010[2]). Note that stars of lower initial mass (known as very-low-mass stars with masses of $0.1 \lesssim M/M_\odot \lesssim 0.8$) follow a different evolution path and were therefore not included here. The upper mass limit for intermediate-

[2] http://www.phys.uu.nl/ pols/education/stev

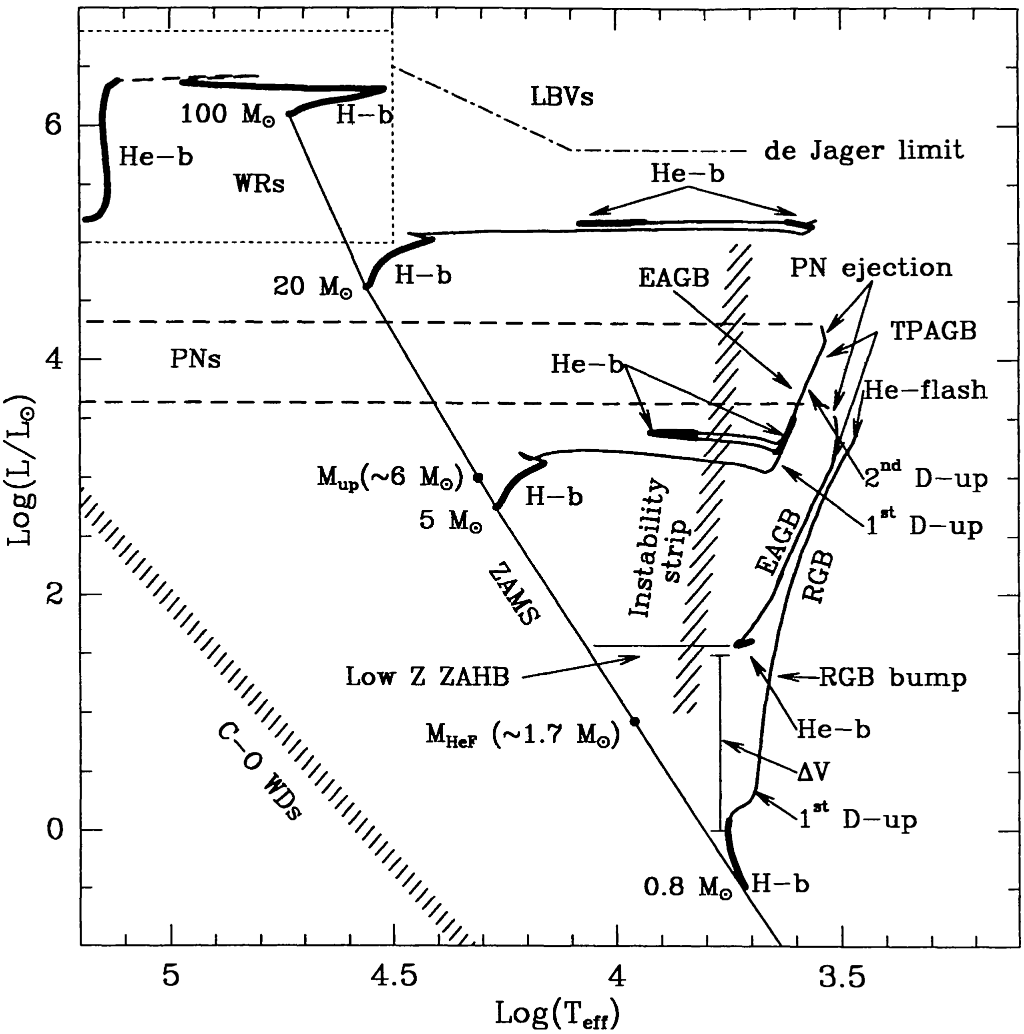

Figure 1.6: Evolutionary paths in the HRD for three different model stars of initial mass $0.8M_\odot$, $5M_\odot$ and $20M_\odot$ with a composition of [Z=0.008, Y=0.25]. H-b and He-b indicate phases of core H- and He-burning, respectively, thick lines mark stages of slow evolution. For further explanations of the different stages see text. This figure was taken from Chiosi et al. 1997.

mass stars is given by the non-degenerately ignition of He followed by the formation of a degenerate carbon-oxygen (C-O) core after He-exhaustion in the centre. Massive stars ignite C (in a non-degenerate core) and heavier elements until iron (Fe). However, these limits are not strict since they also depend on initial composition and other stellar properties.

Since the structural and evolutionary properties are directly related to the diverse burning phases in the central parts of the star, which again depend on the initial mass, they can be used as astrophysical 'clocks'. According to Einstein's relation for the equivalence between mass and energy ($E = mc^2$) the amount of energy, released during different nuclear fusion processes, is well known. The luminosity of a star with a certain mass stays almost constant during the phase of H-burning in the core. The initial energy supply of hydrogen is approximately proportional to the initial mass of a star ($E_H \sim M$). The duration of the H-burning phase (τ_H) is given as $\tau_H = E_H/L$ and, according to the above mentioned mass-luminosity relation of MS stars ($L \sim M^{3.5}$), this duration can be estimated as $\tau_H \sim M^{-2,5}$. Consequently, high mass stars are more luminous and, hence, consume their energy supply much faster.

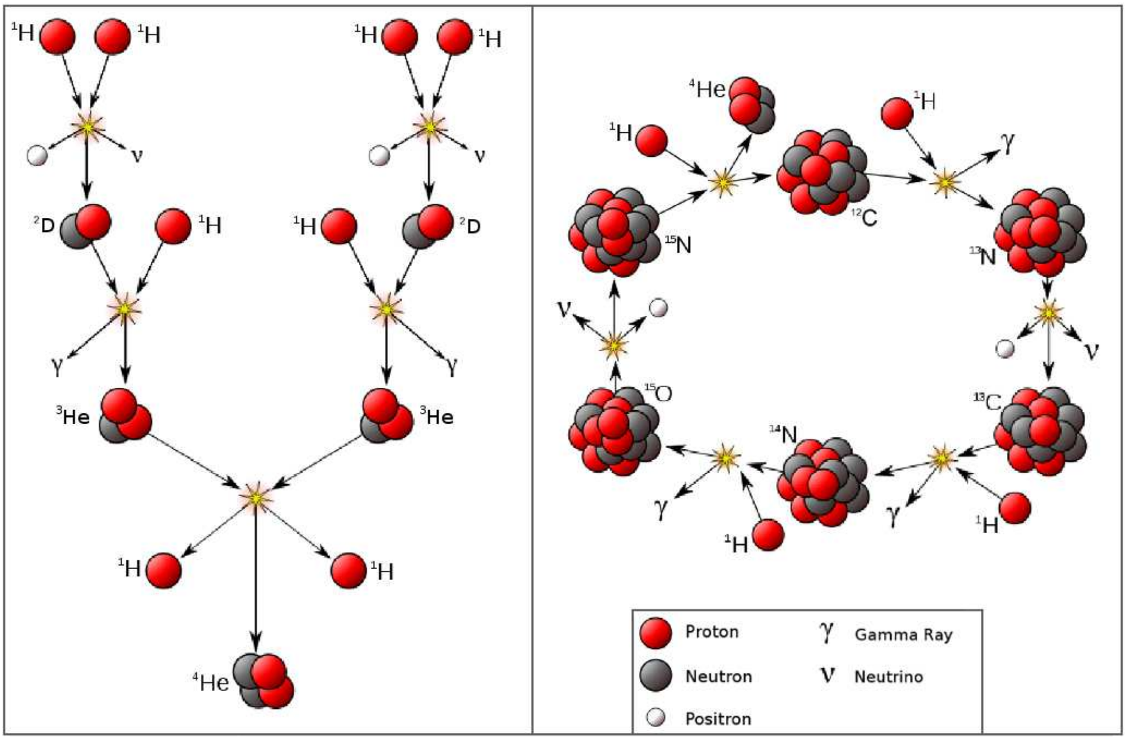

Figure 1.7: Schematic view of the most important H fusion reactions in stars. Left panel: proton-proton chain; right panel: CNO-cycle. Figure courtesy of Wikimedia Commons (http://commons.wikimedia.org).

Among all the different burning processes, the conversion of H into He is the most efficient – the released energy is about 10 times larger than for other nuclear reactions. There are two kinds of fusion reactions of H: the proton-proton (p-p) chain and the carbon-nitrogen-oxygen (CNO) cycle (see Fig. 1.7). The nuclear energy generation (ϵ) is a function of temperature, and for the p-p chain it is proportional to T^4, whereas for the CNO-cycle $\epsilon_{CNO} \propto T^{12}$ to T^{18}. Therefore, the p-p chain dominates at temperatures of 5-15 $\cdot 10^6$ K, and the CNO-cycle dominates at higher temperatures of about 15-30 $\cdot 10^6$ K (see e.g., Weigert & Wendker, 1996). Actually, there are three branches of the p-p chain. Two of them are also involving isotopes like lithium and beryllium, but the first p-p chain (illustrated in Fig. 1.7) is most relevant for stars with masses of about 1.5 $M_\odot$ (see lecture notes of O. Pols, 2010[3]). For MS stars above this mass limit (assuming that they are population I or II stars, that also contain a small fraction of elements heavier than H and He), the CNO-cycle becomes the dominant

[3]http://www.astro.uu.nl/ pols/education/nucleo

source of energy production. In contrast to the p-p chain reaction, the CNO-cycle is a cyclic process, where the CNO-nuclei are acting as catalysts (see Fig. 1.7). In terms of energy production, the CNO-cycle shown in Fig. 1.7 is most relevant, but there are three additional cycles. Cycle two is important for the nucleosynthesis, since it produces a large reservoir of ^{16}O. Cycle three and four require even higher temperatures than cycle one and two, therefore, they are only relevant for massive stars (for more information the reader is referred to Habing & Olofsson, 2003 and the lecture notes of O. Pols, 2010).

During the core H-burning phase, the amount of free particles decreases, and the core slightly contracts in order to stay in hydrostatic equilibrium. The change of mean molecular weight and opacity during the MS phase causes a slow increase of luminosity. At the same time, the star moves towards lower temperatures in a HRD (except stars at the lower end of the mass range for low mass stars, their temperature slowly increases, see Fig. 1.6). As soon as the burning process in the centre has ended, the core contracts. In low mass stars the H-exhausted contracting core becomes electron degenerated, which causes a temporarily cooling until the base of the RGB is reached. At this point, the central temperature is approximately the same as in the surrounding H-shell, that continues the burning process and adds mass to the He-core. Intermediate and high mass stars have convective cores during their MS phase. After the exhaustion of the central H, stars with masses up to about 15$M_{\odot}$ continue H-burning in a thin shell around a contracting and heating core. The time that a star spends on the MS strongly increases with decreasing mass.

1.3 Stellar Evolution: Red Giant to Horizontal Branch

1.3.1 Intermediate and High Mass Stars

In order to stay in thermal equilibrium the He-core needs to be isothermal, and a stable configuration of the star is only possible if the core mass does not exceed the so-called Schönberg-Chandrasekhar limit (≈10% of total mass). Otherwise the pressure within the core is not able to sustain the weight of the overlaying layers. The first part of this sub-giant branch (SGB) phase ($4.05 \leq \lg T \leq 4.2$ in Fig. 1.6) is relatively slow. During that time, the core shrinks slowly until it exceeds the Schönberg-Chandrasekhar limit. This leads to a much faster contraction of the core, whereas the envelope expands at the same time. Compared to the first part of the SGB phase the expansion phase ($3.7 \leq \lg T \leq 4.05$) is relatively short (10^5 yrs), therefore, the chance of observing stars in this stage is very small leading to a gap in the distribution of stars in the HRD (Hertzsprung gap). As the envelope temperature decreases and the opacity in the outer layers rises, the temperature and density gradients become steeper, and the envelope becomes unstable to convection. Since a large fraction of the energy released from H-shell burning is absorbed by the expanding envelope, the luminosity slowly decreases on the SGB. The evolutionary path of a $5M_{\odot}$ star can be seen in the HRD in Fig. 1.6 – an example for the evolution of stars in this mass range.

The star is now close to the Hayashi-line and has therefore a deep convective envelope. Hence, processed material from the bottom of the convective envelope is mixed up to the surface. This process is known as first dredge-up (1^{st} D-up, see Fig. 1.6). The following rise in luminosity at almost constant temperature is known as RGB phase. Along the RGB the star continues to expand due to the contracting core. If the central temperature of high- and intermediate-mass stars has reached approximately 10^8 K, and the density is about 10^4 gcm^{-3}, He-burning ignites in non-degenerate conditions, marking the end of the RGB phase. At the same time the star stops to expand, which corresponds to a local maximum in both, radius and luminosity (also known as tip of the RGB).

After He-ignition, the outer layers contract, and the temperature rises, hence, the star leaves the RGB. Nevertheless, the H-shell burning is still the dominating provider of the stellar luminosity. At this stage, a star is located on the HB in a HRD (or CMD). The mean luminosity of the HB is determined by the total stellar mass, leading to brighter HBs for intermediate-mass stars at the upper mass range than for those at the lower mass range (see range definition given in 1.2). The position of a He-core burning star on the HB mainly depends on its metallicity and on the mass of the H-rich envelope. According to Catelan (2007), stars that have lost a substantial fraction of their envelope mass during their RGB phase, fall on the blue part of the HB in a CMD, whereas those which were least affected by mass loss, are found on the red side of the HB. As stated by Chiosi (1997), metal-rich HB-stars occupy a narrow region near the RGB during the He-burning phase, and metal-poor ones evolve towards higher temperature (or bluer colours) at almost constant luminosity. Depending on the effect of these two above mentioned factors, the HB may intersect the shaded vertical band in Fig. 1.6. This band marks the region of the classical instability strip, where pulsating stars like Cepheids – important distance indicators in this mass range – are found (see chapter 2 for pulsating stars and chapter 4 for methods of distance determination).

The He-burning reactions in the core are also called triple-alpha process, since three nuclei of ^{4}He are fused to produce ^{12}C. The first step is to fuse two alpha particles (He-nuclei) into the very instable beryllium isotope (see Fig. 1.8). However, owing to the energy of the ^{8}Be isotope in its ground state, which is almost the same as for two alpha particles, and the fact that the reaction of ^{8}Be with ^{4}He has almost exactly the energy of ^{12}C in an excited state, still allows the production of carbon. These resonances were first predicted by Hoyle et al. (1953) and later experimentally confirmed by Cook et al. (1957).

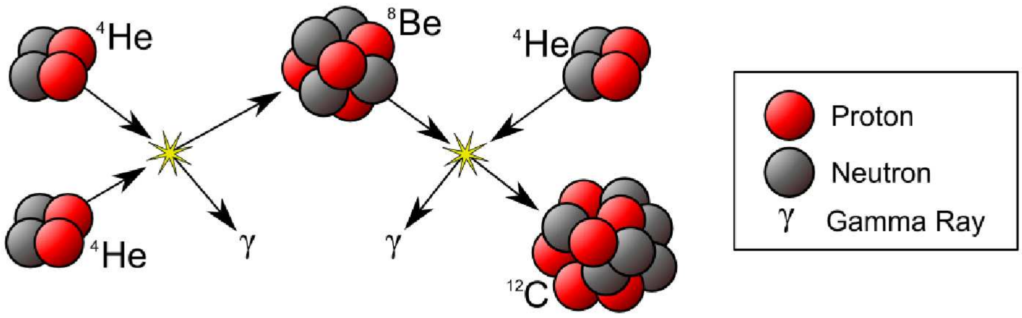

Figure 1.8: Schematic view of the triple-alpha reactions. First, two alpha particles (^{4}He) react to produce ^{8}Be, which then reacts with a further alpha particle to finally produce ^{12}C (see text for more information). Figure courtesy of Wikimedia Commons (http://commons.wikimedia.org).

The triple alpha reactions (labelled as He-b in Fig. 1.6) are very sensitive to temperature and, therefore, concentrated towards the stellar centre, which causes the formation of a convective core that grows with time. As soon as the increasing energy release of the He-core equals the decreasing release of the H-shell, the outer layers are rapidly contracting and become radiative. Consequently, the star moves towards higher temperatures in the HRD. The hottest point during the HB phase corresponds to a minimum in radius of the evolved star and to a maximum efficiency of the H-burning shell. With the decreasing fraction of energy produced in the H-shell, the star moves back towards the Hayashi line. Depending on the mass, the typical lifetime of the core He-burning stage is about 20 to 30% of the MS lifetime.

For stars with initial masses of up to $\approx 12 M_{\odot}$ the evolution is very similar with HBs extending to higher temperatures. In stars more massive than $12 M_{\odot}$, the star becomes hot enough to start He-burning before it reaches the Hayashi track appropriate for its mass, and the HB in the HRD disappears. Stars with $M \lesssim 4 M_{\odot}$ exhibit HBs during that phase that are close to the RGB. Apart from the initial mass of a star, the location and morphology of the HB is sensitive to a number of parameters like chemical composition, He-core mass and mixing processes (e.g., convective overshooting). Among the nuclear fusion processes during stellar evolution, the He-core burning phase is the longest lasting after H-burning phase. Accordingly, a well populated, wedge-shaped region is seen in the CMD of the solar vicinity (see green part in Fig. 1.3 and in CMDs of open clusters with ages of ≈ 1 Gyr.

1.3.2 Low Mass Stars

In contrast to intermediate-mass stars, low mass stars have a relatively dense core when they leave the MS. As soon as the He-core mass has reached $\approx$10% of the total mass, the Schönberg-Chandrasekhar limit is no longer relevant since the electron degeneracy now dominates the pressure (electron degenerated gas is independent of temperature). Low-mass stars remain in hydrostatic and thermal equilibrium during H-shell burning, hence, they exhibit no Hertzsprung gap in the HRD. For a star of $1M_\odot$ the SGB phase lasts about 2 Gyr, enough time to detect stars of this mass range in old globular star clusters (see Fig. 1.4 right panel). The typical turn-off mass of galactic globular clusters is $M \approx 0.85\,M_\odot$ (see e.g., Hippel, 1998), more massive stars are already in a later stage of evolution. Hence, this mean turn-off mass of $0.85\,M_\odot$ is equal to an age of 11×10^9 years. This also puts a lower limit on the age of the universe, in which these clusters must have formed.

The evolution along the RGB mainly depends on the core mass (instead of the total mass on the MS). By reaching the RGB, the He-core has become electron degenerate and a large part of the outer layers are convective – 1^{st} dredge-up (DUP) occurs. Hydrogen burning continues in a shell around the core during the ascent of the star along the RGB close to the Hayashi line. He-ashes from H-shell burning adds mass to the core, which becomes increasingly degenerate. As the envelope of the red giant is expanding, the outer layers become loosely bound, and mass loss occurs. A change in mass corresponds to a change of stellar structure and is therefore of crucial importance to calculate realistic evolution tracks. However, the processes driving the mass loss in red giants are not well understood. For that reason, the empirical Reimers mass loss law is applied in most stellar evolution models. According to this formula, a $1M_\odot$ star is going to lose about $0.3M_\odot$ of envelope mass by the time it reaches the RGB-tip. Near the tip of the RGB, at a central temperature of about 10^8 K, He ignites violently off-centre. As the nuclear He-burning progresses inwards, the degeneracy of the core is lifted. This thermonuclear runaway is also known as He-flash (see evolution track of a $0.8M_\odot$ star in Fig. 1.6) and marks the end of the RGB phase of low mass stars. All low-mass stars at the RGB-tip have about the same core mass ($M_{core} = 0.45$ to $0.50\,M_\odot$, Chiosi, 1997). Consequently, they have similar luminosities, independent of their initial masses and chemical composition. For this reason, stars at the RGB-tip are important standard candles and distance indicators (see section 4.3).

After the He-flash, low mass stars undergo a phase of quiet He-core burning. Their location on the HB is based on the same principles as for intermediate stars (mass loss of the envelope and stellar metallicity). Metal-rich stars in this mass range, that are members of a star cluster, would therefore build a red clump in a CMD, instead of a loop-like HB (as described in the previous subsection). However, during the HB phase of low-mass stars, mass loss is only important for stars below $1M_\odot$ (typical for old globular clusters) – stars above this limit are always located in the red clump (see Chiosi, 1997 and references therein). The CMD of M3, an old globular cluster of low metallicity, is shown in the right panel of Fig. 1.4. Its HB crosses the classical instability strip at a fainter luminosity if compared with intermediate mass stars. In the HB region of M3, a lot of pulsating stars of RR Lyrae type were observed – more than 200 according to Clement et al. (2001). These pulsating low mass stars are commonly found in globular clusters and are often used as standard candles to measure galactic distances (like Cepheid variables, which are more massive and were therefore mentioned in the previous section). RR Lyrae stars are also important objects to study the different HB morphologies of globular clusters, since it is still an open question which factors (beside the ones mentioned above) determine the HB morphology (see Chiosi, 1997 and Suda et al. 2007).

1.4 Stellar Evolution: Asymptotic Giant Branch

The AGB phase is particularly important to understand the origin of various elements heavier than H and He, and how they influence the chemical evolution of their hosting systems. AGB stars are also the major contributors of the integrated light of stellar systems of intermediate age and, therefore, important tools to study extra-galactic systems (Battinelli & Demers, 2004a).

The AGB is populated by evolving stars of low and intermediate mass. As mentioned above, the limits of low mass stars are defined by the development of an electron degenerate core after leaving the MS. Intermediate stars ignite their He-cores under non-degenerate conditions. The AGB phase of low-mass stars and intermediate mass stars up to $8M_{\odot}$ is characterised by an electron degenerate core of O and C, which is surrounded by two thin shells in which nuclear H- and He-burning occurs. AGB stars are also grouped into three different classes (given in MS masses):

low-mass AGB stars:	0.8 to $4M_{\odot}$
massive AGB stars:	4 to $8M_{\odot}$
super AGB stars:	$\gtrsim 8M_{\odot}$ to 10-12$M_{\odot}$.

As illustrated in Fig. 1.9, the mass range of each class is determined by different burning and mixing processes in the stars. During the thermally pulsing AGB (TP-AGB) phase, low mass AGB stars are able to form C-rich stars and produce heavy elements via the s-process (see Sect. 1.4.2). Owing to hot-bottom burning (HBB), massive and super AGB stars remain O-rich, but only super AGB stars are massive enough to ignite C (Pumo & Siess, 2006).

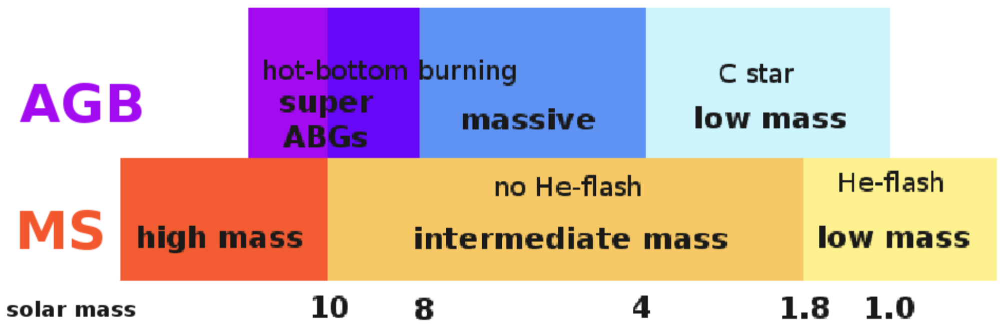

Figure 1.9: Classification of stars on the MS and the AGB according to their initial masses in solar mass units. The figure is based on a idea from Herwig (2005) and has been modified by the author.

After the exhaustion of He in the centre, the star sustains its ascent along the giant branch towards higher luminosities. For low mass AGB stars the AGB is located at similar luminosities but at slightly higher temperatures relative to the RGB. This part of the evolutionary track in a HRD indeed looks asymptotic and is the reason for using the term ’asymptotic giant branch’. However, for stars with $M \gtrsim 2.5M_{\odot}$ the term has no morphological meaning (Iben, 1983). Two phases are usually distinguished: the early AGB (EAGB) phase and the phase, in which the stars start to thermally pulse (TP-AGB phase).

1.4.1 Early AGB Phase

While the abundance of He in the centre goes to zero, He-burning continues in a shell around a degenerate C-O core. The nuclear energy production is dominated by the He-shell that burns outward in mass. In the meantime, the H-layer around the He-shell expands and cools so efficiently that H-shell burning extinguishes. Convection of the envelope sets in and moves inwards.

According to Iben (1983), the convective envelope of stars of $\gtrsim 4.6 M_{\odot}$ (for solar composition), reaches layers with processed material of the CNO-cycle. These elements (mainly He and N), are then dredged up to the surface (second DUP). In the HRD such a star evolves almost parallel to the RGB (see EAGB in Fig. 1.6). Subsequent shrinking of envelope leads to a decrease in luminosity and heats the inner region of the convective envelope. Consequently, the H-shell reignites, which marks the end of the early AGB phase.

In low-mass AGB stars the H-burning shell remains active, which avoids a deeper penetration of the convective envelope, hence, no second DUP occurs.

1.4.2 Thermally Pulsing AGB Phase

At this stage, the He-burning shell is very thin compared to its radius, and nuclear burning becomes thermally unstable. For about 90% of the time during the TP-AGB phase, the H-shell is the dominant source of energy, periodically interrupted by thermonuclear He-shell-flashes (a.k.a. thermal pulse). In the time between two pulses, the H-shell adds its nuclear ashes to the He-rich zone between the shells. At a critical mass limit of this intershell region, the temperature and density at its bottom rise. Triple-alpha reactions occur, and the energy production rate increases. If it exceeds the rate at which energy is carried out by diffusion, a thermonuclear runaway (thermal pulse) occurs (discovered by Schwarzschild & Härm, 1965).

This sudden rise in energy production generates a convective layer between the H- and He-shell, the so called pulse-driven convective zone (PDCZ, see Fig. 1.10). The PDCZ enriches the intershell region with the products of He-burning. After the expansion, the temperature of the He-burning zone decreases, and the burning rate drops dramatically. The PDCZ between the shells disappears, and quiescent He-shell burning sets in. As a further effect of the large energy release, the matter at the bottom of the H-shell is pushed outwards to regions of cooler temperatures, and the H-shell temporarily extinguishes. The outer convective layers are now able to penetrate the intershell region and transport processed $^{12}\mathrm{C}$ further up to the surface. This phenomenon is known as third DUP and repeats with every thermal pulse. Furthermore, the convective envelope also mixes protons to the intershell, which gives rise to the formation of the $^{13}\mathrm{C}/^{14}\mathrm{N}$-pocket (see Fig. 1.10). The matter, that has been pushed outwards, falls back again to regions of higher temperatures and the H-shell reignites. This marks the end of one third DUP event and another long phase of stable H-shell burning follows until the next thermal pulse sets in. Depending on the mass the duration

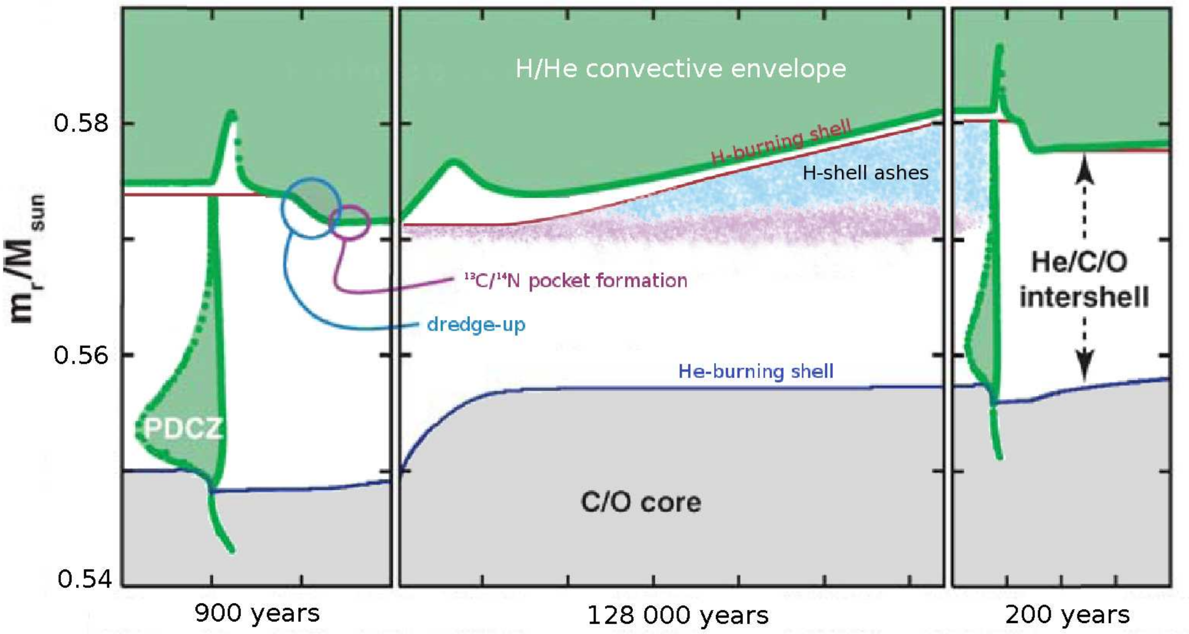

Figure 1.10: A Kippenhahn diagram illustrating two consecutive thermal pulses of a 2 $M_\odot$ star with Z=0.01 and the third dredge-up. Convections zones are drawn in green colours, the ^{13}C pocket is marked in purple, ashes of H-burning are shown in light blue colours and the C-O core is coloured in grey. Note, that the time scales in each panel are different, the ordinate gives the mass coordinate in solar units. This figure was taken from Herwig 2005 and slightly adapted by the author following an idea of Lederer (2009).

of the interpulse period varies between ≈1000 yrs and 50 000 yrs (shorter for more massive stars).

As illustrated in Fig. 1.11, AGB stars are very complex objects characterised by a variety of different processes that take place at different locations within the star. Compared to the small cores, AGB stars have huge atmospheres of low density and low temperature and, therefore, exhibit no well-defined boundaries. Furthermore, they are characterised by dynamical processes as pulsation, shock waves, dust formation and mass loss. The spectral features are significantly different for stars with O-rich and C-rich atmospheres. Initially, the abundance ratio of n(C) over n(O) is smaller than one (C/O$<$1) and most of the stars can be classified as O-rich AGB stars of spectral type M. For AGB stars with initial masses below $\approx 4 M_\odot$ the atmospheric chemical composition can change dramatically since processed elements, most notably ^{12}C, are dredged up to the surface by convective mixing after a thermal pulse. Depending on the C/O-ratio their spectral type changes from K or M via S to C (C/O$\geq$1, C-rich AGB star, see Groenewegen 2007).

Owing to the low temperatures in the atmosphere, most of the C and O atoms are bound into molecules. In the upper half of Fig. 1.11 examples for molecules of O-rich AGB stars are given, and examples of molecules of C-rich stars can be seen in the lower half.

For AGB stars with initial masses exceeding $4 M_\odot$, the outer part of the H-shell is included in

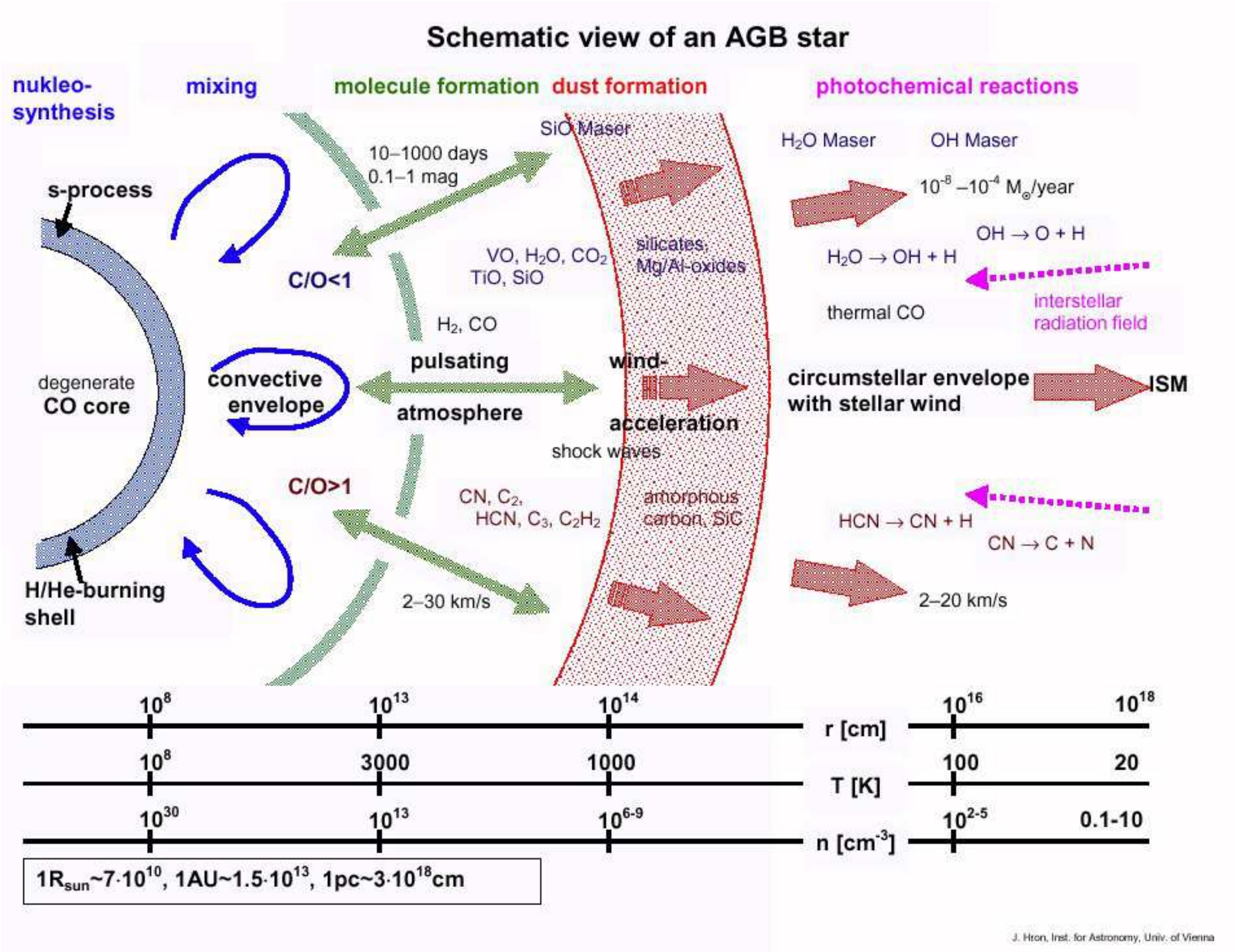

Figure 1.11: Schematic view of an AGB star. This figure clearly illustrates the various and complex processes (see coloured notes at the top) and their location within an AGB star. At the bottom three different scales for distance, temperature and density are given with origin in the centre of the AGB star. For comparison reasons, the box below the scales lists the radius of the sun, the length of an astronomical unit and the length of one parsec. This figure was kindly provided by J. Hron and is available online at http://www.univie.ac.at/agb/.

the convection of the envelope. Consequently, the temperature at the bottom of the convective envelope rises, and the dredged up C is efficiently converted into N. This process, called HBB, causes massive AGB stars to remain O-rich. In the final stages of the AGB phase, the envelope mass has reduced significantly by mass loss processes, and HBB becomes less efficient. According to Frost et al. (1996), the DUP of carbon in intermediate mass stars with small envelope masses might become more efficient than HBB, which would lead to the most luminous C stars. Metallicity also plays an important role, since the lower mass limit for hot-bottom burning to occur, decreases with lower metallicity.

Approximately half of the known elements heavier than iron are produced via the so called s-process (Arlandini et al. 1999). These elements are formed through slow (if compared to the competing β-decay) neutron captures. During a neutron capture process, the mass number of an isotope increases by one, whereas the following β-decay has no influence on the mass number. In this way, heavier elements with mass numbers up to 204 are formed (Herwig, 2005). There are two possible sources of neutrons for the s-process which are found in the interior of AGB stars (e.g., Straniero et al. 2003). One source is the reaction $^{13}\mathrm{C}(\alpha,\mathrm{n})^{16}\mathrm{O}$. The required isotope $^{13}\mathrm{C}$ is built after a third DUP event, when the convective envelope enriches the intershell region with protons, via the $^{12}\mathrm{C}(\mathrm{p},\gamma)^{13}\mathrm{N}(\beta^{+})^{13}\mathrm{C}$ reaction. The second source is the $^{22}\mathrm{Ne}(\alpha,\mathrm{n})^{25}\mathrm{Mg}$ reaction, which requires higher temperatures than at the bottom of the PDCZ. One tracer for the occurrence of the third DUP is the s-process element technetium. It is radioactive without any stable isotopes, however, its half-lifetime is still long enough to be observed in stellar spectra of AGB stars. The counterpart of the s-process is the rapid neutron capture process (r-process), which requires very high temperatures, which are provided in objects like supernovae, novae, and X-ray binaries.

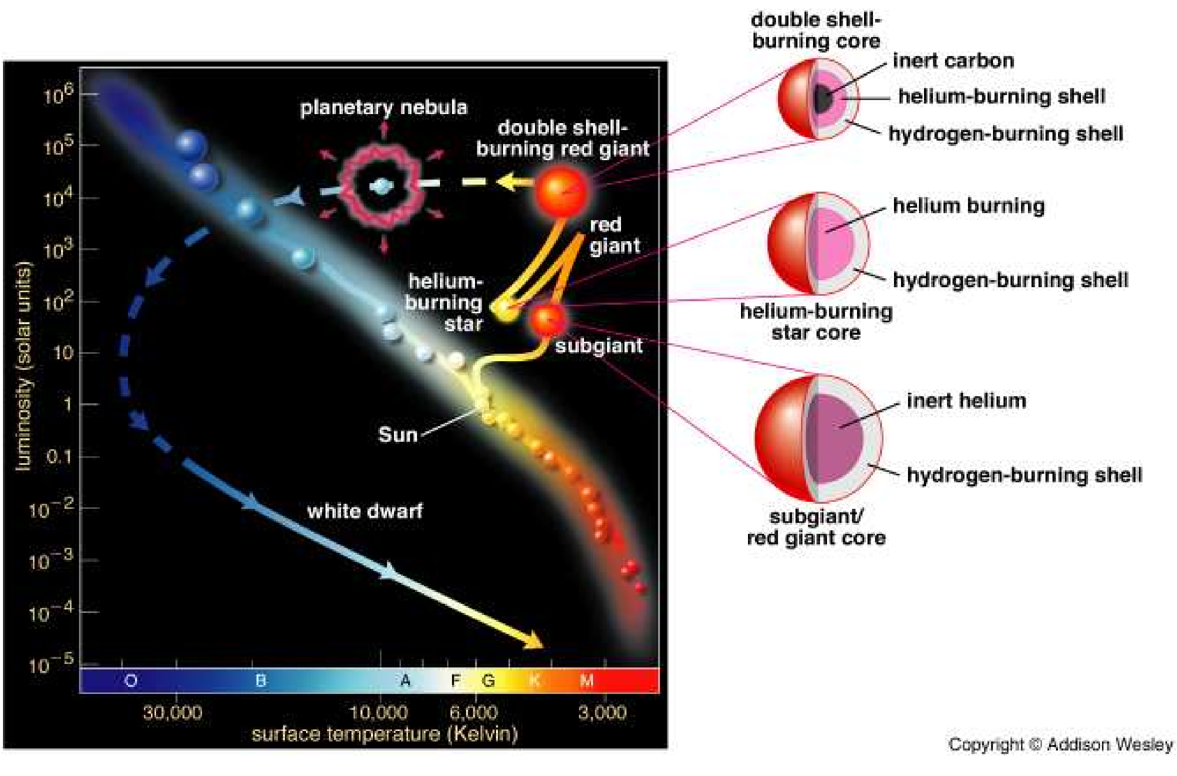

Figure 1.12: Schematic evolution track of a $1M_{\odot}$ star in the HRD. On the right hand side, the mass fractions of the star during different evolutionary phases is shown. The dashed line marks the phases of very fast evolution after the AGB phase (see 1.4). Image credit: Pearson Education Inc. (2004), publishing as Addison Wesley.

Towards the end of the TP-AGB phase, the stars undergo a period of heavy mass loss. Pulsations with increasing amplitudes and dust driven winds push the matter of the outer envelope to distances, where it loses its gravitational bound to the star and merges with the interstellar medium. During that time, the luminosity increases with decreasing mass of the H-shell. The duration of the TP-AGB phase is determined by the growing mass of the degenerate C-O-core and the decreasing mass of the outer layers. As soon as the whole envelope is gone, which marks the end of this phase, low and massive AGB stars turn for a very short time into planetary nebulae and finally end their lives as cooling C-O white dwarfs (see Fig. 1.12). Super AGB stars either form the most massive white dwarfs with ONeMg cores or are going through a electron-capture supernova before collapsing into a neutron star (Pumo & Siess, 2006). The interstellar medium is enriched with the processed material of AGB stars, and forms new clouds of gas and dust, which are the building blocks of the next generation of stars – the cosmic matter circuit closes.

2
Variable Stars

In general, all stars that change their brightness are called variable stars (excluding brightness changes owing to stellar evolution). Depending on their nature of variability, they are divided into extrinsic (e.g., rotating variables, eclipsing variables) and intrinsic variables (e.g., eruptive variables, pre-main-sequence variables, pulsating variables). Stellar pulsation provides information about stellar parameters like mass, radius, chemical composition, and internal structure. This approach is of great help in order to understand the properties and ongoing physical processes of these stars as well as the hosting stellar system to which they belong. There are various types of pulsating stars, which are located in specific regions in the HRD (see Fig. 2.1). This thesis focuses on long period variables (labelled as Mira and SR in Fig. 2.1), which belong to the group of pulsating variables. For more information on variable stars in general, the reader is referred to Percy (2007), where all above mentioned groups are described in more detail.

2.1 Pulsation of Classical Instability-Strip Stars

Our general understanding of pulsating stars relies on the theory developed by Eddington (1917, 1918). The basic idea of stellar pulsation is that perturbations around a hydrostatic equilibrium may grow to the observed level of amplitudes. The perturbation of pressure in the stellar interior causes the propagation of acoustic waves throughout the star. Since sound waves can not travel in vacuum, they are trapped inside the star. If they are close to the eigenfrequencies (depending on the structure of the system), their amplitudes become large and stable enough to observe them.

The most interesting aspect of stellar variability is the information about the internal structure, since

$$P\sqrt{\rho} = Q \tag{2.1}$$

where P is the period, ρ the mean stellar density, and Q the pulsational constant for a given mode of pulsation. The mean density depends on the stellar mass and radius, which are affected by stellar evolution. Furthermore, RGB and AGB stars experience phases of mass loss – leading to a change in mean stellar density and thus pulsation period (see, e.g., Lebzelter & Wood 2005). This period-density relation relates an observational quantity like the pulsation period to structural properties of the star and therefore provides an important

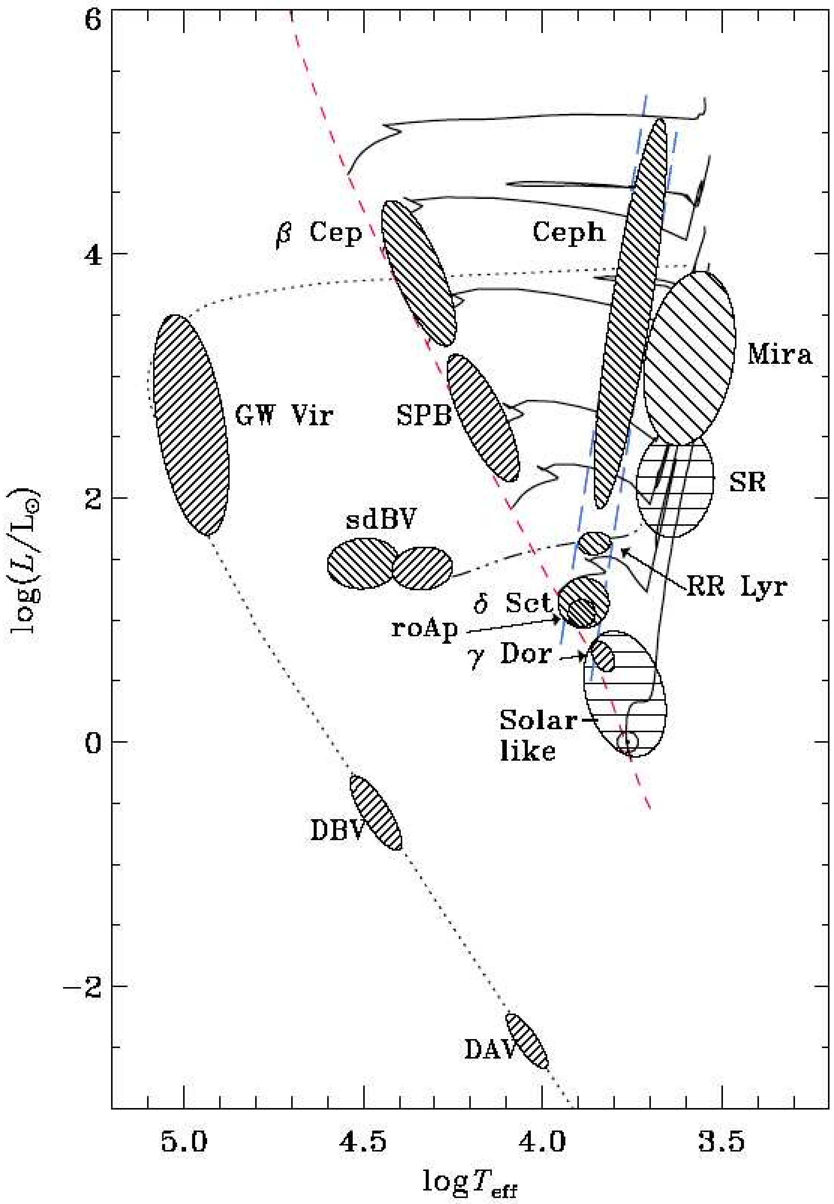

Figure 2.1: The HRD of pulsating variables taken from J. C. Dalsgaard (see http://astro.phys.au.dk/ jcd) and slightly modified by the author. The different types of pulsing stars are marked as hatched regions, the main sequence is drawn as red dashed line and the blue dashed lines indicate the so called instability strip. The continuous lines represent evolution tracks of different initial masses.

input for stellar evolution models.

In the linear analysis of pulsation, the perturbations of the stellar structure are of the form: $r+\delta r$, $P+\delta P, \rho+\delta\rho, L+\delta L$, where r is the radius of the considered mass shell, P the pressure,

ρ the density, and L the luminosity. Terms of second or higher orders are neglected, which is valid for small perturbations. Under the assumption of adiabatic conditions (no exchange of energy during the propagation), one obtains a discrete number of radial eigenfrequencies (ω_n), which are characterised by nodes:

$$P_0 = 2\pi/\omega_0, \quad P_1 = 2\pi/\omega_1, \quad P_2 = 2\pi/\omega_2, ... \tag{2.2}$$

representing the fundamental period (no node), first harmonic (one node) and second harmonic (two nodes), respectively.

In Fig. 2.2 an illustration of a radially pulsating star with two node lines in the stellar interior is given. The arrows indicate regions of expansion and contraction, respectively, whereas the

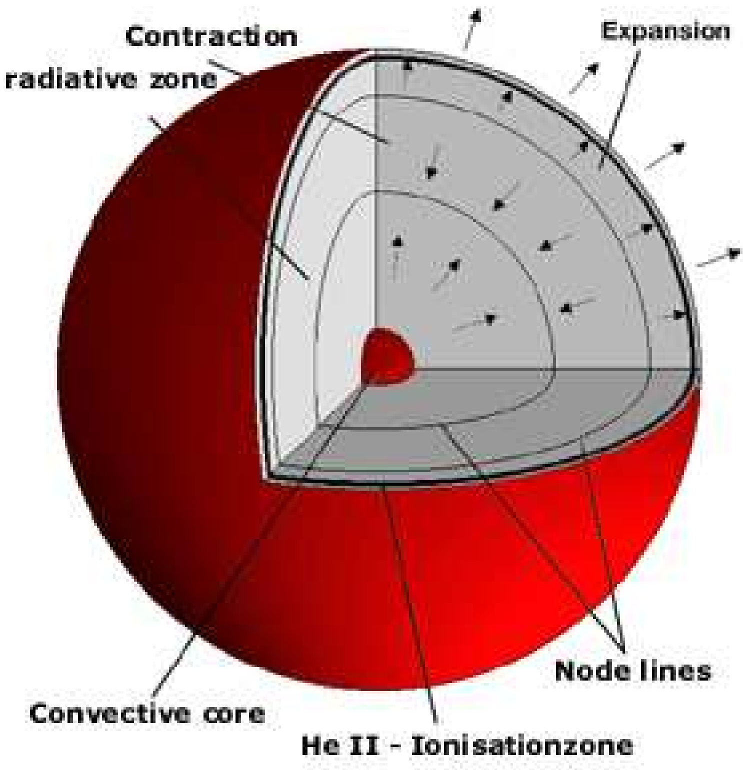

Figure 2.2: A schematic view of a variable star exhibiting two radial nodes (taken from Zima 1999).

location of the node lines remains constant. In order to drive stable stellar pulsation, a certain mass fraction of the star needs to be sensitive to physical perturbations. Stellar atmospheres are reacting to structural changes, but without a driving mechanism these perturbations would be damped out within a few thousand years. The pulsation can only survive if a zone in the stellar provides the energy to compensate the damping mechanisms in the rest of the star. The He- and H-ionization zones, located near the surface of stars populating the instability strip in the HRD (as Cepheids and RR Lyrae stars, see Fig. 2.1), fulfil these requirements, provided that they contain enough mass in order to keep the pulsation stable.

The associated mechanism driving the pulsation in the instability strip is related to the opacity κ, which is the absorption coefficient for radiation. This so called κ-mechanism was first described by Cox & Whitney (1958). An oscillation driven by the κ-mechanism requires that a part of the radiative flux from the stellar interior is trapped in the partially ionised He- and H-layer, which is then converted to the energy of the pulsation. During the phase of compression in a pulsating star, the released energy is mainly used to further ionise material in the H- and He-zones. Therefore, the temperature of those layers remains almost constant instead of heating up. The increasing amount of free electrons adds to the scattering of radiation, because of which the opacity still remains high but pressure is enhanced causing the star to expand again. During expansion the matter in the ionisation zones recombines and the opacity decreases, allowing the release of the stored energy therein until gravity forces the star to contract again.

For stars of higher effective temperature, the ionization zones are found further outwards, their mass fraction decreases and the κ-mechanism can no longer drive the pulsation (see, e.g., Baker & Kippenhahn 1962). On the other hand, for stars of lower effective temperature the outer layers become convective, which affects the pulsational stability (Xiong & Deng, 2007). This explains both, the hot and the cool border of the instability strip in a HRD (or CMD).

Cepheid variables serve as important standard candles, since they follow a well defined period-luminosity relation (PLR, see Leavitt & Pickering 1912). The current P-L relationship is based on Cepheids detected in the Large Magellanic Cloud (LMC). When applying a mean distance modulus of $(m-M)_0 = 18.50 \pm 0.1$ for the LMC, one can obtain the absolute distance from this PLR. In order to decrease the dispersion of the relation, it is of advantage to obtain measurements in two different photometric filters. This has been done by, e.g., Chiosi et al. (1993), Saio & Gautschy (1998) and Bono & Marconi (1999), defining a period-luminosity-colour relation for Cepheids. Taking measurements in the K-band, has the further advantage of being almost unaffected by interstellar extinction. Theoretically, the mean brightness of Cepheids decreases with increasing metallicity but a final empirical calibration (assuming a universal PLR of Cepheids from the LMC) still needs to be established (see e.g., Stift 1995, Kennicutt et al. 1998, Turner et al. 2010).

2.2 Long Period Variable Stars

RGB and AGB stars are highly evolved stars, and variability is a common feature of this evolutionary phase. The He-shell flashes occurring during each thermal pulse (see 1.4.2) additionally affect the pulsational behaviour. Moreover, a fraction of the observed light variations might be caused by circumstellar matter, clustered in orbiting clouds. Hence, understanding the pulsational behaviour of AGB stars is one of the most challenging topics, owing to various different parameters influencing the pulsation (e.g., convection, mass-loss, He-flashes). As already stated by Wood (2000), red giants "are probably the least understood of all variable stars", despite of all the technological progress and increasing number of detected red giant variables we see today.

Long-period variables (LPVs) is the generic term for variable red giant stars – also known as Mira variables, semi-regular and even irregular variables (although the light curves of the last group do not allow to obtain a period). The periods of LPVs range from about 30 up to a few thousands of days with amplitudes ranging from one tenth to approximately ten magnitudes in the visual. According to Jorissen et al. (1997), all red giants redder than $(b-y) = 0.8$ are variable at a level of at least a few percent. By studying HRDs from the Magellanic Clouds obtained from the MACHO survey, it turned out that at least 90% of the red giants above the RGB-tip (excluding Cepheids) are variable (see Lattanzio & Wood 2003). Most of the LPVs are found between the RGB-tip and the minimum brightness of TP-AGB stars, which is approximately 0.75 mag fainter than the RGB-tip in the I-band. Hence, variables above the RGB-tip have to be on the AGB, while stars below the RGB-tip must be on the RGB. Their progenitors have initial masses of ≈0.85-8$M_{\odot}$. A few percent of these stars are located above and below the above mentioned limits.

2.2.1 The Pulsation of Red Giant Stars

Unlike variable stars which are located at the classical instability strip (see subsection 2.1), the nature of the variability of LPVs is not well understood. Because of the deep convective layers in these stars, the κ-mechanism (see subsection 2.1) can not drive the pulsation efficiently in red giant stars any more. Instead, convection dominates the energy transport and becomes the main mechanism of damping and exciting pulsation in the stellar atmosphere, overwhelming the κ-mechanism. One of the major difficulties for the calculations of stellar pulsation models therefore is to properly take convection into account (see Xiong & Deng, 2007).

In first approximation, linear radial pulsation models are calculated (e.g., Fox & Wood, 1982), where convection is treated according to the local mixing-length theory (Böhm-Vitense, 1958) – a simplified picture of the turbulent energy transport. These models are able to explain the general characteristics of the observed LPVs and illustrate the location of the stellar interior where the different radial modes are excited. For a star of $1M_{\odot}$ evolving along the AGB, the growth rate (fractional increase of amplitude per year) of the second overtone is the highest at low luminosities, for the first overtone it is the highest at intermediate luminosities, and for the fundamental mode at high luminosities. Growth rates are good indi-

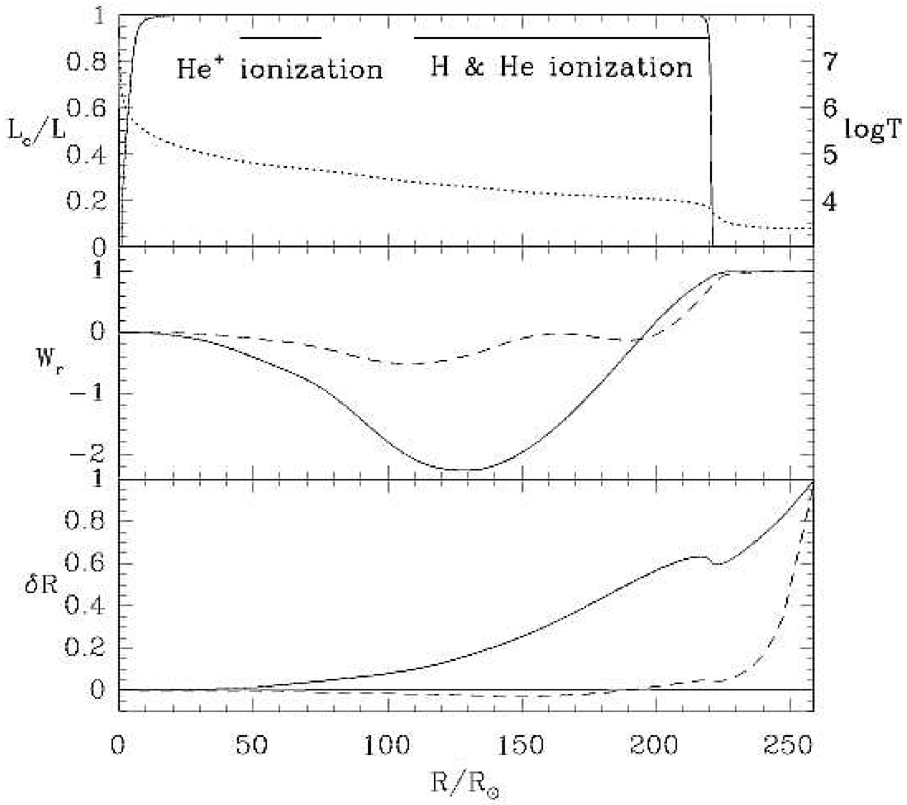

Figure 2.3: This figure displays several theoretical quantities that are associated with pulsation of red giant stars. The continuous line in the upper panel shows the fraction of the energy flux, which is carried by convection, and the dotted line the course of temperature with stellar radius. The second panel gives the partial work integral for the fundamental mode (continuous line) and the first overtone (dashed line), respectively. The third panel demonstrates the amplitude of the radius perturbation relative to the surface (continuous line: fundamental mode, dashed line: first overtone). This figure was taken from Lattanzio & Wood (2003) and adapted by the author.

cators for the pulsation mode, although a high growth rate does not necessarily imply that this mode is indeed excited. Some properties of more recent linear radial pulsation models from Lattanzio & Wood (2003) are shown in Fig. 2.3. These models take the variations of the convective flux during one pulsation cycle into account, but leave out effects of turbulent pressure. According to their results, given in the intermediate panel of Fig. 2.3, the driving zone for pulsation is located at regions where the partial work integral is increasing. Regions further inwards, where the partial work integral decreases, are therefore damping regions. Hence, the regions that are driving the pulsation can be attributed to the H- and first He-ionisation zone in the star (see top panel of Fig. 2.3). From the bottom panel of Fig. 2.3 it can be seen that the amplitude of the fundamental mode is approximately proportional to the radius, while overtones are located in outer regions close to the stellar surface. According to these models, an AGB star first becomes unstable in second or third overtone and, as the star evolves towards higher luminosities, switches to lower overtones or fundamental mode. AGB stars pulsating in more than one mode are theoretically explained by similar growth rates at a certain luminosity. Still, some results have to be treated carefully, owing to the strong dependence of pulsational stability and growth rates on energy transport.

An improvement of these models requires a time-dependent non-local treatment of convection including effects of turbulent pressure, turbulent viscosity (a damping factor), and turbulent energy diffusion. Owing to the huge convective zones in red giant stars, pulsation is driven by the dynamical coupling between convection and oscillation. Models of Xiong et al. (2007) for non-adiabatic oscillations of Red Giants make use of the non-local time-dependent statistical theory of convection from Xiong et al. (1998). Their treatment of the turbulent pressure of convection and its dynamical interaction with pulsation predicts a red giant instability strip (see Fig. 2.4), which is almost parallel to the classical instability strip (where Cepheids are found), but at lower temperatures.

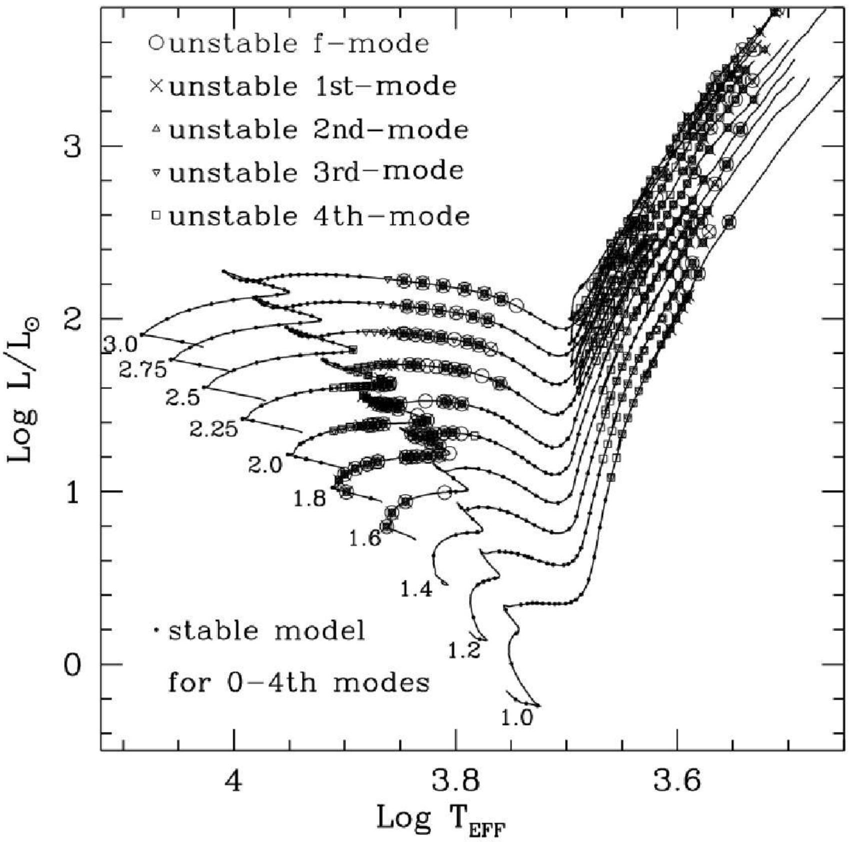

Figure 2.4: The HRD with evolutionary tracks for stars of 1-3$M_\odot$. Superimposed large symbols (see legend in the upper left corner) indicate stars that are pulsationally unstable and small dots show pulsationally stable stars. This figure was taken from Xiong & Deng (2007) and slightly adapted by the author.

This second instability strip has been known from observations, however, Xiong et al. (2007) showed for the first time that this region in the HRD could be explained by theoretical means. Moreover, they also clearly demonstrate why stars located between those instability regions are pulsationally stable. The models relate high order overtones to giants of low luminosity (observed for variable RGB stars), and lower overtones to giants with high luminosity (observed for pulsating AGB stars). Near the tip of this red giant instability strip, the stars are found to pulsate in fundamental or first overtone mode only, as expected for large amplitude LPVs. This behaviour is confirmed by observations of LPVs in star clusters, as for example in the galactic globular cluster 47 Tucanae (Lebzelter & Wood, 2005), where the brightest LPVs are all found to pulsate in the fundamental mode.

In order to explain the asymmetric shape of light curves of large amplitude LPVs (a.k.a. Miras), non-linear effects have to be taken into account. Since the density in the outer regions of these stars is very low, shock waves are building up and propagate through the photosphere. This scenario is hold responsible for the asymmetry in the light curves of these stars. Most challenging is the correct modelling of their amplitudes. As a consequence of the simplifying assumptions on convection, the modelled amplitudes become too large with the tendency of disrupting the star. Olivier & Wood (2005) developed a code for non-linear pulsation making use of the time-dependent turbulent convection model of Kuhfuss (1986). This improved treatment of convection resulted in more realistic values for red giants particularly with large amplitudes. From comparison with conventional pulsation models using the mixing-length theory, they conclude that non-linear pulsation of red giant stars critically depends on the applied convection theory. Furthermore, they assume that the double-peaked structure, which is often seen in light curves of observed red giants, is related to high mass and high luminosity rather than a resonance phenomenon between two excited pulsation modes (also observed in LPVs light curves). Further investigation of Wood (2007) revealed significant differences between linear and non-linear pulsation models (e.g., period lengths, period changes), which seem to depend on the envelope mass of the pulsating red giant star.

2.2.2 Classification of Variable Red Giant Stars[2]

The most common way to classify variable red giant stars follows the definition of Kholopov et al. (1985-88) in the General Catalogue of Variable Stars (GCVS), grouping LPVs into Miras, semi-regular, and irregular variables, respectively. Since the physical reasons for the various shapes of the observed light curves were not well understood, these variables were classified according to phenomenological criteria. The Mira variables exhibit very large amplitudes, long periods, and very regular (almost sinusoidal) light curves. These stars are located at the tip of the AGB in a HRD shortly before they become totally dust-enshrouded objects (OH/IR stars or infrared carbon stars). As their names already indicate, semi-regular and irregular variables have a less regular light curve shape and smaller amplitudes. The classification used in the GCVS may seem obvious when investigating the light curves of

[2]Parts of this section were already published by Lorenz et al. (2011).

LPVs but the borders are not strictly defined and even partially overlap. During the evolution along the AGB, the periods of LPVs tend to increase (Vassiliadis & Wood 1993), but the evolutionary relation between Miras, semi-regular and irregular variables is not clear (see Kerschbaum & Hron 1992, Lebzelter & Hron 1999). The classification used in the GCVS may seem obvious when investigating the light curves of LPVs but the borders are not strictly defined and even partially overlap. In terms of near infrared colours, spectral energy distribution, and mass loss properties (Kerschbaum et al. 1996, Kerschbaum 1999, Olofsson et al. 2002), irregular and semi-regular variables are very similar. Successive microlensing surveys like MACHO[3], EROS[4] and OGLE[5] with a better coverage of the light curves (compared to GCVS), revealed that a significant fraction of formally classified irregular variables should actually be classified as semiregular variables. Moreover, according to Lebzelter & Obrugger (2009), irregular variables rather seem to form a smooth extension of the semi-regular variables instead of forming a distinct group of variables. These authors also support the idea of merging these two classes into one class of small amplitude red variables as already suggested by Percy et al. (1996) and Soszyński et al. (2004a). Hence, the classical definition of LPVs according to the GCVS became a subject of heated controversy, and new attempts to reclassify red giant variables were made.

A first step concerning a reclassification of LPVs was made by Feast et al. (1989) who discovered that Mira stars are grouping along of a sequence in a period luminosity diagram (PLD). Studying Miras of the LMC at near-infrared wavelengths, Feast et al. (1989) were the first to establish PLRs (one for each filter) for this class of variables (see Fig. 2.5). The exis-

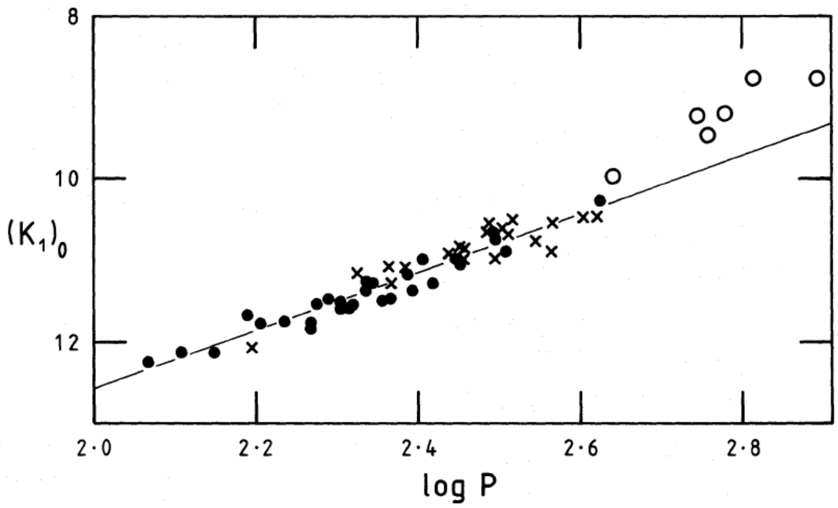

Figure 2.5: A K-$\log P$-diagram for detected Mira variables in the LMC taken from Feast et al. (1989). Filled circles denote O-rich Miras with periods < 420 d, open circles O-rich Miras with periods > 420 d and crosses C-rich Miras.

[3]http://wwwmacho.anu.edu.au/
[4]http://eros.in2p3.fr/
[5]http://ogle.astrouw.edu.pl/

tence of such a relationship was initially suggested already in 1928 by Gerasimovic. Owing to the intrinsic brightness of AGB stars (including LPVs), they also serve as possible probes for measurements of cosmic distances and galactic dynamics. Although there were only about 50 Mira-like stars known in the LMC at that time, the uncertainties of the relation were finally small enough to use Miras as standard candles for distance estimates. Feast et al. (1989) carried out least-squares solutions (linear correlation) in four different filters. The continuous black line in Fig. 2.5 is based on the following equation:

$$m_0 = (-3.57 \pm 0.16) \log P + 19.70 \pm 0.39 \qquad \sigma = 0.15. \tag{2.3}$$

This relation is based on O-rich and C-rich Miras with periods < 420 days. As noted by the authors, this relation may be converted into absolute magnitude by adopting a distance modulus of $(m - M)_0 = 18.47$ for the LMC.

Given that the PLRs of variable stars like Cepheids and Miras are based on observations, one may ask for the theoretical background of such relations. Both, Cepheids and LPVs, are found in narrow, almost vertical regions in the HRD. The temperatures in each of these regions are very similar and only weakly dependent on luminosity. Therefore, it may be assumed that the effective temperature in equation 1.3 is approximately constant, which leads to

$$L \propto R^2. \tag{2.4}$$

As can be seen in equation 2.1, the pulsational constant of a fundamental radial mode of pulsation is proportional to the product of the period and the square root of the mean density. If the mean density ρ is replaced with $\frac{3M}{4\pi R^3}$ (where M is the mass of the star), the period can be written as

$$P \propto \sqrt{R^3/M}. \tag{2.5}$$

Considering the exponents in the last equation, the period is mainly determined by the stellar radius, hence, after eliminating the stellar radius in equation 2.4 and 2.5, one finds

$$P \propto L^{3/4}, \tag{2.6}$$

which clearly relates the luminosity with the period of a pulsating star. For more information on the derivation of this formula, the reader is referred to Weigert & Wendker (1996) and to the lecture notes of G. Knapp[6].

Since the publication of Feast et al. (1989), the sample of observed LPVs (mainly in the Magellanic Clouds) has increased significantly and allowed the detection of not only one but several sequences of LPVs in a PLD (e.g., Wood et al. 1999; Cioni et al. 2001; Lebzelter et al. 2002). Wood et al. (1999) and Wood (2000) were the first to discover that all LPVs, detected by the MACHO survey of the LMC, seem to group around at least five almost parallel sequences in a PLD to which they assigned the letters A to E (see Fig. 2.6). One of these sequences (sequence C) correlated with the PLR of Mira stars from Feast et al. (1989).

[6] http://www.astro.princeton.edu

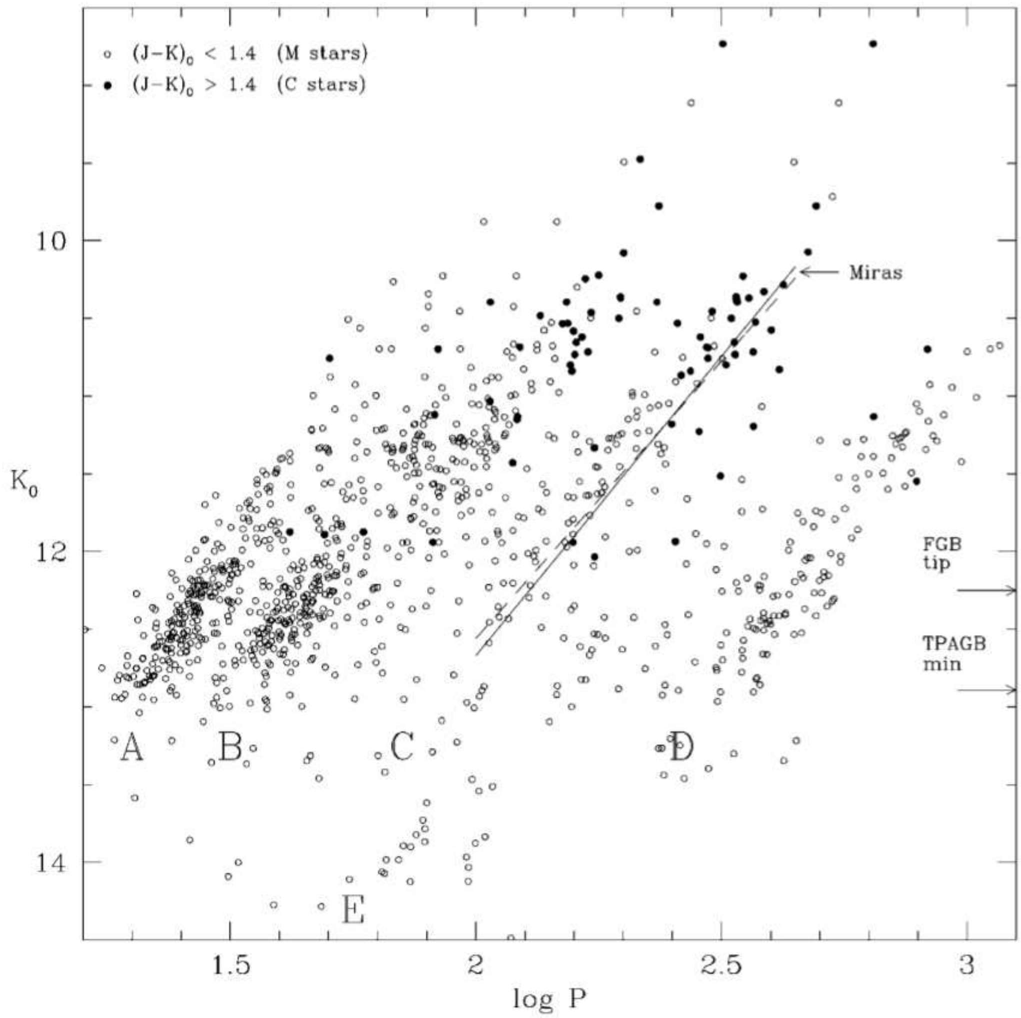

Figure 2.6: A K-$\log P$-diagram of red giant variables detected in the LMC by the MACHO survey taken from (Wood 2000). Open circles show O-rich stars, filled circles C-rich stars (according to the colour criterion given in the upper left corner). Different sequences are labelled as letters from A to E. The solid line represents the K-$\log P$-relation of Hughes & Wood (1990), and the dashed line the PLR of Feast et al. (1989). The arrows on the right edge of the figure indicate the positions of the theoretical brightness maximum of RGB stars (RGB-tip) and the minimum luminosity for TP-AGB stars (TPAGB min).

Later publications of PLRs of the LMC (e.g., Kiss & Bedding 2003; Ita et al. 2004) revealed that sequence B actually splits into two separate sequences, namely B and C′ (see Fig. 2.7). Meanwhile, different authors (e.g., Fraser et al. 2005; Soszyński et al. 2004a) are using different labels in a PLD.

This highly interesting discovery encouraged a completely new way of classifying not only Mira variables but all LPVs for which a period can be determined, namely according to the

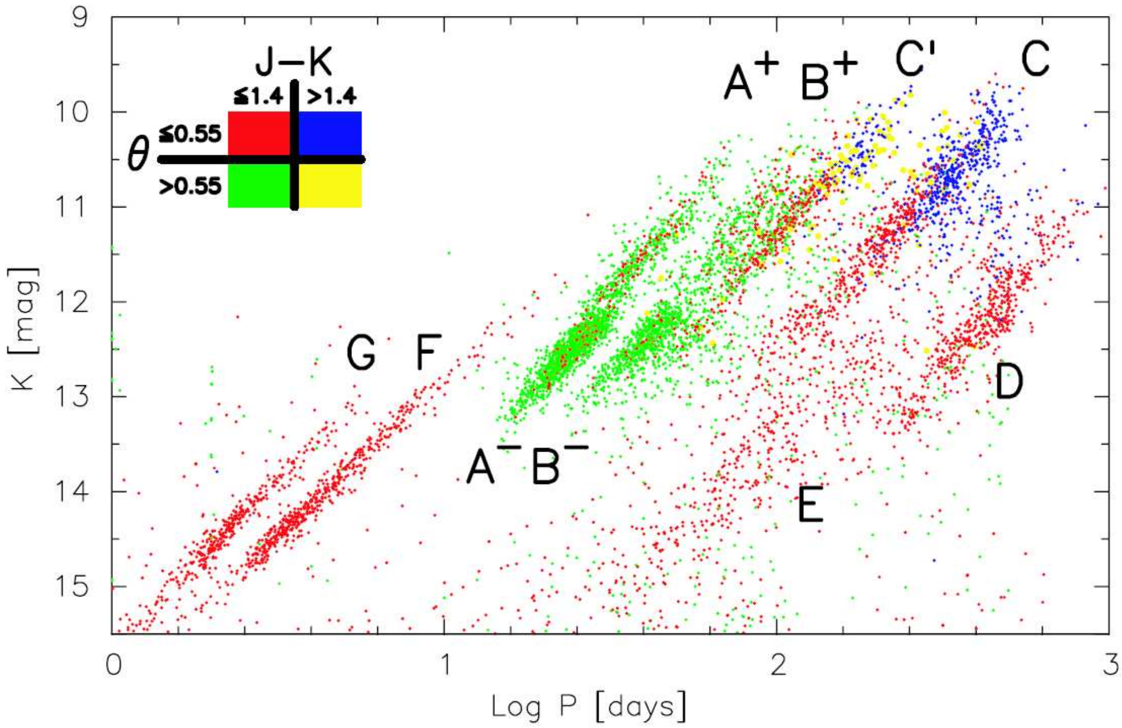

Figure 2.7: A K-$\log P$-diagram for variables detected in the LMC by the OGLE survey. Sequences A and B are split into LPVs below the RGB-tip (A^-, B^-) and above the RGB-tip (A^+, B^+), sequences F and G consist of Cepheid variables. For detailed explanations on the colour code and labelled sequences see text in Sect. 2.2.3. This figure was taken from Ita et al. (2004).

different sequences they occupy within a PLD. Such a new classification method will be applied to LPVs detected with the upcoming Gaia satellite mission. More information on this subject is given in the second part of this thesis, where this method is introduced and discussed in more detail.

2.2.3 On the Nature of Different Period-Luminosity Sequences[8]

A comparison with linear pulsation models revealed that most of the sequences in the PLD could be attributed to LPVs pulsating in the fundamental or overtone mode of low degree (see Fig. 2.8), respectively.

Sequence C is thought to consist of stars pulsating in fundamental mode. LPVs on sequence B were explained as first and second overtone pulsators, and stars on sequence A as higher overtone variables. For stars belonging to sequences E or D the variability cannot be attributed to radial pulsation. Stars on sequence E are thought to be related to close binary systems showing ellipsoidal variability (see Soszyńsky et al. 2004b). Recently, Nicholls

[8]Parts of this section were already published by Lorenz et al. (2011).

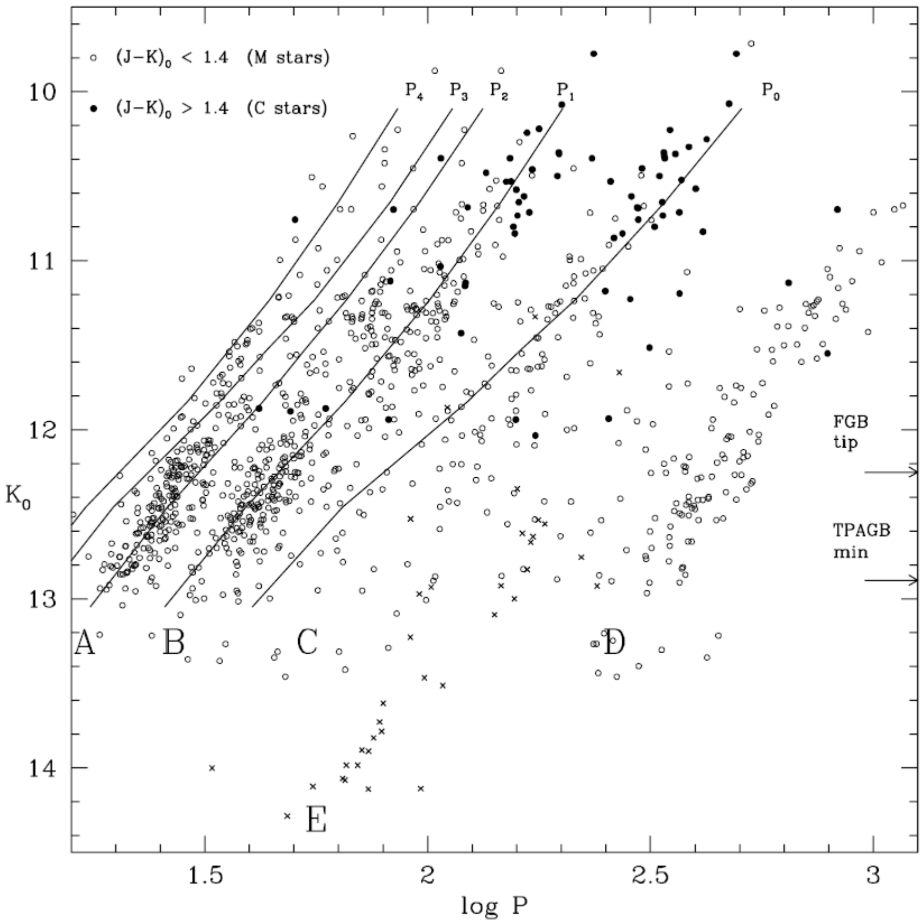

Figure 2.8: Same as Fig. 2.6 but with crosses indicating stars with light curves typical for close binary systems. Continuous lines give the linear pulsation periods of O-rich model stars pulsating in the fundamental (P_0) and low overtone mode (P_1 to P_4), respectively. This figure was taken from Wood (2007).

et al. (2010) confirmed this assumption by comparing the phased light and radial velocity curves of LMC red giant binaries. The results of this study also demonstrated that the variations of stars on sequence E and D are caused by different mechanisms. The LPVs on sequence D show periodicities on two time scales, where the long secondary period (LSP) is about ten times the shorter period. The origin of these LSPs is still unknown (Nicholls et al. 2009). By comparing a sample of sequence D stars with similar red giants (not showing LSPs), Wood & Nicholls (2009) found that such objects have a significant excess in the mid-infrared ($8-24\,\mu$m), which is thought to originate from circumstellar dust. This is not the case for sequence E stars (Nicholls et al. 2010).

Since the discovery of those sequences in the PLD the next intriguing question arose: *Is it possible to assign individual sequences to the historical classification of the GCVS?* Especially the Mira variables with their large amplitudes and regular light curve shape were a matter of debate. According to, e.g., Wood et al. (1999), Bessell, Scholz & Wood (1996), and Hinkle et al. (2002), Mira variables are fundamental mode pulsators, whereas semi-regular variables are pulsating in first or higher overtone modes. However, studies of Haniff et al. (1995) and Whitelock & Feast (2000), making use of diameter measurements of Miras in the Milky Way, favour the pulsation of the first overtone mode for these stars.

According to the collected observations over several decades, the majority of Mira stars is generally interpreted as fundamental mode pulsators. A very revealing statistic parameter (introduced as Θ) concerning this topic was used in the PLD of Ita et al. (2004, see Fig. 2.9). In order to obtain periods from the OGLE data, they made use of the phase dis-

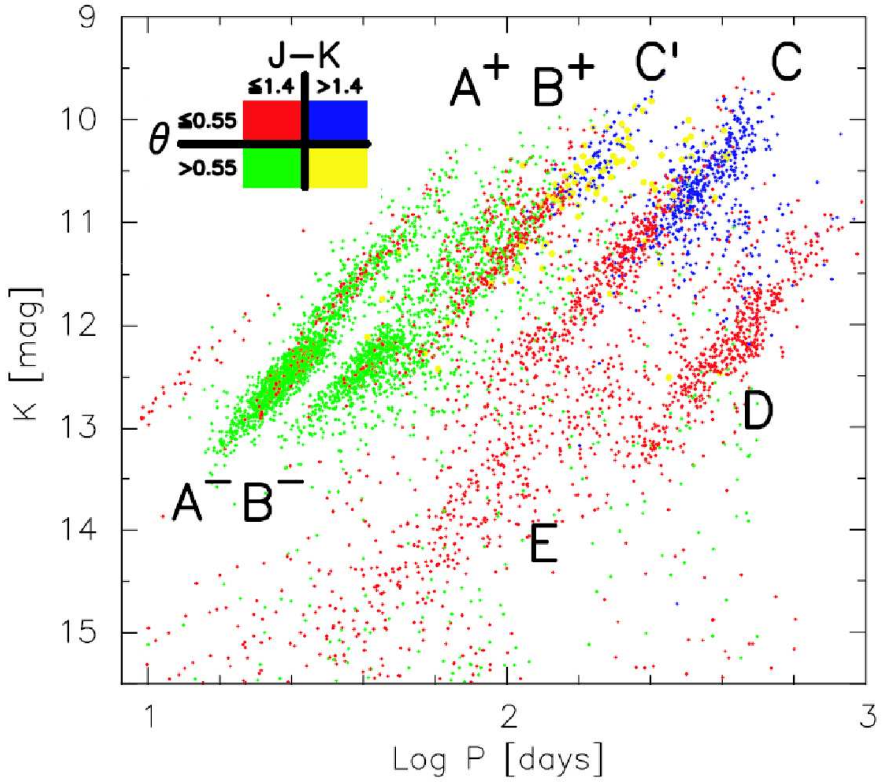

Figure 2.9: Same as Fig. 2.7 but without the Cepheid sequences.

persion minimization method developed by Stellingwerf (1978), which is especially suited for non-sinusoidal variations and patchy data sets. First, the data set (consisting of measured magnitudes x_i at various epochs t_i) is folded with a trial period. The resulting phase diagram is then divided into several bins, and the variance of each bin ($\tilde{v}$) is compared with the overall variance (V) of the time series. Finally, the true period is estimated from the smallest value of the ratio $\Theta = \tilde{v}/V$. Hence, Θ may be interpreted as a measure of the regularity of the light curve with a value close to zero for regular light curves with a good estimate of the true period, and close to one for irregular light variations. Consequently, Ita et al. (2004) separated regularly pulsating stars (with $\Theta \leq 0.55$) from less regularly pulsating variables (with $\Theta > 0.55$). They further distinguished between variables with colours of $J - K \leq 1.4$

and $J - K > 1.4$ – an often used criterion to roughly distinguish between O-rich and C-rich red giant stars (Cioni & Habing, 2003), respectively. Accordingly, regular pulsating stars in Fig. 2.9 assumed to be O-rich are drawn as red points, and C-rich LPVs as blue dots, less regular pulsating are plotted as green (O-rich stars) and yellow dots (C-rich stars), respectively. The labelling of the sequences is nearly the same as defined by Wood (1999) except for sequence C′, which is thought to consist of LPVs pulsating in first overtone mode. Below the RGB-tip at about $K = 12.1$, the sequences A and B are offset and were therefore treated as separate sequences (labelled as A$^-$ and B$^-$ in Fig. 2.9). Stars forming sequence F and G are identified as Cepheid variables pulsating in fundamental and first overtone mode, respectively (see Fig. 2.7).

As expected from theory, sequences A and B mainly comprise less regularly pulsating stars of O-rich surface chemistry. Towards longer periods (sequence C and C′) the detected LPVs are pulsating more regularly and tend to be C-rich at higher luminosities. In agreement with previous studies, sequence C overlaps well with the Mira sequence (e.g., Feast et al., 1989). However, variables forming sequence C′ are also regularly pulsating but have smaller amplitudes (as theoretically predicted for first overtone pulsators). According to their regularity, Ita et al. (2004) consider stars forming both sequences (C and C′) to be Mira variables.

Obviously, the answer to the question of the favoured pulsation mode for Mira variables strongly depends on the (individual) definition of a Mira star. Furthermore, with the detection of several sequences of LPVs within a PLD, and the findings of Kerschbaum & Hron (1992), Lebzelter & Hron (1999) and Lebzelter & Obrugger (2009), the historical classification in the GCVS of these stars seems no longer appropriate. The author of this thesis therefore strongly encourages the idea to reclassify LPVs according to their position in a PLD.

2.2.4 Are Period Luminosity Relations of LPVs Universal?

As every other relation between pulsational behaviour and luminosity, the PLRs of AGB variables provide the opportunity to use these stars as distance indicators for both, stellar and galactic or extragalactic studies. AGB stars are commonly found in any intermediate-age or old stellar populations, and their high intrinsic brightness makes them easy to identify even at large distances. The use of a universal PLR of LPVs is especially interesting as alternative method to determine distances of globular clusters at locations where RR Lyrae stars become too faint to be detected.

Within the last decade, several studies to explore PLRs of LPVs in different stellar systems of the Local Group were carried out (see e.g., Groenewegen 2005 for an overview). Remarkable investigations of Rejkuba et al. (2003) and Rejkuba (2004) of the giant elliptical galaxy NGC 5128 (Cen A, see Fig. 2.10) proved the possibility to study LPVs in stellar systems even beyond the Local Group.

A challenging topic in extragalactic astronomy is to determine the star formation history of galaxies. In particular, the fraction of the intermediate-age population, which is indicated by AGB stars, is difficult to obtain if only two filters – e.g., V and I – are used for the construction of CMDs. Therefore, the results of different studies on this topic are often in contrast. As an example, Harris et al. (1999, 2000), using V and I filters, do not find bright (above the

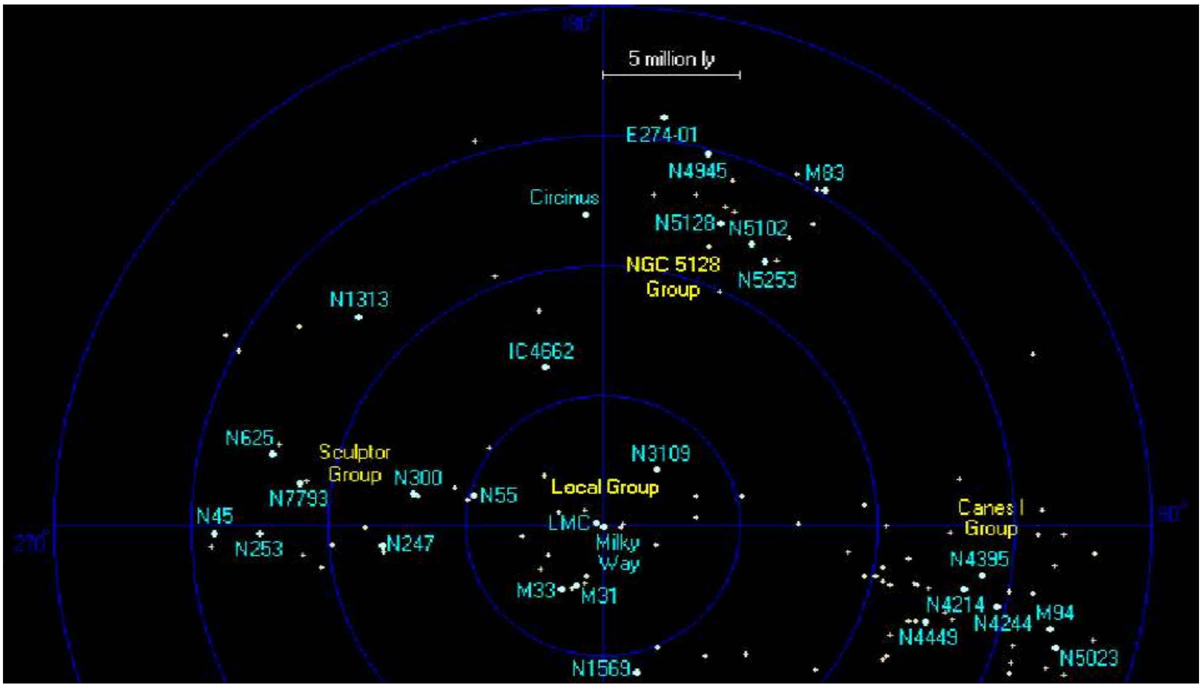

Figure 2.10: A map of nearest groups (within 20 million ly) of galaxies centred on the Local Group. The Centaurus A/M83 Group is located at the top of this figure, galaxy names are given in light blue and the names of galaxy groups in yellow, respectively. This figure was taken from Richard Powell and is available online at www.atlasoftheuniverse.com.

RGB-tip) AGB stars in two halo fields of NGC 5128, whereas Marleau et al. (2000), using the filters J and H, suggest a fraction of bright AGB stars of up to 10%. Since AGB stars have relatively low effective temperatures, the V- and I-filters are not very sensitive to detect such cool objects, and therefore the CMDs might be misleading.

Besides the use of CMDs, a further method to confirm the presence of an intermediate-age population of a stellar system is the search for LPVs therein. Rejkuba et al. (2003) analysed time series of LPVs in two halo fields of NGC 5128 carried out with the Very Large Telescope of the European Southern Observatory. Using J_s, H, and K_s, the authors aimed to study the contribution of intermediate-age stars to the halo population of this system. They detected 897 LPVs with periods ranging from 155 to 1000 days, most of them being brighter than the RGB-tip. Furthermore, they found that the LPVs of NGC 5128 follow the same PLR as LPVs in the Magellanic Clouds, Solar neighbourhood and the Galactic bulge. In a consecutive publication, Rejkuba (2004) determined the distance to NGC 5128 using two methods, the RGB tip (see Sect. 4.3) and the PLR of Mira variables (similar to Feast et al. 1989). The resulting distance moduli are in excellent agreement with those from the literature and illustrate the potential use of the PLR (fundamental mode) of LPVs as distance indicator, even for systems in the CenA/M83 group (see Fig. 2.10). Moreover, the fact that the detected LPVs follow the same PLRs as in other stellar systems, strengthens the assumption of an universal PLR of LPVs.

Before confirming the universality of the LPV-PLR, an accurate understanding of the PLD and the influences of stellar parameters on the PLRs is required. For a star cluster, it may safely be assumed that its members do not differ significantly in age, metallicity, and initial mass. These systems therefore serve as ideal testbed to study the relation between the pulsation of LPVs and other stellar parameters like, e.g., mass loss, surface chemistry, He-abundance, and stellar evolution along the giant branch.

The cluster 47 Tuc (NGC 104) was the first investigated cluster of a LPVs search program (initiated by Lebzelter et al., 2004) of Galactic Globular clusters. Lebzelter & Wood (2005) compared the detected LPVs of 47 Tuc with linear pulsation models of Fox & Wood (1982), assuming a distance module of $(m-M)_V = 13.5 \pm 0.08$ (Gratton et al. 2003), a metal abundance of $Z = 0.004$ (Caretta & Gratton 1997), a helium mass fraction of $Y = 0.27$, an interstellar reddening of $E(B-V) = 0.024$, an age of 11.2±1.1Gyr (Gratton et al. 2003), and a MS turn-off mass of $0.9 M_{\odot}$. Some stars of 47 Tuc are known to have a high infrared excess, indicating that these stars are surrounded by dust (Origlia et al., 2002). Accordingly, Lebzelter & Wood (2005) calculated pulsation models with and without assuming a reduction of envelope mass by mass loss processes along the RGB and AGB, respectively. It turned out that the location of the detected LPVs, which are exhibiting small amplitudes, in the K-$\log P$-diagram could only be explained by the models including mass loss. These stars occupy sequences that are associated with pulsation of low overtone modes. In contrast to models without mass loss, those with mass loss have longer periods and a smaller slope of the K-$\log P$-relations (caused by lower stellar mass and the decrease in mass with luminosity, respectively). The large amplitude LPVs are found to be consistent with the models for fundamental mode pulsation without mass loss. However, as discussed in Sect. 2.2.1, linear pulsation models are not well suited for this type of variable, since nonlinear effects come into play, causing a change in the envelope structure. Hence, nonlinear pulsation models give shorter periods for the fundamental mode and could therefore explain the position of the large amplitude LPVs in the K-$\log P$-diagram of 47 Tuc. Furthermore, the distribution of LPVs in the K-$\log P$-diagram indicates an evolution of their pulsation. The small amplitude variables, populating sequences of low order modes, are fainter than LPVs associated with fundamental mode pulsation. This would agree with the expected behaviour of the growth rates from the linear non-adiabatic models, where stars start to pulsate at overtone modes and then switch to fundamental mode during their evolution to higher luminosities.

Globular star clusters of the LMC have an estimated age of 1 to 5 Gyr (e.g., Girardi et al. 1995) and, therefore, offer the possibility to study LPVs with masses of 1.5 to 2.5 $M_{\odot}$. Galactic Globular clusters, on the contrary, only allow to study LPVs up to about 0.9 $M_{\odot}$. Lebzelter & Wood (2007) examined the LPVs in the LMC cluster NGC 1846 and compared the observations with linear pulsation models of Fox & Wood (1982) in a $\log L/L_{\odot}$-$\log P$-diagram. As mentioned in Sect. 1.3.2, stars in this mass range are not significantly influenced by mass loss, which is not the case for lower mass stars. Correspondingly, only pulsation models without mass loss were used for this comparison. Since information on the spectral types for the LPVs of NGC 1846 was available, the data set was divided into O-rich and C-rich LPVs, providing further information of the influence on the PLRs with respect to the surface chemistry. The general distribution of the LPVs of NGC 1846 in the $\log L/L_{\odot}$-$\log P$-diagram is similar to the one of 47 Tuc – fainter stars populate sequences of the first and second overtone mode, while LPVs with higher luminosities are found the first overtone mode and on the fundamental mode. Moreover, the O-rich LPVs are associated with the first group and the C-rich LPVs with the latter group. As noted by Lebzelter & Wood (2007), this is the first time that the length of the period is related to the atmospheric chemistry. C-rich LPVs have lower effective temperatures and are more extended, therefore, they exhibit longer periods than O-rich stars of the same mass. The authors determined the turn-off mass of this star cluster from their pulsation models to about 1.8 $M_\odot$ which corresponds to an age of 1.4 Gyr. This age is in excellent agreement with the findings of Mackey & Broby Nielsen (2007) based on isochrone fitting. Lebzelter & Wood (2007) thereby offer a completely new way to determine the age of a stellar cluster.

By applying the same pulsation analysis method for the clusters NGC 362 and NGC 2808 as for 47 Tuc, Lebzelter & Wood (2011) investigated the influence of the He-abundance on the PLRs. In particular, NGC 2808 is expected to have a broad spread of He-abundance ranging from $Y = 0.25$ to 0.4 to explain the triple main sequence of this globular cluster (see Piotto et al. 2007). Lebzelter & Wood (2011) calculated linear pulsation models including mass loss for helium mass fractions of Y=0.25, Y=0.30 and Y=0.40. They assumed an age of 10 Gyr for both clusters, NGC 362 and NGC 2808, and used the isochrones of Bertelli et al. (2008) to derive initial masses of 0.86, 0.79 and 0.65 $M_\odot$ for this age and the three helium mass fractions mentioned above, respectively. The authors noted that stars with $Y = 0.4$ do not evolve up the AGB at all, since the remaining H-envelope is already totally consumed by the H-shell during the HB-phase. When plotting the various pulsation models in a K-$\log P$-diagram, the spread of sequences in one pulsation mode for different Y is most significant for the fundamental mode leading to longer periods for higher He-abundances. The observed LPVs of NGC 2808 associated with fundamental mode pulsation seem to support the spread of Y as noted by Piotto et al. (2007). According to the pulsation models, a He-mass fraction of $Y = 0.25$ seems appropriate for most LPVs in NGC 362 (although they are less numerous than for NGC 2808). This method still needs to be confirmed by a larger sample of globular clusters with stars of high He-abundance. However, this test provides a completely new way to confirm a large He-mass fraction in clusters.

Besides studying LPVs in star clusters, it is interesting to see what can be learned by comparing the PLDs of LPVs of larger stellar systems. Schultheis et al. (2004) extracted LPVs of the 2MASS catalogue and cross-correlated them with MACHO data for three fields of different mean metallicity. One field belongs to the Small Magellanic Cloud (SMC), the second to the LMC and the third to a region (of about 32×32 arcmin^2) centred around the star cluster NGC 6522 which is a member of the inner Galactic bulge. The mean metallicity is increasing from the first to the latter. A PLD of each system was constructed using the light curves extracted from MACHO and the K_s-magnitudes from 2MASS (see left row in Fig. 2.11). Following the nomenclature of Ita et al. (2004), Schultheis et al. (2004) fitted lines to the LMC sequences by eye (with the exception of the subdivision of sequence B) and copied them into the PLDs of the other two fields for comparison reasons. Although the dispersion for the NGC 6522 field is higher than for the Magellanic Clouds, all sequences defined for the LMC are also present in the other two fields. Moreover, the slopes of the

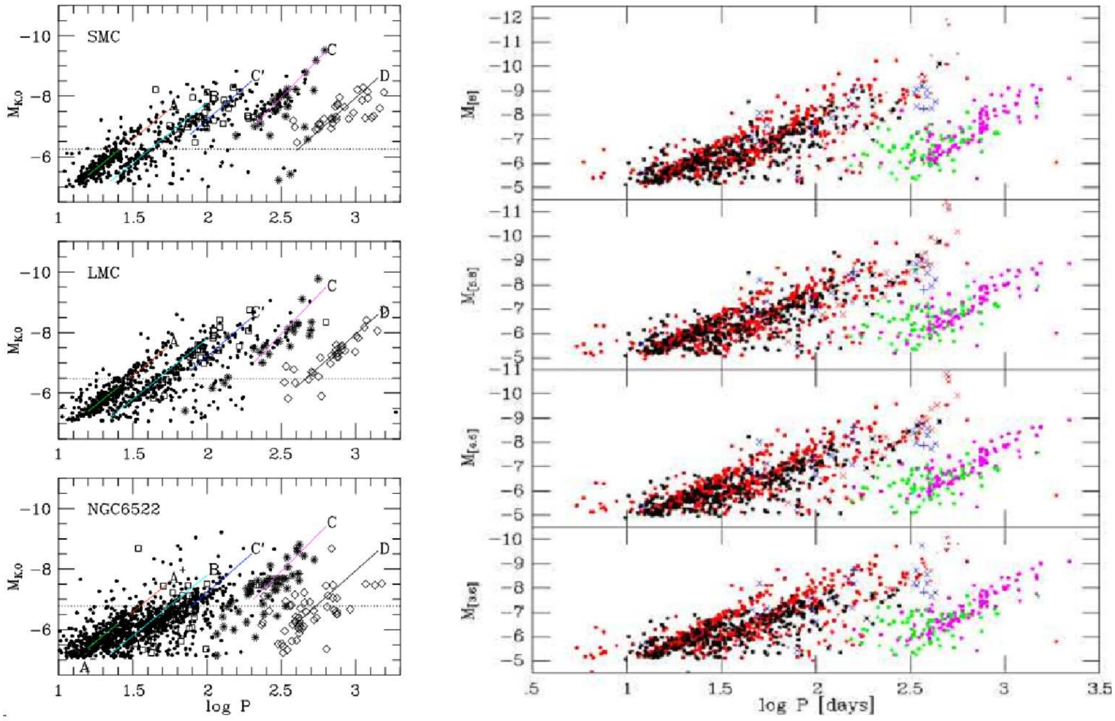

Figure 2.11: *Left row:* PLDs of the SMC (top), LMC (middle) and for the NGC 6522 field. Mira variables are shown as asterisks, semi-regular variables exhibiting two periods as open squares (short period) and as diamonds (long period), and small amplitude variables as filled circles. The dotted line in each panel indicate the RGB-tip and the straight lines are eye fits to the LMC sequences. *Right Row:* PLDs of the LMC and the NGC 6522 field in Spitzer bands (3.6 μm, 4.5 μm, 5.8 μm and 8 μm). LMC Miras variables are drawn as red crosses, semi-regular variables of the LMC exhibiting two periods as red dots (short period) and as magenta dots (long period). Galactic Miras are indicated by black crosses, semi-regular variables as black dots (short period) and green dots (long periods). Blue crosses and pluses are O-rich and C-rich local AGB stars, respectively, of Marengo et al. (2008).

sequences seem to be comparable in each system. However, the RGB-tip is increasing with increasing metallicity as well as the number of stars with small amplitudes. Another strong difference between the NGC 6522 field and the Magellanic Clouds is the proportion of bright variables (above the RGB-tip) in these fields particularly for the overtone sequences. A similar comparison between the LMC and the NGC 6522 field was made by Glass et al. (2009) using the photometric data of the infrared satellite Spitzer. As can be seen in the right row of Fig. 2.11, both fields are superimposed in each PLD using the stars at the short-period end to compensate the difference in distance. As predicted from theory, stars of lower metallicity (LMC stars) tend to reach higher luminosities than stars of higher metallicity (Galactic sample). Glass et al. (2009) further obtained PLRs for the sequences A^-, A^+, B^-, B^+, C and D. They found no systematic change in slope with wavelength.

The growing sample of PLRs for LPVs in various stellar systems seems to support the universality of LPV-PLRs. Furthermore, these relations are also useful to get a better understanding of different stellar systems, allowing to pin down the mass or mass distribution of AGB stars in stellar environments. This is an important step in order to compare the observations with models for stellar evolution, stellar population synthesis, and initial mass function. The great potential of LPVs as distance indicators becomes clearly evident when comparing different distance determination methods for the same stellar system. Table 2.1 therefore lists three well known and examined stellar systems for which distance moduli were derived using different methods. Each of the methods listed in Table 2.1 is described in more detail in chapter 4 (except the Mira-PLR which is explained in the text above and works in exactly the same was as using the PLR of Cepheid variables).

Table 2.1: A comparison of distance moduli $(m-M)_0$ of some stellar systems carried out with different methods.

Systems	Methods				References
	Cepheid-PLR	RR Lyr stars	RGB-tip	Mira-PLR	
LMC	18.50 ±0.07	18.53 ±0.06	18.59 ±0.09	18.48 ±0.10	1, 2, 3, 4
Bulge	14.51 ±0.12	14.48 ±0.17	14.62 ±0.55	14.58 ±0.02	5, 5, 6, 7
Cen A	27.67 ±0.12	—	27.72 ±0.04	27.69 ±0.11	8, 9, 10

[1] Sharma et al. (2010), [2] Borissova et al. (2009), [3] Sakai et al. (2004), [4] Feast (2004),
[5] Groenewegen et al. (2008), [6] Valenti et al. (2007), [7] Matsunaga et al. (2009),
[8] Ferrarese et al. (2007), [9] Rizzi et al. (2007), [10] Rejkuba (2004)

Two further PLRs of the dwarf galaxies NGC 147 and NGC 185 (members of the Local Group) are introduced as the third major part of this thesis. These systems were monitored over a time span of approximately 2.5 years. The light curves of hundreds of newly detected LPVs were analysed and their resulting PLRs were compared to those of other stellar systems. These results, published by Lorenz et al. (2011), additionally contribute to the discussion of the universality of the LPV-PLR.

3

The Gaia Satellite Mission

Gaia will be the follow up mission of the successful Hipparcos satellite. The instruments on board of Gaia will be able to measure distances of stars that are up to 8 magnitudes fainter (down to 20 mag in the visual) than the brightness limit of Hipparcos. The ambitious Gaia mission of the European Space Agency (ESA) aims to measure the positions, distances, space motions, variability, and many physical characteristics (e.g., surface temperatures, chemical abundances, masses) of about one billion stars with an unprecedented precision. With this expected amount of detected stars, the Gaia database will provide a rich scientific playground for a large variety of astrophysical questions.

Originally, the name Gaia was an acronym for ***G**lobal **A**strometric **I**nterferometer for **A**stro-physics*. Although the instrument setting has changed during several planning phases, the name Gaia remained. Since Gaia is also the name of the Greek goddess who created the universe, the name seems to fit the challenging aims that will be tackled by this project. The main goal of the Gaia mission is to create a three dimensional map of the Milky Way and study its structure, kinematics, and history. As can be seen from Fig. 3.1, a large part of our Galaxy will be within the reach of Gaia (effective distance limit: 1 Mpc) – an enormous advance when compared with the effective distance limit of 1 kpc (blue circle in Fig. 3.1) of Hipparcos. However, the science targets are not limited to objects in our own Galaxy. While surveying the sky, each object is going to be observed repeatedly for about 70 times (Jos de Bruijne[1]), providing the possibility to obtain information even on far-distant sources like supernovae and quasars. Due to its unprecedented sensitivity to faint moving objects, Gaia will allow the detection of many small objects within the solar system like minor planets, comets, and asteroids.

Currently ESA is building the Gaia satellite, which is scheduled for launch in spring 2013. The satellite will be placed at the second Lagrange point (a gravitational saddle point) in a distance of 1.5×10^6 km from Earth where it co-rotates with our planet and orbits the sun within one year. This position allows continuous observations in the anti-sun direction. The satellite will operate in a Lissajous-type orbit and scan the sky repeatedly during its expected life time of about five years. The results of the Gaia mission will be summarised in a catalogue which will be available three years after the the end of the operational phase. These results will have an enormous impact on various fields of astronomy (e.g., Galactic structure, stellar astrophysics, extrasolar planets, structure of space time).

[1]taken from *Infosheet: astrometric instrument*

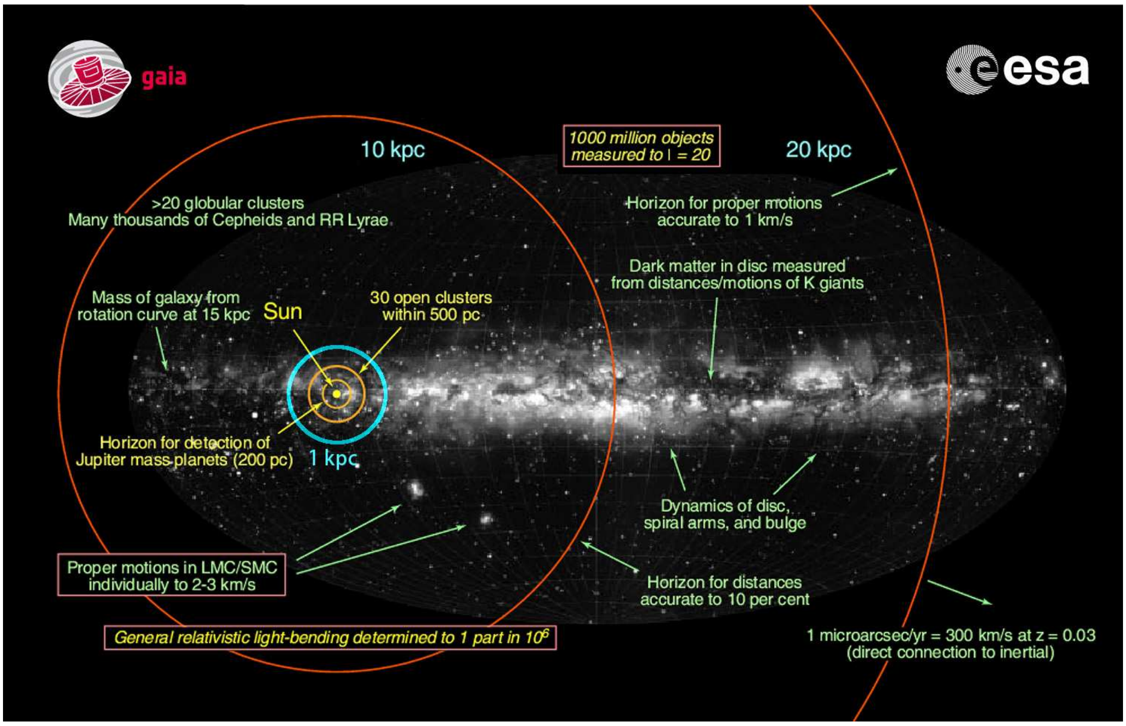

Figure 3.1: A schematic diagram of the various parts of the the Milky Way that will be captured by Gaia. Concentric red circles mark boarders of different accuracy limits for distance measurements dedicated to some of scientific topics to which Gaia will contribute. The blues circle marks the detection limit for distance measurements of the Hipparcos satellite. The background picture was taken from K. Lundmark and the whole image is credited as originating from ESA and was adapted by the author (*http://sci.esa.int/ImagesAndVideos*).

According to Eyer & Cuypers (2000), Gaia is expected to detect approximately 250 000 LPVs. The satellite will carry out astrometric and photometric measurements (like the Hipparcos satellite) and also deliver low and medium resolution spectra. Hence, it will be possible to apply corrections for chromatic effects, which could affect the accuracy of the parallax and luminosity of red giant stars and red supergiant (RSG) stars significantly. This rich database of red giant variables, which will be provided by Gaia, motivated the contribution of a software package suited to deal with this class of stars. One of the major aims of this software is to classify the stars according to their position within a PLD (see e.g., Wood et al. 1999, Lebzelter et al. 2002, Kiss & Bedding 2003; Ita et al. 2004). Moreover, the LPVs detected with the Gaia satellite will provide the necessary data to construct a LPV-PLD of the Milky Way (which is poorly known, see e.g., Glass & van Leeuwen 2007). This will also notably contribute to the clarification of the existence of a universal PLR of LPVs (see discussion in section 2.2.4).

The information presented in this chapter, unless otherwise noted, was taken from the Gaia mission homepage *http://www.rssd.esa.int/Gaia* provided by ESA.

3.1 Distances of Nearby Objects

The only way to directly measure distances to various astronomical objects, is the trigonometric parallax. As the earth orbits the sun, the view point to an object in the sky changes, and so does the apparent position of this object with respect to the background. The apparent displacement of nearby objects is therefore larger than for distant ones. The semi-angle of inclination between those two different lines of sight gives the parallax (measured in radians, see Fig. 3.2).

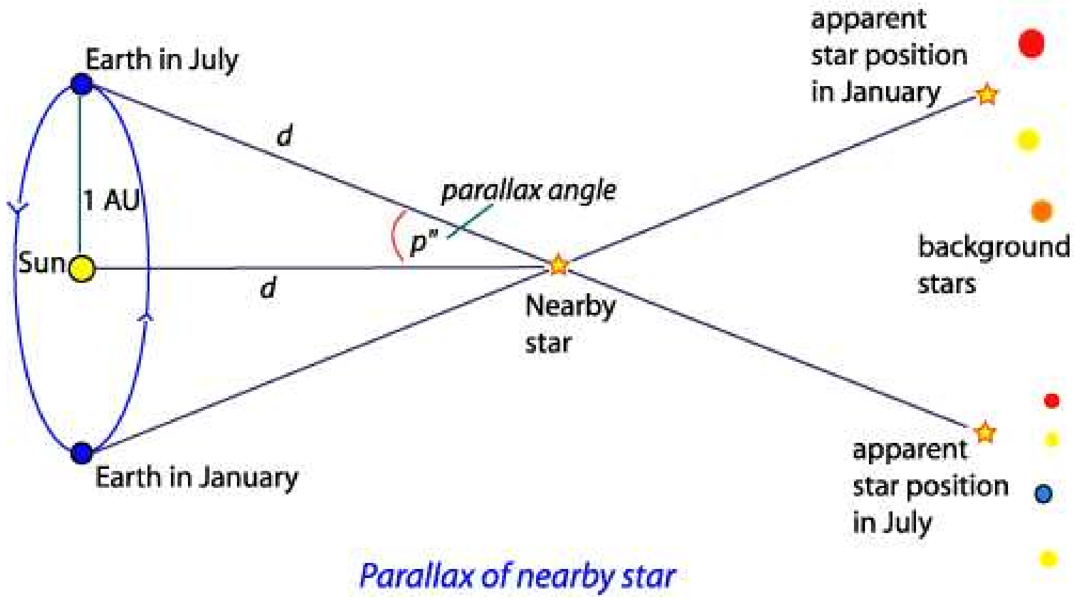

Figure 3.2: A schematic illustration of the principle of parallax measurements. This image was taken from the homepage for outreach and education of the Australia Telescope *http://outreach.atnf.csiro.au*.

In other words, the geometrical distance to an object is approximated as ratio of the parallax angle and the distance between sun and earth (1 astronomical unit, 1 AU). A parallax of 1 arcsecond corresponds to a distance of 2063×10^5 AU or 3.26 light years (i.e. 1 parsec). This method for distance determination, as can be found in several basic lectures for astronomy (e.g., Weigert & Wendker, 1996), is only suitable for objects that are relatively nearby on a galactic scale. The first distance determination of this kind was made by Friedrich Bessel (1838) for the star 61 Cygni (see Fig. 3.3). The first catalogue of stellar positions, however, was created by the Greek mathematician, philosopher and astronomer Hipparchus in the second century B.C., using his naked eyes only. With the development of astronomical devices like the sextant and the quadrant, Tycho Brahe was the first to significantly improve the accuracy of astrometric measurements. The invention of the telescope and its improvement, helped to decrease the errors of stellar positions.

However, owing to the turbulences in the Earth's atmosphere, the accuracy of ground-based measurements is limited. The difference in apparent angular positions of a star (which

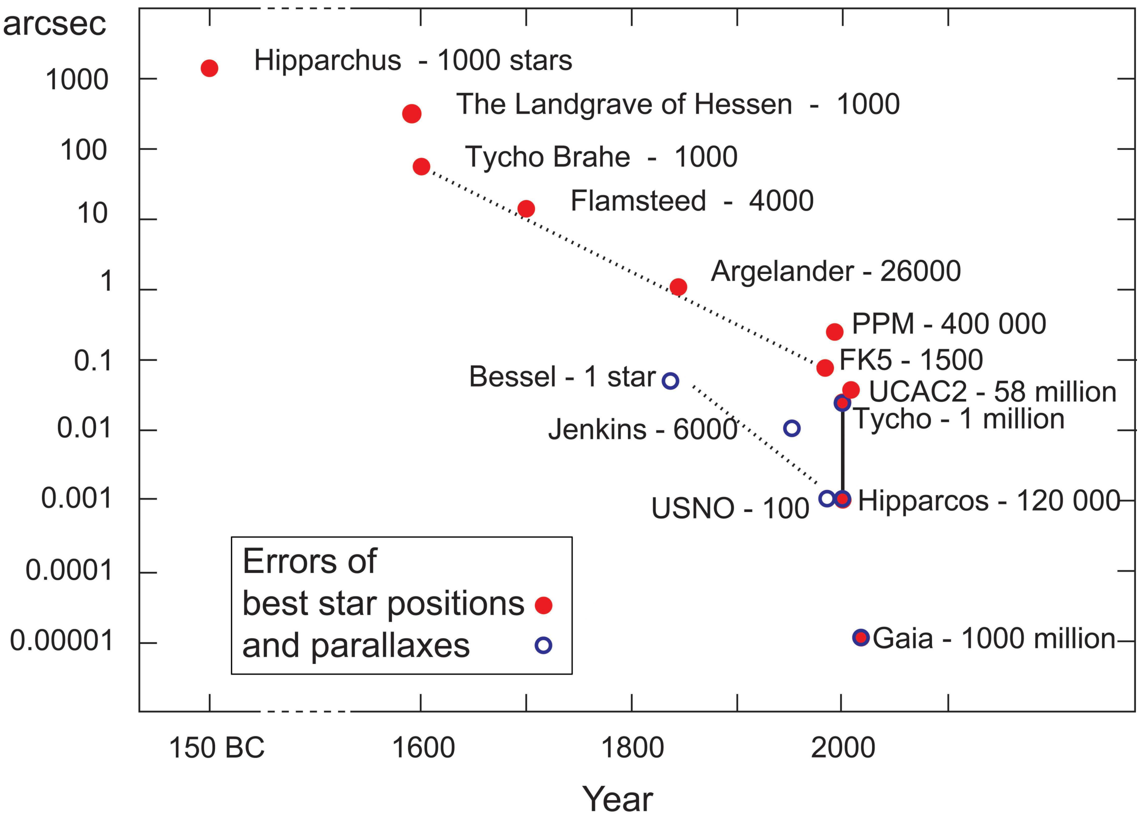

Figure 3.3: A diagram of the accuracy of stellar positions (red dots) and parallax measurements (blue circles). This figure was taken from the ESA homepage (*http://sci.esa.int/*).

determines the parallax angle, see Fig. 3.2) is very small. Even for the next closest star to our sun, Proxima Centauri, this angle is smaller than one arcsecond, and the error of the parallax increases with increasing distance of the object. Therefore, this method using ground-based observations is limited to a distance of about 100 pc (corresponding to an accuracy of 0.01 arcsec, see e.g., Weigert & Wendker, 1996). A significant improvement in terms of accuracy has been achieved by observations from space as with the famous Hipparcos satellite. This satellite measured the parallaxes of about 120 000 stars with an accuracy of 0.001 arcsec (within a distance of 1 kpc, see Fig. 3.1). These parallaxes are the most recent and accurate direct measurements so far. However, compared with the expected performance of the Gaia satellite, as can be seen in Fig.3.1, the reach of Hipparcos is restricted to a relatively small region in our Galaxy.

Other methods for distance determination, that are suited for more distant objects, are briefly summarized in chapter 4.

3.2 Gaia Instruments

3.2.1 The Payload

The payload of Gaia is equipped with two main mirrors that are separated by 106.5°, which map the relative separations of thousands of stars in two directions simultaneously (see Fig. 3.4). To guarantee a constant separation angle of the two main mirrors, a highly ro-

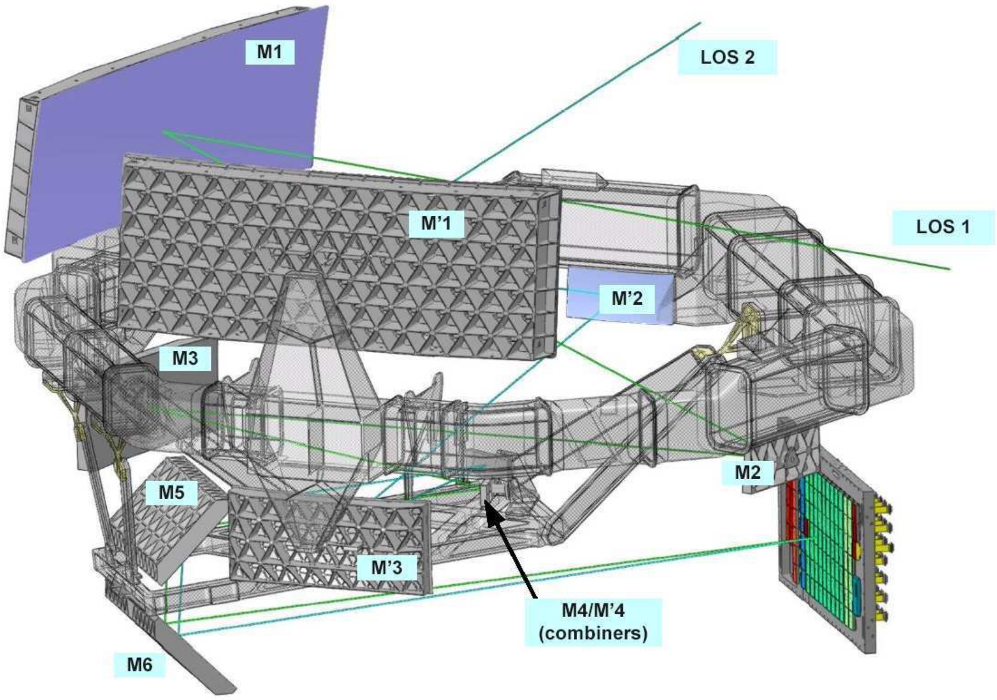

Figure 3.4: The adopted payload design of Gaia. The paths of the two lines of sight (LOS 1 and LOS 2) are drawn as green lines. The mirrors are labelled as M1 to M6 (and M′1 to M′4, respectively). This image was taken from the Gaia information sheet by M. Perryman (2009, *Infosheet payload*).

bust basic angle measurement system is installed measuring possible deviations down to 0.5 μarcsec every five minutes. Each of the primary mirrors (M1 and M′1) has a dimension of $1.45\times0.5\,\mathrm{m}^2$, the focal length of the telescope adds up to 35 m and the astrometric field of view is 0.7×0.7 degrees (along scan $\times$ across scan). The two light beams (labelled as LOS 1 and LOS 2 in Fig. 3.4) are combined in image space with a beam combiner (labelled as M 4/M′4), and sent to one common focal plane which is covered with a large array of CCD detectors. Mirrors and telescope are made of ultra stable silicon-carbide that assures thermo-elastic stability of the payload during launch and over the whole life time of Gaia.

3.2.2 The Focal Plane

In the focal plane different arrays are attributed to different tasks (see Fig. 3.5). The first array acts as sky mapper (see light blue columns in the upper panel of Fig. 3.5), where each object is detected already on board. Its information on position and brightness is processed in real-

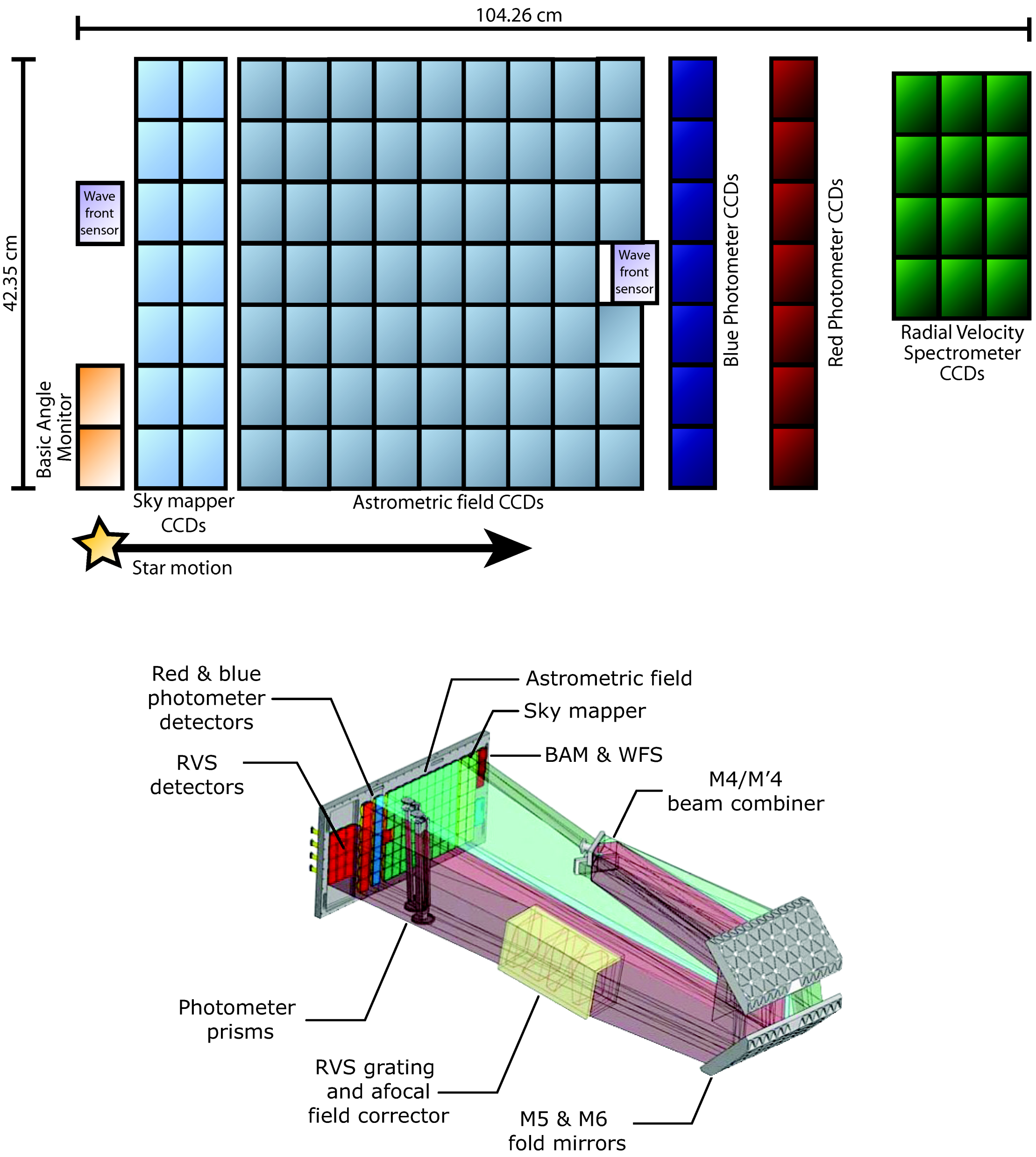

Figure 3.5: The focal plane of Gaia (upper part) and the location of the photometer prisms and the RVS grating (lower part). See text for further information. This image was taken from the Gaia information sheet by M. Perryman (2009, *Infosheet: astrometric instrument*).

time to define the windowed region for the read out of the following CCDs. The read-out itself is in time-delayed integration mode and synchronised with the scanning motion of the satellite. This method has the advantage of reducing the number of CCDs that are read out, as well as limiting the amount of data, which will be sent to the ground. The following field of CCDs (62 single CCDs coloured in grey-blue in the upper panel of Fig. 3.5) is dedicated to the astrometric field covering a wavelength range of 330-1050 nm. From this field the white-light brightness in the Gaia photometric passband (*G*) is obtained, which is particularly useful for stellar variability studies. All objects (e.g., stars, supernovae, quasars) brighter than 20 magnitudes in the G-band will be measured. The next three arrays in the focal plane are dedicated to the blue photometer (*BP*), the red photometer (*RP*), and the radial velocity spectrometer (*RVS*, see dark blue, red, and green columns in the upper panel of Fig. 3.5, respectively). The *BP* and *RP* actually record low-resolution prism spectra in a wavelength range of 330-680 and 640-1000 nm, respectively (a diagram of all Gaia passbands is given in the left panel of Fig. 10.2). This allows not only to obtain the brightness in these bands but also extract the fundamental parameters of the observed objects (e.g., T_{eff}, $\log g$, Z, etc.). The *RVS* has a spectral resolution of R= $\lambda/\Delta\lambda \simeq$ 11 500 and operates at 847-874 nm (according to the ISO scheme this would be in the near-infrared wavelength regime whereas in astronomy the near infrared starts at wavelength between 0.7 and 1 μm[2]). The extracted radial velocities will be very important to study the kinematic and dynamical history of the Milky Way. These instruments – the photometer prisms and the *RVS* grating – are located between the fold mirrors, M 5 and M 6, and the focal plane (see lower part of Fig. 3.5).

3.2.3 Scanning Law

The scanning law of Gaia specifies the movements of the satellite's spin axis during the mission life time of five years. The rotation axis is set to a fixed angle of 45 degrees to the direction of the sun and precesses with a period of 63 days (see Fig. 3.6). With a constant spin rate of 60 arcsec per second, the satellite will complete one great circle (perpendicular to the spin axis) along the sky within 6 hours. The two main mirrors are separated by 106.5 degrees. During one full rotation of the satellite, a target enters the astrometric field of the second main mirror approximately 106 minutes (1h46m) after appearing in the astrometric field of the first main mirror. About 254 minutes (4h14m) later, the observed object reappears again in the first astrometric field but at a different position. This causes a characteristic observing pattern of data points in the time series (Eyer, 2005). Moreover, due to the precession of the spin axis and the orbital motion of the satellite, a star will be observed during four to five orbits followed by a larger gap of about 30 to 40 days until the next group of measurements is carried out. The expected total number of measurements, however, varies between 45 to 210 (with a mean of 82), depending on the ecliptic latitude (see Eyer, 2005).

Further information on the payload and instruments of Gaia can found at diverse information sheets in the Gaia page at menu item: *Information sheets*.

[2]see e.g., www.ipac.caltech.edu

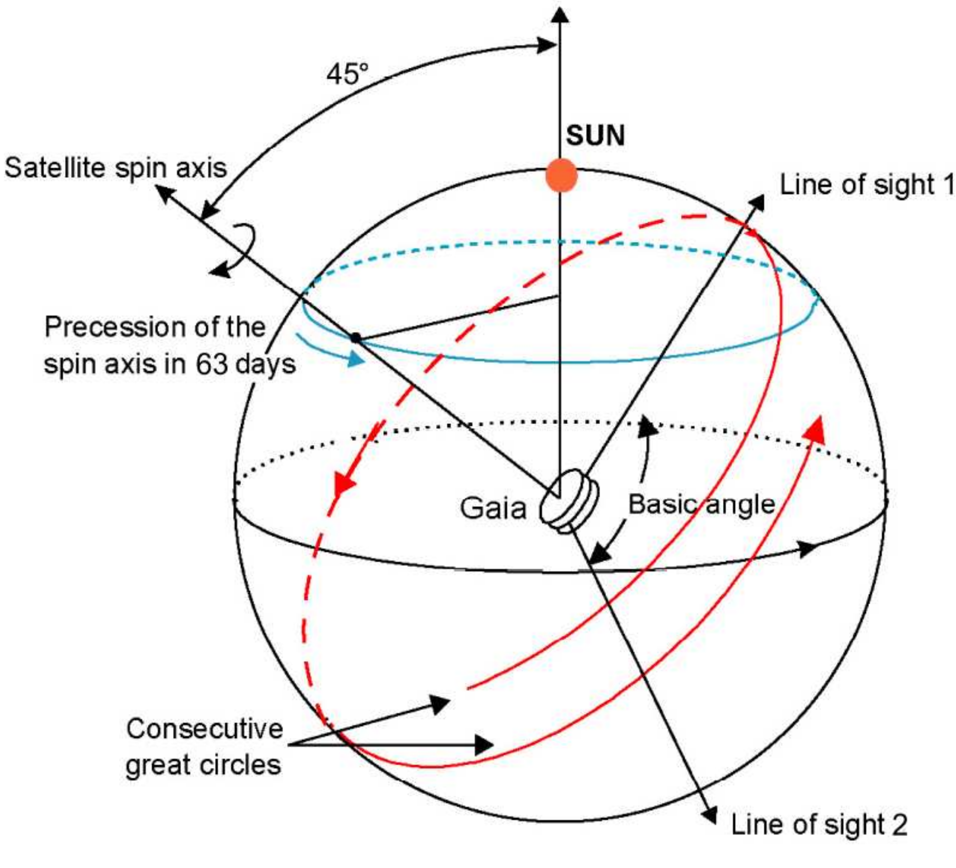

Figure 3.6: The schematic description of the observation principle of Gaia. This image was taken from the Gaia information sheet by J. de Bruijne (2009, *Infosheet: scanning law*).

3.3 The Organisation of Gaia

The satellite and the payload will be designed, built, and tested by Astrium (a wholly owned subsidiary of European Aeronautic Defence and Space Company) under supervision of ESA. The launch and operation of the satellite also lies in the responsibility of ESA. The astronomical community, on the other hand, provides the resources necessary for data reduction, storage, and analysis, respectively. The Gaia Data Processing and Analysis Consortium (DPAC) is in charge of the data processing and consists of more than 400 scientists and software engineers that are spread over more than 20 countries. In order to meet the requirements for such a huge and ambitious project, the DPAC set up an international organisation and management structure and provides the availability of the necessary hardware in six different Data Processing Centres (DPC). The DPAC assigned different key aspects of data processing to specific Coordination Units (CU1 - CU8, see Fig. 3.7). One additional CU

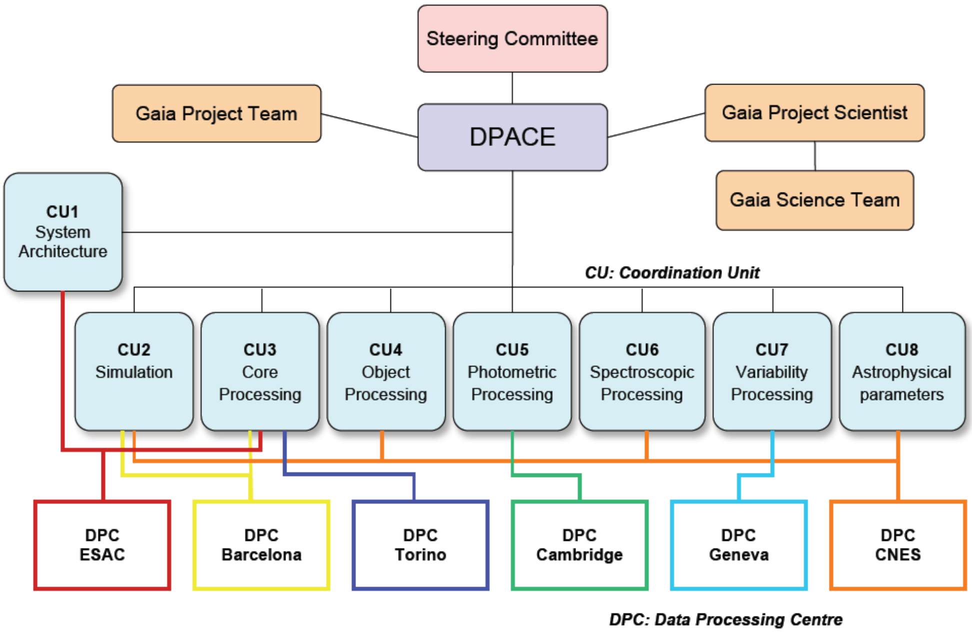

Figure 3.7: The organisation of the DPAC and the CUs with their allocated tasks. This image was taken from the Gaia mission homepage of ESA *http://www.rssd.esa.int/*).

not mentioned in Fig. 3.7 is CU9, which is responsible for preparation of the final catalogue containing all data prepared by the other CUs.

CU1 supports the DPAC in questions concerning the software design and technology and takes care of issues concerning all CUs as the main database or the Gaia transfer system. All data simulations necessary for the work of other CUs are provided by CU2. CU3 is in charge of processing the raw telemetry to the astrometric core solution. CU4 takes care of objects that require a special treatment in the data reduction of other CUs (e.g., non-single stars, eclipsing binaries, extended objects and Solar System objects). The photometric and spectroscopic information obtained with Gaia fall in the remit of CU5 and CU6, respectively. CU7, managed and coordinated by L. Eyer, is responsible for the analysis of brightness variability of stars and quasi stellar objects. CU8 uses the fully calibrated photometry and spectroscopy as well as astrometric information to classify objects (e.g., separating stars, galaxies, asteroids) and determine their astrophysical parameters (e.g., effective temperature, surface gravity, metallicity, interstellar extinction).

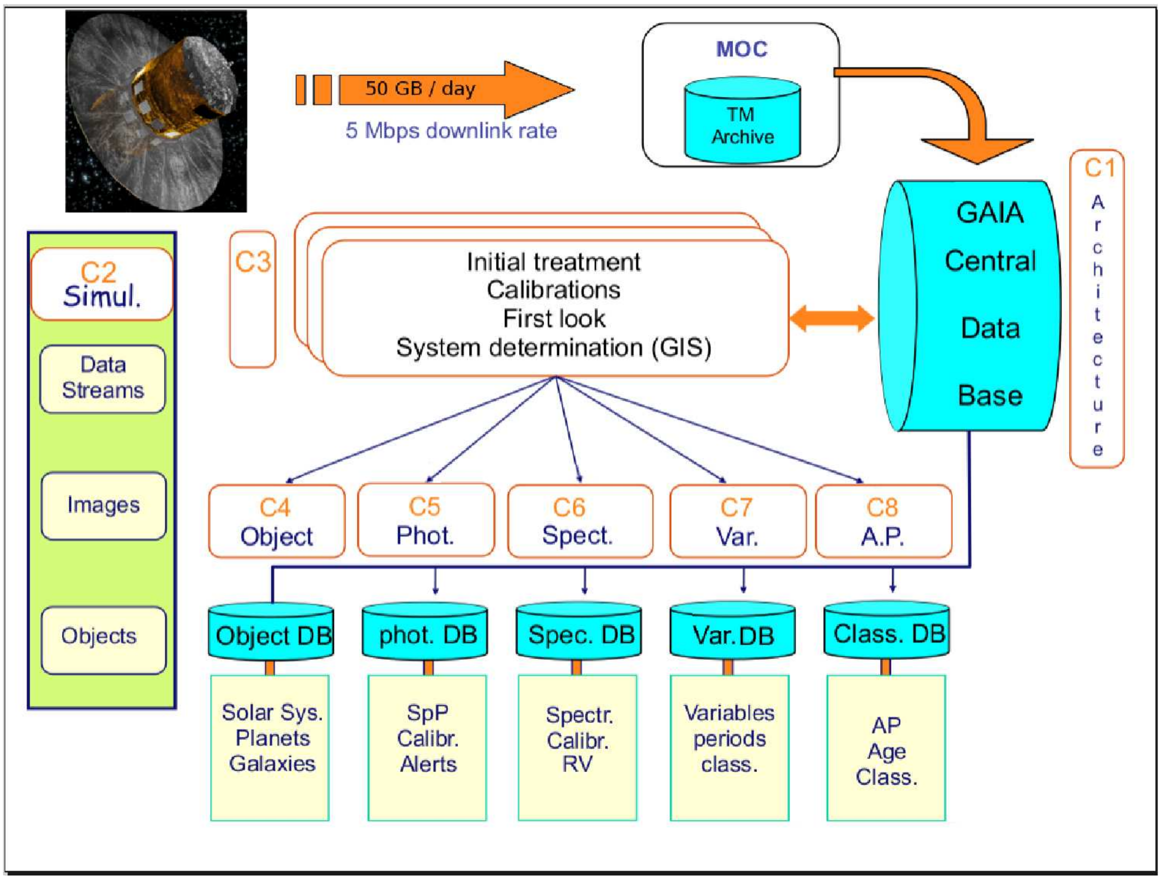

Figure 3.8: A schematic view of the main data flow of Gaia. See text for further explanations. This image kindly provided by X. Luri and was slightly adapted by the author of this thesis. The original figure is available online at: *http://www.isdc.unige.ch*.

The main data flow of the Gaia mission is illustrated in Fig. 3.8. About 50 GB of data are downlinked each day and sent to the Mission Operations Centre (MOC) located at the European Space Operations Centre in Darmstadt, Germany. MOC is the interface between the Gaia Science Ground Segment and the spacecraft. The Science Operations Centre (SOC) is based at the European Space Astronomy Centre near Madrid (Spain) that closely collaborates with the DPAC. SOC hosts the central repository for all data that are produced by Gaia and the DPAC. After a mission life time of five years, the total sum of all collected data is estimated to be about 100 TB. Accordingly, one of the major challenges of this mission is to efficiently process, manage and extract all the scientific results. From the MOC the data are sent to the central database (organised by CU1) and then to CU3, which processes the raw data. After the core processing (providing astrometric results after the calibration) the data are distributed to the CUs 4 to 8, where they are further processed.

Each CU is divided into several Developing Units (DUs), which are again grouped into different work-packages and sub-work-packages, that are specialised for specific tasks. CU7 (variability processing) consists of four DUs – DU0 to DU3, see Fig. 3.9).

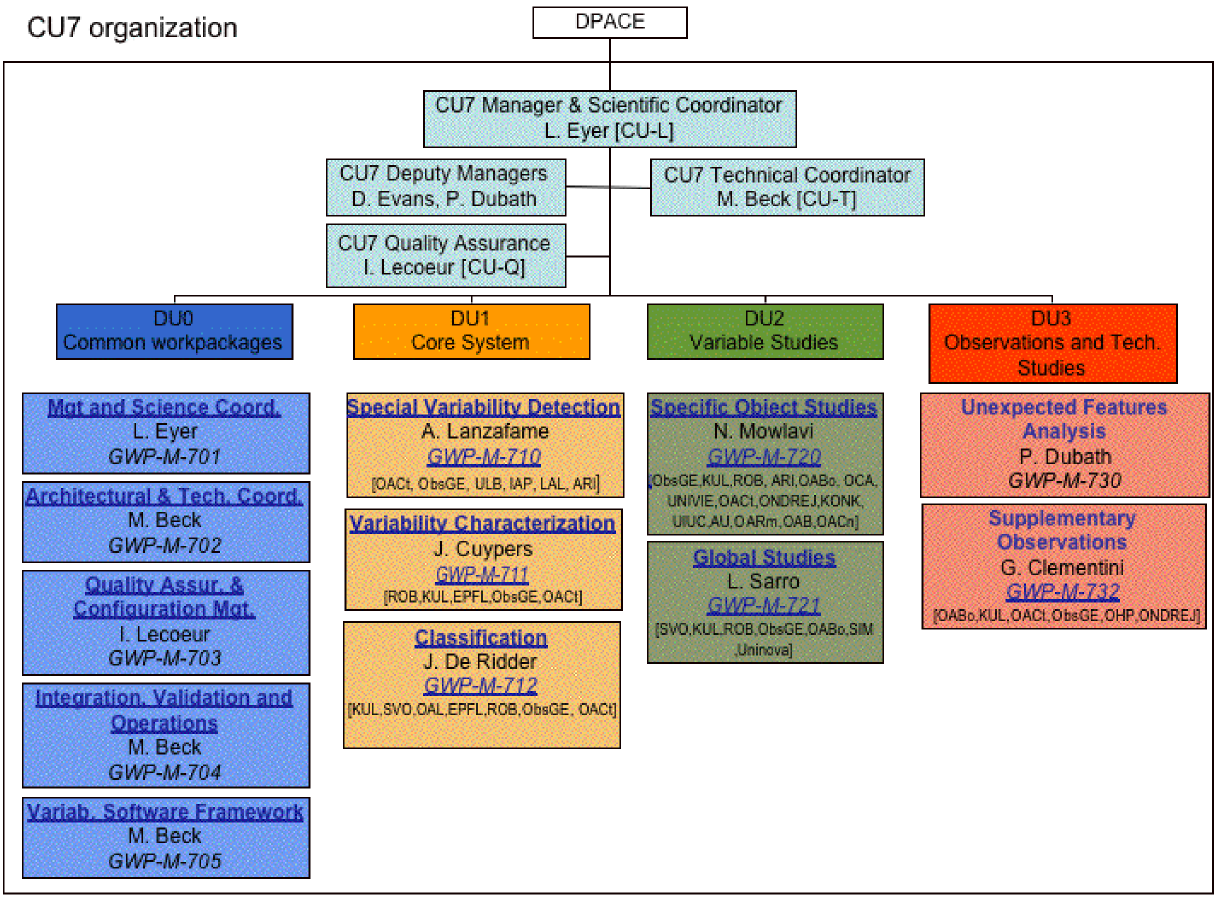

Figure 3.9: The organisation of CU7 and the DUs with their allocated tasks. This image was kindly provided by L. Eyer and is available online at: *http://www.isdc.unige.ch*.

Within CU7, the management, scientific coordination, and setup of the coding environment including technical coordination and quality assurance for CU7 developers is attributed to DU0. The core processing of variables sources is done within DU1, consisting of three work-packages: Special Variability Detection, Characterisation, and Classification. DU2 is in charge of processing the data of variable objects (Specific Object Studies), and of validating and assessing the quality of all results derived within CU7 (Global Variability Studies). The work-package for Unexpected Feature Analysis in DU3 handles sources that were classified as conspicuous objects according to the quality assessment. The work-package for Supplementary Observations (also part of DU3) is required to understand and solve processing issues for some of the variable object classes handled by CU7.

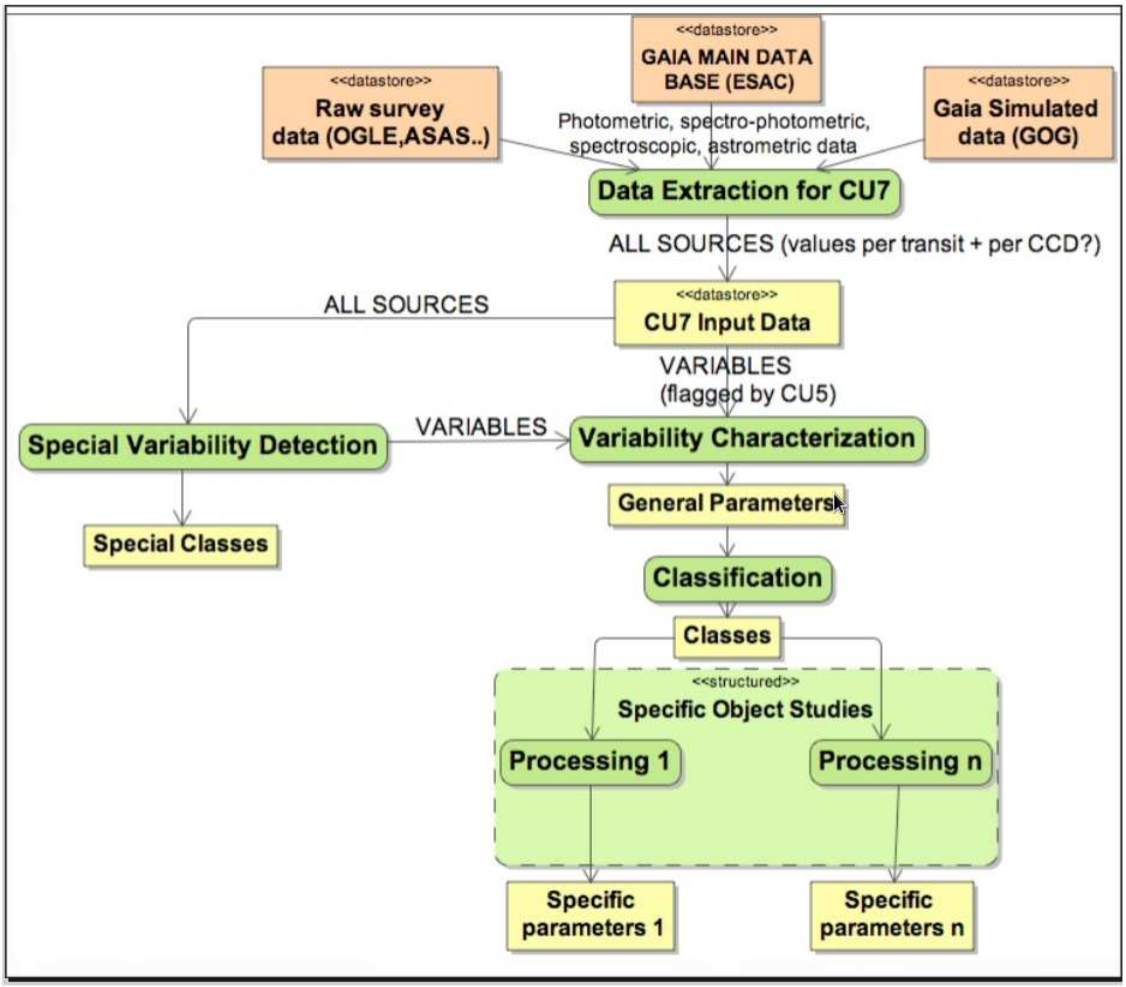

Figure 3.10: A schematic view of the main data flow tasks for variability processing within CU7. Note that all sources first enter the Special Variability Detection before the other tasks are executed. This image was kindly provided by I. Lecoeur-Taibi and is available online at: *http://www.isdc.unige.ch*.

The main data flow within CU7 is presented in Fig. 3.10. Starting from the main data base, the relevant informations for variability processing of all sources and those flagged as variables by CU5 or CU6 are passed to the variability database located at the DPC in Geneva, Switzerland. Within CU7 all sources (irrespective of variability flag) first run through the Special Variability Detection work-package. This work-package contains several methods to verify the membership of the source to one of the predefined classes (e.g., planetary transits, short amplitude variables, extremely short periods, solar-like variability), for which the usual standard variability tests are not applicable. This work-package is followed by the Characterisation, where several algorithms are offered to obtain the period of a variable object (Lomb-Scargle, Deeming, Jurkevich, Kuiper, String Length, Least squares). Depending on the class of variables, different period search methods might be chosen in the following work-packages (see, e.g., Fig. 10.1). Together with the input data mentioned above, the findings of the Characterisation are passed to the Classification work-package, where the different sources are flagged according to their proposed variability type. Again several methods are used within this work-package, e.g., Extractor, Supervised Global Classification, Unsupervised Global Classification. The end of the processing chain is built by the different sub-work-packages within the Specific Object Studies, managed by N. Mowlavi. Each of the 18 sub-work-packages therein focuses on a specific type of variable. The software of the sub-work-packages extracts further information and stores it in the Gaia main database until the Gaia catalogue is released.

The author of this thesis is a member of the work-package for Specific Object Studies within DU2. Under the guidance of T. Lebzelter, the contribution to this international collaboration consists of a software package (LPV-work-package) processing the data of stellar sources classified as LPVs, which are detected by the Gaia satellite.

3.4 LPVs detected with Gaia

According to Eyer & Cuypers (2000), Gaia is going to detect approximately 250 000 LPVs, an outstanding number if compared with the 958 LPVs (consisting of Miras and semiregular variables) in the Hipparcos catalogue. From this huge amount of LPVs, it will be possible to construct a very precise PLD of LPVs of our Galaxy. However, the sampling of the light curves of Gaia (see section 3.2) is clearly not perfectly suited to measure pulsation periods of LPVs. Therefore, the performance of Gaia in analysing periodicities of the photometric measurements has to be tested in detail.

Consequently, Eyer & Mignard 2005 have demonstrated that, despite the peculiar time sampling of Gaia (see Sect. 3.2), it is still possible to obtain reliable periods (particularly for regular pulsating stars). Nevertheless, the results depend strongly on the adequate choice of the period finding algorithm. As a matter of fact, there are several period search methods implemented in the reduction pipeline of Gaia. The scientists of each group within the Specific Object Studies work-package, need to carefully select the algorithm with the best performance for their certain type of variables. The dependencies on other work-packages (mentioned in 3.3) clearly stress the importance of a quality assessment (as in DU3 within CU7) and the need of several software tests using simulated data (provided by CU2) as well as data of former surveys and other observations.

Obtaining reliable periods is of course crucial for the construction of a PLD of the Milky Way, which is one of the main objectives of the LPV work-package. Furthermore, it will be the aim of the Gaia variability database to develop a code that classifies a LPV according to its location within a PLD. The reasons for this classification method were discussed in Sect. 2.2.2. The different regions to classify a LPV are based on the labelling introduced by Wood (1999). Such an approach was already chosen for the MACHO Variable Star Catalogue, where LPVs are classified as type A, B, C, D or E (although stars belonging to sequence E were merged with other stars classified as eclipsing binaries). Since a considerable fraction of LPVs exhibit two significant periods, the classification module of the LPV code for the Gaia mission extends this approach. Hence, LPVs will be classified according to their membership to one or – if more than one significant period is found – two of the predefined regions in the PLD (see 8.6). For this, a model PLD has to be constructed, which will be based on PLRs from all stellar systems that were published so far. This model PLD is going to be gradually refined as soon as the first measurements of Gaia are available.

To classify the LPVs, bolometric luminosities will be used, which are determined in a module specialised for red giant stars. The aim of this module is to obtain a bolometric correction (BC) using Gaia colours. The construction of the relations (see Sect. 8.3) is based on recent stellar atmosphere models for a wide range of typical AGB stellar parameters. Synthetic spectra are calculated to obtain the expected Gaia photometry (provided by CU5), using the software tools of CU2. These preliminary relations of BC and Gaia colours, which were carried out by Lederer (2010, p.c.) and kindly provided to the author of this thesis, will be fine tuned once the first Gaia measurements are available. As noted by Lederer (2010, p.c.), the BCs that need to be applied for these stars, may reach several orders of magnitude.

Furthermore, LPVs with C-rich surface chemistry have to be treated with special care, since the BCs and the expected Gaia colours for C-rich stars with large amplitudes (hydrodynamic models) are significantly larger than for those with small amplitudes (hydrostatic models, see Sect. 8.3). Consequently, it is also of crucial importance to distinguish LPVs with O-rich or C-rich atmospheres, using Gaia measurements only. Additional tests were performed in close collaboration with CU5 (see 10.2), proofing the feasibility to separate C-rich LPVs from other LPVs. Hence, C-rich stars will be treated differently within the BC module (see 8.3 for more information).

Finally, all the classified LPVs of the satellite mission will have highly accurate distance and luminosity measurements, allowing the construction of the most accurate PLD of the Milky Way to date. This PLD will offer the possibility to further investigate the PLRs in different parts of our Galaxy (galactic disk, bulge, halo). In addition, accurate bolometric luminosities (M_{bol}) are essential to distinguish between red supergiants and LPVs populating the AGB and to study them independently. Wood et al. (1983) and Groenewegen et al. (2009) have shown that supergiants occupy a distinct region within a M_{bol}-P-diagram, since AGB stars never exceed a certain M_{bol}-limit (see Sect. 7.2 and 8.4). LPVs with luminosities above this limit are therefore flagged as RSGs within the LPV-work-package.

Once all the different modules are implemented into the LPV code, independent tests of the whole data processing pipeline have to be executed. Depending on the results of these tests, further changes in the code might be necessary and, hence, the complete series of software tests must be repeated. This last testing phase is extremely important for the final performance of the software, and should be ready by the end of 2011. The current status of the work-package as well as the software tests that have been executed so far are described in the second main part of this thesis.

4 Distance Determination

The exploration of the structure of the solar vicinity, the Milky Way, and our universe crucially depends on the knowledge of the spacial distribution of its various astronomical objects. Moreover, the distance is important to derive other fundamental parameters like e.g., absolute brightness, radius and age. Hence, distance determination is of prime importance to all fields in astronomy but at the same time it is also a very challenging task. As mentioned in Sect. 3.1, the first distance measurement was obtained for the star 61 Cygni by Friedrich Bessel in the year 1838 using the trigonometric parallax. It is the only direct method to determine a distance, and it is based on a purely geometrical principle. The apparent spacial displacement of an object, owing to Earth's revolution around the sun, is decreasing with increasing distance. Even space based parallax measurements like those of the upcoming Gaia mission are limited to a distance radius of about 10 kpc, assuming an accuracy limit of 10 % (see Fig. 3.1). Consequently, astronomers have been very creative in establishing methods to obtain distance measurements at increasingly greater distances.

The methods that I present in this chapter make use of distance indicators which were initially used to determine galactic distances of nearby objects. However, today these techniques may be used to obtain distances out to the Virgo cluster of galaxies. Several methods make use of correlations between two stellar parameters, which are calibrated using objects close enough to determine their distances. These objects have well known luminosities and are in the ideal case insensitive to other parameters (e.g., age, metallicity) of the hosting system and therefore serve as so called standard candles.

Once, the apparent magnitude for these standard candles is determined, the distance modulus is obtained by

$$m_V - M_V = -5 + 5\,\lg_{10} d + A_V \tag{4.1}$$

where m_V is the apparent brightness, M_V the absolute brightness, which comes either from theory or empirical calibrations, A_V the interstellar absorption in the visual, respectively, and d the distance in parsec which gives

$$d = 10^{0.2(m-M+5-A_V)}. \tag{4.2}$$

There are various methods to obtain the distance using different standard candles, which serve as rungs in the so called cosmic distance ladder. Each rung thereby depends on the previous one in order to obtain distances of objects at even larger distances.

The following sections will list only some common methods for further information the reader is referred to e.g., Salaris & Cassini (2006) and De Grijs & Cartwright (2011), who give very useful reviews on that subject.

4.1 Cepheid Variables

The Cepheid variables are very important and often used as standard candles in astronomy, which are located in the classical instability strip in the HRD. Stars crossing this region during their evolution change their brightness periodically (see Sect. 2.1). Cepheid variables have well established (empirical and theoretical) relationships between their luminosity and their pulsation period. As already mentioned in Sect. 2.1, Henrietta Leavitt was the first to discover, that these stars follow a well defined PLR by investigating photographic plates of the Magellanic Clouds (see Leavitt & Pickering, 1912). A more recent PLR of galactic Cepheids is given by Feast & Catchpole (1997):

$$\langle M_V \rangle = -2.81 \log P - 1.43, \tag{4.3}$$

where $\langle M_V \rangle$ is the mean absolute V-magnitude of the Cepheid variable and $\log P$ the logarithm of the pulsation period in days. The zero point of this relation was calibrated using Galactic Cepheids with accurate parallax measurements obtained with the Hipparcos satellite. In order to derive the distance of any other Cepheid or of the hosting stellar system to which it belongs, all that is needed are the pulsation period and the mean apparent magnitude from the light curve (and an estimate of the interstellar reddening). First the period is used in equation 4.3 to obtain the absolute magnitude, which is then inserted in equation 4.2 together with the apparent magnitude. However, it has to be noted that an accurate estimate of the distance (see equation 4.2) can only be made, if the interstellar reddening (A_v in the visual) is taken into account. Most Galactic Cepheids are located in the disk of our galaxy, where the reddening is high and difficult to determine. This, of course, influences the accuracy of the resulting distance to the target carried out with this method. The same applies to extragalactic objects, if the interstellar reddening is not known precisely. With the help of the Cepheid-PLR it is possible to obtain distances of galactic and extragalactic objects out to about 25 Mpc.

4.2 RR Lyrae Stars

RR Lyrae stars are not only important tracers of old stellar populations (see chapter 5.1.2) but also very important standard candles, which are commonly found in globular clusters. They are pulsating HB-stars of low initial mass ($\approx 0.8 M_\odot$) located in the classical instability strip in a HRD but at fainter luminosities than the Cepheids (see Fig. 2.1). Compared to Cepheid stars, RR Lyrae stars are old, more frequent, and less luminous, thus limiting their use to a smaller space volume (e.g., members of the Milky Way and the Local Group).

4.3 Tip of the Red Giant Branch

For a given initial chemical composition, the RGB-tip bolometric luminosity only depends on the He-core mass during the He-flash phase. Within an age range of 4 to 14 Gyr the bolometric luminosity of the RGB-tip (TRGB) just changes by a few hundredths of magnitudes. However, for measurements at short and very long wavelengths the dependence on both metallicity and age becomes strong. Therefore, the TRGB-method for distance determination is best suited for I-band measurements (where the metallicity dependence is minimised) of metal poor ($-2 < [\mathrm{Fe/H}] < -0.7$) stellar populations with ages of > 4 Gyr. The location of the TRGB overlaps with the region of AGB stars in a CMD. Because of the shorter evolutionary times on the AGB compared to the RGB, a stellar census of bright red giants of a single population consequently results in a discontinuity of the luminosity function, which corresponds to the TRGB luminosity. The absolute I-band magnitude, necessary for the distance module, is obtained from calibrations as a function of metallicity. This method relies on a large sample of stars populating both regions in the CMD, the RGB and AGB. Owing to the low number of detected stars in the requested regions of globular clusters, this method is only applicable for the most massive star clusters like ω Centauri. The TRGB-method is therefore applied to objects like dwarf galaxies or the halo population of resolvable external galaxies.

4.4 Horizontal Branch Fitting

A long used method to obtain distances of stellar systems containing old stellar populations is the horizontal branch fitting. Since stars populating the HB in a CMD occupy a small range in brightness, it is feasible to use them as standard candles for distance measurements. For stars older than 4 Gyr, the HB brightness is independent on age but is sensitive to the initial metallicity and He-core mass. The observed HB, typically a well expressed feature in a CMD, is compared to its theoretical counterpart which provides the distance modulus. This theoretical relationship of the absolute luminosity has been calibrated with samples of globular clusters in our galaxy of different metallicities resulting in distances that agree well with other methods. The zero point of the HB luminosity suffers from the same uncertainty as the TRGB models because of the dependency of He-core mass.

5 Age Determination

The major source of information for the stars we observe are their emitted photons. Hence, there need to be tools to relate the stellar brightness to other physical parameters. As an example, the colour of a star (an indicator of the effective temperature and accordingly the spectral class) is derived by taking measurements in two different wavelength ranges. As already mentioned in section 1.1, the CMD, relates the stellar luminosity with the colour and serves as important tool for stellar evolution studies. Stellar evolution models aim to explain the physical and chemical changes for a star of given initial mass and chemical composition during its lifetime. An important parameter determining the morphology and the number of stars at a certain location in the CMD of a stellar population is the population's age. As an example the CMDs of two simple stellar populations (SSPs), the young open cluster M45 and the old globular M3, can be seen in Fig. 1.4 – also elliptical galaxies and some dwarf galaxies are seen as observational counterparts of SSPs. In general, SSPs consist of stars that are all born at the same time and with the same initial element composition (although some star cluster, like ω Centauri, show signs of several distinct stellar populations, see e.g., Lee at al. 1999). However, it is also the aim of stellar evolution theory to interpret the CMDs of composite stellar populations (CSP) like the Milky Way or other galaxies. The evolutionary status of the stars hosted in these systems is investigated to better understand their history of star formation and chemical enrichment. This in turn, is a necessary prerequisite for our understanding of the formation and evolution of galaxies and of the universe as a whole.

An important tool to explain the CMD of a SSP with theoretical means is the isochrone. An isochrone is computed from a set of evolutionary tracks of various initial masses at a constant age (examples of evolutionary tracks are given in Fig. 1.6 and ischrones are shown in Fig. 5.1). Each point along the isochrone represents a star with different initial mass, which is increasing towards more evolved phases (from MS to AGB) since high-mass stars evolve faster than low-mass stars. Different regions along the isochrone are named after the evolutionary phase of a star at this location (e.g., MS, TO, RGB). With the help of theoretical isochrones it is also possible to estimate the relative number of stars between two consecutive evolutionary phases, but for a correct interpretation of an observed CMD one has to adopt an initial mass function (IMF). The IMF provides the number and the distribution of stars in a certain mass range and is derived from the luminosity function (more details on the conversion of the luminosity function into an IMF is given in Holtzman et al., 1998).

5.1 Methods

There are various methods to obtain ages of SSPs and CSPs. This chapter will only list some common methods to determine the age of resolved stellar populations – for more information, the reader is referred to e.g., Salaris & Cassisi (2006).

The **vertical method** makes use of the difference in brightness of the TO and the HB and compares between theoretical and observed values of this quantity. At a given metallicity the luminosity of the TO is decreasing with increasing age, whereas the brightness of the HB is largely unaffected by age. It is important to choose the horizontal part of the HB since its morphology depends on the chosen photometric colours in a CMD. The error of this method is almost insensitive to metallicity since the luminosities of the TO and HB scale with $[\mathrm{Fe/H}]$ in about the same way.

The **horizontal method**, on the other hand, compares observed and theoretical differences in colour between the RGB and TO in a CMD. This value is sensitive to age owing to variation of the TO-colour with time, whereas the RGB colour stays more or less constant. Since the TO becomes redder with increasing age the colour difference gets smaller. Although the position of the RGB varies with the composition, the corresponding change in TO-colour compensates this effect. Because of the need of extremely high accuracy from both sides, theoretically and observationally, this method is primarily used for relative age determinations.

5.1.1 Ages of Single Stellar Populations

From observations of **globular clusters** in our galaxy we know that they consist of old, metal-poor stars. They have ages of up to 12 Gyr. Hence, globular clusters are important in order to determine the properties of the oldest stellar populations. The CMD of a globular cluster shows a well populated SGB, RGB and HB, each sensitive to different fundamental stellar parameters. One parameter is the chemical composition given in terms of X, Y and Z (where $X+Y+Z=1$), which denotes the mass fraction of hydrogen, helium and elements heavier than helium, respectively. The solar composition of $Y\approx 0.27$ and $Z\approx 0.02$ is usually used as reference point. The traditional indicator of metal abundance is then

$$[\mathrm{Fe/H}] = \log\left(\frac{Z}{X}\right)_\star - \log\left(\frac{Z}{X}\right)_\odot = \log\left(\frac{N(\mathrm{Fe})}{N(\mathrm{H})}\right)_\star - \log\left(\frac{N(\mathrm{Fe})}{N(\mathrm{H})}\right)_\odot , \tag{5.1}$$

which is the logarithmic difference of abundance ratios of a target star and the sun (assuming that the distribution of heavy elements in the sun is universal). Because of the strong and frequent spectral lines of iron (Fe), this element is used as an abundance indicator. Since $[\mathrm{Fe/H}]$ equals zero for the sun, stars of lower metallicity have negative $[\mathrm{Fe/H}]$-values. As can be seen from Fig. 5.1, the shape and the position of the isochrones in the HRD varies significantly for different values of metallicity (in particular the HB). One approach to obtain an age estimate of a globular cluster is to fit the theoretical isochrone of a generic SSP to the observed CMD. However, the resulting age of the best-fitting isochrone is depending on the

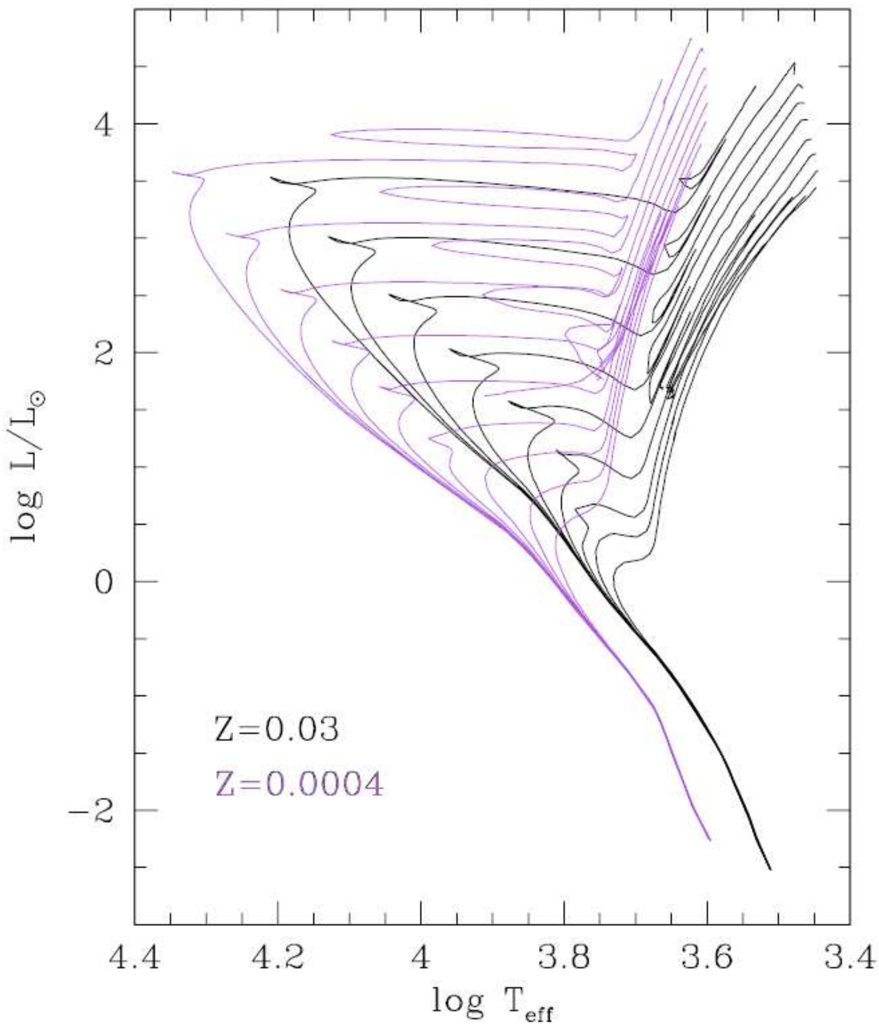

Figure 5.1: Isochrones for a range in age of $\log(t/\mathrm{yr})$=7.8 to 10.2 at equally spaced intervals and two compositions. Black solid lines indicate isochrones with [Z=0.030, Y=0.300] and purple solid lines isochrones with [Z=0.0004, Y=0.230]. The figure was taken from Girardi et al. (2000) and was adapted by the author.

uncertainties of the stellar models, which are often hard to quantify. Consequently, depending on the metallicity of the cluster, either the vertical or the horizontal method is generally used to determine the age of a globular cluster.

As demonstrated in section 1.1 (see Fig. 1.4), the CMDs of young (<4 Gyr) **open star clusters** are very different from the CMDs of old globular star clusters. The TO is commonly used as age indicator for both type of clusters. However, the morphology of the TO-region (the hook-like feature in the isochrones) of young clusters is different because it results from H-burning primarily via the CNO-cycle and not through the p-p-chain as for older populations. For ages <0.5 Gyr the He-burning phase becomes an additional age indicator owing to the increasing extension of the HB (blue loop) with decreasing age. The He-burning phase of stars in young clusters with ages between 0.5 and ~4 Gyr is usually a red clump owing to the very fast evolution on the RGB (higher masses evolve faster). If a significant fraction of cluster stars are found on the HB or red clump, the vertical method may be used to obtain the age of the cluster. However, accurate age determinations of young open clusters are difficult because of the lack of stars in more evolved phases like the SGB or RGB phase. Therefore, theoretical isochrones of different ages are fitted to the data points in the CMD (usually the MS and the TO), and after applying a correction for the cluster distance, the best-fitting isochrone is used to estimate the age of the population.

5.1.2 Ages of Galaxies and Star Formation History

In contrast to stellar cluster, most galaxies are CSP, where each population formed at a different time and with a different initial chemical composition. An example of such a CSP is the CMD of the solar vicinity in Fig. 1.3. The coexistence of bright MS stars as well as SGB and RGB stars proves the presence of both, young and old stars. These populations are described by

a) the amount of stars (or total mass) that have formed (star formation rate - SFR),
b) their initial chemical composition (age-metallicity relation - AMR) and
c) the evolution of the SFR with time (star formation history - SFH).

Because of mass-loss processes of each generation of stars that enrich the interstellar medium, the SFR and the AMR are not independent.

In order to understand the formation and evolution of galaxies it is necessary to study the various stellar populations in that system. This is done by attempting to reproduce a theoretical CMD, which mirrors the observed CMD. The generic CSP is made of a set of theoretical isochrones that cover a large range of age and initial chemical compositions. The contribution of each population is adjusted until the derived SFH explains best the observations. As already mentioned earlier in this chapter, stars in specific evolutionary stages are thereby used as age tracers.

In Fig. 5.2 a possible scheme to use stars of different initial masses at different evolutionary phases as age indicators of CSPs is given. As can be seen from this figure, RGB and AGB stars serve as age tracers for a intermediate-age population. They fill the large gap between an old population (>10 Gyr, e.g., indicated by RR Lyrae variables) and a young population (<1 Gyr, e.g., indicated by Cepheids). Since the near-infrared wavelength domain will be intensely investigated in the future (e.g., using James Webb Space Telescope, Extremely Large Telescope), RGB and AGB stars will be important objects for studies of stellar populations of extragalactic systems. Habing & Whitelock (2003) also mentioned the great potential of AGB stars for a better understanding of populations with ages of 100 Myr to a few Gyr in general. Owing to their spectral energy distribution they are very bright objects in the near-infrared (see Sect. 2.2.2) and therefore contribute significantly to the integrated light of galaxies. Moreover, in more distant galaxies only the brightest objects have a chance to be detected as individual sources. Hence, techniques to obtain information from near-infrared observations of stellar systems hosting AGB stars gain more and more importance.

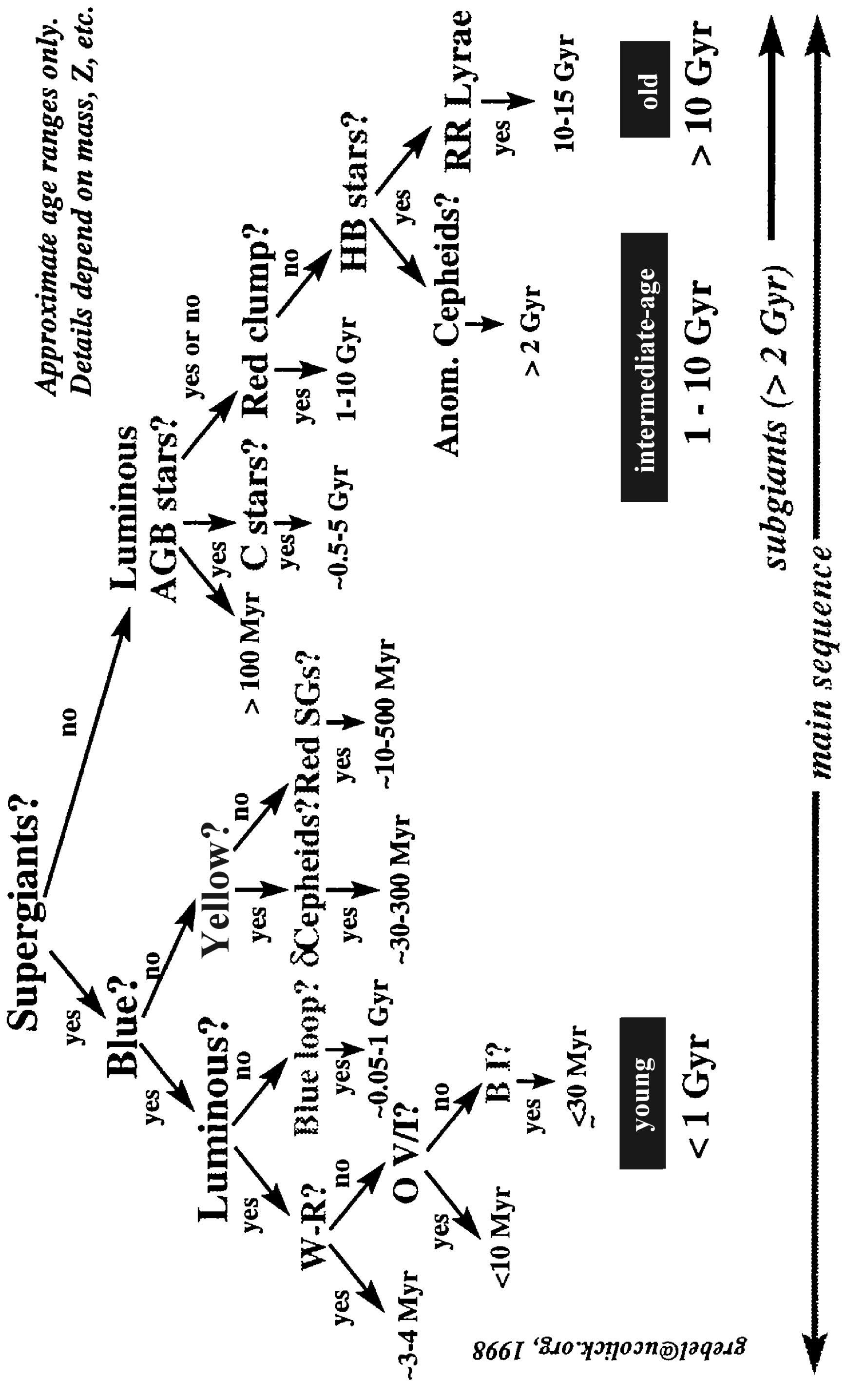

Figure 5.2: A schematic view of stars which are used as tracers for ages. This figure was taken from Grebel (1999).

Part II

LPVs in the Gaia mission

6 The LPV Work-Package in a Nutshell

The aim of the LPV work-package[1] is to provide a classification of the LPVs according to their position within a PLD (see Sct. 8.6). For this purpose luminosities have to be calculated based on the data provided by Gaia. The different types of LPVs treated within this work-package are described in section 7. Since this work-package is part of a huge data processing pipeline, it is dependent on the results of other CUs and DUs therein (see Sect. 3.3). Before the data are passed to the LPV work-package, a detected star must have been classified as a red giant variable by the classification work-package within DU1 of CU7 (see main data flow of CU7 in Sect. 3.3). From the characterisation work-package (also part of DU1 within CU7) it is expected to receive variability periods (with some indication on their significance) and light amplitudes. It is assumed that the following input data (including errors) are made available by other CUs for all classified LPVs:

- Parallax (provided by CU3)
- Mean G-band brightness (provided by CU5)
- Mean BP/RP values (provided by CU5)
- Mean RP spectrum (provided by CU5)
- Interstellar extinction (provided by CU8)

With this information the LPV work-package is going to further classify the various types of variable red giant stars. The data processing is divided into six parts (see Sect. 8) starting with a check of the classification provided by the classification work-package. The classification check is necessary to properly handle two aspects: first, short period variables at the bottom of the AGB may overlap in their variability characteristics with Cepheid variables. Second, an irregularity flag shall mark red giant variable stars that cannot be classified according to their pulsation mode as their main period is not detectable (most probably because of the time sampling of Gaia, see Sect. 3.2). To determine the luminosities, a BC has to be applied to the BP-band magnitudes (see Sect. 8.3). A special treatment of the problem of BC for LPVs is necessary, as previous studies showed that BC relations derived from hotter

[1]The LPV work-package is still a work of progress, which will be ready by the end of 2011. This chapter reports on the current status of the work-package.

stars do not give reasonable results for this kind of objects. After the luminosity determination it shall be checked if a detected LPV should be flagged as RSG (see Sect. 8.5). Besides a good estimate of the LPV luminosity, which critically depends on its parallax, the parallax error and the period are the primary input parameters required for attributing the LPV to a specific pulsation mode.

The final output parameters for each LPV are the star's luminosity and pulsation modes (if more than one significant period is detected) that is going to be published as an endproduct of the Gaia variability analysis in the Gaia data catalogue (provided by CU9).

Section 9 gives an overview of the software that has been developed by the author of this thesis, and in section 10 the different tests to guarantee a good performance of the software are introduced, including the results that were obtained so far.

Parts of this chapter have been published in an internal document (Lebzelter et al. 2011), which is currently only available to the Gaia DPAC team.

7 The LPV Work-Package for Gaia

7.1 RGBs and AGBs

In section 2.2.3 the ground breaking discovery of several almost parallel sequences of LPVs (A, B, C, D, E) of the LMC made by Wood et al. (1999) and Wood (2000) was introduced. Further investigations of LPVs in the LMC from the OGLE survey, published by Kiss & Bedding (2003), revealed that PLRs below the RGB-tip (the theoretical maximum in luminosity for RGB stars) are slightly shifted with respect to more luminous LPVs. The authors suggest that this shift is caused by RGB variables, which are much more frequent in this luminosity range than AGB LPVs. To distinguish these two types of variables, they used an amplitude criterion, because RGB variables exhibit smaller pulsation amplitudes (<0.5 in the I-band). Ita et al. (2004) confirmed their findings (see Fig. 2.8) and labelled those sequences as A^- and B^- in order to separate them from AGB LPVs (labelled as A^+ and B^+).

Accordingly, the classification within the LPV work-package of Gaia includes RGB and AGB variables. As already mentioned in section 2.2.2, it would be much more convenient to categorize these variables according to the PLR they fall onto instead of using the classification scheme of the GCVS. Both RGB and AGB LPVs detected with Gaia will be classified according to the original labelling of Wood et al. (1999) and Wood (2000) – no separation of LPVs above and below the RGB-tip is made, no sequence C′ is used. This decision is based on the following reasons: first, the separation of RGB and AGB LPVs is solely based on PLDs for which K-band measurements were available. Gaia will operate in different wavelength ranges and it is not yet clear which method will be the best to distinguish these two types of variables. Moreover, the shift of the PLRs of RGB and AGB variables only becomes visible if a certain amount of stars with periods below 70 days has been observed. Therefore, the team responsible for the LPV work-package decided for the time being that RGB and AGB LPVs will be classified in the same way. Second, the separation of sequence C′ and sequence B (e.g., Ita et al. 2004) is very small compared to other sequences. Hence, these two sequences will be merged again into one sequence labelled as B. On the basis of the post-mission data a refinement of the scheme and a possible reclassification of the stars in the final catalogue is planned.

The reference PLD, which is currently used to categorize RGB and AGB variables, is based on the findings of Ita et al. (2004) owing to the large number of detected LPVs therein. However, their PLD is only a starting point. To obtain a reference PLD for the final version of the work-package, it will be fine tuned using additional data. Therefore, a large database of well observed light curves of all kinds of LPVs has to be established, which will contain published data from large surveys (e.g., MACHO, OGLE, GCVS) as well as other ground based data. On the one hand, this will offer a well defined sample of LPVs with good periods. These periods generally stem from light curves with a much better coverage than those obtained with Gaia. Hence, if a star detected with Gaia is also listed in the catalogue, the catalogue period will be used for the reference PLD to minimize the uncertainty in the period-axis. On the other hand, the database will also cover the whole zoo of light curves that may be found among the 250 000 expected LPVs of the Gaia mission (Eyer & Cuypers 2000). This aspect is of particular importance for training the period determination software of LPVs. This database is still under construction and shall be ready by the end of 2011.

7.2 RSGs

As already demonstrated by Wood et al. (1983), LPVs are also found above the theoretical luminosity limit of AGB (AGB-tip) stars of $M_{bol} \approx -7.1$ (e.g., Paczyński, 1971). AGB stars near this brightness limit are defined as super AGB stars (see Sect. 1.4). According to Pumo & Siess (2007), these stars fill the gap between intermediate mass stars and massive stars. Hence, LPVs above the brightness limit are considered to be RSG stars (see Fig. 7.1).

From the evolutionary point of view, RSGs are very different from AGB stars. RSGs are defined as stars with initial masses $\gtrsim 9 M_\odot$, that are burning He or C in non-degenerated cores (Wood et al. 1983). Besides the difference in luminosity and pulsation amplitude (which is smaller for RSGs), Wood et al. (1983) further noted that in their sample of AGB and RSG stars, the s-process element zirconium (Zr) was detected in spectra of AGB stars only. According to stellar evolution calculations, this appearance of Zr is expected to occur in AGB stars during the phase of He-shell flashes when C and s-process elements are dredged up to the stellar surface. However, evolution models of RSGs do not predict such enhancements, confirming the division of AGB stars and RSGs, both observationally and theoretically.

Some years later, after the publication of the MACHO data which allowed to classify LPVs according to their belonging to different sequences in a PLD, Kiss et al. (2006) discovered that RSGs seem to follow a PLR as well (see Fig. 7.2).

However, one has to be careful interpreting the results in Fig. 7.2. First, the black dots indicating galactic RSG variables are based on 18 stars and 30 significant periods (see Kiss et al. 2006 for details). Hence, for most of these galactic RSGs more than one period has been obtained, leading to more than one black point per star in this diagram. Second, the light curves stem from observations in the visual wavelength range. For the majority of this sample, K-band magnitudes were obtained as follows: bolometric magnitudes were determined from spectrophotometry of Leveseque et al. (2005) using stellar atmosphere models of Gustafsson et al. (1975) and Plez et al. (1992) (with opacities from Plez, 2003; Gustafsson et al., 2003). These bolometric magnitudes were then calibrated according to the relation of Josselin et al. (2000), which is again only a rough estimate given as $m_{bol} \simeq m_K - 3$. Therefore, this procedure certainly introduced some uncertainties in brightness, which were not

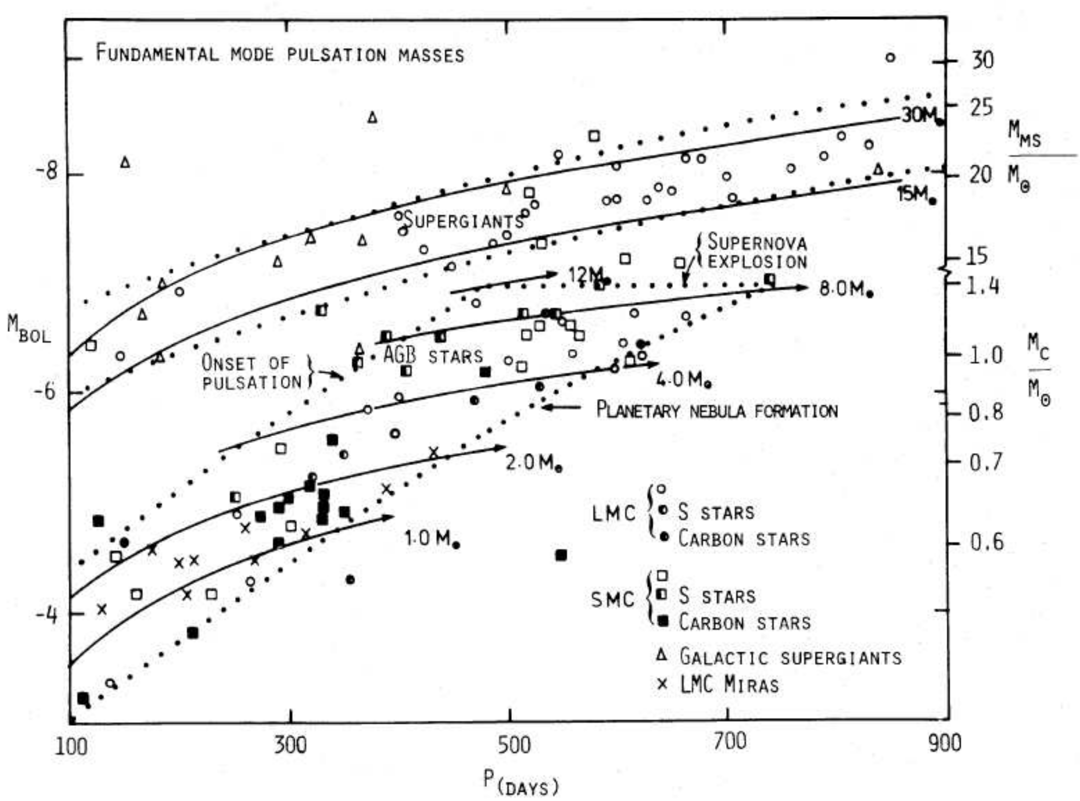

Figure 7.1: A diagram of M$_{bol}$ versus period of variable red giant stars of the Magellanic Clouds. Dotted lines indicate regions for either RSGs or AGB LPVs, continuous lines are lines of constant pulsation mass (present day masses) assuming that LPVs are fundamental mode pulsators. On the ordinate to the right hand side, the initial masses (M_{MS}) of RSGs and the core masses (M_c) of AGB stars are given at each luminosity. The picture is taken from Wood et al. (1983).

discussed by Kiss et al. (2006). Instead, they plotted the RSG variables of the LMC of the MACHO survey taken from Wood et al. (1983) for comparison reasons (blue dots in Fig. 7.2), although they admit that a direct comparison with MACHO data is difficult mainly because of the lack of precise distance estimates for RSGs. In any case, one of the conclusion that can be drawn from Fig. 7.2 is, that RSGs also seem to follow different PLRs, most probably extending the PLRs of AGB stars towards higher luminosities.

In a recent publication of Groenewegen et al. (2009), a sample of AGB stars and RSGs of the Magellanic Clouds was analysed with regard to their mass loss properties that play an important role in the final evolutionary stages of these stars. The authors separate RSGs and AGB stars using a modified version of a PLD as the one introduced by Wood et al. (1983). Beside the maximum luminosity limit of M$_{bol}$ = − 7.1 of AGB stars, which was used by Wood et al. (1983) and Smith et al. (1995), Groenewegen et al. (2009) also took other publications with a different brightness limit of M$_{bol}$ = − 8.0 into account (e.g., Wagenhuber & Groenewegen,

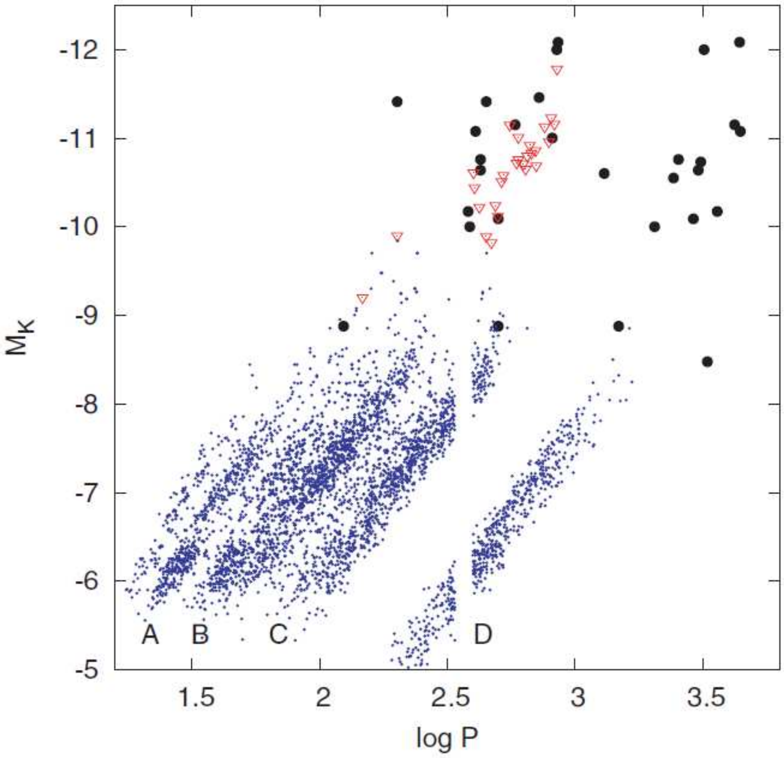

Figure 7.2: A P-$\log K$ diagram of LPVs. Blue dots show data taken from Derekas et al. (2006), black dots RSGs of the Milky Way and red triangles RSG variables of the LMC. The labelling of the different sequences was adopted from Wood (1999, 2000). This picture was taken from Kiss et al. (2006).

1998; Poelarends et al., 2008). Accordingly, Groenewegen et al. (2009) classified all (constant and variable) stars of their sample brighter than $M_{bol} = -8.0$ as RSGs. All variables RSGs of their sample, classified with this new limiting brightness value, have smaller amplitudes than those expected from variable AGB stars. In their PLD, the authors defined a region populated by both types, RSGs and AGB stars (see continuous and dashed line in Fig. 7.3). As already suggested by Wood et al. (1983), Groenewegen et al. (2009) used an amplitude criterion to separate RSGs from AGB stars in this overlap region. Consequently, stars with I-band amplitudes larger than 0.45 mag were classified as AGB stars and those with smaller amplitudes as RSGs.

The results of Wood et al. (1983), Kiss et al. (2006) and Groenewegen et al. (2009) concerning RSG variables, convinced the management of CU7 (see section 3.3) to also include RSG stars in the LPV work-package. However, it is not (yet) possible to classify RSGs in the same way as RGB and AGB LPVs. Owing to the difficulties of brightness determination (as mentioned above) and the low number of detected RSG variables, it seems not advisable to define PLRs to which these variables could be related to. Since it is expected to obtain very precise distance measurements with Gaia, the resulting bolometric brightness and the brightness limit of Wood et al. (1983) are going to be used to distinguish RSGs from other

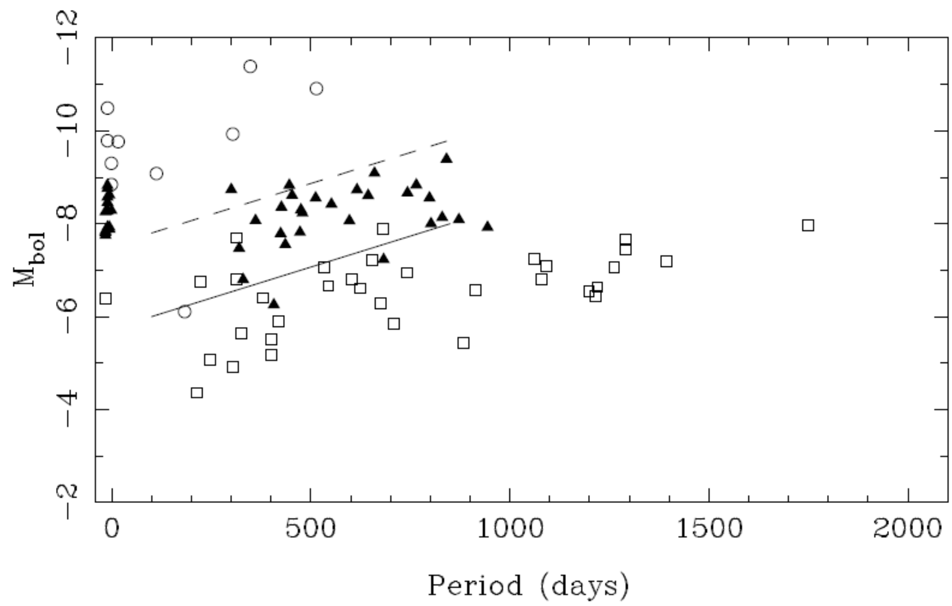

Figure 7.3: A M$_{bol}$-period diagram of RSGs and AGB stars of the Magellanic Clouds. Stars identified as foreground objects are indicated by open circles, AGB stars as open squares and RSGs as filled triangles. Stars without a detected period are plotted at negative values of the abscissa. The continuous line is the lower brightness limit of RSGs of Wood et al. (1983) and the dashed line is placed 1.8 magnitudes above the RSG limit. The figure was taken from Groenewegen et al. (2009).

LPVs. The treatment of LPVs populating the overlap region, as discussed in Groenewegen et al. (2009), is still a matter of debate since their amplitudes are based on observations in the I-band. It has to be tested if a calibration of the Gaia photometry would lead to satisfying results.

7.3 Irregular Variables

According to the classification of the GCVS, a fraction of variable red giants show irregular brightness changes in their light curves. As already mentioned in section 2.2.2, Lebzelter & Obbrugger (2009) have shown that semi-regular and irregular variables most probably belong to the same class. The authors clearly demonstrated that a large fraction of irregulars in the GCVS were misclassified owing to a sparse sampling of the light curve. The scanning law of the Gaia satellite will produce an observing pattern of data points (see Sect. 3.2.3) that increases the probability of a misclassification of semi-regular variables. It is therefore expected that no period is detected for a significant fraction of stars with actually semi-regular brightness changes. Supplementary observations as well as the collected information of the planned database (mentioned in 7.1) of these candidates will improve the coverage of the light curve, and a reclassification according to PLRs of LPVs may be realised at a later time.

Therefore, stars observed with Gaia which are flagged as irregular variables (LPVs for which no period is detected, see Sect. 8.2) would provide an interesting aspect for future studies of LPVs.

Being aware of the Gaia time sampling, the responsible LPV work-package team aims to include all variables that are classified as irregulars (with red colours) by the Classification work-package of DU1 within CU7.

8
The Modules

8.1 Classification Check

This module aims to separate misclassified Cepheids from the long period variables.

Long period variables show periods between about 30 and 1000 days and light amplitudes in the visual between 0.1 and 8 magnitudes. At the lower period end and even more for the stars on the RGB, misclassification of a Cepheid as LPV from the period alone may occur (see e.g., Debosscher et al. 2007, Dubath et al. 2011b). These cases shall be identified and reclassified by this module. First of all, a minimum period for LPVs of 10 days ($\log P = 1$) is defined, stars with shorter periods are not taken into account. Cepheids can be separated from stars on the giant branch by their colours, the latter being redder. Furthermore, LPVs at the lower end of the period range typically have smaller light amplitudes than Cepheids. This criterion can be used to distinguish between the two variability classes in cases where the colours are overlapping. The exact criteria are a matter of debate.

Actually, it is the aim of this module to ensure that a star classified as LPV is really on the giant branch, i.e. no reclassification will be done. If such a colour/amplitude criterion is already included in the primary variability Classification work-package of DU1, this module may be omitted.

8.2 Irregularity Check

Within this module variables that belong to the giant branch (on the basis of a colour criterion) with no distinct periodicity are flagged as irregular variables.

Historically, LPVs for which no periodicity could be determined were classified as irregular variables (subdivided into L, Lb and Lc). The reason for this may either be a truly irregular behaviour or a lack of reliable light curve data to identify an existing period. Both reasons may also be applicable for stars observed by Gaia.

These stars have to be identified at this stage as it is not possible to classify them according to their pulsation mode like it is planned for all other LPVs (excluding RSGs). It is assumed here that the Variability Characterisation work-package providing variability periods includes some indication on the reliability of a derived period. If this is not the case, this module has to be extended with an own period determination algorithm. Based on the final output from the Variability Characterisation work-package, a criterion will be formulated, defining a lower quality limit of a detected period. LPVs with periods of lower significance will be flagged as (red) irregular variables within the LPV work-package. These stars (identified either within the Classification or LPV work-package) will remain in the data analysis to determine the BC and the bolometric brightness (see Sect. 8.3 and 8.4).

If the Classification work-package already contains a minimum accuracy of the derived period and further distinguishes between evolved irregular variables (with red colours) and other irregular stars, this module might be omitted.

8.3 Bolometric Correction

The BC module is optimised to derive the BC of red giant variables, hence, each source entering the LPV work-package will be processed through this module (followed by the module for luminosity determination). Obtaining a reliable BC and, hence, a bolometric brightness for LPVs is of crucial importance to identify RSGs as well as to subclassify these stars according to their PLRs (see Sect. 8.5 and 8.6, respectively). The calculations to obtain the BC of red giants, which is solely based on Gaia Photometry, were carried out by M. Lederer and kindly provided to the author of this thesis (private communication).

First, grids of MARCS model atmospheres for both, C-rich and O-rich stars, with effective temperatures of 3750 K to 6000 K and surface gravities of $0.75 \leqq \log g \leqq 3.0$, taken from Gustafsson et al. (2008) were extracted. The subgrids were separated according to different ratios of C over O and metallicity (Z). On top of these models synthetic spectra were calculated with a resolution of $R = 2500$ and a spectral range of 300 to 1100 nm, using COMARCS/COMA (Aringer et al., 2009). These spectra were then transformed into a format suitable for the Gaia Object Generator (GOG), to extract synthetic Gaia photometry (G, BP, RP, RVS). Finally, these synthetic values were used to to perform a regression calculation and find a function that relates the theoretical BC with the Gaia photometry for the different types of LPVs (O-rich, C-rich).

In case of processing a large amplitude C-rich LPV, a model representing the well known carbon star S Cep (labelled as Mira in Fig. 8.1) was chosen as a representative. Note, that this star is also known to contain a significant fraction of circumstellar dust. It is the only C-rich LPV for which extensive spectroscopic time series with high resolution in the infrared were observed over the whole pulsation cycle (see Nowotny et al., 2005). Hence, S Cep models were used as a calibrator to compare and adapt model parameters of synthetic spectra of C-rich stars. Since the atmospheres of large amplitude LPVs (like S Cep) highly depend on dynamical processes, like shock waves (caused by pulsation) propagating through the atmosphere and dust driven stellar winds, the approach of a hydrostatic model, which neglects all dynamical phenomena, is no longer valid. A dynamical model atmosphere has to be used to obtain synthetic spectra that fit the observations. The first prototype of such a model that takes time-dependent dynamics into account, is described by Höfner (1999). The dynamical models of Höfner et al. (2003), which were used in this module for large amplitude LPVs with C-rich atmospheres, further include frequency-dependent radiative transfer.

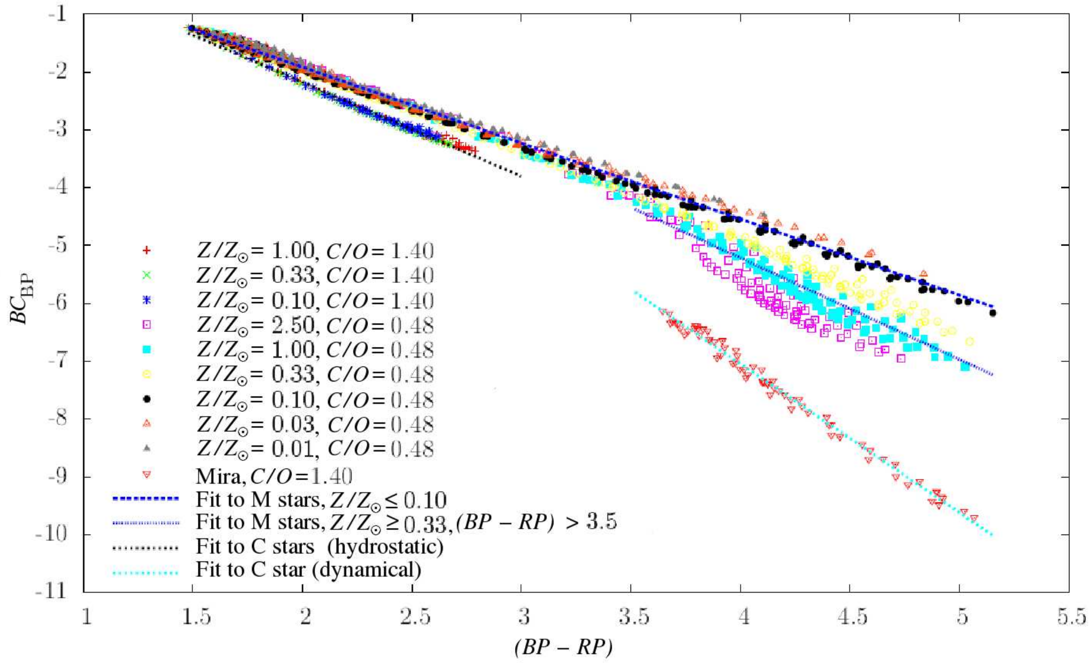

Figure 8.1: A plot of BC for the synthetic BP magnitude (BC_{BP}) versus the $(BP-RP)$ colour. The labels for different input parameters are given at the lower left. For further explanations see text. The figure was kindly provided by M. Lederer (p. c.).

Therefore, using these models is the only consistent way to explain the observed quantities (like e.g., colours, line profiles, low resolution spectra) of large amplitude LPVs. The red triangles in Fig. 8.1 are representing the S Cep models and clearly illustrate the change of colour and BC during one pulsation cycle. Furthermore, it can be seen in Fig. 8.1 that the BC of both hydrostatic and hydrodynamic C-rich stars follow a linear relation for different input parameters (like C/O ratio and metallicity).

In order to test the influence of dust, a dynamical model with the same input parameters excluding circumstellar dust was computed, and the colours obtained in this way during one pulsation cycle were plotted against the values of the BC. The resulting data also follow a linear relation, which is located slightly above the hydrostatic model results. Consequently, the presence or absence of dust as well as assuming different species of C-rich dust, will change the colours during one pulsation cycle significantly (up to several orders of magnitude). According to our understanding of dust formation in pulsating AGB stars, we do not expect to observe large amplitude LPVs without any circumstellar dust. Höfner et al. (2003) also mentioned that only in LPVs with large amplitudes, the outer layers of the atmosphere become cool and dense enough to trigger dust formation. For this reason, the LPV work-package team assume an amplitude criterion as sufficient to select either the hydrostatic or hydrodynamic relation and derive a reliable BC. Hence, in the case of dealing with a large amplitude C-rich LPV that contains less circumstellar dust than the S Cep model, the BC-relation of the dynamical model will extrapolated to bluer colours. In case of a low amplitude C-rich variable showing redder colours than calculated for the hydrostatic models, the hydrostatic BC-relation will be extrapolated.

Since the spread in BC versus colour for O-rich stars in Fig. 8.1 (labelled as M stars) becomes very large for different values of metallicity, especially at red colours, it is not advisable to search for a general correlation in this plot. Consequently, from all the data plotted in in Fig. 8.1 only the BC-relations for C-rich stars are implemented to the BC module of the LPV work-package. The two BC-relations for C-rich stars (hydrostatic and hydrodynamic) are given as:

$$BC_{BP} = a(BP - RP) + b \tag{8.1}$$

$$if \quad amplitude_G < 3 \quad (hydrostatic\ case)$$

$$a = -1.63 \pm 0.01$$
$$b = 1.07 \pm 0.03$$

$$if \quad amplitude_G \geqq 3 \quad (hydrodynamic\ case) \tag{8.2}$$

$$a = -2.57 \pm 0.03$$
$$b = 3.24 \pm 0.13,$$

Given that the colour term $(BP - RP)$ is replaced with Col, the BC uncertainties for C-rich stars can be written as:

$$\sigma_{BC} = \sqrt{(\sigma_a Col)^2 + (\sigma_b)^2 + (a\sigma_{Col})^2} \tag{8.3}$$

For O-rich stars it turned out that a change of the Gaia colour ($(G-RP)$ instead of $(BP-RP)$, see Fig 8.2) solved the problem of a broad spread in BC for different metallicities. In contrast to C-rich stars, the models of hydrodynamical O-rich stars fall onto the same sequences as the hydrostatic ones. Moreover, the models of LPVs with low surface gravities follow the same BC-relation as O-rich AGB stars. Therefore, it may be assumed that this relation is also valid for RSGs. The synthetic values of O-rich AGB stars could be fitted with a polynomial of third order. The data of C-rich stars are included in Fig 8.2 for illustrative reasons only – no further relation was fitted to these values. The BC-relation for O-rich stars is given as:

$$BC_{BP} = a + b(G - RP) + c(G - RP)^2 + d(G - RP)^3 \tag{8.4}$$

$$a = 10.66 \pm 0.50$$
$$b = -36.98 \pm 1.49$$
$$c = 39.46 \pm 1.44$$
$$d = -15.62 \pm 0.45.$$

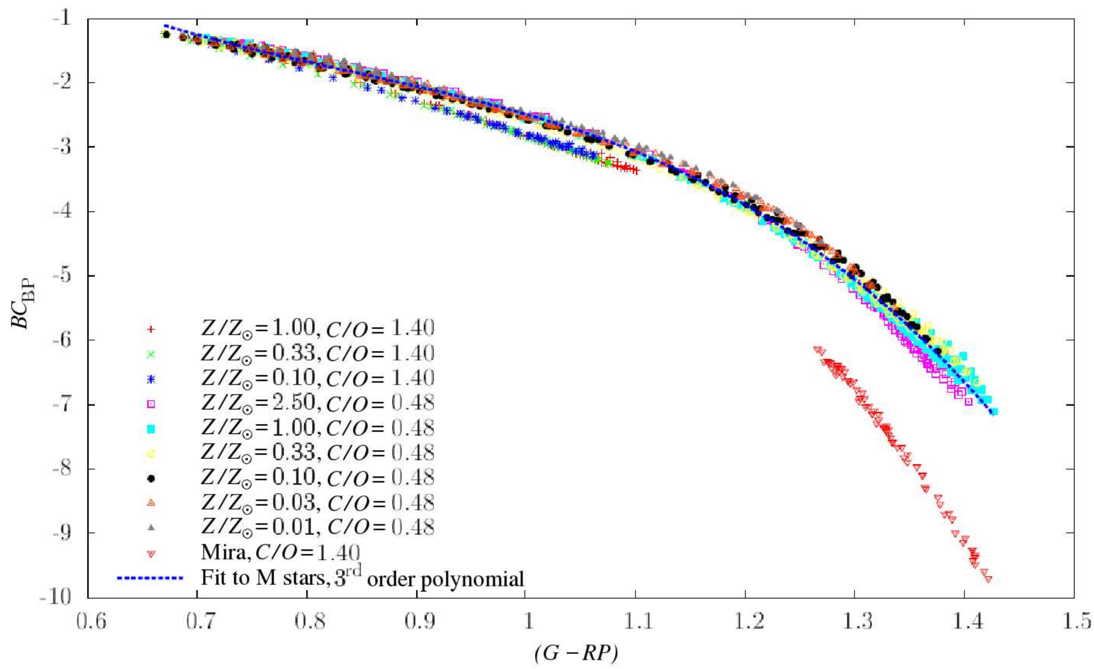

Figure 8.2: A plot of BC for the synthetic BP-band (BC_{BP}) versus the ($G - RP$) colour. The labels for different input parameters are given at the lower left. For further explanations see text. The figure was kindly provided by M. Lederer (p. c.).

Renaming the colour term with Col, the error for BC of O-rich stars can be written as:

$$\sigma_{BC} = \sqrt{\sigma_a^2 + (\sigma_b Col)^2 + (\sigma_c Col^2)^2 + (\sigma_d Col^3)^2 + ((b + 2cCol + 3dCol^2)\sigma_{Col})^2} \tag{8.5}$$

Further diagrams using other colours and BCs of different Gaia passbands were also created but did not lead to satisfying results. The three BC-relations mentioned above (two for C-rich stars and one for O-rich stars) were those with the best correlations.

In order to obtain a PLD of good quality, which uses the bolometric luminosity, it is of crucial importance to separate C-rich and O-rich sources using Gaia photometry only. As can be seen from Fig 8.2, the difference of the BC for each type is in the order of magnitudes, particularly for very red Gaia colours. Tests have been performed to check the feasibility to identify C-rich stars using the low resolution spectra of the RP. The strategy and results of this test are described in detail in section 10.2.

8.4 Luminosity Determination

This module combines the mean BP magnitude, the parallax, the BC and the interstellar absorption in the BP-band to calculate the luminosity of a star.

The uncertainty of the various input parameters shall be transformed into an uncertainty in absolute bolometric magnitude. To keep the calculations as simple as possible, the work-package team decided to focus on the absolute bolometric magnitude since it is easy to convert the bolometric magnitude in luminosity. This module requires a parallax value (π) with some minimum accuracy to achieve reasonable results. Thus, this module shall first check whether the parallax error (σ_π) is sufficiently small. As a first approach the minimum accuracy is set to $\sigma_\pi < 0.5\pi$. If this is not the case, the module for LPV sub-classification will not be executed. If the condition for accuracy of the parallax is fulfilled, the absolute bolometric magnitude can be obtained as follows:

$$M_{bol} = m_{BP} - BC_{BP} + A_{BP} + 5\log\pi + 5 \tag{8.6}$$

where m_{BP} is the mean BP-band magnitude, ABP the interstellar extinction and π the parallax given in arcseconds. The error of the absolute bolometric magnitude is derived from:

$$\sigma_{M_{bol}} = \sqrt{\sigma^2_{m_{BP}} + \sigma^2_{m_{BC_{BP}}} + \sigma^2_{A_{BP}} + 4.715\pi^{-2}\sigma^2_\pi} \tag{8.7}$$

It has to be pointed out that the absolute bolometric magnitude and its error are depending on the calculation type of the mean BP magnitude and its error. The combination of the time sampling of the Gaia observations (see Sect. 3.2) and the variable nature of LPVs might cause misleading mean values of m_{BP} and $\sigma_{m_{BP}}$. In the worst case, the groups of measurements, which are taken every 30 to 40 days by Gaia, could fall in approximately the same pulsation phase, hence, the calculated mean brightness values would not be representative. Moreover, the light amplitudes carried out from the BP and the G-band to obtain a mean magnitude (used in the BC module) could also be different from the real ones, depending on the coverage and gaps in the light curve.

8.5 RSG Classification

After the determination of M_{bol} it has to be checked if the star should be flagged as a red supergiant. Depending on the period (P), AGB stars never exceed a certain value for M_{bol}, therefore, the following relations of Wood et al. (1983) are taken as upper luminosity limits for AGB stars.

$$\begin{aligned} M_{bol_P}\,[mag] &= -0.0069P - 3.7077 \quad if\ P < 490\,d \\ M_{bol_P}\,[mag] &= -7.1000 \quad if\ P \geq 490\,d \end{aligned} \tag{8.8}$$

Accordingly:

$$IF \quad M_{bol_G} < M_{bol_P} \quad THEN \quad RSGflag = yes \tag{8.9}$$

M_{bol_P} is the upper luminosity limit depending on the period of a LPV. Stars with brighter luminosities ($M_{bol_G} < M_{bol_P}$) will be marked by a change in the RSG-flag. As mentioned in section 7.2, the observations of RSGs do not yet allow a classification according to their pulsation sequences as in the case of RGB and AGB stars. Consequently, RSGs will not enter the LPV-classification module and their parameters obtained so far will be saved in the main database.

8.6 Pulsation Mode Classification

Once the luminosity of the star (excluding irregular variables and RSGs) has been determined, the period search results are extracted from the Characterisation work-package. The subclassification of the star is done according to its belonging to one of the predefined regions in the reference PLD. For the time being, as already mentioned in 7, the PLRs of LPVs of the LMC from Ita et al. (2004; see Fig. 8.3) are used as a starting point. Before the satellite is launched, the model PLD will be adjusted by using pulsation models and findings of other available studies on that subject. As soon as the first measurements of Gaia are available, this reference PLD will be further adapted and gradually refined.

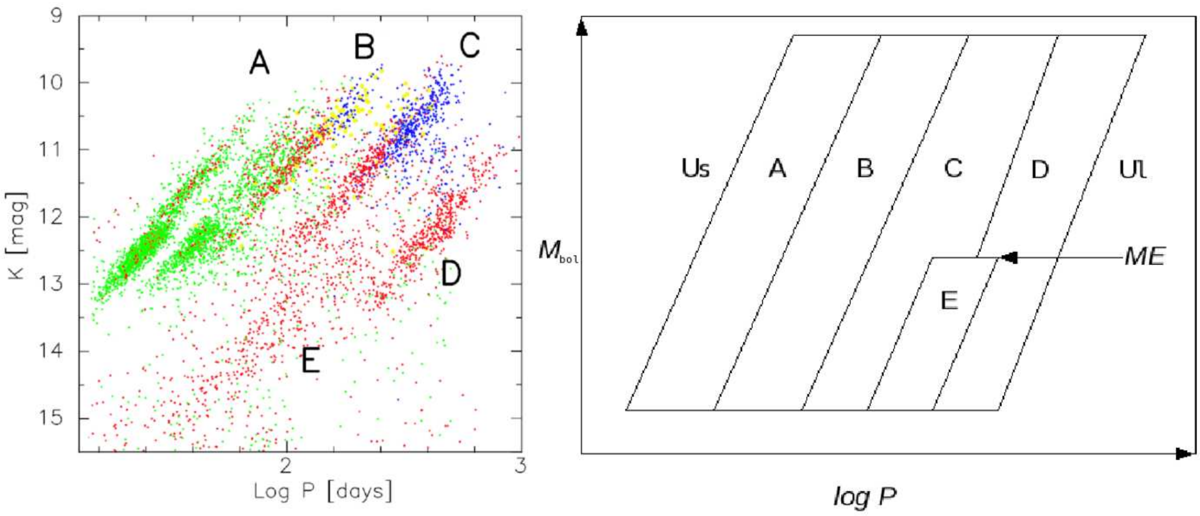

Figure 8.3: Left panel: same as Figure 2.8 but with the labelling of Wood et al. (1999) and Wood (2000). Right panel: a schematic view of the five different classification areas (A, B, C, D, E) around the PLRs (see text) in a $logP$-M_{bol}-diagram. 'ME' marks the limiting maximum brightness for RGB stars (RGB-tip). 'Us' describes unclassified LPVs outside the classification region at short periods and 'Ul' unclassified LPVs at long periods.

The different classification regions around the $logP$-M_{bol}-sequences in Fig. 8.3 are named after the PLRs discovered by Wood et al. (1999). The reasons for the choice of this labelling are mentioned in section 7, and the method that was used to define the border between those areas is described in section 8.6.2. If the star has more than one significant period, which is quite common among LPVs, the star will receive a multiple classification. To give one example, a star for which the most significant period is related to pulsation mode B and the second period is related to sequence A, will be classified as LPV of type BA. RGB stars, identified by their location at the lower luminosity end of the PLD (below the RGB-tip), will be classified in the same way. Stars flagged as irregular variables in the Irregularity Check module, are excluded from the Pulsation Mode Classification module. The error boxes that are produced by the error of $\log P$ and the error of M_{bol} will be used to decide, which of the predefined classification areas is the most probable one (see Sect. 8.6.3 for more details). Stars located outside of the predefined classification boxes will be labelled as LPVs of either class 'Us' (undefined LPV at the short period end) or class 'Ul' (undefined LPV at the long period end).

8.6.1 Inputs for Classification

Each Gaia source enters this module with some uncertainty in bolometric luminosity and period. This means that an observational box, defined by the uncertainties of the measurements, will actually be related to a predefined area around the pulsation sequence. As illustrated in Fig. 8.3, the sequences have some natural width as they are mixtures of stars of different mass, metallicity and pulsation mode (particularly in the case of the overtone pulsators, see Sect. 2.2.2 and 2.2.3). In our approach, the areas around the pulsation sequences are defined in a way that there are no gaps between the individual boxes (see right panel in Fig. 8.3). The motivation for our choice of the individual borders between the sequences is described in more detail in section 8.6.2. From the error boxes of each source the upper left point (ULP), the lower right point (LRP) and the central point ($centreP$) of this error box will mainly be used for the classification. The coordinates of these points, which are defined below, are used as variables in the code of the LPV work-package.

$$ULP = \begin{pmatrix} ULPer \\ ULM_{bol} \end{pmatrix} = \begin{pmatrix} \log(P - errP) \\ M_{bol} - errM_{bol} \end{pmatrix} \tag{8.10}$$

$$LRP = \begin{pmatrix} LRPer \\ LRM_{bol} \end{pmatrix} = \begin{pmatrix} \log(P + errP) \\ M_{bol} + errM_{bol} \end{pmatrix} \tag{8.11}$$

The abscissa of the point ULP ($ULPer$) is derived from the minimum possible period ($logP$ minus error), and the ordinate of ULP (ULM_{bol}) is the maximum possible brightness (arithmetic M_{bol} minus error). For the LRP the abscissa ($LRPer$) corresponds to the maximum period ($logP$ plus error) and the ordinate (LRM_{bol}) to minimum brightness (arithmetic M_{bol} plus error).

$$centreP = \begin{pmatrix} midLgP \\ M_{bol} \end{pmatrix} = \begin{pmatrix} (\log(ULPer) + \log(LRPer))/2 \\ M_{bol} \end{pmatrix} \tag{8.12}$$

$$inputP = \begin{pmatrix} realLgPer \\ M_{bol} \end{pmatrix} = \begin{pmatrix} \log(P) \\ M_{bol} \end{pmatrix} \tag{8.13}$$

The abscissa of $centreP$ ($midLgP$) is derived from the half of the sum of $ULPer$ and $LRPer$, and its ordinate is the M_{bol} (without taking errors into account). The real input point ($inputP$) is determined by the logarithm of the period ($realLgPer$, abscissa) and M_{bol} (ordinate). Note that $centreP$ and $inputP$ have the same ordinate (M_{bol}), but since the logarithm of the period is used, the abscissa of $centreP$ ($midLgP$) constantly deviates from the abscissa of $inputP$ ($realLgPer$).

It should be mentioned that the team of the LPV work-package is well aware of the bias, which is produced by the use of $midLgP$ (which will always be smaller than $realLgPer$) to categorise the majority of LPVs detected with Gaia. However, the effect of this bias on the classification is expected to be very low, since only a small fraction of the LPVs are located between the different PLRs (see e.g., Fig. 2.6 and Fig. 2.7).

8.6.2 Classification Areas

The borders of the different classification areas are given as linear equations of the form

$$M_{bol}(P) = a(i)\log P + b(i), \tag{8.14}$$

where $a(i)$ defines the slopes of and $b(i)$ the intercepts of the sequence borders, respectively. Ita et al. (2004) calculated linear regression lines for each of the sequences they defined in the PLD, therefore, the values of the slopes are slightly different for each sequence. In order to avoid gaps or overlaps between the classification areas, the LPV work-package team has chosen the slope of sequence C of Ita et al. (2004) as representative for all classification areas in the LPV work-package. This decision is based on the assumption that within a classification box the small differences in slope with respect to the other (almost parallel) PLRs is negligible. Moreover, the slope of sequence C is very close to the values obtained from other studies (see table 14.3 in Sect.14.2 and e.g., Feast et al., 1989; Groenewegen & Whitelock, 1996; Wood 2000), which were using different data sets.

For the construction of the parallel borders in the reference PLD, the following strategy was applied. According to the distribution of the LPVs in Ita et al. (2004), most stars are found at a K-band luminosity of 12.5 mag. Therefore, the $\log P$ values of all PLRs of Ita et al. (2004) were obtained at this luminosity and subsequently used to derive new intercepts (using the slope of sequence C for all PLRs). This produced a series of parallel PLRs with the labelling of Ita et al. (2004). As mentioned in section 7.1, the separation of RGB and AGB stars (e.g., sequence A^- and A^+) is not taken into account in the LPV work-package. To determine one single sequence, a regression line was calculated, which is located in the centre of e.g., sequence A^- and A^+. The same method was applied to determine sequence B (merging sequence B^- with B^+ and then sequence B with C) and the borders between two neighbouring sequences. Sequence E, which was not defined by Ita et al. (2004), was defined as centre line between sequence C and D below the RGB-tip. The outer borders of the LPV classification boxes (between areas Us-A and D-UL) were placed one magnitude offset to the (parallel) sequences A and D, respectively. The classification borders of the LPV work-package as well as the modified linear relations (as described above) were superimposed to the K-$\log P$-diagram of ita et al. (2004, see Fig. 8.4) for comparison reasons.

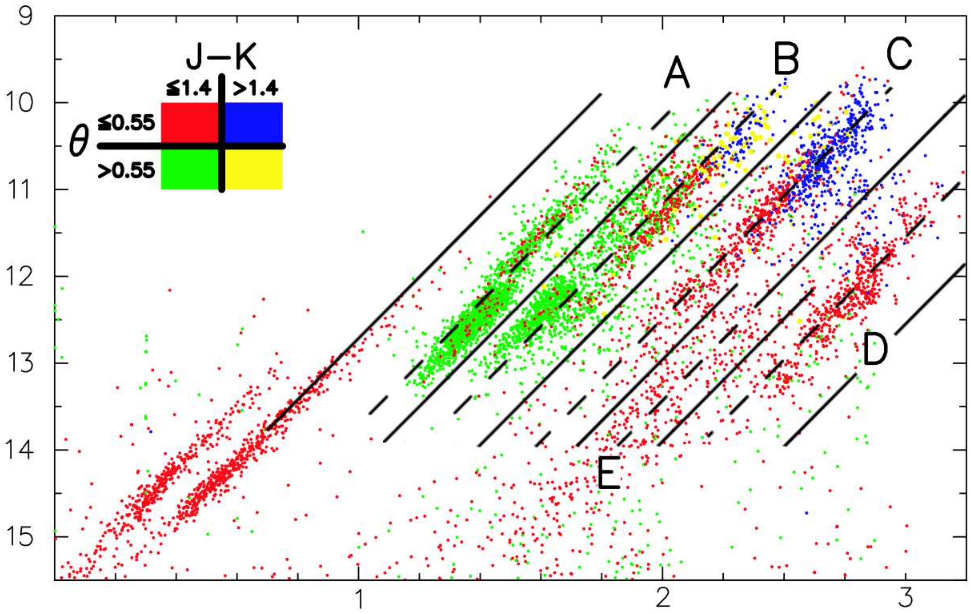

Figure 8.4: Same as Fig. 2.7 but with superimposed borders (continuous lines) and PLRs (dashed lines) of the LPV work-package. The labels of used in the PLD of Ita et al. (2004) were replaced with those of Wood et al. (1999, see text for more infomartion).

The K-band intercepts were converted into bolometric ones using a distance modulus of the LMC of $(m - M) = 18.5$ mag (Pietrzyńsky et al., 2009) and a mean BC of –3.2 mag based on the findings of Kerschbaum et al. (2010). The bolometric RGB-tip luminosity (–3.2 mag) was used as an upper limit for sequence E in the reference PLD. A list of the different borders used for the LPV classification boxes is given in Table 8.1.

Table 8.1: A list of the slope and various intercepts for the borders of the classification areas.

border	slope	intercepts
Us - A	–3.52	0.941
A - B	–3.52	2.429
B - C	–3.52	3.580
C - D	–3.52	5.185
C - E	–3.52	4.714
E - D	–3.52	5.656
D - Ul	–3.52	7.126

8.6.3 Classifiying LPVs

Depending on the brightness of the LPV that needs to be classified, the total number of the various classification borders is different. If the star is brighter than the RGB-tip the total number of borders for the classification is five, otherwise six borders have to be taken into account (see Fig.8.3). The next step is to identify the border just below the central point ($centreP$; see Sect. 8.6.1)of the error box. The area to the left of this border is consequently the LPV subclass that is assigned to the star.

To identify this border, a loop (equation 8.15) is executed, which runs through the list of the slopes ($a(i)$) and intercepts ($b(i)$) of the border relations, until the resulting brightness of the sequence border ($M_{bol}Onborder$) is brighter than the luminosity of the input point (M_{bol}; see equation 8.16).

$$M_{bol}Onborder = a(i)\log P + b(i) \qquad Loop\ until \qquad (8.15)$$

$$M_{bol} > (M_{bol}Onborder + M_{bol}Tolerance) \qquad is\ true \qquad (8.16)$$

Note that the value in M_{bol} of bright sources is smaller than for fainter ones. From a numerical point of view, the values of M_{bol} may become very close to $M_{bol}Onborder$ but they would rarely be exactly the same. Hence, to avoid infinite loops of the software, a tolerance interval in equation 8.16 ($M_{bol}Tolerance$) has to be defined. If the centre point is located beyond sequence D, a different termination condition has to be used. Within the LPV work-package the slope ($a(i)$) is defined as a vector whose length is increasing with each iteration. This vector has a maximum length of either '5' (number of borders above the RGB-tip) or '6' (number of borders below the RGB-tip). The second condition to terminate the loop therefore is if the length of the vector equals the iteration number (see Sect. 9 for details). If the point in the centre of the error box happens to fall exactly onto one of the borders, $\log P$ in equation 8.15 is replaced with $realLgP$ to determine the membership of the real input point.

After clarifying the sequence membership of the input point ($centreP$ or $inputP$), the various error classes, as illustrated in Fig. 8.5, have to be calculated. The error class of a LPV is derived by checking the location of the ULP and the LRP (replacing $\log P$ with $\log(ULPer)$ and $\log(LRPer)$ in equation 8.15, respectively). Because of the different intrinsic properties of LPVs like mass, total amount of mass loss, and metallicity, the LPV error class parameter can not be seen as a probability. Instead, these error classes are given as single digit numbers (numbers '1' to '4', see Fig. 8.5) which should primarily help to locate a star relative to a certain P-L-area.

In the best and most simple case, all three points of the error box are members of the same sequence and the error class is set to 1 (see example '1' in Fig. 8.5). If the ULP or the LRP falls onto a border between two sequences, the error class is set to 2 (see examples '2' in Fig. 8.5). In the case of having one of the points in a different classification box as the other two points, the error class is set to 3 (see example '3' in Fig. 8.5). In the rare case, where the $centreP$ falls exactly onto the border between two pulsation sequence areas, the location of the real input point ($inputP$) decides on the membership of the LPV class and the error class is set to 4 (see example '4' in Fig. 8.5).

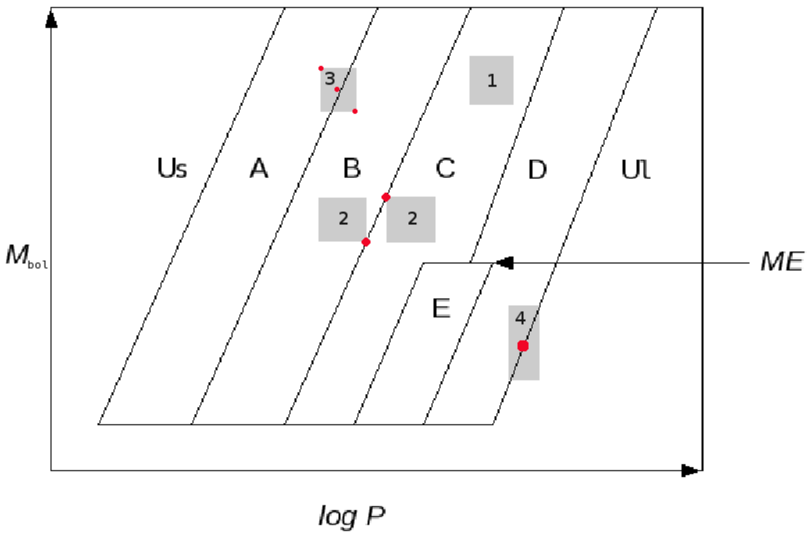

Figure 8.5: Same as right panel in Fig. 8.3 but including examples for the different error cases that might occur (labelled as 1, 2, 3 and 4).

If a second period is found for a target, the same algorithm is run again producing a two digit class as described above. To give a concrete example: if a LPV exhibits two significant periods, where the first one falls into area C having error class '1' and the second periods falls into area A with error class '3', its LPV sub-class will be C1A3.

9 The Code

All the codes written for the Gaia mission are programmed in Java. Since the work for this mission is done by a very large community over an estimated time of about 15 years, this object orientated programming language and a continuously updated software documentation management is best suited to meet the requirements of this project. Using Java enables each work-package member to write the needed code independently, and allows to easily implement this piece of code into the final structure. The code is written within the software development environment Eclipse, which offers various plug-ins. A plug-in of great importance to Gaia developers is Subversion, which is a software versioning and revision control system. With this powerful tool, simultaneous committing of data to the repositories by different users can be performed without any conflicts.

9.1 Main Dataflow

The main features of the LPV-code are illustrated in Fig. 9.1. After declaring the various variables, the properties are read out from the properties file, which is stored as a separate file in the Subversion repository of CU7.

Instead of showing the original code of the LPV work-package, which would be rather confusing for the reader, this section describes the main structure and data flow of the software. In general, the main routine of object oriented programs (purple box in Fig. 9.1) is always kept as simple as possible. All routines (green and yellow boxes in Fig. 9.1), which are called by the main program, are written as separate modules outside the main routine. Depending on the outcome of the individual modules, the other ones are either executed or not. Details for diverse conditions were described in section 8, and the programming structure of the most important ones is given below. In the final module (orange box in Fig. 9.1) all the output parameters determined by the different modules are stored in the so called object model of the CU7 variability data base. The object model can be seen as a piece of code that is used as an interface to exchange data from the disk storage to the scientific algorithms by passing instances of classes (Dubath et al., 2011a). After the validation of the data, all the information carried out and processed by the different work-packages is then passed to the main data base until the Gaia catalogue is published.

Fig. 9.2 shows how the different modules of this work-packages are interacting with each other. First, the code is populated with a source, which was classified as LPV by the Classi-

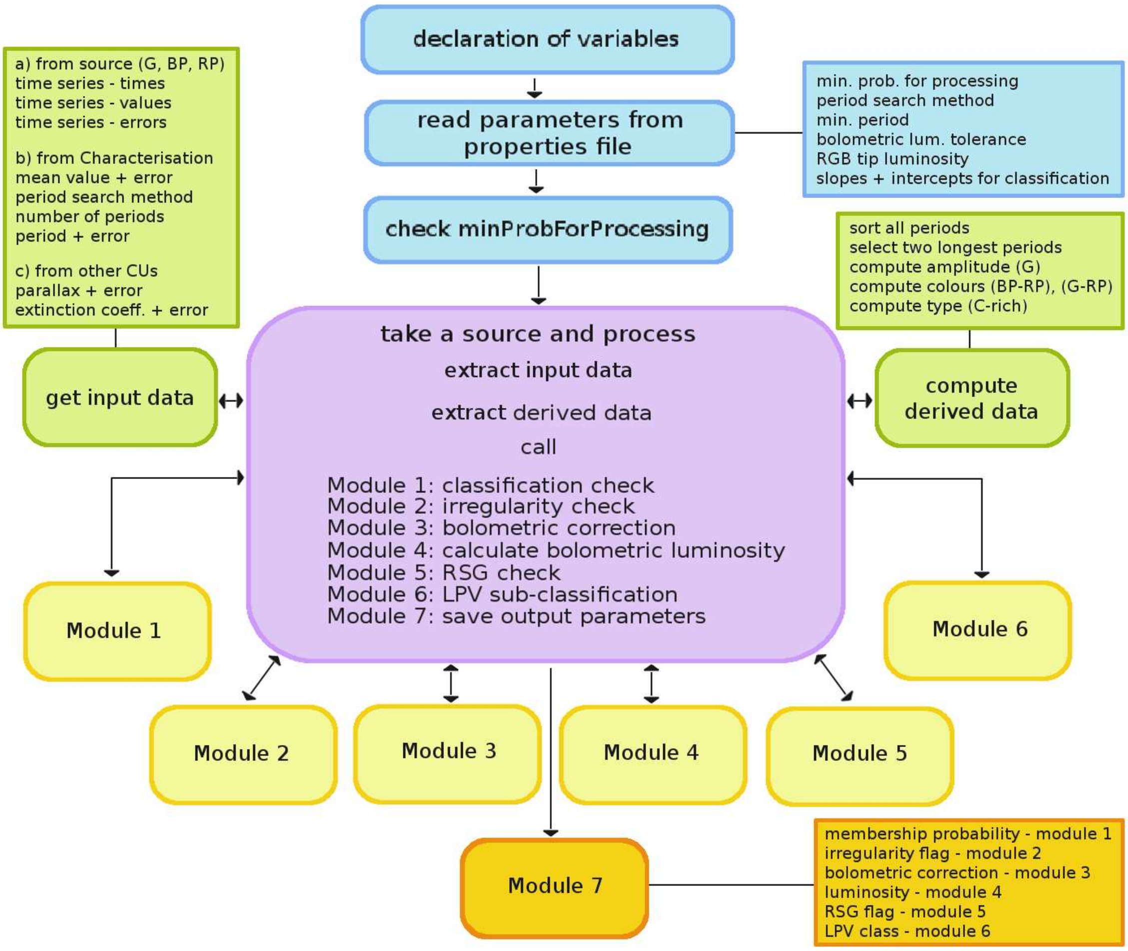

Figure 9.1: The main structure and data flow of the LPV work-package.

fication work-package of DU1. This source has a certain probability of being a LPV, which needs to be higher than the minimum classification probability defined in the LPV work-package in order to be further processed, otherwise the next LPV source is called. If the classification probability is high enough, the following module of the LPV-code tests whether the LPV source is an irregular LPV or not. LPVs that are flagged as irregular are processed until the module for luminosity determination. Their parameters are stored in the object model and the next source is called. The next module determines the BC, which is depending on the chemical type and the pulsation amplitude of the LPV (O-rich stars, C-rich stars and C-rich stars with a large amplitude, see 8.3). The next step is to check if the LPV has to be classified as a RSG. As mentioned in section 7.2, RSGs do not enter the module for LPV subclassification. After being processed through the module for luminosity determination their parameters (including the period derived from the Classification work-package) are saved to the object model. All other LPVs enter the subclassification module (once or twice depending on the number of significant periods) and obtain a LPV class as explained in 8.6.

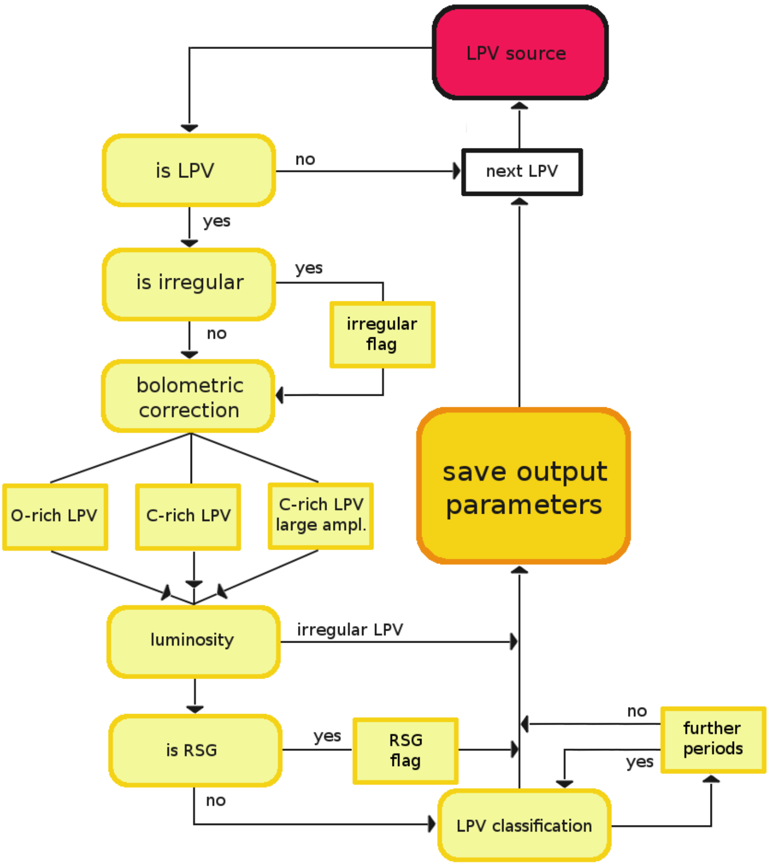

Figure 9.2: The data flow and interactions between the modules of the LPV work-package.

9.2 LPV Subclassification

The programming structure of the LPV sub-classification is the most complex part of the code. During the process of writing the code, acknowledging valuable support from the work-package leader of Specific Object Studies, N. Mowlavi, it was decided to divide this module into two functions (instead of one rather large and complex function). One function to determine the sequence membership of an input point (using ULP, LRP, $centreP$, $realP$ see 8.6) and one to derive the final classification area of the error box and its error class. This strategy keeps the code as simple as possible and makes it very efficient. The structure for the function of sequence membership determination is illustrated in Fig. 9.3. As can be seen in the right panel of Fig. 8.3, the number of classification areas is different for sources which are brighter or fainter than the RGB-tip luminosity. Accordingly, this piece of code starts with a statement to select the correct slopes and intercepts of the borders defined in the properties file. Each of the border receives a number, which is then used as iteration number to identify the location of the input point. The formula and the condition used in this loop, is given in the third row of Fig. 9.3.

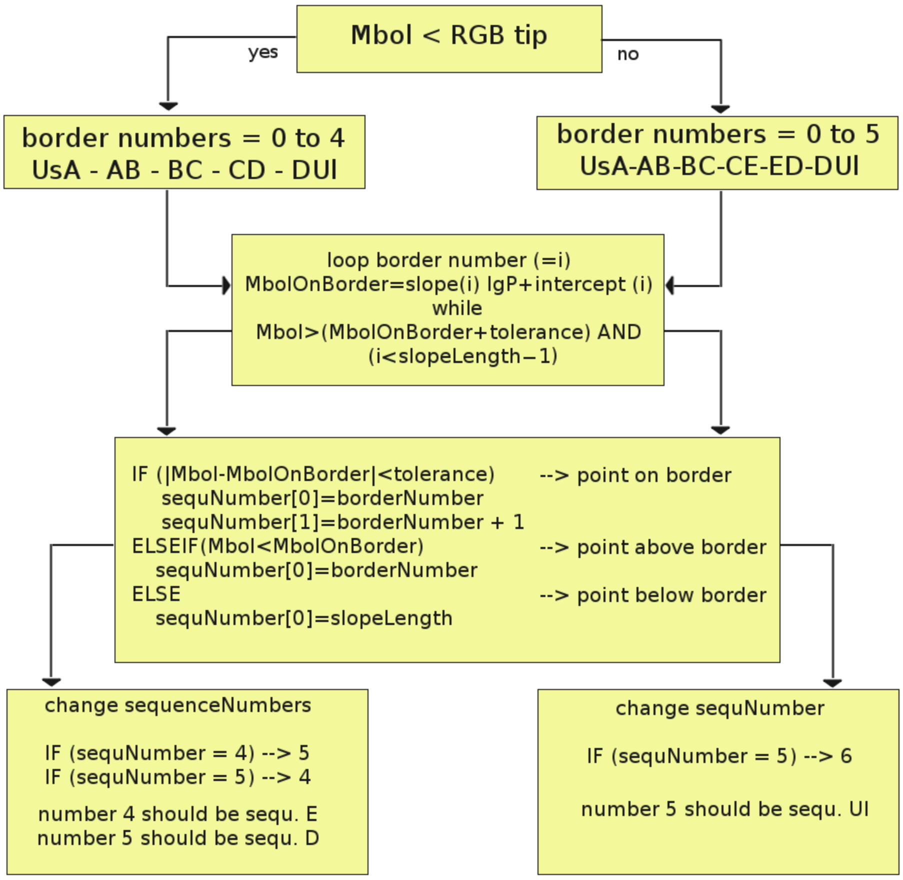

Figure 9.3: The code structure to determine the sequence membership of an input point.

The loop is executed until one of the two termination conditions is reached. As long as the input point ($centreP$ or $inputP$) lies in an area to the left of the long period border of sequence D, the first condition is always met unless the input point falls exactly onto the border (within the tolerance interval, see box in the third row of Fig. 9.3). If the input point is located at longer periods, the second termination condition in this box comes into play. All slopes and intercepts are declared as vectors within the LPV-code ($slope(i)$ and $intercept(i)$ in Fig. 9.3). Hence, the length of such a vector grows with each iteration of the loop until the last border is reached. The starting value for the boarder number in this loop is $i = -1$, the maximum length of the slope vector ($slopeLength$) is either '5' or '6', depending on M_{bol} of the input point. In the iteration after the last border, the first condition is still fulfilled, but the $slopeLength - 1$ now equals the iteration number and therefore terminates the loop. The next step is to check the reason for terminating the loop, or in other words where the input point is located with respect to the border (see forth row of Fig. 9.3). The sequences are assigned to numbers just like the borders. Depending on the M_{bol} of the input point, these numbers need to be changed, in order to attribute the correct sequence to the studied LPV in the following routine (see last row of Fig. 9.3).

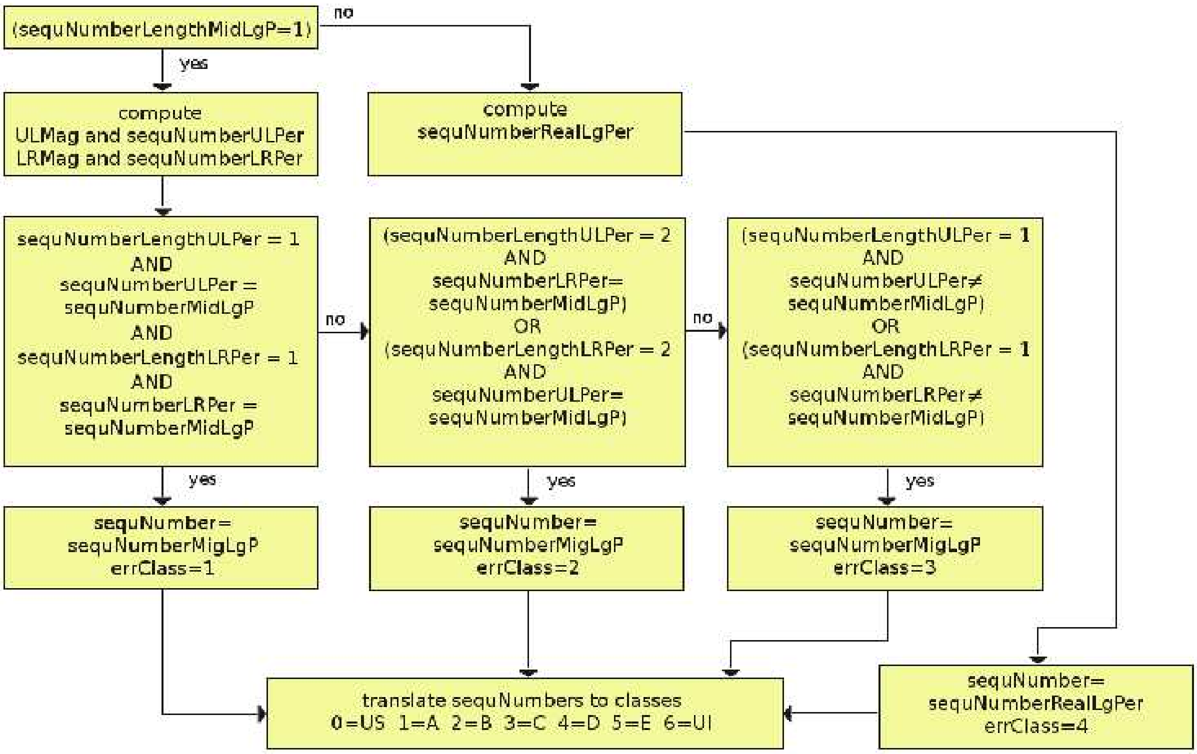

Figure 9.4: The programming structure to derive the LPV class and its associated error class.

The parameter *sequenceNumber* is defined as a vector in the LPV work-package. Consequently, the routine for sequence assignment and error class determination starts with a statement that checks the length of this vector for the centre point (see Fig. 9.4). As explained in 8.6, if the centre point falls onto a border ($sequNumberLengthMidLgP = 2$), the sequence membership of the real input point ($inputP$) has to be calculated and the error class is set to '4' (see right path in Fig. 9.4). For the other error cases, the sequence membership of the ULP and LRP has to be computed (see left box in second row and subsequent boxes in the third row in Fig. 9.4). The conditions to assign error classes '1', '2' or '3' are given in the boxes of the third row of Fig. 9.4. Finally, the corresponding sequence numbers are translated to the different LPV classes (see left box of the last row in Fig. 9.4). The LPV classes (including error classes) which are stored as output parameters in the object model.

10 Tests For The LPV work-package

In general, software tests can be seen as a process of validating and verifying, which ensures that a piece of code can be executed without any errors and meets the requirements of the quality assurance. All software tests are usually part of a software development process and are often grouped into different levels. The main levels are unit-, integration- and system testing. The set of tests that have to be performed within CU7 also include scientific and performance tests, respectively. The writing and execution of all these tests is distributed over different DUs of CU7. The developers of the work-package for Specific Object Studies are responsible for the unit- and scientific tests.

Unit tests are used to verify individual units of a source code. A unit is the smallest part of an application that can be tested. The purpose of unit tests is not to test if the results of a specific function or class are correct, but rather assure that the building blocks of the software are working independently of each other and that they behave as intended. These tests are executed through the unit testing framework JUnit for the Java programming language. The execution results are regularly checked through the distributed build management and the continuous integration system TeamCity. The tool Cobertura is used to provide metrics on the code coverage by Unit Tests for CU7. Since the developers are most familiar with their code, they have to ensure that a specific function is working as expected.

In addition, the developers of each sub-work-package have to perform scientific tests, which are needed to verify either if a specific method is applicable or if the general goals of the code are realisable. The scientific tests for the LPV work-package, which were obtained so far, are described in the following subsections.

All other test can be performed without having a precise knowledge of the content of each code. They are managed and performed by the different work-packages of DU0 and are therefore not further described in this chapter. However, there are several books (e.g., I. Sommerville, 2006) and tutorials about software engineering and software tests to which the reader is referred to obtain more information.

10.1 Scientific Test: Period Search Method

As already mentioned in 3.3, it is essential to test which of the period search methods offered by the Characterisation work-package is best suited to obtain periods of LPVs. For this purpose, a dataset of LPVs detected with the Hipparcos satellite (with a time sampling of data points similar to Gaia) was created and processed through the Gaia Characterisation pipeline (responsible for period determination, see Lebzelter & Lorenz 2010). From the offered period determination methods, those of Deeming (1975) and Lomb-Scargle (Lomb, 1976; Scargle, 1982) produced the best results. Using the Hipparcos sample, a comparison of those two methods (see Fig.10.1) revealed that the Lomb-Scargle method gives somewhat better results (Lebzelter & Lorenz 2010).

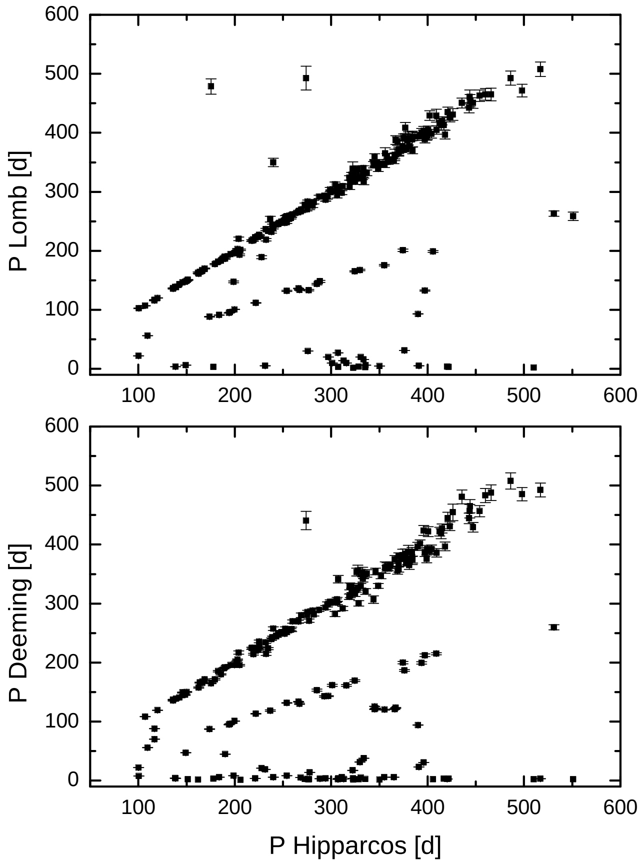

Figure 10.1: A comparison of the two period determination methods Deeming (1975) and Lomb-Scargle (Deeming, 1975; Scargle, 1982) using stars that were classified as Mira or semi-regular variables, respectively. This image was taken Lebzelter & Lorenz (2010).

However, for a significant number of sources both methods lead to deviating results, either resulting in a period of only a few days or producing periods that were approximately half of the true period. Further examinations of Lebzelter & Lorenz (2010) revealed that the solution to most of these deviations is found, when merging data points obtained within 24 hours (which is certainly valid for LPVs). These tests have demonstrated that Gaia will indeed be able to produce reliable periods for LPVs, yet unveiled the need for combining measurements taken within one day to avoid erroneous period search results. However, further tests using light curves with the simulated Gaia sampling need to be performed in the near future, to strengthen the assumptions made above.

10.2 Scientific Test: Identifying Carbon Stars

One way to distinguish between C-rich and O-rich LPVs using a subset of the eight-filter system of Wing (1971) was originally suggested by Wing & Stock (1973). The filters are labelled from '1' to '8' with increasing wavelength. A list of their central wavelengths and full widths at half of the maximum transmission (FWHM) is found in White & Wing (1978). This method was then applied by Palmer & Wing (1982) with slightly modified bandwidths of two filters, which were then renamed to filter A and B. Nowotny et al. (2001) also used narrowband filters (similar to filter A and B) to conduct a census of O-rich and C-rich AGB stars in Local Group galaxies. The properties of the Wing filters and their modifications are given in table 10.1[1]. All the above mentioned narrow-band filters are located at two specific

Table 10.1: A comparison of the central wavelength (λ_c) and the FWHM ($\Delta\lambda$) of two filters (Wing "3" and Wing "4") of the original eight-filter system of Wing (1971) and their modified versions by Palmer & Wing (1982, in the table A-PW82 and B-PW82) and by Nowotny et al. (2001, in the table A-Now01, B-Now01). The last column gives the spectral resolution of the RP of Gaia as published by Hudec et al. (2010).

	λ_c [$\AA$]	$\Delta\lambda$ [$\AA$]	Gaia RP resolution [$\AA$/pixel]
Wing "3"	7810	40	
Wing "4"	8120	50	
A-PW82	7780	100	
B-PW82	8120	100	
A-Now01	7780	110	70 - 150
B-Now01	8113	85	

regions of molecular absorption features, namely the band head of titanium oxide (TiO), prominent in O-rich stars, and a feature of carbon nitrate (CN), which is prominent in C-rich stars. The central wavelengths and FWHM of filter A and B (given on top of the transmission curves in the right panel of Fig. 10.2) were chosen such that filter A measures the continuum flux of C-rich stars and the strength of the TiO feature in O-rich stars, while filter B measures the continuum in O-rich stars and CN in C-rich stars. This strong contrast of the measured fluxes in both filters, and hence the colour index (TiO-CN), efficiently separates the two types of stars.

Both Wing-filters are within the wavelength coverage of the RP spectra of Gaia (see left panel of Fig. 10.2). Note that the figures are using different units for the wavelength. The wavelength coverage of the different Gaia bands has been described in chapter 3.2 and is illustrated here for comparison reasons only. According to Hudec et al. (2010), the resolution of the RP spectra varies from 7 to 15 nm per pixel (see last column in table 10.1). These spectra shall be folded with the transmission curves of the Wing-filters A and B (as defined

[1]For the LPV work-package we used the filters of Nowotny et al. (2001).

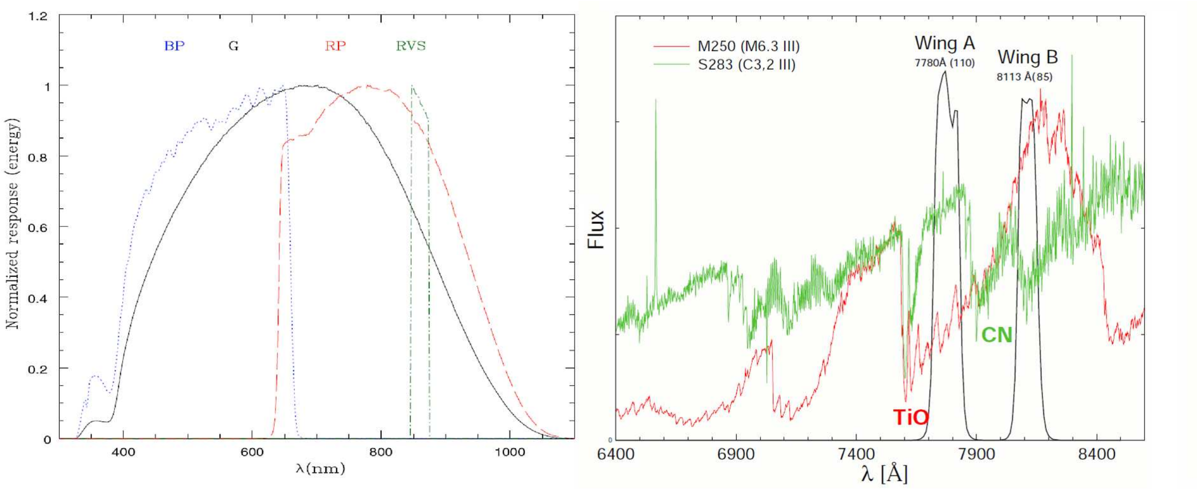

Figure 10.2: Left panel: normalised Gaia passbands (solid line: G-band, dotted line: BP, dashed line: RP, dot-dashed line: RVS). The figure was taken from Jordi et al. (2010). Right panel: a spectrum of a typical C-rich (green line) and an O-rich (red line) AGB star. Superimposed are the transmission curves of the filters A and B from the Wing photometry. The figure was kindly provided by W. Nowotny based on the publication of Nowotny et al. (2001). The spectra shown in this plot were taken from Schultheis (1998).

in Nowotny et al., 2001) which is quite challenging since the passbands spread only over one ore two pixels. Mainly owing to the low resolution of the RP spectra, it has to be clarified if the expected difference in flux of the Wing-filters A and B will still be high enough to distinguish between C-rich and O-rich sources.

The necessary tests for this approach were carried out in close collaboration with CU5. A set of synthetic spectra (spectral range = 300 to 1100 nm; resolution $R = 2500$) of C-rich (C/O=1.4) and O-rich (C/O=0.48) LPVs, covering a temperature range of 2400 to 4000 K, a metallicity ($Z/Z_{\odot}$) range of 0.01 to 2.5, and a range of surface gravities ($\log g$) of +1 to −1, was provided to CU5. These spectra were fed into a program that simulates the expected RP spectra (spectral range = 640-1000 nm; resolution $R = 50$ to 115). Noise was added to the spectra, which were computed for stars assuming a G-band brightness of 18 mag. To obtain Wing-colours (TiO – CN) these simulated RP spectra were then folded with the passbands of the Wing filters A and B. The test results are shown in a plot of temperature versus Wing colour in Fig. 10.3. The spread in colour of one temperature bin is caused by the different field of views of the single CCDs in the focal plane (see Fig. 3.5 in Sect. 3.2). Despite of the spread in colour, a clear bifurcation of O-rich and C-rich stars can be seen. These test results are very encouraging with respect to the feasibility to separate C-rich and O-rich LPVs using the RP spectra. As demonstrated in Sect. 8.3, this information is crucial to obtain reliable BCs for the LPVs that will be observed with Gaia. However, note that the RP spectra are certainly not suited to obtain good estimates of (TiO – CN), the only important information here is to identify C-rich sources.

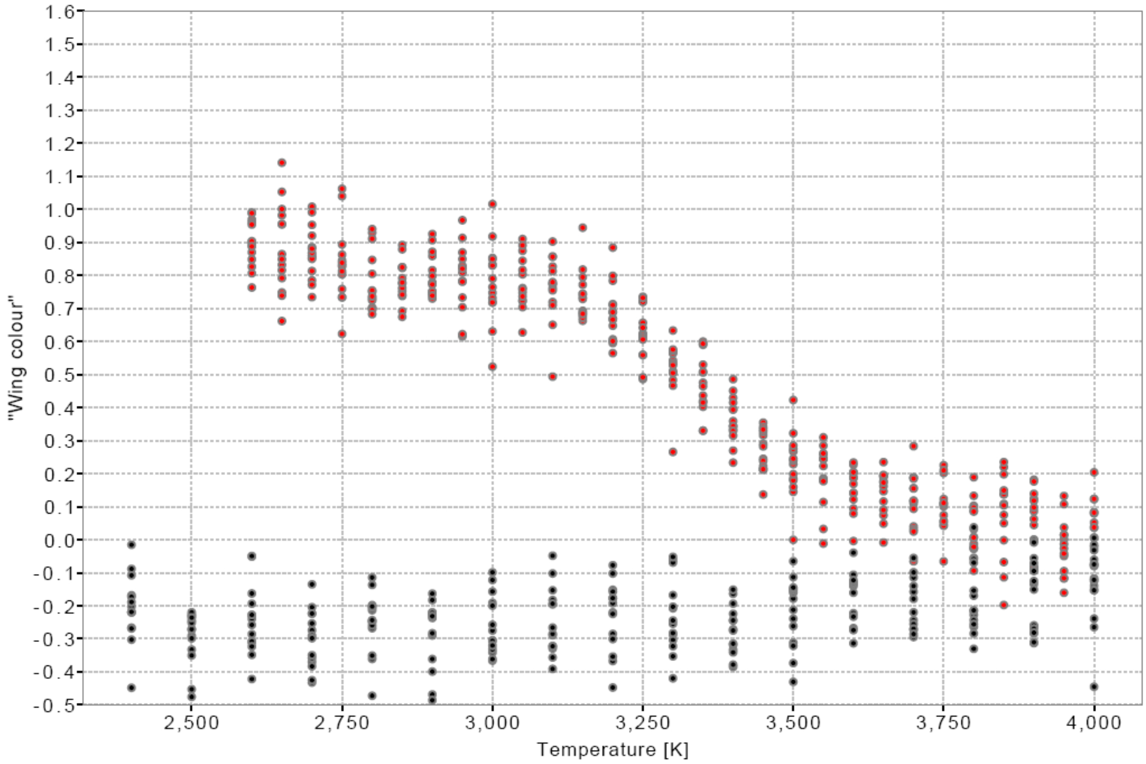

Figure 10.3: Test results of CU5 using simulated *RP* spectra. O-rich stars are plotted as red dots and C-rich stars as black dots. The figure was taken from Evans & Angeli (2011).

10.3 Scientific Test: LPV Classification

As a first test of the LPV-code (described in chapter 9), a small sample of LMC stars from the OGLE catalogue, which are known to be LPVs, was chosen and processed through the subclassification module. The light curves of these stars are shown in Fig. 10.4.

In order to run such a test, a separate piece of code needs to be written, where all the input parameters, that are needed in the LPV-code but which are not yet obtainable, are predefined (e.g., classification probability, Gaia photometry, C-rich or O-rich LPV). The main focus was to test the module for LPV sub-classification. Accordingly, all other modules, except the module for luminosity determination and the RSG module, were replaced with the predefined parameters. The periods for this test were obtained in the same way as in the original code by calling the period search method of Deeming from the Characterisation work-package. After setting up the test program, the expected results (using the predefined parameters) need to be calculated manually. In this way, it is possible to compare the expected results with the results of the testing software. In the test code a plotting program is called to create a PLD, where the sequence borders and all the test objects are drawn (see Fig. 10.5). For

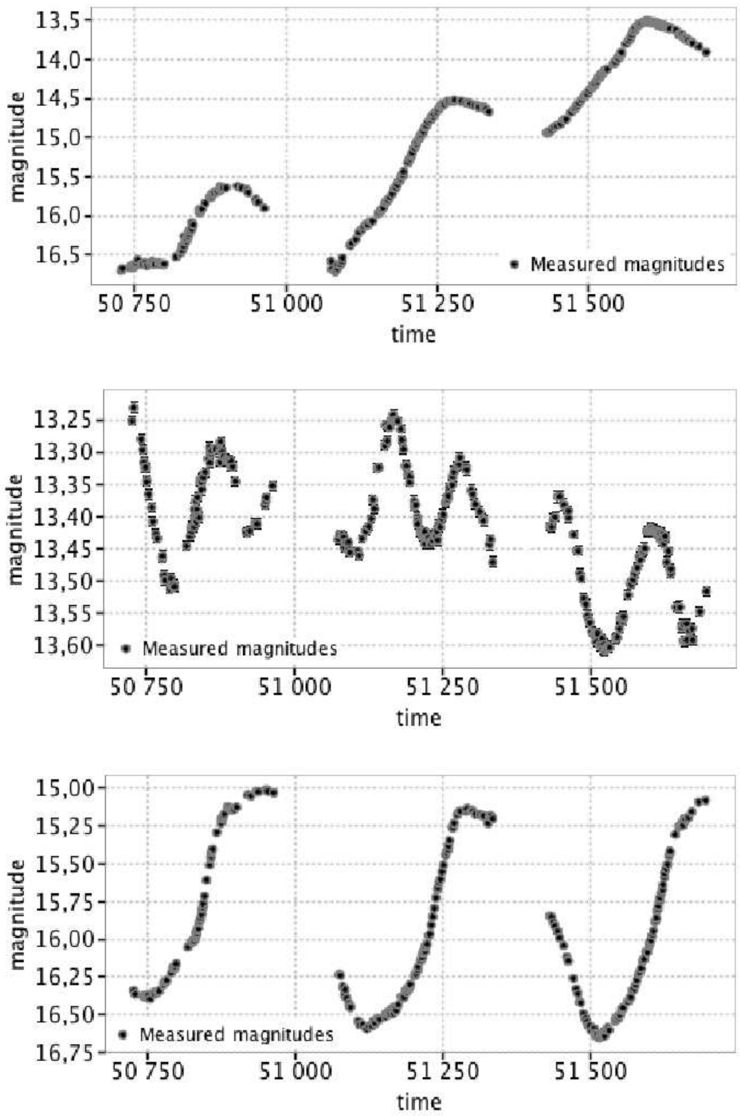

Figure 10.4: The light curves of the three randomly chosen LPVs from the OGLE catalogue.

comparison reasons, also the luminosity range of the RSGs has been included in this plot.

It should be noted that these tests were done at the time where, the Characterisation work-package did not yet offer a possibility to obtain a significance or an error of the period. Hence, only the longest period of the three OGLE stars was chosen to be shown in the resulting PLD. The values of the other periods of the Characterisation work-package were either very c lose to the first period or clearly aliases, which are false periods that are obtained when analysing a light curve with rather regular gaps of individual measurements. The period of the expected and the test results are listed in table 10.2, and the PLD produced by the testing software (see Fig. 10.5) demonstrates the correct assignment of the individual LPV classes.

Table 10.2: A comparison of the periods of the three example stars from the OGLE-II catalogue (Field LMC-SC20) carried out by the LPV work-package (LPV-WP), by the SIGSPEC software (Reegen 2007) and by the Period04 software (Lenz & Breger, 2005).

OGLE-II ID	SigSpec period [d]	Period04 period [d]	LPV-WP period [d]
107126	359.6	346.8	357.1
66596	389.8	385.7	384.6
195468	145.1	146.1	144.9

Furthermore, the RSG flag for one of the OGLE sources was also set correctly. Just by looking at Fig. 10.5 and equation 8.8, it is clear that the brightest star in this figure must be a RSG.

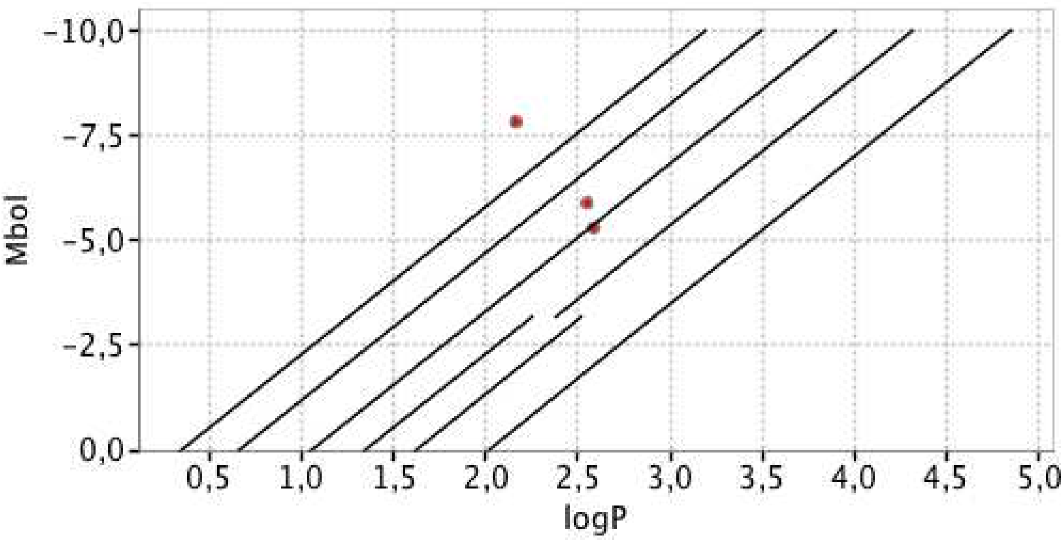

Figure 10.5: PLD obtained from the LPV work-package containing three randomly chosen LPVs from the OGLE-II catalogue (red dots). The continuous lines show the borders of the different classification areas.

As a next step, this test will be repeated using a large sample of LPVs from the OGLE catalogue followed by a test where the input light curves are modified according to the Gaia time sampling (see Sect. 3.2). These tests are currently under development and shall be completed by the end of 2011.

Part III

PLR of NGC 147 and NGC 185

11 The Galaxies

The two target galaxies, NGC 147 and NGC 185, which are known to be members of the M 31 subgroup, were discovered by J. Herschel in September 1829 and by W. Herschel in November 1787, respectively. Together with NGC 205, they are the most luminous dwarf galaxies in the Local Group and are located at an angular distance of approximately 12 degrees from the Andromeda nebula (van den Bergh 1998; Corradi 2005). According to van den Bergh (1998), they are separated by only 58 arcmin on the sky without any indication of interaction (Battinelli & Demers 2004a; Geha et al. 2010). Although these galaxies appear fairly similar concerning their CMDs, some differences are found with respect to their SFHs, most notably for recent epochs (<1 Gyr see Mateo 1998). Owing to the lack of main-sequence turn-off stars with $M_V < -1$, the most recent large-scale star-forming activity in NGC 147 must have occurred at least 1 Gyr in the past (Han et al. 1997). Based on broad-band near-infrared CMDs, Riebel (2010) stated that this event happened ≈3 Gyr ago, whereas Dolphin (2006)

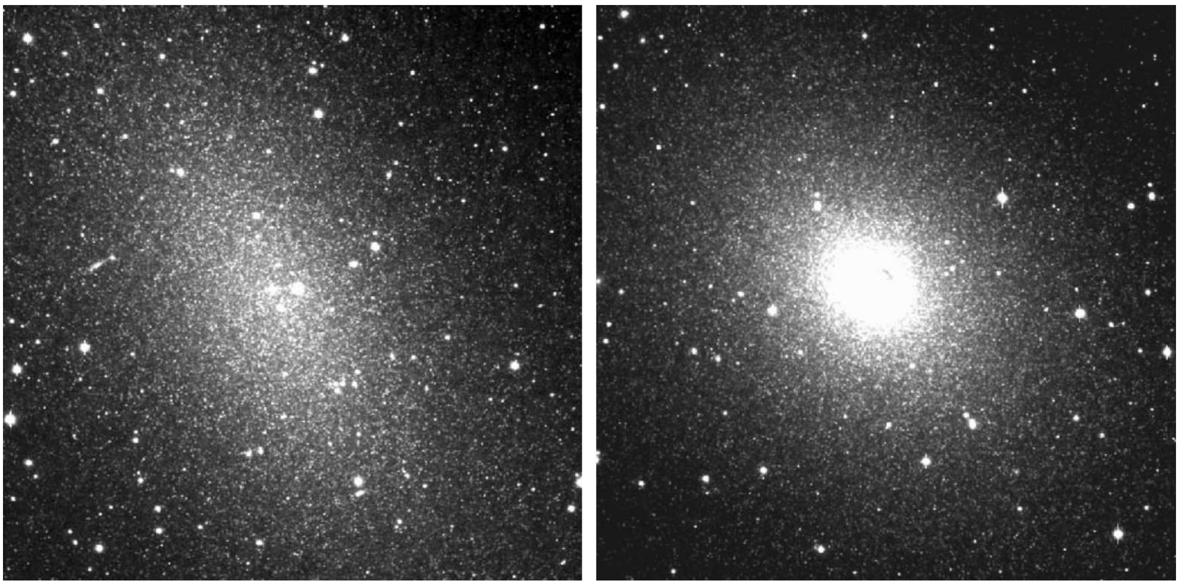

Figure 11.1: Left panel: NGC 147; right panel: NGC 185. Both CCD image were obtained at the Nordic Optical Telescope in Spain. The dark spot near the dense center of NGC 185 is a real dust feature.

derived a value of 4 Gyr using images of the Hubble Space Telescope. The idea that star formation ceased long ago is further supported by the fact that no signs of dust and gas were detected in this galaxy, which could serve as building material for new stars (Young and Lo 1997, Sage 1994). Using the relation between the AGB-tip (in the K-band) and age (as predicted from isochrones of Girardi et al. 2000), Sohn et al. (2006) assumed that most of the M-giants in NGC 147 formed between $log(t_{yr}) \approx 8.2$ and 8.6. However, in the centre of NGC 185, various authors found a significant amount of gas and dust (Young & Lo 1997; Lee et al. 1999; Martinez-Delgado & Aparicio 1999; Martinez-Delgado et al. 1998). Butler & Martinez-Delgado (2005) obtained an age of about 400 Myr for the youngest, centrally concentrated stars. Kang et al. (2005) speculate that the M-giant population in NGC 185 contains stars with a wide range of ages, possibly representing two different epochs of star formation, one at $log(t_{yr}) \approx 9.0$ to 9.4 and another at $log(t_{yr}) \approx 7.8$ to 8.5. In the outer parts of NGC 185, stars with ages of at least 1 Gyr are found.

The content of red giants in these galaxies was analysed by Nowotny et al. (2003, hereafter Paper I). AGB stars therein were characterised according to the chemical properties of their atmospheres by applying an efficient photometric method to single out C-rich stars. For this purpose they made use of narrow-band wing-type filters centred around spectral molecular features of TiO and CN (at $\lambda \approx 0.8\,\mu$m). Within a field of view (FOV) of 6.5×6.5 arcmin, the authors identified 154 C-rich stars in NGC 185, 146 C-rich stars in NGC 147, and several hundred M-Type stars of the upper giant branch in both galaxies. The enormous number of identified AGB stars motivated a search for LPVs in these systems. One of the most interesting aspects to investigate was if the different mean metallicities and SFHs of both galaxies would be reflected in the PLRs of their LPVs.

Hence, the major aim of this work was to identify LPVs in NGC 147 and NGC 185 (see Fig. 11.1) and compare their distribution within a PLD. Chapter 12 describes the observations and the data reduction is given in chapter 13. The outcome of the photometric monitoring in the i-band is presented in Sect. 13.2 and summarised in a catalogue of red giant variables. In chapter 14 we discuss the results of this study.

12 Observations

12.1 Photometric monitoring

We obtained multi-epoch observations in the *Gunn-i*-band with the 2.56 m Nordic Optical Telescope (NOT). The target galaxies were observed on 38 nights in service mode between October 2003 and February 2006 with the Andalucia Faint Object Spectrograph Camera (ALFOSC). It has a pixel scale of 0.19 arcsec/pixel resulting in a FOV of approximately 6.4×6.4 arcmin. At every epoch we obtained a single image pointing towards the centre of each galaxy. Our field covered a region corresponding to approximately one scale length derived from the stellar density distribution of NGC 147 (Battinelli & Demers 2004b) and NGC 185 (Battinelli & Demers 2004a), respectively. We obtained 35 images of NGC 147 and 34 frames of NGC 185 with a sampling period of ≈14 days. One example image of the time series for each of our science targets is shown in Fig. 13.1. The time series exhibits two larger gaps of approximately six months during which the targets were not observable. Calibration frames to correct for sky and bias were recorded for each night of observation. In the rare cases of missing sky flats, these were replaced by average flats from the previous and the following observation.

12.2 K_s-band photometry

As can be seen from spectral energy distributions of cool AGB stars (Nowotny et al. 2010), they emit most of their flux in near-infrared wavelengths. Hence, the K_s-band is a good measure of the bolometric flux. The most evolved, dust-enshrouded AGB stars can be detected only at infrared wavelengths. Therefore, the K_s-band has been widely used (e.g., Wood 2000) to construct PLRs of LPVs. To allow a comparison of our results with previous studies, we carried out single-epoch K_s-band photometry for our target systems using NOTCam during two consecutive nights in September 2004. This camera is equipped with a 1024×1024 HgCdTe Rockwell Hawaii array with a plate scale of 0.234 arcsec/pixel resulting in a FOV of 4×4 arcmin using the wide-field imaging mode of NOTCam. To resemble the FOV of ALFOSC, we obtained a mosaic of four partly overlapping dithered images per galaxy. Accordingly, the combined FOV of the four quadrants is ≈ 6×6 arcmin.

13

Data reduction

13.1 Monitoring data

All frames obtained for this study were bias-, sky- and flatfield-corrected using standard data reduction routines. As in Paper I, the whole sample of stars was corrected for interstellar reddening adopting the values from the NASA Extragalactic Database (see Tab. 13.1) following the calculations of Schlegel et al. (1998).

Table 13.1: Reddening values from NASA Extragalactic Database.

galaxy	A_V [mag]	A_i [mag]	A_{K_s} [mag]
NGC 147	0.574	0.336	0.064
NGC 185	0.604	0.354	0.067

Images taken in the i-band with ALFOSC also suffer from fringing. To compensate for this effect, it would have been necessary to obtain flatfield images before and after each integration of the science target to create a fringe map. Without these additional calibration images, a correction for this effect was not possible. The maximum amplitude of variations caused by fringing is about 0.07 mag, which is well below the minimum amplitude expected for LPVs (paek-to-peak amplitude A_i=0.3 mag). The detection of variable stars was carried out using the image subtraction tool ISIS 2.1[1] of Ch. Alard (2000). One carefully chosen i-band image was taken as reference frame to obtain differences in flux relative to each image of the time series. To produce light curves from these differences, we measured fluxes for each star on the reference frame by using a point spread function (PSF) fitting software written by Ch. Alard. Short descriptions of the code, which was originally developed for the DENIS project[2], can be found in Schuller et al. (2003) or Beaulieu et al. (2008).

As can be seen in Fig. 13.1, the central region of NGC 185 is more compact towards the centre. Hence, the identification of variable stars towards central regions is incomplete because of crowding. The photometric zero-point correction was determined using a sample of constant stars on the reference frame that were cross-correlated with their counterparts in Paper I. To estimate a photometric error, two samples of randomly chosen constant stars

[1] http://www2.iap.fr/users/alard/package.html

[2] Deep Near Infrared Survey of the Southern Sky, see http://cdsweb.u-strasbg.fr/denis.html

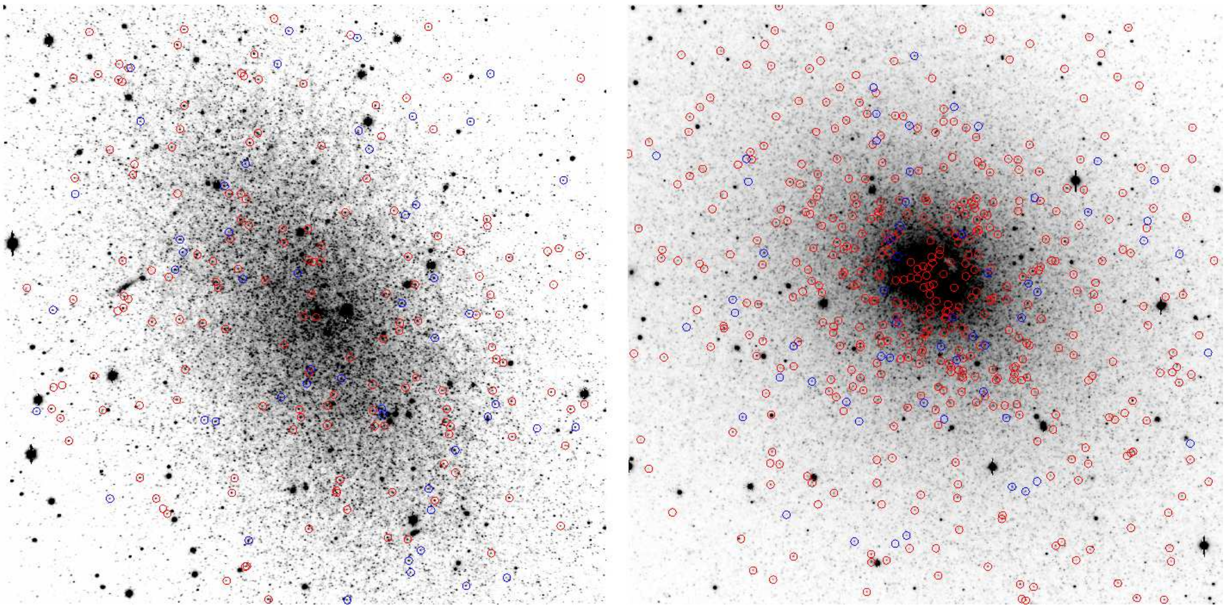

Figure 13.1: Inverted CCD images of NGC147 (left panel) and NGC185 (right panel) obtained with NOT in the i-band. North is up and east is to the left. Designated with blue circles are objects which were identified as LPVs in this work and for which the narrow-band photometry in Paper I indicates C-rich atmospheric chemistry. The red circles mark all other stars (presumably O-rich) found to show long-period variability.

common to all images of the time series were selected. Following the same approach as for the reference frame, mean zero-points were calculated from one sample of constant stars for each frame and subsequently used to remove zero-point variations between the various frames. Then, the differences between the corrected magnitudes of all stars of the second sample and the corresponding values from Paper I were determined. Their standard deviations served as an estimate for the photometric errors. The resulting errors in the i-band at a mean luminosity of 19.5 mag for the various epochs range between 0.085 mag for NGC 147 and 0.094 mag for NGC 185, respectively.

13.2 Catalogue of variables

The i-band light curves were searched for periodicities using SIGSPEC[3] (Reegen 2007). The periods obtained from the light curves of LPVs in both galaxies range from about 90 to 800 days. These limits are caused by time sampling of the monitoring data (one observation approximately every two weeks distributed over 2.5 years). A maximum of two periods was derived from the Fourier analysis if the criterion for significance was fulfilled. The significance (sig) of a period is defined in SIGSPEC as the inverse of the logarithmic scaled false-alarm-probability (FAP) that a discrete Fourier transform amplitude is caused by noise (see Reegen

[3]http://www.sigspec.org/

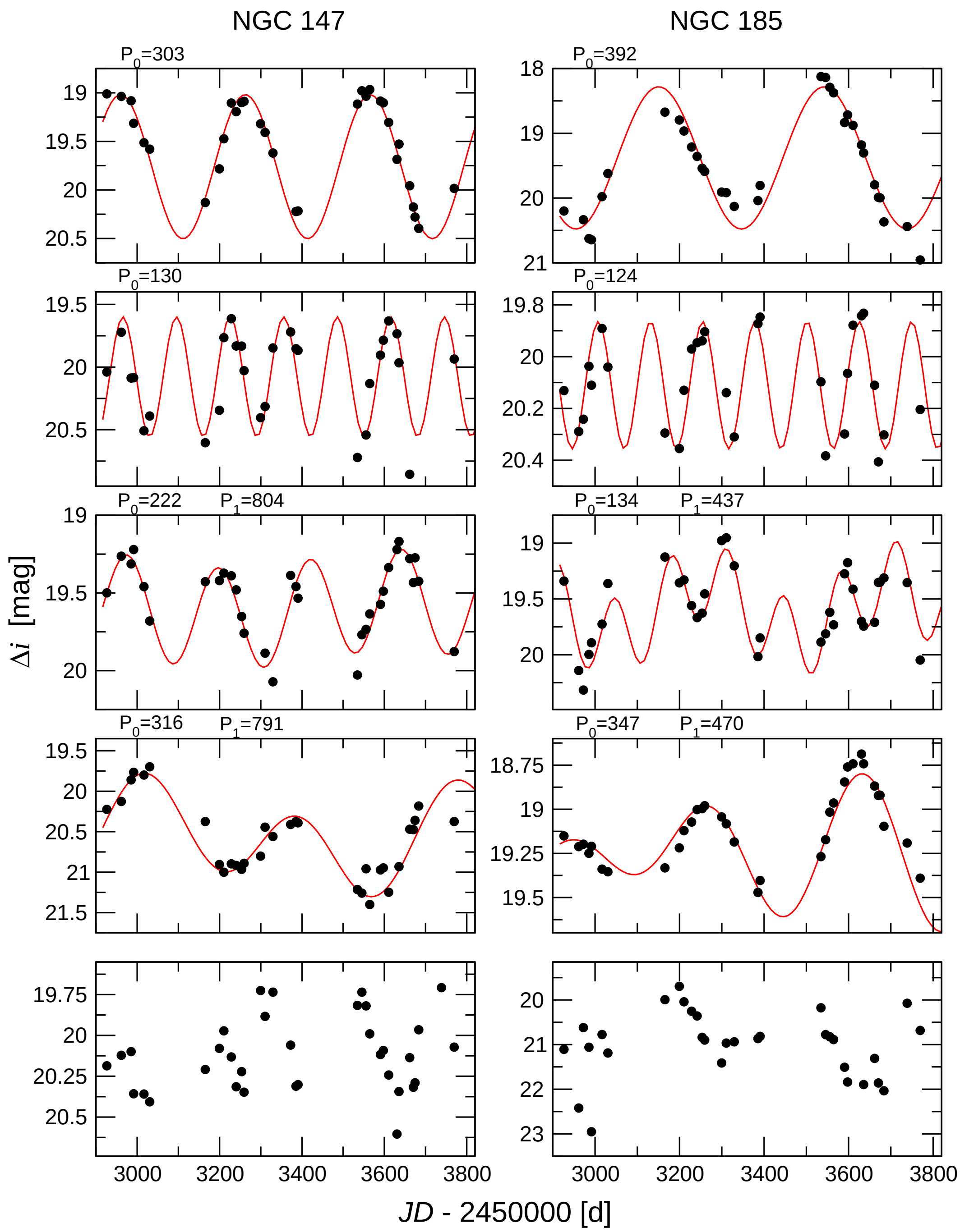

Figure 13.2: Example light curves of detected LPVs in each of the target galaxies (NGC 147 on the left and NGC 185 on the right side). The black dots illustrate the observational data, while the red lines display the fitted light curve derived with SIGSPEC (Reegen 2007). Shown are different types of LPVs (mono-periodic variations, two periods and LPVs with no significant period).

2007 for details). A spectral significance of 5 therefore corresponds to an inverse FAP of 10^5 or, in other words, the risk of the amplitude being just caused by noise is $1{:}10^5$. Example light curves showing different types of LPVs from both galaxies together with our best model fit are shown in Fig. 13.2. The results of the period search are summarised in Table 13.3 and 13.4, which are available online only. Besides the periods and corresponding significance of the detected LPVs, the table also lists the mean i-magnitudes that were obtained from the light curve. The corresponding photometric errors of the mean brightness in the i-band after the calibration are listed in Table 13.2 for different ranges of magnitude.

Table 13.2: Photometric uncertainties for both galaxies obtained in the i and K_s filters.

i	e_{phot}	K_s	e_{phot}
>19	0.03	>16	0.09
19-20	0.04	16-17	0.11
20-21	0.06	17-18	0.13
21-22	0.09	18-19	0.18
<22	0.16	<19	0.26

We only used Fourier-amplitudes from the SIGSPEC-output to fit the light curves (see red line in Fig. 13.2). Additionally, we defined a σ-amplitude that is twice the statistical standard deviation from the mean brightness of the variable. A purely sinusoidal light curve, for example, with a peak-to-peak-amplitude $A = 1.0$ mag would result in a corresponding σ-amplitude of $A_\sigma = 0.701$ mag (hereafter Δi). This allows us to have a better understanding of the overall variability of the detected LPVs in both galaxies even for LPVs for which no significant period could be asserted. In addition, this parameter is not sensitive to outliers of the observed light curve mainly caused by dead pixels on the frame or cosmic rays during the integration. Depending on the results of the period search, we were able to assign one, two, or no period to each LPV. For some stars (starting from ID 147V000169 in Table 13.3 and ID 185V000420 in 13.4) it was not possible to detect a significant period, although they clearly are variable. Therefore, we listed their σ-amplitudes Δi to obtain a better impression of their variability.

Table 13.3: Period search results of NGC 147. This table lists in the first five columns the internal IDs, the coordinates (J2000), mean i magnitudes (obtained from the time series) as well as K_s magnitudes. Periods, σ-amplitudes and the SIGSPEC-significance are found in the next three columns. LPVs exhibiting two significant periods have entries in the ninth and tenth columns listing the second period and its SIGSPEC-significance. The last two columns give the types of different chemistry and the IDs carried out by the authors of Paper I.

ID	RAJ2000 h:m:s	DEJ2000 d:m:s	i [mag]	K_s [mag]	P_0 [d]	Δi [mag]	sig_0	P_1 [d]	sig_1	type	ID_{PaperI}
147V000001	00 33 30.99	48 32 18.07	20.06	—	241	1.01	2.1	—	—	S	00971672
147V000002	00 33 28.57	48 29 33.85	20.20	—	258	0.85	4.6	—	—	C	02190795
147V000003	00 33 27.59	48 29 48.00	20.47	—	206	0.74	5.3	—	—	u	—
147V000004	00 33 27.66	48 30 33.00	19.70	16.66	300	0.57	5.7	—	—	C	02691110
147V000005	00 33 27.19	48 29 29.93	19.91	—	196	0.71	5.6	—	—	u	02920773
147V000006	00 33 26.68	48 29 16.68	19.88	17.30	211	0.54	4.6	—	—	M	03180702
147V000007	00 33 26.43	48 30 38.81	20.60	16.55	314	0.87	4.3	—	—	S	03351141
147V000008	00 33 25.15	48 32 50.78	20.12	17.24	231	0.55	4.5	—	—	M	04081845
147V000009	00 33 24.73	48 29 34.89	20.36	—	158	0.86	5.3	—	—	S	04220799
147V000010	00 33 24.32	48 27 28.13	20.04	—	168	0.74	3.6	—	—	M	04390122
147V000011	00 33 23.95	48 32 47.62	19.70	17.39	206	0.79	5.8	—	—	M	04711828
147V000012	00 33 23.63	48 31 01.95	20.16	17.31	234	1.43	5.5	—	—	M	04841264
147V000013	00 33 23.26	48 32 54.61	20.34	16.65	299	0.76	5.2	—	—	C	05081865
147V000014	00 33 21.58	48 28 43.51	19.92	17.42	203	0.47	5.8	—	—	M	05870523
147V000015	00 33 20.96	48 30 52.56	19.89	16.77	245	1.61	5.4	—	—	M	06251212
147V000016	00 33 20.82	48 32 08.39	20.11	17.30	178	0.56	4.3	—	—	M	06351618
147V000017	00 33 20.57	48 30 56.92	19.84	16.15	167	0.40	4.6	—	—	C	06461236
147V000018	00 33 20.53	48 33 08.16	19.71	17.51	150	0.61	4.5	—	—	M	06531937
147V000019	00 33 20.30	48 30 28.00	19.87	16.98	233	0.68	6.1	—	—	S	06591081
147V000020	00 33 20.30	48 31 14.54	19.79	16.27	329	0.61	6.6	—	—	C	06601330
147V000021	00 33 20.13	48 31 07.14	20.12	16.69	280	0.91	5.6	—	—	C	06691290
147V000022	00 33 20.13	48 32 32.56	19.68	16.25	313	0.77	6.2	—	—	M	06731747
147V000023	00 33 19.30	48 31 05.73	19.77	17.26	166	0.87	5.5	—	—	S	07131282
147V000024	00 33 18.81	48 29 29.38	19.89	17.10	218	0.69	6.4	—	—	C	07350767

Table 13.3: continued.

ID	RAJ2000 h:m:s	DEJ2000 d:m:s	i [mag]	K_s [mag]	P_0 [d]	Δi [mag]	sig_0	P_1 [d]	sig_1	type	ID_{PaperI}
147V000025	00 33 18.15	48 29 28.57	19.86	16.30	343	0.37	4.7	—	—	C	07700763
147V000026	00 33 18.08	48 30 46.26	19.58	—	183	0.47	4.8	—	—	S	07771178
147V000027	00 33 17.74	48 31 45.94	20.17	15.74	293	1.15	6.0	—	—	C	07971497
147V000028	00 33 17.65	48 30 22.56	19.85	16.64	276	0.36	5.7	—	—	M	07991051
147V000029	00 33 17.46	48 31 18.94	21.18	17.05	306	1.65	5.3	—	—	C	08111352
147V000030	00 33 17.03	48 28 55.63	20.13	16.59	285	0.71	6.1	—	—	S	08280586
147V000031	00 33 16.75	48 31 26.32	21.23	16.52	337	1.41	3.7	—	—	u	08491392
147V000032	00 33 16.53	48 31 58.91	20.38	16.42	302	0.81	5.2	—	—	C	08621566
147V000033	00 33 16.28	48 32 11.16	19.83	16.09	427	0.46	4.6	—	—	S	08761631
147V000034	00 33 16.08	48 33 03.13	19.98	17.08	212	0.35	3.7	—	—	u	08891909
147V000035	00 33 15.83	48 32 16.86	20.13	16.96	217	0.79	5.2	—	—	M	09001662
147V000036	00 33 15.82	48 32 48.11	19.85	16.90	280	0.49	4.9	—	—	S	09021829
147V000037	00 33 15.43	48 29 37.70	20.09	17.22	218	0.98	5.3	—	—	M	09140810
147V000038	00 33 15.01	48 27 45.25	19.93	17.34	114	0.43	5.2	—	—	M	09320209
147V000039	00 33 14.71	48 32 57.13	20.44	16.54	297	0.87	5.7	—	—	C	09611877
147V000040	00 33 14.37	48 29 42.97	20.18	16.50	411	0.50	5.1	—	—	C	09710838
147V000041	00 33 14.18	48 30 13.77	19.96	—	152	0.65	5.2	—	—	M	09821003
147V000042	00 33 13.31	48 29 36.14	19.57	17.26	151	0.36	5.5	—	—	M	10270801
147V000043	00 33 13.20	48 29 31.41	18.96	16.45	265	0.28	5.4	—	—	M	10320776
147V000044	00 33 13.21	48 32 45.73	19.82	17.08	201	0.39	4.1	—	—	S	10401815
147V000045	00 33 13.09	48 30 30.14	19.60	16.90	206	0.44	5.3	—	—	M	10401090
147V000046	00 33 12.83	48 31 21.27	19.66	16.59	245	0.68	5.8	—	—	u	10561364
147V000047	00 33 12.69	48 28 26.45	20.45	17.60	200	1.02	5.7	—	—	M	10560428
147V000048	00 33 12.72	48 29 57.35	19.11	16.05	161	0.38	6.4	—	—	M	10580915
147V000049	00 33 12.14	48 31 02.73	20.10	17.61	183	1.09	5.7	—	—	M	10921264
147V000050	00 33 12.14	48 32 09.62	21.03	18.16	129	1.49	4.9	—	—	M	10951622
147V000051	00 33 11.67	48 29 38.35	20.20	17.14	229	0.82	4.7	—	—	M	11130813

Table 13.3: continued.

ID	RAJ2000 h:m:s	DEJ2000 d:m:s	i [mag]	K_s [mag]	P_0 [d]	Δi [mag]	sig_0	P_1 [d]	sig_1	type	ID_{PaperI}
147V000052	00 33 11.30	48 29 44.64	20.09	17.77	171	0.48	5.8	—	—	S	11330846
147V000053	00 33 11.07	48 28 47.60	20.10	17.68	194	0.65	5.1	—	—	M	11430541
147V000054	00 33 10.89	48 28 54.96	19.56	17.01	203	0.27	4.5	—	—	S	11530580
147V000055	00 33 10.47	48 28 37.76	20.07	17.82	130	0.68	3.8	—	—	S	11750488
147V000056	00 33 10.42	48 27 45.13	19.91	16.06	370	0.70	5.5	—	—	C	11750206
147V000057	00 33 10.49	48 33 14.27	20.10	17.18	216	0.78	5.8	—	—	M	11851968
147V000058	00 33 10.09	48 33 12.70	19.70	16.55	264	0.50	5.6	—	—	C	12061959
147V000059	00 33 09.02	48 29 35.53	20.22	17.90	161	0.76	5.0	—	—	S	12540797
147V000060	00 33 08.99	48 32 33.29	19.93	17.38	149	0.61	5.4	—	—	S	12631748
147V000061	00 33 08.50	48 29 36.66	19.65	16.44	316	0.31	4.2	—	—	C	12810802
147V000062	00 33 08.43	48 29 33.56	20.65	16.99	198	1.54	4.9	—	—	C	12850786
147V000063	00 33 08.46	48 30 17.49	20.06	17.68	195	1.12	5.4	—	—	S	12851021
147V000064	00 33 07.85	48 28 48.17	20.12	18.00	147	0.42	5.6	—	—	M	13130543
147V000065	00 33 07.53	48 30 22.15	20.04	17.67	128	0.75	5.7	—	—	M	13341046
147V000066	00 33 07.14	48 29 49.17	20.01	17.23	205	0.57	5.5	—	—	M	13530869
147V000067	00 33 07.22	48 31 29.62	20.25	16.28	394	0.59	5.1	—	—	C	13541407
147V000068	00 33 06.92	48 28 20.66	20.06	18.01	167	0.53	5.9	—	—	M	13610395
147V000069	00 33 07.05	48 31 05.04	20.25	17.24	200	1.20	5.8	—	—	u	13621275
147V000070	00 33 06.84	48 28 08.27	19.93	16.92	260	0.50	6.4	—	—	C	13650329
147V000071	00 33 06.74	48 28 01.40	19.73	16.94	317	0.75	6.0	—	—	C	13700292
147V000072	00 33 06.83	48 32 26.95	19.77	16.42	319	0.30	4.8	—	—	C	13771714
147V000073	00 33 06.61	48 31 35.60	20.04	16.84	223	0.95	6.4	—	—	C	13861439
147V000074	00 33 06.44	48 30 27.95	19.51	15.78	386	1.06	6.5	—	—	M	13921076
147V000075	00 33 06.15	48 28 14.38	20.33	—	194	0.85	6.0	—	—	C	14020361
147V000076	00 33 05.73	48 28 50.21	19.64	16.90	304	0.40	6.1	—	—	C	14260553
147V000077	00 33 05.36	48 28 43.42	19.93	18.05	159	0.88	4.6	—	—	M	14450516
147V000078	00 33 05.32	48 31 17.48	19.75	17.03	208	0.63	5.4	—	—	S	14541341

Table 13.3: continued.

ID	RAJ2000 h:m:s	DEJ2000 d:m:s	i [mag]	K_s [mag]	P_0 [d]	Δi [mag]	sig_0	P_1 [d]	sig_1	type	ID_{PaperI}
147V000079	00 33 04.98	48 29 47.57	20.25	16.94	235	0.57	5.2	—	—	M	14680860
147V000080	00 33 04.72	48 29 36.61	20.17	17.82	160	0.45	4.3	—	—	M	14810801
147V000081	00 33 04.81	48 32 49.75	20.14	17.19	179	0.78	5.7	—	—	M	14851835
147V000082	00 33 04.50	48 29 26.70	19.78	17.34	152	0.76	6.4	—	—	M	14920748
147V000083	00 33 03.50	48 27 53.84	20.44	17.11	234	0.99	5.8	—	—	C	15410250
147V000084	00 33 03.44	48 30 32.32	20.07	17.01	258	0.58	6.0	—	—	C	15511099
147V000085	00 33 03.47	48 32 24.17	19.53	16.15	303	0.99	6.9	—	—	C	15551698
147V000086	00 33 03.04	48 30 31.54	19.74	16.80	248	0.43	5.1	—	—	M	15721095
147V000087	00 33 02.87	48 30 54.07	20.01	17.53	196	0.57	4.9	—	—	M	15821215
147V000088	00 33 02.46	48 31 27.43	19.88	17.09	234	0.36	4.2	—	—	M	16061394
147V000089	00 33 02.44	48 31 23.39	20.17	18.12	157	1.13	4.0	—	—	S	16071372
147V000090	00 33 02.24	48 30 43.61	20.48	17.52	421	0.44	4.4	—	—	M	16151159
147V000091	00 33 02.11	48 30 13.02	20.49	17.57	186	0.78	5.6	—	—	M	16210995
147V000092	00 33 01.88	48 29 39.69	19.73	17.07	278	0.54	6.1	—	—	C	16310817
147V000093	00 33 01.12	48 27 58.71	20.23	17.72	165	0.73	5.8	—	—	C	16670275
147V000094	00 33 01.14	48 31 05.04	20.06	17.55	168	0.75	5.4	—	—	S	16741274
147V000095	00 33 01.01	48 28 45.23	20.11	17.74	193	0.62	4.6	—	—	S	16750524
147V000096	00 32 58.55	48 30 49.40	20.53	17.34	200	1.05	5.7	—	—	u	18111189
147V000097	00 32 58.26	48 31 10.67	20.07	—	161	0.65	5.5	—	—	S	18271303
147V000098	00 32 58.02	48 31 50.20	20.54	17.66	214	1.14	4.4	—	—	C	18421515
147V000099	00 32 57.77	48 29 15.81	20.19	17.79	179	0.65	4.3	—	—	M	18480687
147V000100	00 32 57.48	48 29 36.95	20.04	17.81	185	0.88	5.4	—	—	M	18640800
147V000101	00 32 57.19	48 29 26.57	20.34	17.46	206	0.85	5.1	—	—	C	18790745
147V000102	00 32 57.06	48 31 06.58	20.07	17.42	206	0.92	4.8	—	—	S	18911281
147V000103	00 32 57.06	48 32 49.75	20.64	—	180	1.26	4.5	—	—	u	18951834
147V000104	00 33 23.57	48 30 34.46	19.51	17.13	270	0.89	6.4	—	—	u	—
147V000105	00 33 17.39	48 31 15.19	19.94	17.36	238	1.15	4.6	—	—	u	—

Table 13.3: continued.

ID	RAJ2000 h:m:s	DEJ2000 d:m:s	i [mag]	K_s [mag]	P_0 [d]	Δi [mag]	sig_0	P_1 [d]	sig_1	type	ID_{PaperI}
147V000106	00 33 09.47	48 31 50.70	19.69	17.15	211	0.64	5.3	—	—	u	—
147V000107	00 33 09.20	48 27 27.16	20.16	16.77	271	1.08	2.9	—	—	u	—
147V000108	00 33 04.56	48 29 21.92	19.72	17.22	387	0.46	4.2	—	—	u	—
147V000109	00 33 29.20	48 30 45.91	20.51	—	270	1.09	3.6	—	—	u	—
147V000110	00 33 26.54	48 32 48.50	19.93	17.12	219	0.63	7.7	—	—	S	03341833
147V000111	00 33 26.41	48 31 40.98	20.61	16.71	321	0.86	7.3	—	—	C	03381473
147V000112	00 33 25.68	48 33 15.14	21.92	16.09	406	1.71	4.4	—	—	u	—
147V000113	00 33 25.27	48 29 54.83	19.76	—	140	0.38	3.5	—	—	u	—
147V000114	00 33 24.44	48 32 06.63	21.38	17.15	226	1.25	4.3	—	—	u	—
147V000115	00 33 24.26	48 28 43.27	19.86	17.50	209	0.44	7.0	—	—	C	04450523
147V000116	00 33 23.93	48 32 56.76	20.54	—	149	0.40	2.9	—	—	S	04731877
147V000117	00 33 23.75	48 32 46.45	19.96	17.07	98	0.47	4.0	—	—	M	04821822
147V000118	00 33 23.38	48 32 54.19	21.67	—	298	1.58	5.6	—	—	u	—
147V000119	00 33 22.53	48 28 55.57	19.94	16.73	304	0.82	6.5	—	—	u	—
147V000120	00 33 21.94	48 30 56.48	21.40	—	124	0.78	2.4	—	—	u	—
147V000121	00 33 21.89	48 30 26.45	20.07	17.96	110	0.38	4.7	—	—	S	05751073
147V000122	00 33 20.41	48 29 41.12	19.93	—	143	0.34	5.1	—	—	u	06510831
147V000123	00 33 19.94	48 29 58.91	20.25	17.48	226	1.24	8.4	—	—	u	—
147V000124	00 33 16.79	48 31 41.36	20.52	15.86	438	1.20	5.7	—	—	u	—
147V000125	00 33 16.82	48 32 51.88	21.99	—	88	1.02	1.7	—	—	u	08491849
147V000126	00 33 16.69	48 32 49.67	22.21	—	313	1.12	6.2	—	—	u	08551837
147V000127	00 33 16.49	48 31 38.27	20.64	16.65	406	1.05	4.2	—	—	u	—
147V000128	00 33 16.26	48 28 04.49	20.08	17.20	223	0.36	5.3	—	—	u	—
147V000129	00 33 16.31	48 31 23.08	20.41	16.51	341	0.83	6.0	—	—	u	—
147V000130	00 33 15.33	48 30 50.77	20.48	17.99	143	1.05	4.6	—	—	S	09231201
147V000131	00 33 14.93	48 33 23.72	20.24	17.22	200	0.71	6.3	—	—	M	09502019
147V000132	00 33 14.24	48 31 12.86	19.98	17.84	157	0.57	4.8	—	—	S	09811319

Table 13.3: continued.

ID	RAJ2000 h:m:s	DEJ2000 d:m:s	i [mag]	K_s [mag]	P_0 [d]	Δi [mag]	sig_0	P_1 [d]	sig_1	type	ID_{PaperI}
147V000133	00 33 12.79	48 31 02.92	20.70	16.51	379	1.01	8.6	—	—	u	—
147V000134	00 33 12.64	48 29 59.52	19.71	16.83	246	0.34	5.3	—	—	C	10630926
147V000135	00 33 12.58	48 31 01.90	20.81	16.53	346	1.47	4.4	—	—	u	—
147V000136	00 33 12.36	48 30 29.70	20.33	17.10	257	1.88	6.7	—	—	u	—
147V000137	00 33 11.09	48 28 48.81	20.04	16.60	178	0.88	5.7	—	—	u	—
147V000138	00 33 09.02	48 29 50.59	21.02	—	133	0.88	6.6	—	—	u	—
147V000139	00 33 08.32	48 29 26.70	20.24	17.09	109	0.58	5.2	—	—	u	—
147V000140	00 33 08.07	48 28 21.69	19.84	17.16	202	0.38	5.2	—	—	M	13000401
147V000141	00 33 07.87	48 31 32.07	20.11	17.15	186	0.41	3.7	—	—	u	—
147V000142	00 33 07.19	48 32 37.74	20.11	17.48	145	0.53	6.0	—	—	M	13581771
147V000143	00 33 06.40	48 29 55.81	20.65	17.37	525	0.57	4.2	—	—	S	13930904
147V000144	00 33 02.05	48 29 47.60	20.16	16.82	218	0.62	4.0	—	—	u	—
147V000145	00 33 01.85	48 30 06.08	20.23	17.61	153	0.64	5.7	—	—	u	—
147V000146	00 32 58.61	48 29 46.87	19.64	17.36	184	0.42	5.5	—	—	M	18050854
147V000147	00 32 57.69	48 27 41.80	20.10	16.76	254	0.58	4.5	—	—	u	18480183
147V000148	00 33 04.22	48 29 12.83	19.42	16.15	348	0.35	4.5	—	—	C	15070673
147V000149	00 33 14.36	48 31 21.40	19.92	16.34	345	0.56	4.3	690	3.0	S	09751365
147V000150	00 33 10.37	48 30 06.46	20.38	16.33	406	0.78	6.2	813	0.7	u	—
147V000151	00 33 20.48	48 31 41.33	20.44	17.04	234	2.22	3.5	373	1.5	M	06521473
147V000152	00 33 20.35	48 32 18.83	19.52	16.70	222	0.46	4.5	804	0.8	M	06611673
147V000153	00 33 14.07	48 33 16.54	20.25	17.16	226	0.72	3.2	371	1.5	C	09951980
147V000154	00 33 07.38	48 30 38.03	20.40	17.26	178	0.93	4.2	238	1.4	C	13431131
147V000155	00 33 22.65	48 32 23.44	19.95	16.74	267	0.61	5.0	293	2.5	C	05391698
147V000156	00 33 16.18	48 28 19.31	19.75	16.43	280	0.50	4.9	363	0.7	C	08710392
147V000157	00 33 12.89	48 29 50.98	19.75	16.58	316	0.33	5.3	790	1.0	C	10500881
147V000158	00 33 05.44	48 30 18.10	20.49	16.71	226	1.31	4.9	293	0.9	C	14451023
147V000159	00 33 02.32	48 29 32.13	19.76	16.77	305	0.52	5.0	1023	1.2	C	16080776

Table 13.3: continued.

ID	RAJ2000 h:m:s	DEJ2000 d:m:s	i [mag]	K_s [mag]	P_0 [d]	Δi [mag]	sig_0	P_1 [d]	sig_1	type	ID_{PaperI}
147V000160	00 33 00.92	48 29 41.43	19.66	16.17	378	1.68	6.1	564	3.3	M	16820825
147V000161	00 33 00.66	48 27 40.70	21.40	—	371	2.74	3.2	446	1.0	u	16900179
147V000162	00 32 59.44	48 29 25.74	20.41	16.91	266	1.09	4.4	548	0.8	C	17600741
147V000163	00 32 56.70	48 29 39.82	20.60	17.11	377	0.91	4.9	832	1.0	u	19060816
147V000164	00 33 04.76	48 29 29.04	19.48	16.98	232	0.64	4.6	302	1.4	u	—
147V000165	00 33 22.99	48 31 58.23	21.21	16.80	348	1.09	9.1	784	2.2	u	—
147V000166	00 33 16.37	48 28 04.20	20.46	16.81	292	0.79	8.1	822	3.5	u	—
147V000167	00 33 07.47	48 30 26.76	20.09	17.25	250	1.29	7.2	388	5.6	u	—
147V000168	00 33 04.17	48 28 59.64	20.22	16.80	304	1.49	7.2	822	4.7	u	—
147V000169	00 33 18.39	48 31 01.83	20.06	17.11	—	0.55	—	—	—	M	07611261
147V000170	00 33 17.44	48 31 41.06	21.09	16.22	—	1.63	—	—	—	S	08131471
147V000171	00 33 05.58	48 28 37.77	21.54	17.33	—	1.39	—	—	—	C	14330486
147V000172	00 33 27.70	48 29 35.30	19.78	17.36	—	0.73	—	—	—	M	02650802
147V000173	00 33 26.44	48 31 50.12	20.02	—	—	0.44	—	—	—	M	03371522
147V000174	00 33 23.51	48 30 41.14	19.71	17.25	—	0.26	—	—	—	M	04891152
147V000175	00 33 20.93	48 28 34.61	19.96	—	—	0.56	—	—	—	M	06210475
147V000176	00 33 20.07	48 33 17.28	20.01	17.36	—	0.61	—	—	—	S	06781986
147V000177	00 33 18.96	48 30 25.85	19.70	16.75	—	0.50	—	—	—	M	07291069
147V000178	00 33 17.45	48 27 55.86	19.90	16.75	—	0.46	—	—	—	M	08030267
147V000179	00 33 17.18	48 28 47.15	19.75	17.27	—	0.34	—	—	—	u	—
147V000180	00 33 16.90	48 30 57.62	19.98	17.63	—	0.54	—	—	—	S	08401238
147V000181	00 33 13.63	48 29 24.23	20.09	17.06	—	0.39	—	—	—	u	—
147V000182	00 33 13.46	48 30 55.17	20.01	16.83	—	0.44	—	—	—	C	10221224
147V000183	00 33 12.63	48 30 43.45	19.83	17.01	—	0.48	—	—	—	u	—
147V000184	00 33 10.85	48 29 54.19	19.69	17.23	—	0.53	—	—	—	C	11570897
147V000185	00 33 10.70	48 31 30.87	20.54	16.99	—	1.67	—	—	—	S	—
147V000186	00 33 09.98	48 32 18.45	20.10	17.84	—	0.49	—	—	—	C	12091669

Table 13.3: continued.

ID	RAJ2000 h:m:s	DEJ2000 d:m:s	i [mag]	K_s [mag]	P_0 [d]	Δi [mag]	sig_0	P_1 [d]	sig_1	type	ID_{PaperI}
147V000187	00 33 09.34	48 32 07.84	20.28	16.67	—	0.75	—	—	—	C	12431612
147V000188	00 33 08.27	48 32 43.73	20.24	17.63	—	0.44	—	—	—	u	—
147V000189	00 33 06.62	48 30 49.13	19.84	18.09	—	0.60	—	—	—	S	13841190
147V000190	00 33 05.96	48 33 19.34	19.66	18.04	—	0.36	—	—	—	S	14261994
147V000191	00 33 05.62	48 32 19.62	20.01	17.01	—	0.60	—	—	—	u	—
147V000192	00 33 05.50	48 30 52.88	19.28	16.20	—	0.37	—	—	—	C	14431210
147V000193	00 33 02.33	48 32 52.16	20.12	16.78	—	0.81	—	—	—	C	16161848
147V000194	00 33 01.70	48 30 31.87	19.78	16.78	—	0.30	—	—	—	M	16441096
147V000195	00 32 58.91	48 31 08.84	20.30	17.64	—	0.67	—	—	—	S	17931293
147V000196	00 32 58.00	48 28 28.95	20.09	17.86	—	0.51	—	—	—	M	18330436
147V000197	00 33 08.90	48 29 26.45	21.20	—	—	1.70	—	—	—	u	—
147V000198	00 33 04.84	48 29 04.69	21.17	—	—	1.64	—	—	—	u	—
147V000199	00 33 27.10	48 29 49.27	21.28	—	—	0.75	—	—	—	u	—
147V000200	00 33 23.90	48 30 32.65	21.31	—	—	0.71	—	—	—	u	04691107
147V000201	00 33 23.28	48 30 39.71	20.90	—	—	0.59	—	—	—	u	05011145
147V000202	00 33 23.07	48 31 52.27	20.24	16.87	—	0.53	—	—	—	u	—
147V000203	00 33 22.59	48 29 37.69	20.75	—	—	0.62	—	—	—	S	05350813
147V000204	00 33 21.17	48 28 37.66	21.64	—	—	0.99	—	—	—	u	—
147V000205	00 33 18.20	48 30 50.04	21.13	17.85	—	1.16	—	—	—	u	—
147V000206	00 33 16.65	48 30 51.67	20.01	17.86	—	0.30	—	—	—	C	08531206
147V000207	00 33 12.08	48 31 11.36	19.74	16.41	—	0.43	—	—	—	u	—
147V000208	00 33 11.67	48 29 26.87	20.10	17.69	—	0.42	—	—	—	M	11130751
147V000209	00 33 08.64	48 32 15.42	21.41	18.31	—	1.16	—	—	—	u	—
147V000210	00 33 03.98	48 31 08.43	21.46	—	—	1.12	—	—	—	u	—
147V000211	00 33 02.06	48 28 12.73	20.26	19.19	—	0.49	—	—	—	u	—
147V000212	00 33 01.44	48 30 03.94	20.12	17.01	—	0.45	—	—	—	u	—
147V000213	00 33 00.88	48 29 20.82	19.72	16.98	—	0.26	—	—	—	M	16840715

Table 13.4: Same as Table 13.3 but for NGC 185.

ID	RAJ2000 h:m:s	DEJ2000 d:m:s	i [mag]	K_s [mag]	P_0 [d]	Δi [mag]	sig_0	P_1 [d]	sig_1	type	ID_{PaperI}
185V000001	00 39 14.67	48 20 40.97	19.68	—	139	0.43	4.0	—	—	S	01961242
185V000002	00 39 14.42	48 18 37.24	19.84	—	114	0.43	4.4	—	—	S	02020584
185V000003	00 39 14.12	48 21 31.49	20.03	—	153	0.66	2.8	—	—	M	02281511
185V000004	00 39 13.29	48 20 28.43	19.58	—	147	0.55	5.7	—	—	M	02681175
185V000005	00 38 52.03	48 20 10.21	19.28	16.31	371	0.46	6.0	—	—	C	13961070
185V000006	00 39 13.12	48 19 25.54	19.57	17.48	163	0.46	5.6	—	—	S	02740840
185V000007	00 39 12.54	48 17 54.78	20.41	—	311	0.84	6.1	—	—	u	02990357
185V000008	00 39 12.44	48 21 06.86	20.41	—	123	0.86	3.8	—	—	M	03161379
185V000009	00 39 11.84	48 19 43.23	20.18	16.89	277	0.72	5.9	—	—	C	03430934
185V000010	00 39 11.74	48 21 11.84	19.70	18.04	169	0.91	5.9	—	—	M	03531405
185V000011	00 39 11.78	48 21 46.36	19.31	17.54	226	0.46	4.8	—	—	M	03531589
185V000012	00 39 11.23	48 19 53.03	20.06	—	109	0.48	4.5	—	—	S	03760986
185V000013	00 39 11.12	48 20 20.59	19.99	17.85	124	0.58	5.0	—	—	M	03831132
185V000014	00 39 10.87	48 20 17.89	19.58	17.09	588	0.31	3.7	—	—	M	03961118
185V000015	00 39 10.41	48 20 52.43	20.78	—	168	1.07	4.9	—	—	M	04231301
185V000016	00 39 09.69	48 19 44.06	20.35	—	120	0.87	4.9	—	—	S	04570937
185V000017	00 39 09.65	48 19 42.87	19.67	—	203	0.87	6.1	—	—	S	04590931
185V000018	00 39 09.79	48 21 01.08	19.66	—	142	0.29	3.9	—	—	M	04561347
185V000019	00 39 09.34	48 20 26.12	19.68	17.93	144	0.56	4.4	—	—	M	04781161
185V000020	00 39 09.09	48 18 42.08	19.27	17.25	200	0.43	5.3	—	—	M	04860607
185V000021	00 39 09.18	48 19 59.60	19.47	17.24	240	0.41	6.3	—	—	C	04851020
185V000022	00 39 09.03	48 19 51.86	19.95	16.54	301	0.76	6.0	—	—	C	04930978
185V000023	00 39 09.17	48 22 56.02	19.51	17.21	204	0.68	5.8	—	—	S	04951959
185V000024	00 39 08.91	48 23 00.90	19.43	17.21	185	0.32	3.4	—	—	M	05091985
185V000025	00 39 08.53	48 18 50.95	19.55	16.96	249	0.57	5.6	—	—	C	05160654
185V000026	00 39 08.46	48 21 22.09	20.30	16.40	421	0.48	4.4	—	—	C	05281459
185V000027	00 39 08.51	48 22 17.14	19.89	17.50	391	0.41	4.5	—	—	M	05281752

Table 13.4: continued.

ID	RAJ2000 h:m:s	DEJ2000 d:m:s	i [mag]	K_s [mag]	P_0 [d]	Δi [mag]	sig_0	P_1 [d]	sig_1	type	ID_{PaperI}
185V000028	00 39 08.35	48 19 57.81	19.73	17.50	169	0.95	5.7	—	—	M	05291010
185V000029	00 39 08.33	48 21 08.51	20.55	16.69	338	0.90	4.8	—	—	C	05341386
185V000030	00 39 08.18	48 19 39.03	19.32	17.45	168	0.55	6.4	—	—	S	05370910
185V000031	00 39 08.23	48 21 25.98	19.70	17.72	186	0.73	4.0	—	—	M	05401479
185V000032	00 39 08.15	48 21 21.75	19.35	17.27	176	0.33	2.7	—	—	M	05441457
185V000033	00 39 07.84	48 17 21.27	19.55	—	148	0.59	5.1	—	—	M	05480176
185V000034	00 39 07.79	48 20 34.30	19.25	16.63	137	0.27	4.0	—	—	M	05611204
185V000035	00 39 07.46	48 20 20.22	19.97	17.78	154	0.53	4.7	—	—	S	05771129
185V000036	00 39 07.47	48 22 28.94	20.04	16.70	305	0.74	5.1	—	—	u	05841814
185V000037	00 39 07.19	48 19 04.86	19.69	17.34	215	0.61	4.3	—	—	M	05880728
185V000038	00 39 07.08	48 22 16.59	19.50	17.32	195	0.40	5.7	—	—	M	06041748
185V000039	00 39 06.81	48 18 30.65	20.25	17.52	217	1.16	6.6	—	—	u	—
185V000040	00 39 06.67	48 17 15.92	19.65	—	313	0.88	3.5	—	—	u	06090147
185V000041	00 39 06.77	48 21 46.92	19.80	17.29	237	1.14	6.7	—	—	M	06181590
185V000042	00 39 06.67	48 22 51.48	19.30	17.19	172	0.65	5.3	—	—	M	06271934
185V000043	00 39 06.69	48 23 05.96	19.73	16.89	288	0.78	4.7	—	—	C	06272011
185V000044	00 39 06.36	48 18 23.61	19.50	17.33	199	0.39	5.9	—	—	M	06300508
185V000045	00 39 06.40	48 19 14.30	20.37	16.91	326	1.42	6.1	—	—	C	06300777
185V000046	00 39 06.36	48 19 19.69	20.04	—	128	0.77	6.1	—	—	S	06320806
185V000047	00 39 05.93	48 17 54.05	20.10	17.28	189	0.51	5.8	—	—	C	06510350
185V000048	00 39 06.05	48 20 45.86	19.89	17.38	122	0.59	3.7	—	—	M	06541265
185V000049	00 39 06.13	48 22 56.61	19.32	16.01	399	1.06	5.0	—	—	M	06561961
185V000050	00 39 05.92	48 21 08.54	19.75	17.39	183	0.79	6.3	—	—	M	06621386
185V000051	00 39 05.68	48 20 01.49	19.79	—	161	0.67	5.3	—	—	M	06711028
185V000052	00 39 05.62	48 19 32.81	20.01	17.21	247	0.70	5.9	—	—	C	06720876
185V000053	00 39 05.50	48 20 21.72	19.71	17.92	132	0.60	6.5	—	—	M	06811136
185V000054	00 39 05.34	48 19 35.25	19.12	16.92	95	0.19	3.9	—	—	M	06870889
185V000055	00 39 05.35	48 21 07.57	19.86	16.70	262	0.43	5.2	—	—	M	06921380

Table 13.4: continued.

ID	RAJ2000 h:m:s	DEJ2000 d:m:s	i [mag]	K_s [mag]	P_0 [d]	Δi [mag]	sig_0	P_1 [d]	sig_1	type	ID$_{PaperI}$
185V000056	00 39 05.26	48 21 19.33	20.30	—	133	1.15	5.3	—	—	M	06971443
185V000057	00 39 05.12	48 20 04.63	20.60	18.13	141	0.98	5.0	—	—	M	07011045
185V000058	00 39 04.74	48 18 16.68	19.60	—	107	0.33	3.5	—	—	S	07150470
185V000059	00 39 04.86	48 22 15.07	19.46	17.23	467	0.29	3.9	—	—	M	07211739
185V000060	00 39 04.73	48 20 50.01	19.83	16.78	229	1.15	6.6	—	—	S	07241286
185V000061	00 39 04.53	48 19 12.11	19.47	16.83	252	0.49	6.0	—	—	C	07290765
185V000062	00 39 04.43	48 21 38.13	20.13	16.65	219	0.90	6.2	—	—	u	07421543
185V000063	00 39 04.11	48 18 00.35	20.33	—	107	0.78	3.9	—	—	S	07480383
185V000064	00 39 04.18	48 20 08.44	19.51	17.52	192	0.94	6.7	—	—	M	07501065
185V000065	00 39 04.21	48 22 19.71	20.14	17.73	146	0.72	4.5	—	—	M	07561764
185V000066	00 39 03.99	48 20 03.78	20.18	16.49	325	0.80	6.3	—	—	u	07601040
185V000067	00 39 03.53	48 19 06.36	19.72	—	92	0.59	4.2	—	—	S	07820734
185V000068	00 38 41.55	48 19 30.40	19.98	17.17	237	0.70	5.5	—	—	C	19500854
185V000069	00 38 42.10	48 19 40.52	19.78	17.71	340	0.31	4.4	—	—	M	19210908
185V000070	00 39 03.20	48 18 06.89	19.87	—	157	0.51	5.5	—	—	u	07960417
185V000071	00 39 03.33	48 21 40.27	19.58	17.52	167	0.37	4.4	—	—	M	08011554
185V000072	00 39 03.15	48 20 33.42	19.39	—	140	0.50	5.0	—	—	M	08071198
185V000073	00 39 03.21	48 21 22.16	19.85	17.31	95	0.32	1.8	—	—	M	08061457
185V000074	00 39 03.08	48 19 47.34	19.69	16.41	286	0.49	4.2	—	—	S	08080952
185V000075	00 39 02.69	48 21 44.92	20.08	—	139	0.58	4.9	—	—	M	08351578
185V000076	00 39 02.52	48 19 00.32	21.15	16.31	358	1.23	4.5	—	—	C	08350701
185V000077	00 39 02.58	48 20 31.21	19.39	—	151	0.59	5.9	—	—	S	08371186
185V000078	00 39 02.28	48 19 18.53	20.45	16.07	420	0.65	5.4	—	—	S	08490798
185V000079	00 39 02.29	48 20 48.95	19.80	—	159	0.47	5.5	—	—	M	08531280
185V000080	00 39 01.98	48 17 38.70	19.70	17.11	225	0.43	5.4	—	—	C	08600266
185V000081	00 39 02.17	48 21 00.07	19.61	17.47	210	0.73	6.2	—	—	M	08601339
185V000082	00 39 02.06	48 20 56.13	19.25	16.90	235	0.58	6.3	—	—	M	08661318
185V000083	00 39 01.77	48 18 48.91	19.70	16.79	280	0.52	6.3	—	—	C	08740640

Table 13.4: continued.

ID	RAJ2000 h:m:s	DEJ2000 d:m:s	i [mag]	K_s [mag]	P_0 [d]	Δi [mag]	sig_0	P_1 [d]	sig_1	type	ID_{PaperI}
185V000084	00 39 01.92	48 21 55.53	19.28	17.53	127	0.42	4.4	—	—	S	08761635
185V000085	00 39 01.76	48 19 34.17	18.93	16.42	239	0.22	4.1	—	—	M	08770881
185V000086	00 39 01.75	48 19 32.45	19.48	16.82	222	0.56	6.2	—	—	M	08780872
185V000087	00 39 01.70	48 20 38.90	19.75	16.84	131	0.41	3.9	—	—	M	08841226
185V000088	00 39 01.59	48 19 07.12	19.65	16.32	339	0.56	5.2	—	—	S	08850737
185V000089	00 39 01.66	48 23 08.84	19.38	17.17	183	0.32	3.1	—	—	S	08942025
185V000090	00 39 01.01	48 17 31.20	19.19	16.93	154	0.15	2.8	—	—	M	09110226
185V000091	00 39 00.93	48 19 59.41	19.09	16.37	302	0.22	5.4	—	—	S	09231016
185V000092	00 39 00.98	48 22 01.18	20.23	17.45	192	0.92	5.3	—	—	M	09271664
185V000093	00 39 00.93	48 21 48.81	19.63	16.37	280	0.69	6.6	—	—	C	09281598
185V000094	00 39 00.91	48 21 33.04	20.14	16.78	236	0.85	5.2	—	—	C	09281514
185V000095	00 39 00.68	48 19 01.60	20.16	16.56	315	0.70	4.9	—	—	u	09330707
185V000096	00 39 00.66	48 20 57.39	19.38	17.27	193	0.43	5.4	—	—	S	09401324
185V000097	00 39 00.68	48 21 36.07	20.17	—	121	0.99	4.9	—	—	S	09411530
185V000098	00 39 00.53	48 19 16.75	20.07	—	127	0.73	3.9	—	—	S	09420788
185V000099	00 39 00.53	48 19 27.13	20.65	17.43	287	1.09	5.4	—	—	C	09420843
185V000100	00 39 00.58	48 20 26.85	19.23	15.22	494	1.41	6.5	—	—	S	09431162
185V000101	00 39 00.42	48 18 00.55	20.78	—	133	1.40	5.9	—	—	S	09430382
185V000102	00 39 00.57	48 20 52.10	19.65	17.79	121	0.54	4.1	—	—	S	09451296
185V000103	00 39 00.57	48 21 20.26	19.25	16.93	224	0.64	5.2	—	—	M	09461446
185V000104	00 39 00.36	48 20 32.63	18.96	15.81	302	0.61	5.8	—	—	S	09551192
185V000105	00 39 00.10	48 20 28.07	19.46	16.70	230	0.66	5.5	—	—	S	09681168
185V000106	00 39 00.03	48 22 19.33	19.71	16.10	330	0.49	5.6	—	—	S	09781761
185V000107	00 38 59.62	48 17 37.61	20.62	17.40	234	0.67	4.6	—	—	C	09850259
185V000108	00 38 59.86	48 21 47.85	19.50	17.24	192	0.63	5.9	—	—	M	09851593
185V000109	00 38 59.73	48 20 11.69	20.28	17.25	206	1.03	2.8	—	—	M	09871081
185V000110	00 38 59.67	48 19 47.12	20.16	16.51	306	0.92	6.3	—	—	C	09890950
185V000111	00 38 59.54	48 19 46.21	19.72	16.74	140	1.09	6.5	—	—	M	09960945

Table 13.4: continued.

ID	RAJ2000 h:m:s	DEJ2000 d:m:s	i [mag]	K_s [mag]	P_0 [d]	Δi [mag]	sig_0	P_1 [d]	sig_1	type	ID_{PaperI}
185V000112	00 38 59.58	48 20 39.46	19.33	17.34	111	0.26	3.3	—	—	S	09961228
185V000113	00 38 59.55	48 20 58.61	19.29	16.56	248	0.88	5.7	—	—	M	09991330
185V000114	00 38 59.50	48 20 43.15	19.39	16.94	167	0.57	3.9	—	—	C	10011248
185V000115	00 38 59.39	48 21 47.63	19.04	17.51	165	0.32	6.2	—	—	S	10101592
185V000116	00 38 59.27	48 20 11.89	19.63	17.64	172	0.59	5.0	—	—	M	10121081
185V000117	00 38 59.21	48 20 57.33	19.67	16.27	358	0.41	5.7	—	—	C	10171324
185V000118	00 38 59.28	48 22 54.66	20.09	17.03	103	0.50	3.2	—	—	S	10191949
185V000119	00 38 58.97	48 19 26.65	19.07	16.89	137	0.30	3.2	—	—	M	10250840
185V000120	00 38 59.03	48 21 42.05	19.44	16.52	314	0.63	6.6	—	—	C	10291562
185V000121	00 38 58.78	48 17 34.79	20.65	17.55	199	1.10	4.8	—	—	u	—
185V000122	00 38 58.97	48 21 15.09	19.68	17.15	273	0.82	6.9	—	—	C	10311418
185V000123	00 38 58.67	48 19 56.06	19.88	17.17	116	0.65	3.7	—	—	M	10420997
185V000124	00 38 58.49	48 21 15.74	19.88	16.93	217	1.15	6.7	—	—	M	10561421
185V000125	00 38 58.30	48 19 22.84	19.65	17.60	192	0.71	6.0	—	—	M	10600820
185V000126	00 38 58.17	48 18 06.23	19.97	17.22	202	0.58	5.6	—	—	M	10640411
185V000127	00 38 58.22	48 19 04.48	20.53	—	104	0.69	3.0	—	—	S	10640722
185V000128	00 38 58.18	48 19 37.05	20.01	17.56	511	0.34	4.0	—	—	M	10670895
185V000129	00 38 58.14	48 19 30.85	19.27	17.09	208	0.39	6.2	—	—	S	10690862
185V000130	00 38 58.04	48 18 59.95	19.88	17.07	253	0.52	5.1	—	—	C	10730698
185V000131	00 38 58.10	48 20 07.57	18.69	16.01	232	0.50	4.9	—	—	S	10731058
185V000132	00 38 58.14	48 20 48.40	19.46	16.23	277	0.35	4.9	—	—	M	10731276
185V000133	00 38 58.02	48 19 39.68	19.24	17.06	155	0.43	5.8	—	—	M	10760909
185V000134	00 38 58.05	48 20 59.64	20.11	17.82	223	1.45	6.7	—	—	S	10781336
185V000135	00 38 57.95	48 19 41.21	20.10	16.91	240	1.30	5.8	—	—	M	10800917
185V000136	00 38 57.73	48 22 09.78	19.96	—	119	0.50	3.7	—	—	S	10991709
185V000137	00 38 57.53	48 20 09.41	19.00	16.70	157	0.41	3.6	—	—	M	11041068
185V000138	00 38 57.51	48 21 37.74	19.38	17.13	168	0.59	4.2	—	—	S	11091538
185V000139	00 38 42.59	48 21 41.79	20.33	16.37	323	0.88	4.6	—	—	u	19001556

Table 13.4: continued.

ID	RAJ2000 h:m:s	DEJ2000 d:m:s	i [mag]	K_s [mag]	P_0 [d]	Δi [mag]	sig_0	P_1 [d]	sig_1	type	ID_{PaperI}
185V000140	00 38 57.35	48 18 56.01	19.53	17.40	199	0.39	6.0	—	—	S	11100676
185V000141	00 38 57.26	48 17 35.11	19.94	—	130	0.81	4.7	—	—	S	11100245
185V000142	00 38 42.56	48 21 23.55	19.92	—	185	0.56	6.0	—	—	M	19011458
185V000143	00 38 57.07	48 19 33.09	19.56	16.94	246	0.50	5.2	—	—	C	11260874
185V000144	00 38 56.91	48 19 07.43	20.64	17.44	206	0.64	5.2	—	—	u	11330737
185V000145	00 38 42.52	48 19 17.57	19.83	17.84	134	0.48	4.8	—	—	M	18980786
185V000146	00 38 57.03	48 21 51.90	19.86	17.43	175	0.69	5.9	—	—	M	11351614
185V000147	00 38 56.75	48 20 48.19	20.18	17.15	211	0.45	3.7	—	—	M	11471274
185V000148	00 38 56.69	48 20 40.91	20.12	15.94	343	0.72	4.6	—	—	S	11501235
185V000149	00 38 56.84	48 22 59.45	19.62	17.38	209	0.44	5.8	—	—	M	11491974
185V000150	00 38 56.51	48 18 59.92	20.33	16.81	231	1.59	6.2	—	—	M	11540697
185V000151	00 38 56.16	48 18 25.41	20.25	—	166	1.41	5.8	—	—	S	11710513
185V000152	00 38 56.01	48 18 12.58	20.17	17.68	150	0.85	6.4	—	—	M	11780444
185V000153	00 38 56.13	48 20 33.95	18.83	17.03	178	0.40	4.9	—	—	S	11791198
185V000154	00 38 56.03	48 19 19.52	20.85	—	132	1.73	6.2	—	—	M	11810801
185V000155	00 38 56.01	48 19 56.10	19.93	16.37	406	1.23	6.1	—	—	S	11840996
185V000156	00 38 56.09	48 20 53.50	19.26	16.94	217	0.68	6.5	—	—	M	11821302
185V000157	00 38 55.84	48 19 06.82	19.84	17.10	112	0.32	4.9	—	—	M	11900733
185V000158	00 38 55.99	48 22 38.72	19.86	17.91	150	0.76	5.6	—	—	S	11931863
185V000159	00 38 55.79	48 19 26.22	19.72	17.37	182	1.06	6.8	—	—	M	11940837
185V000160	00 38 42.54	48 18 37.26	20.94	16.62	361	0.99	3.8	—	—	C	18950571
185V000161	00 38 55.77	48 19 15.06	20.08	—	114	0.56	5.7	—	—	S	11940777
185V000162	00 38 55.77	48 20 50.61	20.14	—	116	0.66	4.0	—	—	S	11991287
185V000163	00 38 55.72	48 21 40.91	19.55	16.68	285	0.50	6.1	—	—	u	—
185V000164	00 38 55.47	48 20 35.56	19.26	15.91	453	0.74	4.6	—	—	S	12141206
185V000165	00 38 55.25	48 20 56.07	19.98	16.39	370	1.67	6.9	—	—	M	12271316
185V000166	00 38 55.19	48 20 18.10	19.94	16.41	361	0.74	3.0	—	—	M	12281113
185V000167	00 38 55.10	48 19 15.63	19.96	17.15	107	0.50	3.7	—	—	M	12300780

Table 13.4: continued.

ID	RAJ2000 h:m:s	DEJ2000 d:m:s	i [mag]	K_s [mag]	P_0 [d]	Δi [mag]	sig_0	P_1 [d]	sig_1	type	ID_{PaperI}
185V000168	00 38 55.14	48 21 35.46	19.85	16.41	308	0.69	6.3	—	—	S	12351525
185V000169	00 38 55.08	48 20 59.78	19.32	15.92	402	0.54	6.0	—	—	S	12361335
185V000170	00 38 55.03	48 20 05.16	20.34	16.83	272	1.35	6.2	—	—	u	—
185V000171	00 38 55.05	48 20 47.04	19.16	17.03	91	0.26	2.7	—	—	S	12371267
185V000172	00 38 55.04	48 21 21.21	19.81	—	176	0.76	6.3	—	—	M	12391450
185V000173	00 38 55.02	48 21 42.04	20.32	16.67	287	0.93	5.6	—	—	C	12411561
185V000174	00 38 42.54	48 18 27.86	19.80	17.56	160	0.56	6.1	—	—	M	18950520
185V000175	00 38 54.81	48 19 33.64	19.82	17.61	153	0.74	5.6	—	—	M	12460876
185V000176	00 38 54.59	48 19 06.97	19.64	16.26	394	0.44	5.4	—	—	C	12570734
185V000177	00 38 54.23	48 17 24.52	19.71	17.45	170	1.02	5.9	—	—	M	12710187
185V000178	00 38 54.38	48 20 15.87	19.78	16.63	280	0.83	6.2	—	—	C	12711101
185V000179	00 38 54.31	48 21 14.94	19.83	16.93	296	1.01	6.1	—	—	u	—
185V000180	00 38 54.06	48 19 19.72	19.68	17.50	187	0.64	6.4	—	—	M	12850801
185V000181	00 38 54.01	48 18 58.37	19.62	17.82	154	0.53	5.8	—	—	M	12870688
185V000182	00 38 53.77	48 20 39.45	19.57	16.54	739	0.33	3.5	—	—	u	13041226
185V000183	00 38 53.44	48 17 52.39	19.54	16.25	392	1.52	6.5	—	—	u	—
185V000184	00 38 53.43	48 17 54.60	19.04	16.83	263	0.37	6.4	—	—	S	13150347
185V000185	00 38 53.34	48 18 58.91	20.06	17.76	141	0.75	5.6	—	—	M	13230690
185V000186	00 38 53.29	48 20 00.66	19.39	17.25	112	0.20	4.5	—	—	M	13281019
185V000187	00 38 53.25	48 21 22.94	20.27	—	97	0.46	3.4	—	—	S	13341458
185V000188	00 38 53.13	48 19 42.43	20.41	16.39	303	1.01	5.6	—	—	M	13360922
185V000189	00 38 53.24	48 22 21.16	20.18	—	92	0.46	4.5	—	—	S	13371769
185V000190	00 38 52.86	48 18 11.09	19.62	16.44	300	0.41	6.1	—	—	C	13460435
185V000191	00 38 52.84	48 19 14.08	19.83	—	94	0.47	3.3	—	—	S	13500771
185V000192	00 38 52.85	48 19 20.93	19.95	—	154	0.61	5.0	—	—	M	13500807
185V000193	00 38 52.43	48 19 50.16	18.90	—	397	0.25	4.2	—	—	C	13740963
185V000194	00 38 52.49	48 22 57.80	20.22	17.81	172	1.21	4.7	—	—	S	13791964
185V000195	00 38 52.35	48 20 14.19	19.19	17.16	115	0.22	2.6	—	—	M	13791091

Table 13.4: continued.

ID	RAJ2000	DEJ2000	i	K_s	P_0	Δi	sig_0	P_1	sig_1	type	ID_{PaperI}
	h:m:s	d:m:s	[mag]	[mag]	[d]	[mag]		[d]			
185V000196	00 38 52.09	48 18 08.68	20.34	17.76	236	1.04	5.5	—	—	C	13860422
185V000197	00 38 52.08	48 19 15.15	19.31	16.97	241	0.45	4.8	—	—	M	13900776
185V000198	00 38 52.06	48 19 58.40	19.53	16.17	257	0.68	6.4	—	—	S	13931007
185V000199	00 38 51.78	48 20 17.38	19.57	17.01	180	0.67	5.7	—	—	S	14091108
185V000200	00 38 51.42	48 18 14.65	19.93	16.88	285	0.83	6.0	—	—	C	14220453
185V000201	00 38 51.40	48 20 58.43	19.49	16.76	206	0.75	6.1	—	—	S	14311327
185V000202	00 38 51.34	48 20 19.89	20.11	17.01	289	1.28	5.0	—	—	u	14321121
185V000203	00 38 51.04	48 20 36.08	19.38	17.41	168	0.31	4.0	—	—	M	14491208
185V000204	00 38 50.65	48 18 17.71	19.71	17.15	122	0.36	4.6	—	—	M	14640469
185V000205	00 38 50.47	48 20 23.29	19.52	17.22	200	0.64	4.6	—	—	S	14791139
185V000206	00 38 50.31	48 17 36.98	19.19	17.18	205	0.40	6.8	—	—	M	14800252
185V000207	00 38 50.36	48 18 53.58	19.67	17.67	208	0.45	4.6	—	—	M	14810661
185V000208	00 38 50.45	48 20 52.35	19.39	17.02	152	0.58	4.8	—	—	M	14811294
185V000209	00 38 50.24	48 19 32.47	19.82	17.82	161	0.37	4.2	—	—	M	14890868
185V000210	00 38 49.94	48 17 39.17	19.83	—	119	0.32	3.8	—	—	S	14990263
185V000211	00 38 50.03	48 22 15.85	19.87	17.32	158	1.01	5.6	—	—	S	15071739
185V000212	00 38 49.93	48 20 34.82	18.61	16.43	312	0.79	6.4	—	—	S	15081200
185V000213	00 38 49.84	48 21 05.87	19.56	17.42	220	0.77	6.4	—	—	S	15151366
185V000214	00 38 49.43	48 18 27.55	19.73	18.21	171	0.62	5.8	—	—	S	15290521
185V000215	00 38 49.37	48 19 28.71	19.59	17.16	188	0.39	4.8	—	—	M	15340848
185V000216	00 38 49.41	48 20 15.68	19.61	17.56	205	0.63	4.9	—	—	M	15341098
185V000217	00 38 49.10	48 17 28.60	19.75	17.82	160	0.45	5.8	—	—	M	15430207
185V000218	00 38 49.02	48 18 15.42	19.59	17.64	190	0.57	6.1	—	—	S	15500456
185V000219	00 38 48.86	48 21 05.05	19.43	17.17	112	0.39	3.9	—	—	M	15661361
185V000220	00 38 48.63	48 18 34.52	19.56	—	133	0.32	4.8	—	—	M	15710558
185V000221	00 38 48.60	48 20 52.10	18.91	16.14	303	0.25	5.0	—	—	C	15791292
185V000222	00 38 48.49	48 19 13.87	19.67	17.49	92	0.22	2.1	—	—	M	15810768
185V000223	00 38 48.30	48 17 34.86	19.82	17.75	164	0.86	5.1	—	—	M	15860240

Table 13.4: continued.

ID	RAJ2000 h:m:s	DEJ2000 d:m:s	i [mag]	K_s [mag]	P_0 [d]	Δi [mag]	sig_0	P_1 [d]	sig_1	type	ID_{PaperI}
185V000224	00 38 48.18	48 20 04.06	19.75	16.91	187	0.35	4.5	—	—	M	15991036
185V000225	00 38 48.11	48 20 10.83	20.24	16.89	313	0.95	5.8	—	—	S	16031072
185V000226	00 38 47.96	48 19 56.27	19.69	17.76	158	0.46	5.1	—	—	M	16110994
185V000227	00 38 47.75	48 20 23.68	19.72	17.84	123	0.70	5.1	—	—	S	16231140
185V000228	00 38 47.65	48 21 36.64	19.51	—	100	0.34	4.6	—	—	S	16321530
185V000229	00 38 47.38	48 20 47.94	20.17	—	167	0.93	6.1	—	—	S	16441270
185V000230	00 38 42.88	48 20 49.54	19.74	16.98	222	0.58	4.9	—	—	M	18831277
185V000231	00 38 47.08	48 19 24.84	19.86	17.70	207	1.20	6.0	—	—	M	16560826
185V000232	00 38 46.93	48 18 50.94	19.96	17.84	193	0.78	6.8	—	—	M	16620645
185V000233	00 38 46.95	48 22 11.21	19.91	17.71	141	0.84	5.4	—	—	S	16711714
185V000234	00 38 46.67	48 17 15.30	19.70	—	191	1.04	5.1	—	—	u	16720135
185V000235	00 38 43.03	48 20 04.03	19.15	16.89	211	0.44	5.9	—	—	S	18731034
185V000236	00 38 46.61	48 21 03.26	19.70	—	185	0.37	3.8	—	—	M	16851351
185V000237	00 38 46.56	48 20 30.31	20.03	17.84	131	0.41	3.7	—	—	S	16871175
185V000238	00 38 46.21	48 18 29.68	20.26	17.19	393	1.10	6.0	—	—	u	17000531
185V000239	00 38 46.33	48 22 40.02	19.29	17.61	160	0.62	5.3	—	—	M	17051867
185V000240	00 38 43.00	48 18 06.39	19.36	17.14	238	0.99	5.3	—	—	M	18690406
185V000241	00 38 45.99	48 18 31.54	19.33	17.89	206	0.57	5.9	—	—	S	17120541
185V000242	00 38 45.92	48 19 01.99	19.00	16.11	303	1.28	6.3	—	—	M	17160704
185V000243	00 38 45.86	48 18 32.29	19.58	17.15	259	1.65	6.6	—	—	M	17180545
185V000244	00 38 43.25	48 20 28.08	19.58	16.68	249	0.62	6.3	—	—	C	18621162
185V000245	00 38 43.58	48 19 30.92	19.99	17.35	210	0.90	5.8	—	—	S	18420857
185V000246	00 38 45.68	48 22 06.22	19.80	17.38	165	0.39	3.9	—	—	S	17381687
185V000247	00 38 43.63	48 19 18.87	19.74	17.57	161	0.52	5.5	—	—	M	18390793
185V000248	00 38 45.54	48 21 18.22	19.58	16.68	279	0.53	4.3	—	—	M	17431431
185V000249	00 38 45.36	48 19 57.27	20.38	16.97	231	0.96	6.4	—	—	u	17490999
185V000250	00 38 43.60	48 17 28.18	19.75	17.26	206	0.48	3.9	—	—	u	18360202
185V000251	00 38 45.33	48 20 35.60	19.77	17.21	187	0.29	4.0	—	—	C	17521203

Table 13.4: continued.

ID	RAJ2000 h:m:s	DEJ2000 d:m:s	i [mag]	K_s [mag]	P_0 [d]	Δi [mag]	sig_0	P_1 [d]	sig_1	type	ID_{PaperI}
185V000252	00 38 45.14	48 20 47.11	20.41	16.68	229	0.91	6.4	—	—	C	17631265
185V000253	00 38 44.80	48 20 54.68	19.44	17.11	163	0.36	5.6	—	—	M	17811305
185V000254	00 38 44.34	48 19 18.45	20.06	—	117	0.51	5.0	—	—	S	18010791
185V000255	00 38 44.27	48 23 04.59	20.59	—	104	0.74	3.9	—	—	u	18151998
185V000256	00 38 44.13	48 21 17.99	19.75	—	140	0.36	4.1	—	—	S	18181429
185V000257	00 38 43.69	48 17 36.07	20.04	—	129	0.59	4.7	—	—	S	18310244
185V000258	00 38 44.05	48 20 02.83	19.80	17.78	172	0.70	6.5	—	—	M	18191028
185V000259	00 39 07.40	48 19 35.47	20.77	16.70	262	1.74	4.6	—	—	M	05780891
185V000260	00 39 05.60	48 19 20.89	21.08	—	634	1.87	2.5	—	—	u	—
185V000261	00 39 01.11	48 22 04.11	21.76	17.13	439	2.09	3.1	—	—	C	09201680
185V000262	00 38 59.26	48 19 39.42	20.45	17.50	188	1.13	5.5	—	—	S	10110908
185V000263	00 38 59.20	48 19 57.65	20.36	17.34	173	1.60	5.3	—	—	u	—
185V000264	00 38 58.08	48 19 49.24	20.91	16.70	146	0.76	2.0	—	—	u	10730960
185V000265	00 38 56.89	48 19 41.08	20.70	17.21	194	1.16	4.4	—	—	u	11360916
185V000266	00 38 55.78	48 19 18.83	20.55	16.35	291	1.50	4.9	—	—	u	—
185V000267	00 38 55.67	48 20 14.19	20.43	16.84	215	0.69	5.1	—	—	u	—
185V000268	00 39 06.88	48 18 11.59	19.55	17.39	212	1.00	6.4	—	—	u	—
185V000269	00 39 04.82	48 20 17.53	19.98	17.12	227	0.99	6.3	—	—	u	—
185V000270	00 39 03.86	48 21 55.50	19.56	17.06	216	0.47	3.2	—	—	u	—
185V000271	00 39 03.32	48 19 40.79	20.32	—	122	0.94	5.0	—	—	u	—
185V000272	00 39 02.78	48 20 29.63	19.73	16.50	149	0.53	5.4	—	—	u	—
185V000273	00 39 02.17	48 20 08.29	20.34	17.20	246	0.91	4.6	—	—	u	—
185V000274	00 39 02.14	48 22 11.45	20.17	16.85	226	1.53	6.6	—	—	u	—
185V000275	00 39 01.49	48 20 00.86	19.86	17.12	226	0.96	6.0	—	—	u	—
185V000276	00 39 01.05	48 19 59.55	20.42	16.30	163	0.76	4.9	—	—	u	—
185V000277	00 39 00.71	48 18 13.05	19.79	17.24	236	0.51	5.9	—	—	u	—
185V000278	00 39 00.61	48 20 15.23	20.49	17.31	253	1.54	2.9	—	—	u	—
185V000279	00 39 00.32	48 20 38.44	20.38	17.85	162	0.99	4.7	—	—	u	—

Table 13.4: continued.

ID	RAJ2000 h:m:s	DEJ2000 d:m:s	i [mag]	K_s [mag]	P_0 [d]	Δi [mag]	sig_0	P_1 [d]	sig_1	type	ID_{PaperI}
185V000280	00 38 59.76	48 18 46.22	19.83	17.38	192	0.70	5.7	—	—	u	—
185V000281	00 38 59.41	48 19 25.57	20.00	16.64	156	0.56	5.1	—	—	u	—
185V000282	00 38 58.96	48 18 57.15	19.85	18.00	162	0.59	5.2	—	—	u	—
185V000283	00 38 58.91	48 19 34.50	20.61	16.22	408	1.15	5.7	—	—	u	—
185V000284	00 38 57.20	48 19 09.35	19.67	17.57	167	0.57	5.6	—	—	u	—
185V000285	00 38 56.52	48 21 23.72	20.32	17.80	162	1.15	4.6	—	—	u	—
185V000286	00 38 55.80	48 20 57.65	19.78	16.89	258	0.90	6.4	—	—	u	—
185V000287	00 38 55.61	48 19 40.35	19.78	17.36	196	0.72	6.4	—	—	u	—
185V000288	00 38 54.64	48 20 50.72	19.75	16.83	236	0.56	5.1	—	—	u	—
185V000289	00 38 54.48	48 19 04.08	20.18	16.11	389	0.54	6.6	—	—	u	—
185V000290	00 38 54.30	48 20 42.92	19.99	16.21	371	0.96	5.6	—	—	u	—
185V000291	00 38 52.79	48 19 17.12	20.30	17.77	160	0.81	5.6	—	—	u	—
185V000292	00 38 52.72	48 19 21.51	19.92	17.65	176	0.72	5.5	—	—	u	—
185V000293	00 38 52.48	48 18 53.38	19.60	16.56	354	0.64	6.7	—	—	u	—
185V000294	00 38 52.35	48 17 14.19	19.57	—	205	0.91	4.0	—	—	u	—
185V000295	00 38 52.23	48 17 05.67	19.56	—	251	0.95	4.4	—	—	u	—
185V000296	00 38 50.70	48 20 23.70	21.07	16.68	252	2.27	5.6	—	—	u	—
185V000297	00 38 50.52	48 18 44.91	20.22	—	184	1.80	5.7	—	—	u	—
185V000298	00 38 49.13	48 20 44.39	20.28	16.86	271	1.80	6.3	—	—	u	—
185V000299	00 38 48.63	48 22 34.45	19.57	17.19	151	0.38	5.0	—	—	u	—
185V000300	00 38 43.38	48 19 21.84	19.70	17.43	189	0.68	5.6	—	—	u	—
185V000301	00 38 43.23	48 19 12.78	19.64	17.23	193	1.00	5.3	—	—	u	—
185V000302	00 38 59.61	48 19 50.13	20.12	16.87	124	0.36	4.1	—	—	u	—
185V000303	00 38 58.87	48 20 22.17	20.58	17.35	113	0.91	3.7	—	—	u	—
185V000304	00 38 58.44	48 20 12.75	20.88	16.90	182	1.48	4.1	—	—	u	—
185V000305	00 38 56.56	48 20 22.39	21.44	17.02	170	2.13	4.9	—	—	u	—
185V000306	00 38 53.27	48 20 08.36	19.75	16.37	416	0.63	6.1	—	—	u	—
185V000307	00 38 52.60	48 20 58.65	20.56	17.63	201	1.21	5.8	—	—	u	—

Table 13.4: continued.

ID	RAJ2000	DEJ2000	i	K_s	P_0	Δi	sig_0	P_1	sig_1	type	ID_{PaperI}
	h:m:s	d:m:s	[mag]	[mag]	[d]	[mag]		[d]			
185V000308	00 39 15.40	48 19 25.31	19.58	—	169	0.81	4.4	—	—	M	01530840
185V000309	00 39 15.30	48 20 16.03	19.45	17.28	175	0.56	6.0	—	—	S	01611110
185V000310	00 39 14.86	48 19 27.66	19.69	—	236	0.48	5.0	—	—	M	01820852
185V000311	00 39 11.83	48 21 37.69	20.06	—	56	0.51	5.6	—	—	S	03501543
185V000312	00 39 11.18	48 21 52.31	19.52	17.27	113	0.24	5.0	—	—	S	03851620
185V000313	00 39 08.95	48 21 18.59	21.69	15.93	519	1.78	5.0	—	—	u	—
185V000314	00 39 09.01	48 22 53.98	19.35	16.44	144	0.30	6.9	—	—	C	05041948
185V000315	00 39 08.57	48 17 39.76	20.43	—	220	0.84	7.7	—	—	u	—
185V000316	00 39 07.74	48 19 26.81	19.16	17.18	111	0.27	4.8	—	—	S	05600845
185V000317	00 39 07.39	48 20 27.02	19.16	16.66	171	0.26	4.4	—	—	C	05811165
185V000318	00 39 05.46	48 21 55.99	19.86	—	137	0.36	5.4	—	—	u	—
185V000319	00 39 04.98	48 20 51.17	19.85	17.12	102	0.43	5.3	—	—	M	07111293
185V000320	00 39 04.66	48 20 56.25	20.09	16.72	127	0.54	4.3	—	—	u	—
185V000321	00 39 04.50	48 20 30.15	19.66	—	164	0.27	3.7	—	—	M	07351181
185V000322	00 39 04.32	48 21 13.31	20.13	—	130	0.48	3.9	—	—	S	07471410
185V000323	00 39 03.93	48 19 46.72	20.18	17.45	239	0.72	7.1	—	—	u	—
185V000324	00 39 03.68	48 22 40.07	19.75	—	128	0.32	3.5	—	—	S	07851872
185V000325	00 39 03.36	48 20 26.12	20.09	17.10	197	0.52	4.0	—	—	M	07951159
185V000326	00 39 02.72	48 20 16.13	20.23	17.23	101	0.47	4.6	—	—	u	—
185V000327	00 39 01.72	48 19 14.40	20.13	16.84	139	0.70	3.3	—	—	M	08780776
185V000328	00 39 01.23	48 17 09.18	19.76	17.58	212	0.66	6.7	—	—	u	08980109
185V000329	00 39 01.47	48 21 48.87	19.65	—	168	0.42	3.9	—	—	S	09001599
185V000330	00 39 00.98	48 17 26.66	19.87	—	128	0.60	4.5	—	—	M	09120202
185V000331	00 39 00.77	48 19 23.14	19.96	17.09	235	0.52	4.8	—	—	M	09300822
185V000332	00 39 00.81	48 20 49.14	19.94	—	143	0.51	5.3	—	—	u	—
185V000333	00 39 00.66	48 19 39.05	19.84	16.79	113	0.35	4.2	—	—	u	—
185V000334	00 39 00.45	48 19 45.57	20.71	—	131	0.82	5.4	—	—	M	09480942
185V000335	00 38 59.83	48 18 27.74	19.68	—	160	0.43	5.5	—	—	M	09760527

Table 13.4: continued.

ID	RAJ2000 h:m:s	DEJ2000 d:m:s	i [mag]	K_s [mag]	P_0 [d]	Δi [mag]	sig_0	P_1 [d]	sig_1	type	ID_{PaperI}
185V000336	00 38 59.65	48 19 58.49	19.50	—	152	0.45	6.5	—	—	u	—
185V000337	00 38 58.49	48 17 57.21	19.76	17.25	196	0.35	3.8	—	—	M	10460363
185V000338	00 38 57.85	48 20 19.06	18.94	15.29	200	0.30	4.9	—	—	u	—
185V000339	00 38 57.72	48 19 52.26	19.71	16.90	99	0.18	3.5	—	—	M	10930976
185V000340	00 38 57.75	48 20 43.55	19.90	16.24	890	0.50	7.1	—	—	u	—
185V000341	00 38 57.18	48 18 47.20	20.28	17.09	188	0.61	4.0	—	—	u	—
185V000342	00 38 57.18	48 20 29.45	22.09	—	175	1.61	3.0	—	—	u	—
185V000343	00 38 57.05	48 23 12.68	20.36	16.65	229	1.47	3.9	—	—	u	—
185V000344	00 38 56.79	48 19 49.73	19.37	16.60	266	0.40	6.0	—	—	M	11420962
185V000345	00 38 56.71	48 19 52.85	19.08	16.19	189	0.26	3.3	—	—	u	—
185V000346	00 38 56.66	48 19 57.68	19.51	16.78	809	0.30	5.0	—	—	M	11491005
185V000347	00 38 56.59	48 19 23.10	19.97	17.35	102	0.44	4.7	—	—	u	—
185V000348	00 38 56.46	48 19 20.99	19.57	17.17	197	0.30	4.8	—	—	S	11580809
185V000349	00 38 56.42	48 21 44.64	20.16	—	154	0.36	3.2	—	—	S	11671575
185V000350	00 38 56.43	48 21 53.15	19.90	17.36	193	0.45	5.0	—	—	C	11671620
185V000351	00 38 56.34	48 20 07.43	20.12	16.24	270	0.97	6.6	—	—	u	—
185V000352	00 38 56.28	48 20 38.37	20.23	16.72	212	0.78	6.5	—	—	u	—
185V000353	00 38 56.14	48 19 25.17	19.21	16.08	195	0.27	6.4	—	—	C	11750831
185V000354	00 38 56.03	48 19 30.98	20.15	17.41	182	0.46	4.0	—	—	M	11810862
185V000355	00 38 55.94	48 20 38.78	19.14	16.36	159	0.25	4.4	—	—	C	11901224
185V000356	00 38 55.36	48 20 57.89	20.44	16.88	209	0.54	3.1	—	—	u	—
185V000357	00 38 54.96	48 20 26.88	19.58	17.17	110	0.32	4.6	—	—	M	12411160
185V000358	00 38 54.56	48 19 52.00	20.62	—	207	0.89	4.9	—	—	u	—
185V000359	00 38 54.42	48 22 48.90	19.65	18.78	105	0.15	4.1	—	—	S	12761917
185V000360	00 38 54.21	48 20 00.68	20.05	—	150	0.74	5.7	—	—	u	—
185V000361	00 38 54.10	48 20 57.57	20.21	—	170	0.53	5.2	—	—	u	—
185V000362	00 38 54.01	48 20 01.80	20.43	16.81	123	0.51	3.8	—	—	u	—
185V000363	00 38 53.86	48 19 13.71	20.03	—	87	0.33	4.0	—	—	u	—

Table 13.4: continued.

ID	RAJ2000 h:m:s	DEJ2000 d:m:s	i [mag]	K_s [mag]	P_0 [d]	Δi [mag]	sig_0	P_1 [d]	sig_1	type	ID_{PaperI}
185V000364	00 38 52.64	48 18 59.56	20.51	17.80	108	0.72	3.9	—	—	u	—
185V000365	00 38 52.67	48 20 52.47	21.53	—	218	1.70	4.6	—	—	u	—
185V000366	00 38 52.01	48 17 04.84	19.60	—	138	0.40	3.9	—	—	u	—
185V000367	00 38 52.10	48 19 35.18	19.61	17.46	188	0.26	6.5	—	—	u	—
185V000368	00 38 51.93	48 19 34.25	19.65	—	82	0.38	3.9	—	—	S	13990878
185V000369	00 38 51.55	48 17 12.81	19.54	—	163	0.32	5.1	—	—	u	14120124
185V000370	00 38 51.70	48 21 00.12	19.57	16.79	303	0.41	6.9	—	—	C	14151336
185V000371	00 38 48.89	48 21 58.67	19.92	16.98	108	0.41	3.6	—	—	M	15671647
185V000372	00 38 48.46	48 18 24.96	19.65	—	145	0.24	5.5	—	—	u	—
185V000373	00 38 48.27	48 19 16.59	20.53	—	98	0.74	6.1	—	—	M	15930783
185V000374	00 38 46.10	48 20 28.43	19.54	—	99	0.19	4.5	—	—	M	17111165
185V000375	00 38 45.60	48 17 07.01	20.11	—	178	0.46	2.5	—	—	u	17280090
185V000376	00 38 45.05	48 19 46.28	19.78	17.67	462	0.25	4.6	—	—	S	17640940
185V000377	00 38 41.45	48 18 15.15	19.91	—	103	0.44	5.2	—	—	S	19520452
185V000378	00 38 57.76	48 20 03.72	20.78	15.48	535	1.27	5.8	—	—	u	10911037
185V000379	00 38 52.32	48 19 25.86	20.91	16.75	90	0.86	1.5	—	—	u	—
185V000380	00 38 55.08	48 20 40.45	19.99	16.84	168	0.42	3.0	—	—	u	—
185V000381	00 38 49.06	48 21 22.88	19.55	—	137	0.29	3.6	—	—	M	15561457
185V000382	00 39 00.10	48 20 35.47	19.63	16.22	363	0.48	4.5	725	2.9	C	09691207
185V000383	00 39 04.47	48 18 12.81	19.10	15.78	450	1.73	6.1	899	1.1	u	—
185V000384	00 39 03.30	48 19 44.34	21.32	17.25	82	0.80	1.7	164	4.1	S	07960936
185V000385	00 39 00.01	48 19 26.39	19.43	16.84	121	0.34	2.5	243	5.1	C	09700839
185V000386	00 38 58.19	48 19 29.57	19.83	—	81	0.44	2.4	161	4.9	M	10670855
185V000387	00 38 56.96	48 20 15.41	19.53	17.16	198	0.50	1.1	397	3.9	u	11341099
185V000388	00 38 56.46	48 19 18.01	20.59	—	60	0.45	1.4	120	2.9	M	11580793
185V000389	00 38 56.42	48 19 44.63	20.11	16.96	118	0.60	2.2	236	5.3	u	—
185V000390	00 39 05.52	48 17 29.54	19.33	16.74	354	1.34	5.4	1204	4.6	M	06710219
185V000391	00 38 58.97	48 17 42.37	19.63	17.04	279	0.76	4.3	1067	3.9	C	10200285

Table 13.4: continued.

ID	RAJ2000 h:m:s	DEJ2000 d:m:s	i [mag]	K_s [mag]	P_0 [d]	Δi [mag]	sig_0	P_1 [d]	sig_1	type	ID_{PaperI}
185V000392	00 38 51.50	48 20 05.26	19.08	16.00	347	0.41	4.3	440	3.2	C	14231043
185V000393	00 39 00.18	48 19 36.15	19.56	16.89	329	1.43	6.8	985	3.1	M	09610891
185V000394	00 38 51.45	48 21 15.53	19.63	—	134	0.66	4.2	437	4.7	M	14291418
185V000395	00 38 48.07	48 21 21.79	19.78	17.60	213	0.88	4.4	800	3.8	C	16091450
185V000396	00 38 44.76	48 21 10.92	20.57	17.02	234	1.69	5.6	472	1.0	C	17841392
185V000397	00 39 02.92	48 19 33.16	20.56	—	153	1.48	3.4	414	1.0	S	08160876
185V000398	00 39 04.35	48 21 00.38	19.94	16.05	427	1.07	3.0	1088	0.6	u	—
185V000399	00 39 04.06	48 20 43.22	21.59	17.09	406	1.79	4.2	829	1.3	u	—
185V000400	00 38 51.26	48 19 49.71	20.76	16.80	372	1.05	4.0	664	1.5	u	—
185V000401	00 38 43.97	48 17 05.80	18.17	—	185	0.59	3.1	873	2.7	u	—
185V000402	00 38 43.78	48 17 56.79	19.72	17.42	103	0.69	1.0	205	5.2	u	—
185V000403	00 39 00.68	48 20 13.99	19.74	16.10	374	0.74	5.9	574	2.2	u	—
185V000404	00 39 00.53	48 19 34.64	20.17	15.89	367	0.86	6.5	840	3.1	u	—
185V000405	00 38 55.52	48 20 26.87	18.98	16.29	116	0.29	2.6	325	4.1	u	—
185V000406	00 38 52.07	48 22 30.33	20.53	16.77	193	1.02	3.2	234	1.8	u	—
185V000407	00 39 12.39	48 20 22.12	19.66	—	110	0.43	4.3	131	3.6	u	—
185V000408	00 39 10.98	48 21 16.09	20.10	—	93	0.37	3.4	963	3.3	M	03941428
185V000409	00 39 03.42	48 19 13.30	20.23	16.83	112	0.60	2.3	127	4.7	M	07880771
185V000410	00 38 57.77	48 19 43.34	19.57	18.43	98	0.19	3.2	553	4.0	S	10900929
185V000411	00 38 56.85	48 19 49.68	20.05	16.23	166	0.48	3.5	195	4.9	u	—
185V000412	00 38 57.06	48 21 18.17	19.06	15.95	197	0.28	4.5	489	3.0	u	11321434
185V000413	00 38 55.34	48 19 27.73	19.59	16.10	132	0.27	5.5	293	4.1	M	12180845
185V000414	00 38 54.19	48 19 59.79	19.63	—	119	0.37	4.2	749	4.6	u	—
185V000415	00 38 53.77	48 19 14.80	19.46	16.46	171	0.28	3.2	236	3.8	u	—
185V000416	00 38 52.64	48 21 16.71	19.88	—	122	0.36	3.7	416	4.3	S	13661425
185V000417	00 38 52.37	48 19 13.63	20.51	16.64	122	0.52	2.6	865	4.5	u	—
185V000418	00 38 52.03	48 21 31.35	19.79	—	90	0.33	3.2	397	6.5	S	14001503
185V000419	00 38 51.41	48 18 37.93	19.83	17.17	104	0.35	3.0	911	4.7	M	14240578

Table 13.4: continued.

ID	RAJ2000 h:m:s	DEJ2000 d:m:s	i [mag]	K_s [mag]	P_0 [d]	Δi [mag]	sig_0	P_1 [d]	sig_1	type	ID_{PaperI}
185V000420	00 39 13.96	48 18 20.15	20.24	—	—	0.43	—	—	—	S	02260493
185V000421	00 39 13.33	48 20 23.69	19.03	16.96	—	0.34	—	—	—	S	02661150
185V000422	00 38 41.24	48 20 24.20	19.72	—	—	0.47	—	—	—	S	19691141
185V000423	00 39 10.02	48 22 25.13	20.48	—	—	0.64	—	—	—	u	04481795
185V000424	00 39 04.25	48 21 04.40	19.72	—	—	0.52	—	—	—	S	07501363
185V000425	00 39 02.12	48 20 29.88	19.91	17.29	—	0.35	—	—	—	M	08611178
185V000426	00 39 00.38	48 20 05.65	19.44	16.54	—	0.23	—	—	—	C	09521049
185V000427	00 38 59.83	48 21 11.05	19.64	17.30	—	0.35	—	—	—	M	09851397
185V000428	00 38 59.66	48 20 25.67	20.99	16.75	—	0.87	—	—	—	C	09921155
185V000429	00 38 58.56	48 21 40.59	19.94	17.83	—	0.28	—	—	—	M	10541554
185V000430	00 38 57.37	48 19 59.50	20.24	17.30	—	0.92	—	—	—	S	11111015
185V000431	00 38 55.17	48 20 54.15	19.10	—	—	0.35	—	—	—	S	12311305
185V000432	00 38 54.94	48 20 41.41	19.76	16.77	—	0.38	—	—	—	u	—
185V000433	00 38 54.79	48 21 19.01	19.92	17.38	—	0.74	—	—	—	M	12521438
185V000434	00 38 53.24	48 18 51.51	19.49	17.09	—	0.24	—	—	—	C	13270651
185V000435	00 38 49.41	48 19 40.18	19.52	17.49	—	0.31	—	—	—	M	15330909
185V000436	00 38 49.20	48 20 06.23	19.55	17.15	—	0.41	—	—	—	M	15451048
185V000437	00 38 45.95	48 17 47.61	19.75	—	—	0.32	—	—	—	M	17120307
185V000438	00 38 56.84	48 18 50.58	21.32	16.80	—	1.45	—	—	—	C	11360647
185V000439	00 38 55.32	48 20 01.70	20.11	16.66	—	0.66	—	—	—	M	12211026
185V000440	00 38 54.45	48 20 49.69	20.95	—	—	1.24	—	—	—	S	12691281
185V000441	00 39 06.45	48 20 52.64	19.52	16.78	—	0.46	—	—	—	u	—
185V000442	00 39 01.54	48 21 10.56	19.80	16.83	—	0.63	—	—	—	u	—
185V000443	00 38 57.97	48 20 58.10	19.64	17.38	—	0.43	—	—	—	u	—
185V000444	00 38 56.04	48 18 04.53	19.76	17.14	—	0.44	—	—	—	u	—
185V000445	00 38 55.83	48 19 15.82	20.50	17.01	—	0.75	—	—	—	u	—
185V000446	00 38 54.99	48 19 00.60	19.90	16.70	—	0.48	—	—	—	u	—
185V000447	00 38 51.60	48 19 06.70	20.01	16.62	—	0.60	—	—	—	u	—

Table 13.4: continued.

ID	RAJ2000 h:m:s	DEJ2000 d:m:s	i [mag]	K_s [mag]	P_0 [d]	Δi [mag]	sig_0	P_1 [d]	sig_1	type	ID_{PaperI}
185V000448	00 38 51.43	48 20 17.92	20.33	16.88	—	0.75	—	—	—	u	—
185V000449	00 38 59.82	48 20 36.92	20.23	—	—	0.50	—	—	—	u	—
185V000450	00 38 57.74	48 19 54.99	19.61	17.26	—	0.41	—	—	—	u	—
185V000451	00 38 57.65	48 20 25.18	19.69	17.51	—	0.48	—	—	—	u	—
185V000452	00 39 15.30	48 21 24.61	20.11	—	—	0.37	—	—	—	S	01651474
185V000453	00 39 13.68	48 21 23.58	20.44	16.90	—	1.05	—	—	—	C	02511468
185V000454	00 39 12.29	48 22 22.82	19.58	—	—	0.33	—	—	—	S	03281783
185V000455	00 39 10.59	48 21 57.83	19.74	—	—	0.32	—	—	—	S	04171650
185V000456	00 39 10.41	48 19 31.99	19.80	—	—	0.49	—	—	—	M	04180873
185V000457	00 39 07.73	48 19 57.15	20.26	—	—	0.38	—	—	—	M	05621006
185V000458	00 39 07.45	48 21 29.86	19.65	—	—	0.39	—	—	—	M	05821500
185V000459	00 39 06.89	48 18 24.18	20.83	—	—	0.69	—	—	—	u	06010511
185V000460	00 39 06.88	48 18 52.43	18.61	15.44	—	1.13	—	—	—	u	—
185V000461	00 39 06.88	48 22 37.38	19.50	17.23	—	0.24	—	—	—	M	06151859
185V000462	00 39 06.71	48 20 44.67	19.39	16.65	—	0.32	—	—	—	u	—
185V000463	00 39 04.62	48 20 10.86	20.00	17.09	—	0.40	—	—	—	u	—
185V000464	00 39 03.37	48 20 47.83	20.40	—	—	0.39	—	—	—	S	07961274
185V000465	00 39 03.11	48 19 03.15	20.11	17.43	—	0.47	—	—	—	M	08040717
185V000466	00 39 03.08	48 22 04.28	19.76	17.28	—	0.28	—	—	—	M	08151681
185V000467	00 39 02.87	48 20 42.50	20.55	17.30	—	0.52	—	—	—	M	08221246
185V000468	00 39 02.81	48 20 14.76	19.16	16.99	—	0.20	—	—	—	M	08241098
185V000469	00 39 02.69	48 18 54.96	21.99	—	—	1.36	—	—	—	u	—
185V000470	00 39 02.50	48 21 10.82	19.81	—	—	0.26	—	—	—	M	08431397
185V000471	00 39 02.15	48 19 09.34	19.83	16.71	—	0.42	—	—	—	S	08560749
185V000472	00 39 01.98	48 20 08.93	19.03	16.80	—	0.21	—	—	—	u	—
185V000473	00 39 01.80	48 19 44.05	21.32	16.95	—	1.10	—	—	—	u	—
185V000474	00 39 01.77	48 20 16.48	21.36	—	—	0.85	—	—	—	u	—
185V000475	00 39 01.72	48 22 55.08	19.69	17.78	—	0.28	—	—	—	S	08901952

Table 13.4: continued.

ID	RAJ2000 h:m:s	DEJ2000 d:m:s	i [mag]	K_s [mag]	P_0 [d]	Δi [mag]	sig_0	P_1 [d]	sig_1	type	ID_{PaperI}
185V000476	00 39 01.36	48 20 22.39	20.39	17.18	—	0.53	—	—	—	u	—
185V000477	00 39 01.19	48 20 47.22	20.59	—	—	0.55	—	—	—	M	09111270
185V000478	00 39 01.14	48 21 30.87	19.44	—	—	0.30	—	—	—	S	09161503
185V000479	00 39 00.74	48 18 26.45	21.75	—	—	0.98	—	—	—	u	09280520
185V000480	00 39 00.80	48 20 51.49	20.64	—	—	0.46	—	—	—	M	09321293
185V000481	00 39 00.10	48 17 27.80	19.86	17.33	—	0.59	—	—	—	M	09590207
185V000482	00 38 59.09	48 20 50.51	19.75	17.37	—	0.44	—	—	—	u	—
185V000483	00 38 58.86	48 20 13.25	18.70	15.50	—	0.23	—	—	—	u	—
185V000484	00 38 58.76	48 22 22.87	19.17	16.41	—	0.26	—	—	—	C	10451779
185V000485	00 38 58.47	48 20 18.18	20.44	16.93	—	1.06	—	—	—	u	—
185V000486	00 38 58.13	48 20 19.74	19.91	16.38	—	0.68	—	—	—	M	10721123
185V000487	00 38 57.95	48 20 14.51	19.46	16.01	—	0.51	—	—	—	u	—
185V000488	00 38 57.77	48 20 08.43	19.77	16.47	—	0.48	—	—	—	u	—
185V000489	00 38 57.72	48 20 34.95	20.15	—	—	0.46	—	—	—	u	—
185V000490	00 38 57.60	48 20 21.92	20.35	16.01	—	0.84	—	—	—	u	—
185V000491	00 38 57.11	48 17 19.14	19.91	17.14	—	0.47	—	—	—	u	11180160
185V000492	00 38 57.21	48 20 26.79	19.26	16.21	—	0.31	—	—	—	u	—
185V000493	00 38 57.11	48 19 24.40	20.77	17.09	—	0.64	—	—	—	u	11240828
185V000494	00 38 57.02	48 21 44.51	20.81	—	—	0.52	—	—	—	S	11351574
185V000495	00 38 56.81	48 19 53.50	21.09	16.85	—	1.32	—	—	—	u	—
185V000496	00 38 56.43	48 19 50.15	19.46	16.11	—	0.28	—	—	—	C	11610965
185V000497	00 38 56.41	48 20 55.93	19.73	—	—	0.51	—	—	—	M	11651315
185V000498	00 38 56.13	48 19 53.30	21.46	16.76	—	1.00	—	—	—	u	11770981
185V000499	00 38 55.91	48 17 45.91	21.61	—	—	1.34	—	—	—	u	—
185V000500	00 38 55.82	48 19 43.96	19.60	16.72	—	0.36	—	—	—	u	11930931
185V000501	00 38 55.68	48 20 21.70	19.76	16.74	—	0.36	—	—	—	u	—
185V000502	00 38 55.22	48 19 39.14	19.76	16.98	—	0.43	—	—	—	C	12240905
185V000503	00 38 54.95	48 20 41.27	19.74	16.76	—	0.37	—	—	—	u	—

Table 13.4: continued.

ID	RAJ2000 h:m:s	DEJ2000 d:m:s	i [mag]	K_s [mag]	P_0 [d]	Δi [mag]	sig_0	P_1 [d]	sig_1	type	ID_{PaperI}
185V000504	00 38 54.50	48 19 33.95	19.44	16.41	—	0.42	—	—	—	C	12620877
185V000505	00 38 54.37	48 22 32.96	20.75	17.74	—	0.68	—	—	—	S	12781832
185V000506	00 38 54.22	48 20 18.55	20.71	16.99	—	1.11	—	—	—	u	—
185V000507	00 38 52.70	48 21 22.57	19.98	16.38	—	0.40	—	—	—	u	13631456
185V000508	00 38 52.56	48 19 38.45	19.63	16.67	—	0.29	—	—	—	u	—
185V000509	00 38 47.95	48 22 24.99	21.63	—	—	0.91	—	—	—	u	—
185V000510	00 38 47.26	48 18 52.42	19.59	—	—	0.35	—	—	—	S	16450653
185V000511	00 38 46.32	48 18 54.72	22.33	—	—	1.49	—	—	—	M	16950665
185V000512	00 38 45.09	48 18 50.49	19.79	—	—	0.31	—	—	—	M	17600642
185V000513	00 38 45.18	48 20 43.02	20.36	16.86	—	0.37	—	—	—	S	17601243

13.3 Near-infrared data

K_s-band images taken with the NOTCam suffer from distortion that severely increases towards the edge of the frame. Thus, the frames had to be corrected for this effect before carrying out the standard image reduction steps. Gålfalk (2005) constructed a model of the NOTCam WF camera distortion based on his observations of B335. This NOTCam-model[4] was implemented in a software provided by Gålfalk (2005, written in IDL, which performs additional corrections), which was used for distortion correction of all K_s-band images. Subsequently, the usual reduction steps of near-IR imaging were applied to the dithered K_s-band images. All frames belonging to one quadrant were aligned and merged to one image to achieve a higher signal to noise ratio. PSF fitting photometry was carried out using the DAOPHOT/ALLSTAR photometry package (Stetson & Harris 1998). The photometric zero-points to calibrate K_s were derived using constant stars in each quadrant of the target galaxy, which were also found in the 2MASS Point Source Catalogue (Cutri et al. 2003). K_s-magnitudes of the detected variables in both galaxies are listed in the fifth column of Table 13.3 and 13.4, respectively, which are available online only. The corresponding mean

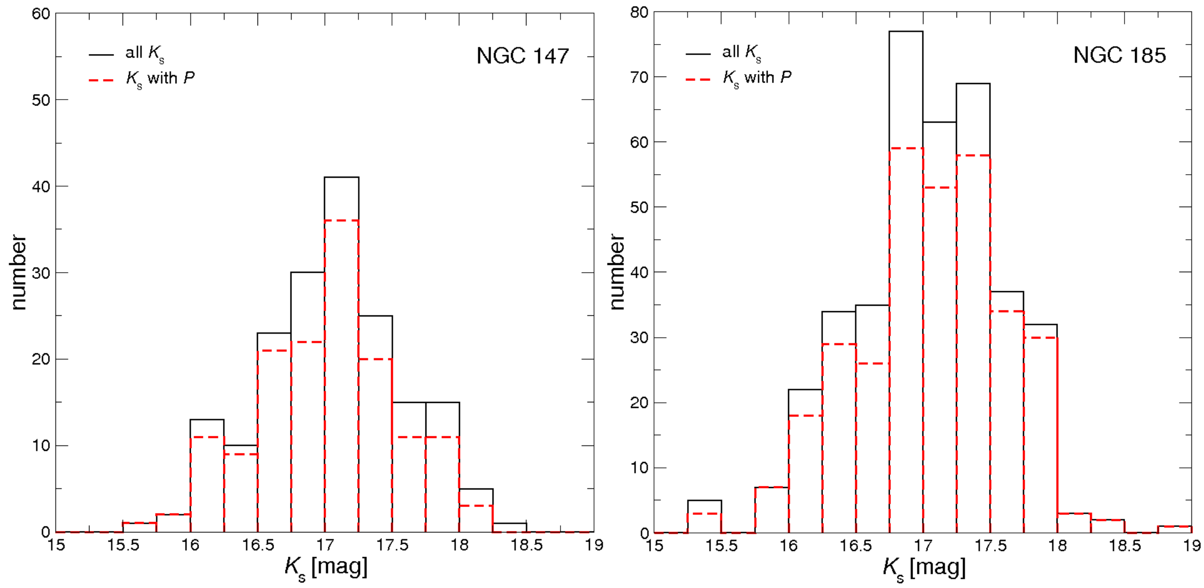

Figure 13.3: K_s-luminosity functions of objects in NGC 147 and NGC 185. The black line shows the distribution for all detected LPVs with K_s-magnitudes available (182 in NGC 147 and 387 in NGC 185). The red dashed line represents LPVs for which it was in addition possible to determine a period (147 in NGC 147 and 323 in NGC 185) as described in Sect. 13.2.

photometric uncertainties after the calibration are listed in Table 13.2 for different bins of magnitude within the range $16 < K_s < 19$. In Fig. 13.3 the luminosity function in K_s of stars

[4] http://www.astro.su.se/~magnusg/NOTCam_dist/

detected in NGC 147 and NGC 185 is shown as a black continuous line. The red dashed line represents the distribution of LPVs for which we were able to assign a period as well. With the instrument setting mentioned above, the photometry in K_s for both galaxies is probably complete down to ≈17 mag. At a mean K-band luminosity of 17 mag, the typical photometric errors for NGC 147 and NGC 185 are 0.15 mag and 0.16 mag, respectively.

13.4 Cross-correlation with photometry from literature

In Paper I, single epoch Vi photometry was discussed as part of a photometric survey of Local Group galaxies. Furthermore, narrow-band filters (wing-type) were used to derive information on the probable spectral types of the bright red giant stars in these galaxies. To discuss LPVs of NCG 147 and NGC 185 in more detail, a cross-correlation with the results obtained in Paper I was performed using the DENIS software 'Cross Color' written by E. Copet. This allows us to distinguish C-rich LPVs from other detected variables in our sample and to study their distribution in consecutive diagrams. For approximately 75 % of the identified variables we could assign counterparts in Paper I. The reason for the incompleteness was threefold. First, some stars were obviously at light minimum and, thus, too weak at the epoch of the observations of Paper I. Second, we had to exclude all variables where the cross-correlation was ambiguous because of crowding. Third, a few stars visible on the frames studied in Paper I had photometric errors that were too large to be included in the final list there.

14 Results & Discussion

14.1 Variable stars

In Table 14.1 we list the number of objects in each of the two galaxies for which certain sets of data are available. We thereby describe the size of several sub-samples grouped according to the information available. For the 163 variables in NGC 147 and the 381 objects in

Table 14.1: Summary of detected variables in NGC 147 (upper table) and NGC 185 (lower table), grouped according to the information available for different sub-samples (left column).

LPVs	×	×	×	×	×	×	×
Period		×			×	×	×
V, i			×			×	×
TiO, CN						×	×
K_S				×	×		×
NGC 147 objects	213	168	163	182	147	122	113

LPVs	×	×	×	×	×	×	×
Period		×			×	×	×
V, i			×			×	×
TiO, CN						×	×
K_S				×	×		×
NGC 185 objects	513	419	381	387	323	298	229

NGC 185 where we have broad-band photometry from Nowotny et al. (2003), the locations in the CMDs are shown in Fig. 14.1 together with the full sample of Paper I. The LPVs are superimposed as red crosses and those classified as C-rich stars (according to Paper I) are drawn as black circles. Evidently, most of the identified LPVs are located in the upper region of the giant branch where AGB stars, and in particular classical carbon-rich stars, are expected. Approximately two thirds of the variable red giant stars in both galaxies clearly show mono-periodic light variations. Two periods could be assigned to 20 variables of NGC 147, and for 45 LPVs of this system no significant period was found. In NGC 185 we find 38 LPVs exhibiting two periods and 94 LPVs for which no period could be detected.

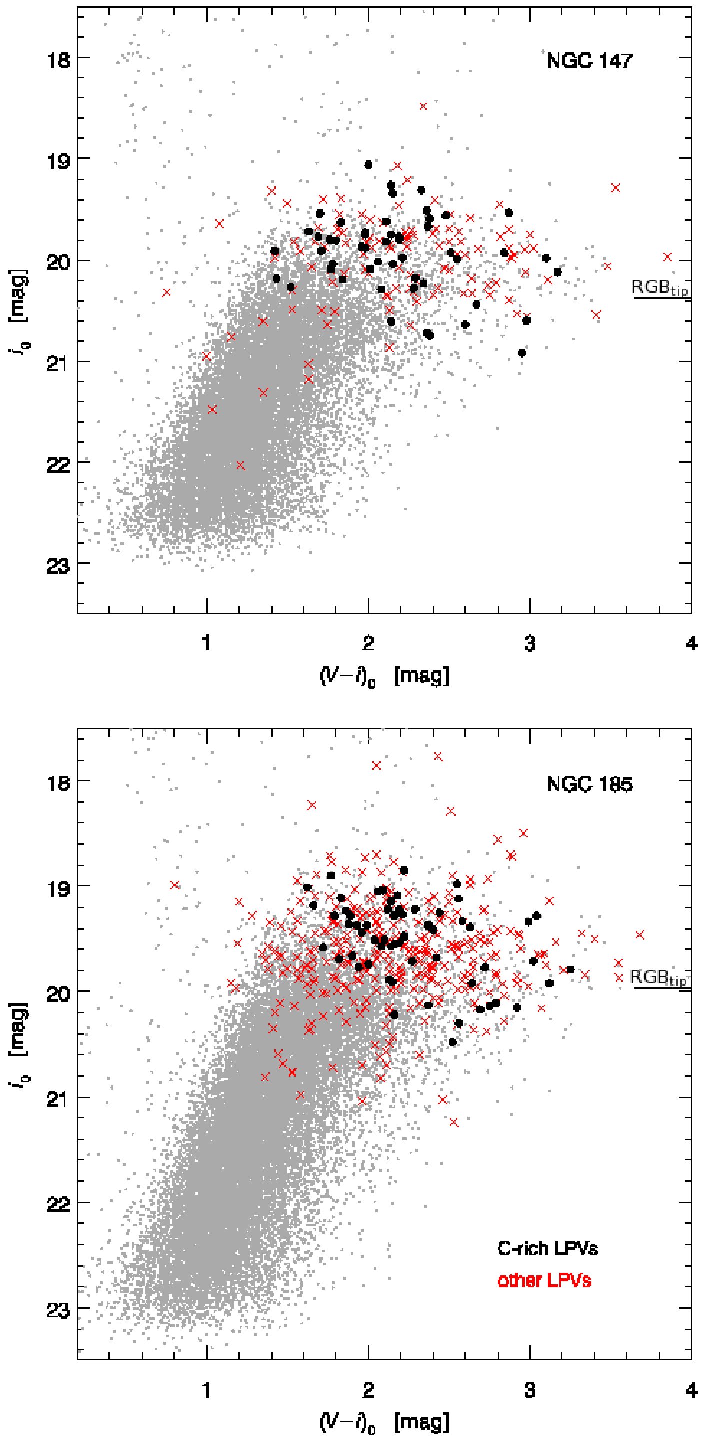

Figure 14.1: Color magnitude diagrams of stars in NGC 147 (upper panel) and NGC 185 (lower panel) using data from Paper I (grey dots). Overplotted are identified LPVs of the present study (see legend). The lines on the right side of the diagram mark the tip of the RGB of NGC 147 (I=20.36 mag) and NGC 185 (I=19.96 mag), respectively and were taken from Paper I.

The light curves of LPVs without a significant period show a wide variety of shapes. A part of them definitely shows very long variations that exceed the length of our time series. On the other hand, we also have a short period limit because of the sampling interval of our observations, which amounts to approximately 90 days. We also found objects with irregular light variations, sometimes alternating with phases of comparably constant brightnesses. A selection of different LPV light curves detected in both galaxies is presented in Fig. 13.2. Mono-periodic cases can be found in the panels of the upper two rows. Examples of LPVs exhibiting two significant periods are plotted in the following two rows, which show a beating phenomenon in the second panel of the fourth row. In the last row of Fig. 13.2, two cases out of the ≈20% of our sample stars are given for which no significant period could be determined from the observations. However, taking into account their $(V-i)$, σ-amplitudes and the time scales of their light variations, they can still clearly be classified as LPVs.

Using the narrow-band photometry from Paper I, we can assign a probable atmospheric chemistry to most of the LPVs in our sample, and study the variability characteristics in relation to these defined subgroups. Of special interest are carbon stars, which we assume to be intrinsic post-third-dredge-up objects. Table 14.2 groups the identified variable stars according to the designated chemistry type. To search for possible correlations between the location of LPVs within the galaxy and their chemistry, we chose one of the CCD images from the i-band time series and indicated the detected variables as red circles and C-rich LPVs as blue circles (see Fig. 13.1).

Table 14.2: LPVs identified in the two target galaxies grouped according to their atmospheric chemistry as derived from the narrow-band photometry of Paper I.

	NGC 147	NGC 185
C	51	61
M/S	98	288
unclass.	64	164
Σ	213	513

The radial distribution for identified AGB stars in NGC 147 and NGC 185 has been discussed in Paper I. The authors find similar distributions for all AGB stars and for only C-rich AGB stars. If the sample is reduced to detected LPVs in those galaxies, the trend in radial distribution for C-rich LPVs is similar as that for the full sample of LPVs. The number ratio of carbon-rich over oxygen-rich LPVs amounts to 0.52 for NGC 147 and 0.21 for NGC 185, respectively. These values fall between the corresponding ratios for the whole population and the ratios when limiting the O-rich sample to spectral types M5 and later, as presented in Paper I. Thereby, our sample selected on variability provides a good representation of the AGB population with which the LPV class is typically associated. If we look at the histograms in Fig. 14.2, we notice that the amplitude distributions of the O-rich objects is dominated by small-amplitude variables. Indeed, the histograms suggest that the peak at 0.35 mag is not real, but that we are missing stars with the shortest amplitudes owing to the limited sampling rate of our monitoring. In contrast, C-rich stars exhibit a much flatter distribution in

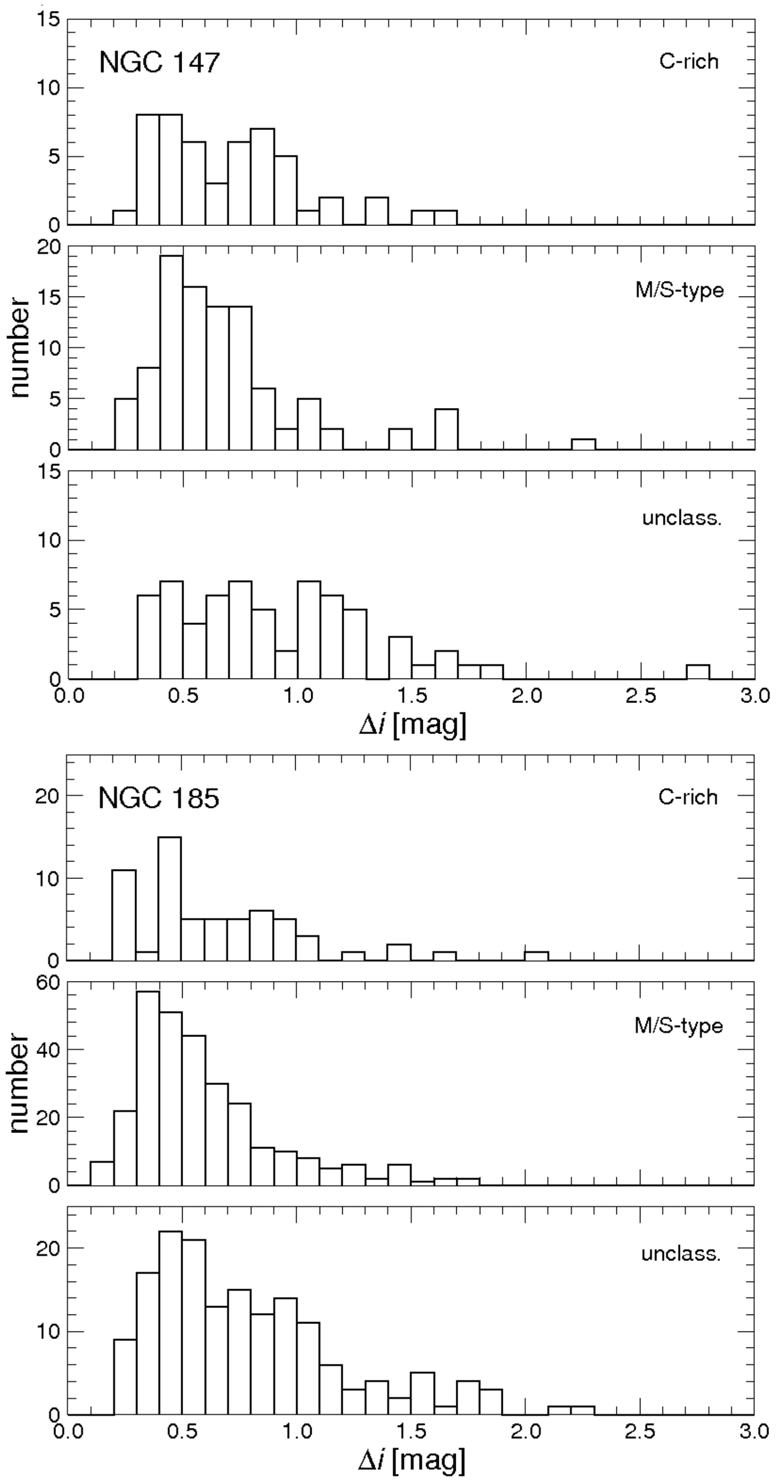

Figure 14.2: Histogram of σ-amplitudes Δi of LPVs with different surface chemistry in NGC 147 and NGC 185. The first panel shows the distribution of C-rich, the second panel displays O-rich LPVs and the last panel shows LPVs for which no chemical information was available (mainly due to missing narrow-band photometry).

these plots. For the sake of completeness, the distribution of LPVs without narrow-band photometry is given in the last panels of Fig. 14.2 for each of the galaxies.

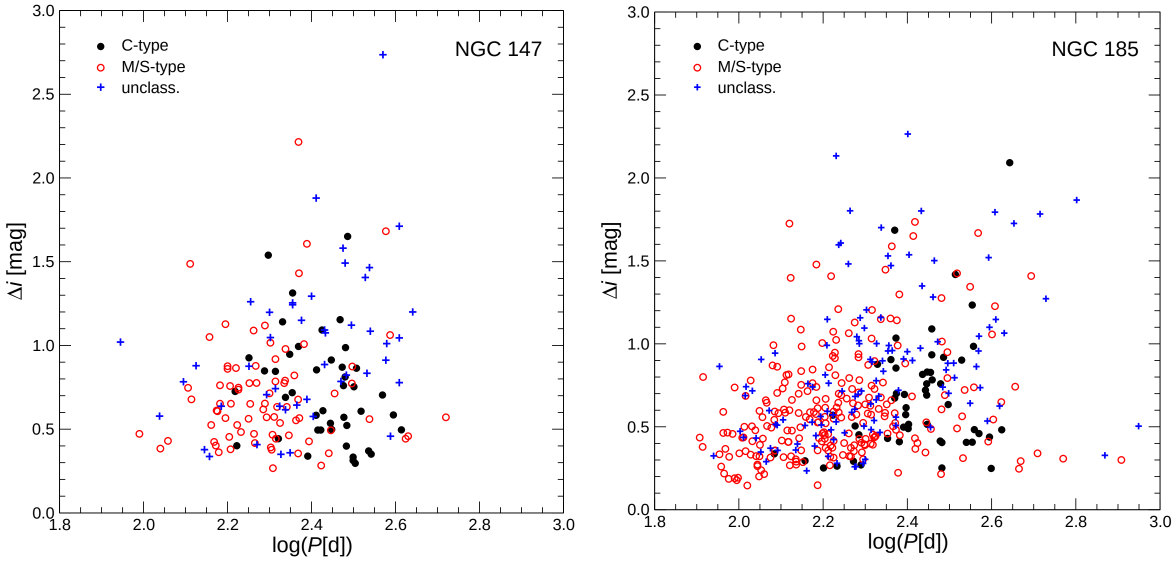

Figure 14.3: Photometric amplitudes Δi versus periods for LPVs identified in NGC 147 (upper panel) and NGC 185 (lower panel). C-rich objects are indicated by black filled circles, while M/S-type stars are plotted with red open circles, and unclassified LPVs are drawn as blue crosses.

The period distributions of the LPVs in the two galaxies can be seen in the Δi vs. $\log P$ diagrams in Fig. 14.3. Here, we plotted only the first significant period of all detected LPVs. The range of periods covered by the variables is similar in both systems ($\approx$ 90–600$^{\mathrm{d}}$) and a weak tendency of larger amplitudes with increasing period may be visible. Considerably more LPVs with shorter periods were found in NGC 185. In this galaxy, we also found a small group of stars with very long periods and small amplitudes. These are likely candidates for LSPs, but no other significant periodicities were found from our times series. Splitting up the stars according to their chemistry reveals a concentration of C-rich targets around $\log P = 2.5$, while the O-rich stars are found predominantly at shorter periods. This behaviour is expected from theory.

14.2 Period-luminosity relations of NGC 147 and NGC 185

To construct PLDs for both target systems, NGC 147 and NGC 185, the datasets of the i-time series and the K_s-band photometry were combined. This resulted in 182 LPVs with K_s-magnitudes and detected periods in NGC 147 and 387 LPVs in NGC 185, respectively, which could be used for the construction of the PLDs. The resulting K_s-$\log P$ diagrams for both galaxies are shown in Fig. 14.4. Different symbols denote the various classes of

LPVs, namely C-rich, O-rich, and unclassified variables according to the narrow-band photometry adopted from Paper I. Furthermore, the amplitude was used to group the variables into four sub-samples indicated by the symbol sizes in Fig. 14.4. Obviously, most LPVs in both galaxies seem to form a distinct sequence at the very same location in the PLDs as the sequence of fundamental mode pulsators (labeled sequence C) found by various authors for the Magellanic Clouds. For illustration purposes, we overplotted the relations of Ita et al. (2004). To shift their relations according to the difference in distance between the Magellanic Clouds and our galaxies, we adopted the distance moduli determined via the brightness of HB stars for our target systems by Butler et al. (2005). They derived distance moduli of $(m-M)_0 = 24.38\pm0.01$ mag and 24.09 ± 0.06 mag for NGC 147 and NGC 185, respectively. For the LMC we adopted the distance modulus obtained by Pietrzyńsky et al. (2009) of $(m-M)_0 = 18.50\pm0.06$ mag. With respect to the atmospheric chemistry, we find O-rich stars along the whole sequence (with a slight thinning in number towards the top), while C-rich stars mainly occupy the upper part of the sequence. This agrees with findings of other studies (e.g., Wood 2000 or Ita et al. 2004). After applying a 3.0 σ-clipping to exclude stars that are considered not to belong to sequence C, a least-squares fitting was performed to obtain PLRs for this sample of stars. The linear regression ($m_K = a \log P + b$); black dashed lines in Fig. 14.4) of this selection resulted in a slope a of –3.55 for NGC 147 and –3.47 for NGC 185. For the intercepts b of each relation we obtained 25.46 mag and 25.22 for NGC 147 and NGC 185, respectively.

Table 14.3: Comparison of our P-L relations with literature values for different stellar systems. All relations were shifted to an absolute scale M_K using the distance moduli given in the text.

	$M_{K_s} = a \log P + b$					
	a	σ	b	σ	$(m–M)$	Refs.
Galactic	–3.56	0.17	1.14	0.42		1
LMC	–3.52	0.03	1.04	0.08	18.50	2
	–3.34	0.02	0.40	0.05	18.50	3
	–3.57	0.16	1.20	0.39	18.50	4
Cen A	–3.37	0.11	0.80	0.29	27.87	5
NGC 147 all	–3.55	0.15	1.08	0.36	24.38	6
NGC 147 O	–3.81	0.25	1.68	0.58	24.38	6
NGC 185 all	–3.47	0.11	1.13	0.27	24.09	6
NGC 147 O	–3.72	0.16	1.68	0.38	24.09	6

(1) Groenewegen & Whitelock (1996); (2) Ita et al. (2004); (3) Riebel et al. (2010); (4) Feast et al. (1989); (5) Rejkuba (2004); (6) this work.

In Table 14.3 we contrast PLRs derived by different studies with those found here. This comparison of results for different stellar systems is of interest for studying the aspect of the universality of the PLRs of Sequence C stars, which may then serve as an additional tool to measure distances in extragalactic systems. Owing to the limited number of carbon

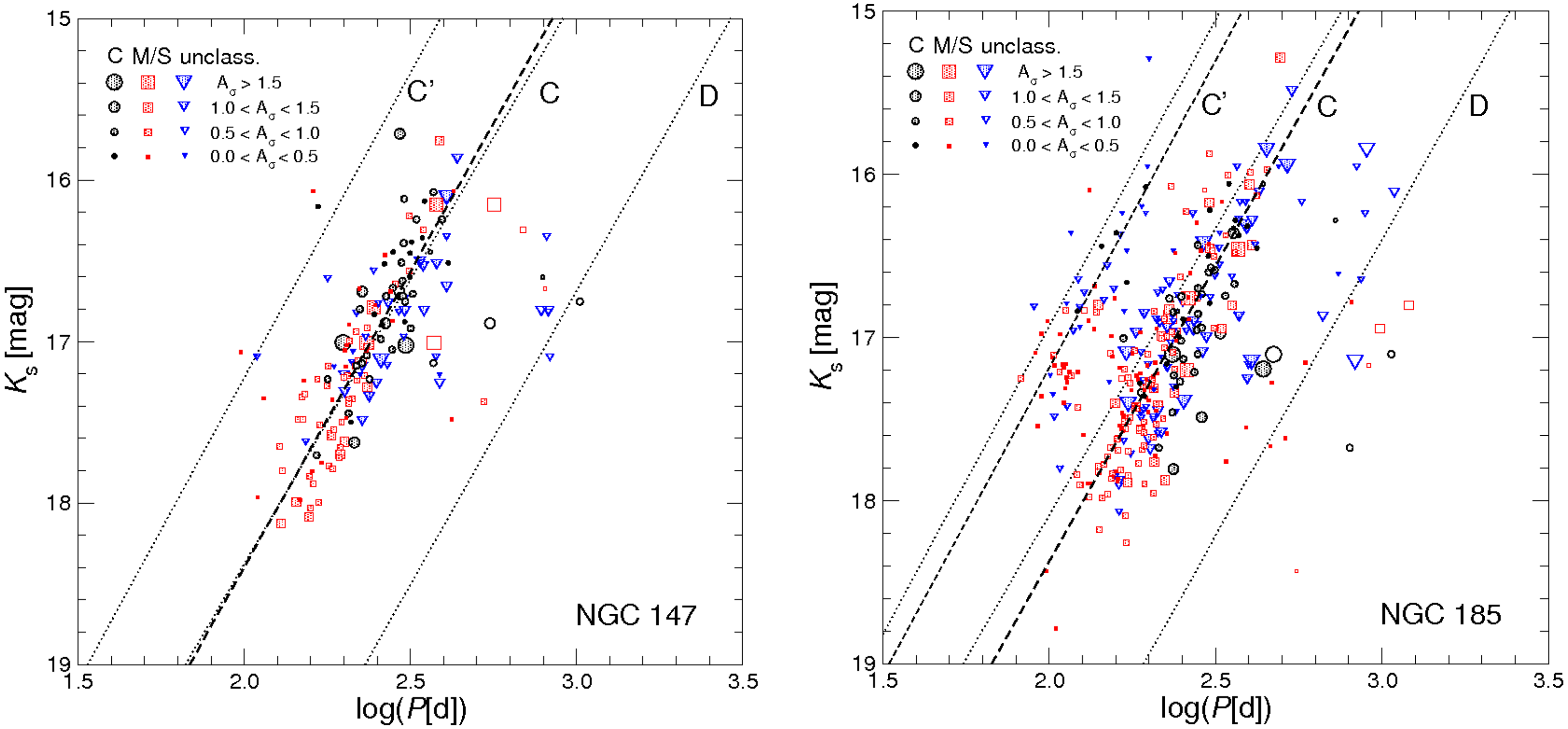

Figure 14.4: Period-K_S-diagram of NGC 147. C-type LPVs are plotted as black circles, M/S-type LPVs as red squares and unclassified variable red giant stars as blue triangles. The sizes of the plot symbols are scaled corresponding to the photometric amplitudes A_σ (see legend). For LPVs with two detected periods, open symbols indicate the second, longer period of both. The black dotted lines (C′, C, D) mark the PLRs found for the LMC by Ita et al. (2004). They were adopted and shifted according to the distance moduli differences between the LMC and our galaxies (see text). The black thick dashed line shows the PLRs derived by using the LPVs identified in this work. The black thin dashed line in the lower panel is plotted for demonstration purpose only (see text).

stars in our samples, we did not analyse C-rich and O-rich stars separately. However, for comparison reasons we calculated PLRs for our samples with and without C-rich LPVs. The small differences of the values demonstrate that the results are robust against slight changes of the sample selection. For additional calculations we only consider the results of the complete 3.0 σ-clipping sample. The slopes a found for NGC 147 and NGC 185 are close to those given for the combined samples in other stellar systems.

In the right panel of Fig. 14.4 an obvious offset between the shifted LMC-PLRs and those derived for NGC 185 can be seen. The numbers in Table 14.3 suggest that this shift amounts to approximately 0.2–0.4 mag (depending on sample selection and regression method). A mild difference in the zero-point b is expected owing to the difference in metallicity (Wood 1990). However, for the lower metallicity of NGC 185 relative to the LMC, a star should be brighter at a given period, making the discrepancy even larger. A simple but not necessarily final explanation for this difference would be an error in the distance modulus of NGC 185. When attempting to bring our observations in line with the LMC relations of Ita et al. (2004), a distance modulus of about 24.3 mag (more precisely 24.34 ±0.22 according to our linear regression of the 3.0σ-sample) seems to be more appropriate for this galaxy. This value is obtained by subtracting the resulting K_s-magnitudes derived from the relation of Ita et al. (2004) and from this work at a constant value of $\lg P = 2.31$. For NGC 147, the distance modulus from the literature ($(m - M)_0 = 24.38 \pm 0.01$ mag) excellently agrees with our data ($(m - M)_0 = 24.34 \pm 0.22$ mag according to our linear regression of the 3.0σ-sample). The zero-point problem for NGC 185 needs further exploration. However, if the reason for the offset PLRs is indeed an error in the distance modulus, this would be the first correction of a distance to a galaxy based on PLRs of LPVs.

For NGC 185 there are indications of another parallel sequence of LPVs shifted towards shorter periods (sequence C′). On average, stars on this sequence exhibit smaller amplitudes than objects on sequence C (see lower panel of Fig. 14.4). A similar PLR was found in the LMC (e.g., Ita et al. 2004, Fraser et al. 2008) and is associated with first overtone pulsation. The smaller light amplitude of this group identified in our sample agrees with this interpretation. Note that the trend for the zero point of sequence C is also visible for sequence C′ but the number of detected LPVs populating sequence C′ in NGC 185 prohibits another linear regression. For demonstration purpose only, we plotted sequence C′ of Ita et al. (2004) and shifted it according to the difference in distance obtained for sequence C. This line is drawn as thin dashed line in Fig. 14.4. A handful of targets in NGC 147 may also be located on this sequence. Variables corresponding to higher overtone pulsation were not accessible to our study owing to the sampling rate limitations.

From studies in various stellar systems it is known that the LSPs, visible in a significant fraction of all LPVs, form another sequence to the right of sequence C in the PLD. This sequence D, taken from Ita et al. (2004), is overplotted in both panels of Fig. 14.4 as well. Evidently, we found objects in our variability study for which LSPs derived from the light curve seem to cluster around this sequence D. In these cases, the primary period is typically located close to the fundamental mode pulsation sequence. Note that a detailed determination of these LSPs in our sample is hampered by the limited length of our time series. As described in Sect. 2.2.3, the interpretation of this kind of variability is still a matter of debate. Picking up the results of Wood & Nicholls (2009) that LSP-stars show a significant mid-infrared excess (circumstellar dust), the corresponding targets from our monitoring could be expected to be promising candidates for detecting signatures of circumstellar material.

14.3 A hidden link to star formation history?

The similar datasets for the two galaxies with comparable properties (cf., Paper I) encouraged us to make a detailed comparison of the derived PLDs (Fig. 14.4). Besides the different number of LPVs detected (Table 14.2), which is likely related to the different masses of the systems, the most obvious distinction is the fraction of luminous stars found along sequence C′. For NGC 185 roughly 10 % of all LPVs can be attributed to this sequence for first overtone pulsation, while only less than 3 % of these stars were detected in NGC 147. This raises the question whether some fundamental differences between the two galaxies are mirrored in the recognised discrepancy. A possible interpretation of the lack of stars on sequence C′ in NGC 147 could involve a difference in the mass distribution of these objects. Linear pulsation models (Fox & Wood 1982) as well as observational results from LPVs in stellar clusters (Lebzelter & Wood 2005 and 2007) suggest an evolutionary path of an AGB star through the PLD starting on an overtone sequence and later, at higher luminosities, switching to the fundamental mode sequence. Because there are variables in NGC 185 on sequence C′ with the same luminosity as the bulk of the stars along sequence C, this points towards a higher mass of these stars.

How can this difference in the mass distribution be explained? The most obvious approach would be to assume that the two galaxies differ in their SFH. Indications for this were found in previous studies and become apparent, for example, in the SFH diagrams of Mateo (1998; Fig. 8). Hints for a recent star-formation episode can be found for NGC 185, namely a small population of younger stars concentrated in the central regions, a significant amount of interstellar gas, and prominent dust patches (chapter 11 and Paper I). On the other hand, NGC 147 seems to be free of dust and gas, and there are no indications for a population younger than 1 Gyr (Han et al. 1997, Paper I). Another hint in this direction may be the possible detection of a small shift in the light amplitude distribution of the LPVs (Fig. 14.2) in the two systems. A younger system is expected to contain more stars with higher masses and, thus, smaller amplitudes (Lebzelter & Wood 2007) compared to older systems.

Theory predicts a linear trend between the mean metallicity and the ratio of C-type to M-type stars (C/M) of a galaxy, which has been confirmed by observations (Iben & Renzini, 1983; Mouhcine & Lançon 2003). For systems with lower mean metallicities the production of C-type stars is favoured. According to the values obtained in Paper I, NGC 185 is considered as the more metal-poor galaxy. However, the number of C-type stars is approximately the same in both systems, which leads to a much lower C/M for NGC 185 than for NGC 147 (0.21 and 0.52, respectively). Note that one has to be careful with the interpretation of this result because Battinelli & Demers (2005) clearly demonstrated how severely the C/M depends on the selection criterion (see their Figs. 3 and 4). In addition, the mean metallicity of a galaxy is an elusive parameter because galaxies consist of multiple populations with a mixture of ages and metallicities. The small separation (within the uncertainties) of our target galaxies in Fig. 3 of Battinelli & Demers (2005) does not allow us to draw any conclusions.

The SFHs of the two galaxies should be explored in more detail to arrive at a final interpretation of this question. Because both galaxies, NGC 147 and NGC 185, are comparable in properties (distance, luminosity, C-star content) but differ in their SFHs, they appear to be ideal candidates to shed light on this challenging topic.

15 Summary and Future Outlook

15.1 The LPV Work-Package of Gaia

About 250 000 stars among all the objects that will be observed by Gaia are expected to be LPVs. These LPVs will be handled by a software package specially developed to classify these stars according to their position within a PLD. Different classification areas (labelled as A, B, C, D and E) were defined with respect to detected period-luminosity sequences of LPVs. Each classification box in the PLD was chosen such that all sequences are clearly separated from the neighbouring ones. A large fraction of LPVs are known to exhibit more than one significant period, therefore, the LPV work-package of Gaia will take two periods into account (assuming that both of them are significant). Each input point will have uncertainties in period and luminosity which define an error box. This error box will be used to define the membership of an input point to one of the predefined classification areas.

Besides the classification module, which is the last and most important one in the data flow of this analysis software, the LPV work-package consists of several modules with different tasks. The classification module aims to assure that the source which is going to be processed is indeed an LPV, the irregularity module flags all sources with red colours and for which no period could be found. Since the BC is significantly different for O-rich and C-rich atmospheres, the BC module uses three different relations: for C-rich LPVs with large and small amplitudes, respectively, and for O-rich sources (for which the pulsation amplitude has little effect on the BC). The next module calculates the bolometric brightness of an LPV. The source is flagged as an RSG in the following module if the bolometric brightness exceeds the limit defined by Wood et al. (1983). Otherwise the source is processed through the module for LPV subclassification.

In order to assure that the LPV software is working as expected and meets the requirements of the quality assurance of the Gaia software, several tests need to be performed. Besides unit tests that are used to verify individual units of a source code, we prepared scientific tests to verify if the chosen method is applicable and if the general goals of the code are realisable. Up to now, three scientific tests were executed. Several methods are offered to determine the period of a variable source within the Gaia software. Our test for period determination showed that the Lomb-Scargle method (Scargle, 1982) is best suited to obtain reliable periods of LPVs. As mentioned above, it is of crucial importance to determine a good BC to correctly classify a source as an RSG or to assign the right LPV class. With a set of synthetic spectra of C-rich and O-rich LPVs, which were converted to low resolution to match the expected output of RP, it has been demonstrated that it is possible to distinguish O-rich from C-rich sources and, hence, chose the correct BC-relation. Finally, we tested the LPV classification module with a small sample of OGLE stars. For each star the LPV class was calculated beforehand for comparison reasons. All stars of the test sample were correctly classified by the LPV software.

However, this classification test still needs to be repeated using a large sample of stars to make sure that all possible variations are correctly classified. As a next step, the input light curves need to be modified according to the Gaia time sampling. Furthermore, the predefined classification boxes are currently only based on the PLD of LMC-LPVs of Ita et al. (2004). The final reference PLD will consist of all available data on this topic. It has to be expected that the simulated values (Gaia time sampling, model dependent RP spectra, mean brightness) will deviate from the real measurements, therefore, the classification areas and BC relations will be fine tuned, once the first data of Gaia are made available.

The LPVs observed with the Gaia mission will be used to construct a reliable PLD for the Milky Way. Additional spectrophotometric information (in comparison with Hipparcos) even allows to correct the distance measurements of LPVs for chromatic effects. This very precise PLD will cover several structures of the Milky Way, like the Galactic bulge, the disk, the halo and the galactic anticentre, allowing to construct PLDs of different stellar populations and compare their PLRs with respect to other parameters. The accurate parallax measurements will also allow to calibrate the PLRs of LPVs in order to use them as additional tool for distance determination (even beyond the Local Group). Several studies of various stellar properties of nearby LPVs and AGB stars available but their conclusions often depend on uncertain distances. Thanks to the parallax measurements of Gaia, the results of these studies will be improved significantly. Accurate distances to Galactic globular star clusters will further allow to investigate the mass loss properties of LPVs as well as their evolutionary path within a PLD. This also offers a possibility to determine the mass distribution in a stellar environment, which is important to compare models for stellar evolution, stellar population and initial mass function with the observations. Furthermore, there are indications that RSG stars also follow different sequences in a PLD but up to now the number of detected RSGs is too low to draw any conclusions. Gaia will certainly increase the number of RSGs allowing to study their period-luminosity relations in more detail.

15.2 The LPVs of NGC 147 and NGC 185

A photometric monitoring in the i-band of the two Local Group dwarf galaxies NGC 147 and NGC 185 led to the identification of 213 and 513 long-period variables, respectively. Narrow-band photometry adopted from Paper I allowed us to investigate the number of C-rich and O-rich stars among this variability class. Thus, our study is one of the few (e.g., Groenewegen 2004) that uses a more elaborated chemistry separation than the often used broad-band colour criterion (e.g., $(J-K) > 1.4$). Because the attribute of long-period variability is more significant than a pure brightness limit to select the AGB stars among all late-type giants of a population, the ratio of C-/M-type LPVs is a more reliable measure of the corresponding ratio on the AGB. From our study we determine a value of 0.52 for NGC 147 and 0.21 for NGC 185. Our large sample of LPVs allowed us to investigate the corresponding period-luminosity relations in the K_s-$\log P$-plane as well.

Most variables in both galaxies are located along sequence C, where fundamental mode pulsators are theoretically expected. A linear regression ($m_K = a \log P + b$) was fitted to the data of these stars. The resulting fit parameters agree well with the corresponding values found for the LMC in the literature (e.g., Ita et al. 2004). This allows us to speculate further about the universality of the P-L-relation of LPVs. However, we noticed a discrepancy in b for NGC 185, which may point to an error in the previously derived distance modulus of this galaxy. This would be the first correction of a distance to a galaxy based on PLRs of LPVs.

The most significant difference between the PLDs of the two target systems is the presence of a group of first overtone pulsators (sequence C′) in NGC 185, whereas such stars are almost completely missing in NGC 147. According to linear pulsation models of Fox & Wood (1982) and observational results LPVs in stellar clusters of Lebzelter & Wood (2005), the evolutionary path of a LPV through the PLD starts in an overtone sequence. During its evolution the variable switches to a lower overtone sequence or to the sequence for fundamental mode pulsation while becoming more luminous. As mentioned by Lebzelter & Wood (2011), variability and mass loss of AGB stars are linked – LPVs exhibiting large amplitudes (i.e., sequence C stars) also have high mass loss rates. Therefore, stars in NGC 185 that are populating sequence C′ are expected to have higher masses than sequence C stars with the same luminosity. Thus, the lack of first overtone pulsators in NGC 147 may be explained by a difference in the star-formation history compared to NGC 185 and, accordingly, a different mass distribution on the AGB.

In order to further investigate this approach, it would be of crucial importance not only to increase the number of LPVs at the faint end of sequence C′ but also to detect LPVs populating sequence B. According to our sampling interval, periods shorter than 90 days could not be detected. With an additional observing proposal that has been submitted to the NOT, we intend to extend our monitoring of the two galaxies NGC 147 and NGC 185 by obtaining more observations at a higher sampling rate to allow the detection of these periods. Moreover, additional data points would allow to explore the period range beyond 400 days where the LSPs of LPVs are found. The shorter period variation of such stars is more easily detected, and typically assigned to one of the other sequences within a PLD. According to Wood & Nicholls (2009), LSPs are associated with mass ejection. However, the nature of this kind of variability is still unclear (e.g., Nicholls et al., 2010). A good coverage of LPVs populating sequence D is certainly crucial to improve the chances of understanding this mysterious type of variability. As a side result, the slope of sequence C will be determined with much higher accuracy for both galaxies, since we expect to detect more LPVs at the short-period end of this sequence. It would be of great importance to discuss whether the PLR of stars along sequence C is of universal validity or not. For this purpose more observations of galaxies (most of them will be dwarf galaxies) within the Local Group and beyond are needed. Their LPVs have to be detected and the distribution of these stars within a PLD should be investigated. The slopes of LPVs on sequence C (Mira sequence) of a large sample of stellar systems (star clusters and galaxies) should be compared with respect to other parameters (e.g., metallicity, He abundance, mass loss). Furthermore, the use of LPVs as distance indicator, which are found along overtone sequences should also be tested. These stars are still intrinsically brighter than Cepheids and their amplitudes (although they are smaller than those of sequence C stars) should still be large enough to detect them. Owing to the significantly shorter periods of these stars their PLRs could be determined much faster as those of LPVs along sequence C. It would also be interesting to compare the PLDs of various galaxies that are known to have different star formation histories. This would allow to study a possible connection of the distribution of LPVs (assuming a range of detected periods from about 30 to 600 days) within a PLD and the star formation history of a galaxy.

References

Alard, C. 2000, A&AS, 144, 363

Aringer, B., Girardi, L., Nowotny, W., et al. 2009, A&A, 503, 913

Arlandini, C., Käppeler, F., Wisshak, K., et al. 1999, AJ, 886, 525

Baker, N. & Kippenhahn, R. 1962, ApJ, 142, 868

Battinelli, P. & Demers, S. 2004a, A&A, 417, 479

Battinelli, P. & Demers, S. 2004b, A&AS, 418, 33

Battinelli, P. & Demers, S. 2005, A&AS, 434, 657

Beaulieu, J. P., Carey, S., Ribas, I., & Tinetti, G. 2008, ApJ, 677, 1343

Bertelli, G., Girardi, L., Marigo, P., & Nasi, E. 2008, A&A, 484, 815

Bessel, M. S., Scholz, M., & Wood, P. R. 1996, A&A, 307, 481

Böhm-Vitense, E. 1958, ZA, 46, 108

Bono, G. & Marconi, M. 1999, IAU Symp., 190, 527

Borissova, J., Rejkuba, M., Minniti, D., et al. 2009, A&A, 502, 505

Butler, D. J. & Martinez-Delgado, D. 2005, AJ, 129, 2217

Caretta, E. & Gratton, R. G. 1997, A&AS, 328, 95

Catelan, M. 2007, AIPConf. Proc, 930, 39

Chiosi, C. 1997, Stellar astrophysics for the local group : VIII Canary Islands Winter School of Astrophysics. Edited by A. Aparicio, A. Herrero, and F. Sanchez. Cambridge ; New York : Cambridge University Press, 1

Chiosi, C., Bertelli, G., & Bressan, A. 1992, Ann. Rev. A&A, 30, 235

Chiosi, C., Wood, P. R., & Capitanio, N. 1993, ApJ, 86, 541

Cioni, M.-R. L. & Habing, H. J. 2003, Asymptotic Giant Branch Stars by Habing, H. J. & Olofsson, H.

Cioni, M.-R. L., Marquette, J. B., Loup, C., et al. 2001, A&A, 377, 945

Clement, C. M., Muzzin, A., Dufton, Q., et al. 2001, AJ, 2587, 122

Cook, C. W., Fowler, W. A., Lauritsen, C. C., & Lauritsen, T. 1957, Phys. Rev., 508, 107

Corradi, R. L. M., Magrini, L., Greimel, R., et al. 2005, A&A, 431, 555

Cox, J. P. & Whitney, C. 1958, ApJ, 127, 561

Cutri, R. M., Skrutskie, M. F., Van Dyk, S., et al. 2003, Expl. Supplement to the 2MASS All Sky Data Release, http://www.ipac.caltech.edu/2mass/releases/allsky/doc/explsup.html

De Grijs, R. & Cartwright, S. 2011, Published by John Wiley & Sons

Deeming, T. J. 1975, Ap&SS, 36, 137

Derekas, A., Kiss, L. L., Bedding, T. R., et al. 2006, ApJ, 650, 55

Dosscher, J., Sarro, L. M., Aerts, C., et al. 2007, A&A, 475, 1159

Dubath, P., Lecoeur-Taibi, I., Mowlavi, N., & Beck, M. 2011a, GAIA-C7-SP-GEN-PD-006

Dubath, P., Rimoldini, L., Süveges, M., et al. 2011b, MNRAS, 414, 2602

Eddington, A. S. 1917, The Observatory, 40, 290

Eddington, A. S. 1918, MNRAS, 79, 2

Ehrenfreund, P. & K., M. 2001, Lecture Notes in Physics: Astrobiology, 7

Evans, D. W. & F., D. A. 2011, GAIA-C5-TN-IOA-DWE-031-1

Eyer, L. 2005, ESASP, 576, 513

Eyer, L. & Cuypers, J. 2000, ASP Conf. Ser., 203, 71

Eyer, L. & Mignard, F. 2005, MNRAS, 361, 1136

Feast, M. 2004, ASPCS, 310, 304

Feast, M. & Catchpole, R. M. 1997, MNRAS, 286, 1

Feast, M., Glass, I., Whitelock, P., et al. 1989, MNRAS, 241, 375

Ferrarese, L., Mould, J. R., Stetson, P. B., et al. 2007, ApJ, 654, 186

Fox, M. & Wood, P. 1982, ApJ, 259, 198

Fraser, O. J., Hawley, S. L., & Cook, K. H. 2008, AJ, 136, 1242

Fraser, O. J., Hawley, S. L., Cook, K. H., & Keller, S. C. 2005, AJ, 129, 768

Frost, C. A. & Lattanzio, J. C. 1996, AJ, 383, 473

Geha, M., van der Marel, R. P., Guhathakurta, P., et al. 2010, ApJ, 711, 361

Gerasimovic, B. P. 1928, PNAS, 14, 963

Girardi, L., Bressan, A., Bertelli, G., & C., C. 2000, A&ASS, 141, 371

Girardi, L., Chiosi, C., Bertelli, G., & Bressan, A. 1995, A&A, 298, 87

Glass, I. S., Schultheis, M., Blommaert, J. A. D. L., et al. 2009, MNRAS, L11, 395

Gålfalk, M. 2005, NOT Annual report 2004, 18

Gratton, R. G., Bragaglia, A., Carretta, E., et al. 2003, A&A, 408, 529

Grebel, E. K. 1999, IAU Symp., 192, 17

Groenewegen, M. A. T. 2004, A&A, 425, 595

Groenewegen, M. A. T. 2005, ASP Conf. Ser., arXiv:astro

Groenewegen, M. A. T. 2007, ASP Conf. Ser., 378, 433

Groenewegen, M. A. T. & A., W. P. 1996, MNRAS, 281, 1347

Groenewegen, M. A. T., Sloan, G. C., Soszyński, I., & Petersen, E. A. 2009, A&A, 506, 1277

Groenewegen, M. A. T., Udalski, A., & Bono, G. 2008, A&A, 481, 441

Gustafsson, B., Bell, R. A., Eriksson, K., & Nordlund, A. 1975, A&A, 42, 407

Gustafsson, B., Edvardsson, B., Eriksson, K., et al. 2003, ASP Conf. Ser., 288, 331

Gustafsson, B., Edvardsson, B., Eriksson, K., et al. 2008, A&A, 486, 951

Habing, H. J. & Olofsson, H. 2003, editors

Habing, H. J. & Whitelock, P. A. 2003, Asymptotic Giant Branch Stars by Habing, H. J. & Olofsson, H., 411

Han, M., Hoessel, J. G., Gallagher III, J. S., et al. 1997, AJ, 131, 1001

Haniff, C. A., Scholz, M., & Tuthill, P. G. 1995, MNRAS, 276, 640

Harris, G. L. H. & Harris, W. E. 2000, AJ, 120, 2423

Harris, G. L. H., Harris, W. E., & Poole, G. B. 1999, AJ, 117, 855

Herwig, F. 2005, Ann. Rev. A&A, 43, 435

Hinkle, K., Lebzelter, T., Joyce, R. R., & Fekel, F. C. 2002, AJ, 123, 1002

Hippel, T. 1998, AJ, 115, 1536

Höfner, S. 1999, A&A, 346, L9

Höfner, S., Gautschy-Loidl, R., Aringer, B., & Jørgensen, U. G. 2003, A&A, 399, 589

Holtzman, J. A., Afonso, C., & Dolphin, A. E. 2006, ApJ, 166, 534

Holtzman, J. A., Watson, A. M., Baum, W. A., et al. 1998, AJ, 115, 1946

Hoyle, F., Dunar, D. N. F., Wenzel, W. A., & Whaling, W. 1953, Phys. Rev., 1095, 92

Hudec, R., Šimon, V., & Hudec, L. 2010, AdAst, Article

Hughes, S. M. G. & Wood, P. R. 1990, AJ, 99, 784

Iben, I. J. 1983, ARA&A, 21, 271

Ita, Y., Tanabé, T., Matsunaga, N., et al. 2004, MNRAS, 347, 720

Jordi, C., Gebran, M., Carrasco, J. M., et al. 2010, A&A, 523, A48

Jorissen, A., Mowlavi, N., Sterken, C., & Manfroid, J. 1997, A&A, 324, 578

Josselin, E., Blommaert, J. A. D. L., Groenewegen, M. A. T., et al. 2000, A&A, 357, 225

Kang, A., Sohn, Y.-J., Rhee, J., et al. 2005, A&A, 437, 61

Kennicutt, R. C. J., Stetson, P. B., Saha, A., et al. 1998, ApJ, 498, 181

Kerschbaum, F. 1999, A&A, 351, 627

Kerschbaum, F. & Hron, J. 1992, A&A, 263, 97

Kerschbaum, F., Lazaro, C., & Habison, P. 1996, A&A, 118, 397

Kerschbaum, F., Lebzelter, T., & Mekul, L. 2010, A&A, 524, 87

Kholopov, P., Samus, N., Frolov, M. S., et al. 1985-88, Moscow: Nauka Publishing House, 372, 1721

Kiss, L. L. & Bedding, T. R. 2003, MNRAS, 343, 79

Kiss, L. L., Szabó, G. M., & Bedding, T. R. 2006, MNRAS, 372, 1721

Kuhfuss, R. 1986, A&A, 160, 116

Lattanzio, J. C. & Wood, P. R. 2003, Asymptotic Giant Branch Stars by Habing, H. J. & Olofsson, H.

Leavitt, H. S. & Pickering, E. C. 1912, Harvard College Obs. Circular, 1, 173

Lebzelter, T. & Hron, J. 1999, A&, 351, 533

Lebzelter, T. & Lorenz, D. 2010, Gaia Technical Note, GAIA-C7-TN-UVIE-TLZ-003-0D

Lebzelter, T., Lorenz, D., Groenewegen, M., & Jorissen, A. 2011, SOS: Long Period Variables Software Requirement Specification, GAIA-C7-SP-UVIE-TLZ-002

Lebzelter, T. & Obbruger, M. 2009, AN, 330, 390

Lebzelter, T., Schultheis, M., & Melchior, A. L. 2002, A&A, 393, 573

Lebzelter, T. & Wood, P. R. 2005, A&A, 441, 1117

Lebzelter, T. & Wood, P. R. 2007, A&A, 475, 643

Lebzelter, T. & Wood, P. R. 2011, A&A, 529, 137

Lebzelter, T., Wood, P. R., Hinkle, K. H., et al. 2004, Proc. IAU Coll., 193, Variable stars in the Local Group, ASP Conf. Ser., 310, 144

Lederer, M. 2009, Ph.D. Thesis, Univ. of Vienna

Lee, Y. W., Joo, J. M., Sohn, Y. J., et al. 1999, Nature, 402, 55

Lenz, P. & Breger, M. 2005, CoAst, 146, 53

Levesque, E. M., Massey, P., Olsen, K. A. G., et al. 2005, ApJ, 628, 973

Lomb, N. R. 1976, Ap&SS, 39, 447

Lorenz, D., Lebzelter, T., Nowotny, W., et al. 2011, A&A, 78L, 532A

Mackey, A. D. & Broby Nielsen, P. 2007, MRAS, 379, 151

Marengo, M., Reiter, M., & Fazio, G. G. 2008, AIP Conf. Proc., 1001, 331

Marleau, F. R., Graham, J. R., Liu, M. C., & Charlot, S. 2000, AJ, 120, 1779

Martínez-Delgado, D. & Aparicio, A. 1998, AJ, 115, 1462

Martínez-Delgado, D., Aparicio, A., & Gallart, C. 1999, AJ, 118, 2229

Mateo, M. 1998, ARA&A, 36, 435

Matsunaga, N., Kawadu, T., Nishiyama, S., et al. 2009, MNRAS, 399, 1709

Mouhcine, M. & Lançon, A. 2003, MNRAS, 338, 572

Nicholls, C. P., Wood, P. R., & L., C. M.-R. 2010, MNRAS, 405, 1770

Nicholls, C. P., Wood, P. R., L., C. M.-R., et al. 2009, MNRAS, 399, 2063

Nowotny, W., Höfner, S., & Aringer, B. 2010, A&A, 514, A35

Nowotny, W., Kerschbaum, F., Olofsson, H., et al. 2003, A&A, 403, 93

Nowotny, W., Kerschbaum, F., Schwarz, H. E., & Olofsson, H. 2001, A&A, 367, 557

Nowotny, W., Lebzelter, T., Hron, J., & Hfner, S. 2005, A&A, 437, 285

Olivier, E. A. & Wood, P. R. 2005, MNRAS, 362, 1396

Olofsson, H., González Delgado, D., Kerschbaum, F., & Schöier, F. L. 2002, A&A, 391, 1053

Origlia, L., Ferraro, F. R., Fusi Pecci, F., & Rood, R. T. 2002, ApJ, 571, 458

Paczyńsky, B. 1971, AcA, 21, 417

Palmer, L. G. & Wing, R. F. 1982, AJ, 87, 1739

Percy, J. R. 2007, Cambridge University Press

Percy, J. R., Desjardins, A., Yu, L., & Landis, H. J. 1996, PASP, 108, 139

Pietrzyńsky, G., Thompson, I. B., Graczyk, D., et al. 2009, AJ, 697, 862

Piotto, G., Bedin, L. R., Anderson, J., et al. 2007, ApJ, 661, 53

Plez, B. 2003, ASP Conf. Ser., 298, 189

Plez, B., Brett, J. M., & Nordlund, A. 1992, A&A, 256, 551

Poelarends, A. J. T., Herwig, F., Langer, N., & Heger, A. 2008, ApJ, 675, 614

Pumo, M. L. & Siess, L. 2007, ASP Conf. Ser., 378, 133

Reegen, P. 2007, A&A, 467, 1353

Rejkuba, M. 2004, A&A, 413, 903

Rejkuba, M., Minniti, D., & Silva, D. R. 2003, A&A, 406, 75

Riebel, D., Meixner, M., Fraser, O., et al. 2010, ApJ, 723, 1195

Rizzi, L., Tully, R. B., Makarov, D., et al. 2007, ApJ, 661, 815

Sage, L. J., Welch, G. A., & Mitchell, G. F. 1994, AJ, 507, 726

Saio, H. & Gautschy, A. 1998, ApJ, 498, 360

Sakai, S., Ferrarese, L., Kennicutt, R. C. J., & Saha, A. 2004, ApJ, 608, 42

Salaris, M. & Cassisi, S. 2006, Published by John Wiley & Sons

Scargle, J. D. 1982, ApJ, 263, 835

Schlegel, D. J., Finkbeiner, D. P., & Davis, M. 1998, ApJ, 500, 525

Schubert, E. F. 2006, Cambridge University Press, Cambridge , UK, 2nd Edition, chapter 18 figure 2

Schuller, P., Ganesh, S., Messineo, M., et al. 2003, A&A, 403, 955

Schultheis, M. 1998, Ph.D. Thesis, Univ. of Vienna

Schultheis, M., Glass, L. S., & Cioni, M.-R. 2004, A A, 427, 945

Schwarzschild, M. & Härm, R. 1965, ApJ, 142, 855

Sharma, S., Borissova, J., Kurtev, R., et al. 2010, AJ, 139, 878

Siess, L. & Pumo, M. L. 2006, Mem. S.A.It., 77, 822

Smith, V. V., Plez, B., Lambert, D. L., & Lubowich, D. A. 1995, ApJ, 441, 735

Sohn, Y.-J., Kang, A., Rhee, J., et al. 2006, A&A, 445, 69

Sommerville, I. 2006, Addison Wesley

Soszyński, I., Udalski, A., Kubiak, M., et al. 2004a, Acta Astron., 54, 129

Soszyński, I., Udalski, A., Kubiak, M., et al. 2004b, Acta Astron., 54, 347

Stellingwerf, R. F. 1978, ApJ, 224, 953

Stetson, P. B. & Harris, W. E. 1998, AJ, 96, 909

Stift, M. J. 1995, A&A, 301, 776

Straniero, O., Domínguez, I., Cristallo, R., & Gallino, R. 2003, Publications of the Astronomical Society of Australia, 389, 20

Suda, T., Tsujimoto, T., Shigeyama, T., et al. 2007, AJ, 671, 129

Turner, D. G., Majaess, D. J., Lane, D. J., et al. 2010, OAP, 23, 119

Valenti, E., Ferraro, F. R., & Origlia, L. 2007, AJ, 133, 1287

van den Bergh, S. 1998, AJ, 116, 1688

Vassiliadis, E. & Wood, P. R. 1993, ApJ, 413, 641

Wagenhuber, J. & Groenewegen, M. A. T. 1998, A&A, 340, 183

Weigert, A. & Wendker, H. J. 1996

White, N. M. & Wing, R. F. 1978, AJ, 222, 209

Whitelock, P. & Feast, M. 2000, MNRAS, 319, 759

Williams, J. P., Blitz, L., & McKee, C. F. 2000, Protostars and Planets IV; University of Arizona Press), eds., Mannings, V., Boss, A.P., Russell, S. S., 97

Wing, R. F. 1971, Conf. Proc. KPNO Contr. No., 554, 145

Wing, R. F. & Stock, J. 1973, ApJ, 186, 979

Wood, P. R. 1990, ed. M. O. Mennessierand A. Omont (Gif-sur-Yvette: Éditions Frontières), 431, 67

Wood, P. R. 1999, IAU Symp., 191, 151

Wood, P. R. 2000, Proc. Astron. Soc. Aust, 17, 18

Wood, P. R. 2007, IAU Symp., 239, 343W

Wood, P. R., Bessell, M. S., & Fox, M. W. 1983, ApJ, 272, 99

Wood, P. R. & Nicholls, C. P. 2009, ApJ, 707, 573

Xiong, D. R. & Deng, L. 2007, MNRAS, 378, 1270

Xiong, D. R., Deng, L., & Cheng, Q. L. 1998, ApJ, 499, 355

Young, L. M. & Lo, K. 1997, AJ, 476, 127

Zima, W. 1999, Master Thesis, Univ. of Vienna

Appendix

List of Figures

List of Tables

List of Acronyms

AGB	asymptotic giant branch
AMR	age-metallicity relation
AU	astronomical unit
BC	bolometric Correction
BP	blue photometer
C	carbon
CCD	charged coupled device
CMD	colour magnitude diagram
CN	carbon nitrate
CSP	composite stellar populations
CU	Coordination Unit
DPAC	Data Processing and Analysis Consortium
DPC	Data Processing Centre
DU	Developing Unit
DUP	dredge-up
EAGB	early AGB
ESA	European Space Agency
FAP	false-alarm-probability
Fe	iron
FOV	field of view
FWHM	full width half maximum
G	Gaia white-light brightness
GCVS	General Catalogue of Variable Stars
H	hydrogen
HB	horizontal branch
HBB	hot-bottom burning
He	helium
HRD	Hertzsprung-Russell diagram
IMF	initial mass function
LPV	long period variable
LMC	Large Magellanic Cloud
LSP	long secondary period
MOC	Mission Operations Centre
MS	main sequence
N	nitrogen
NOT	Nordic Optical Telescope
O	oxygen
PDCZ	pulse-driven convective zone
PLD	period luminosity diagram
PLR	period luminosity relation
p-p	proton-proton

PSF	point spread function
RGB	red giant branch
RP	red photometer
RSG	red supergiant
RVS	radial velocity spectrometer
SFH	star formation history
SFR	star formation rate
SGB	sub-giant branch
SMC	Small Magellanic Cloud
SOC	Science Operations Centre
SSP	simple stellar population
TiO	titanium oxide
TO	turn off point
TP-AGB	thermally pulsing AGB
TRGB	tip of the red giant branch
ZAMS	zero-age main sequence

Acknowledgements

I would like to thank all the many, many people who actually made this thesis possible and unfortunately there is never enough place to mention all of them.

First, I owe my deepest gratitude to Thomas Lebzelter for giving me the opportunity to study LPVs – a group of stars which are not at all well understood due to all the various effects that come into play, but this actually makes them even more fascinating. Thank you for all the discussions we had, I learned so much and still I need to know more. Thank you for giving me the chance to participate in a ESA cornerstone mission like Gaia and sending me to conferences and workshops to broaden my mind and improve my skills. Thank you for always giving me input and feedback and for patiently answering all my questions. And finally, thank you for supporting and supervising me! You were the best (in this case I prefer the German term) *Doktorvater* I could ever wish for.

I also like to thank Walter Nowotny-Schipper for all the fruitful discussions and for always patiently answering all my questions. Thank you very, very much for providing me with the large amount of data of NGC 147 and NGC 185 and preparing all the successful observing proposals for these galaxies.

Furthermore, I am indebted to my collaborators Franz Kerschbaum, John Telting and Hans Olofsson who kindly supported me during the process of writing the paper and the observing proposal. Thanks to your help, input, and advice, these documents certainly improved significantly.

I would also like to thank all the institutes, facilities and research foundations that allowed me to publish my first paper in the field of AGB stars. The data presented in third part of this work (LPVs in NGC 147 and NGC 185) have been taken using ALFOSC, which is owned by the *Instituto de Astrofisica de Andalucia* (IAA) and operated at the *Nordic Optical Telescope* under agreement between IAA and the NBIfAFG of the *Astronomical Observatory of Copenhagen*. This work was supported by the *Fonds zur Förderung der Wissenschaftlichen Forschung* (FWF) under project numbers P18939-N16, P20046-N16 and P21988-N16.

Many thanks to Laurent Eyer and the whole CU7 team in Geneva! I am very grateful for all the meetings and coding workshops that were especially organised for CU7 developers – they were indeed very helpful and productive. My deepest gratitude to Nami Mowlavi who always offered his support and spend a lot of time in order to improve our LPV work-package. I am also very grateful for all the fruitful discussions and for the kind working atmosphere during my stays in Geneva.

I also wish to thank my referees, Mathias Schultheis and Werner Zeilinger, for all their nice comments and suggestions which certainly improved the thesis.

I am grateful for spending my PhD studies with professors and student colleagues that provided a stimulating and entertaining atmosphere in which I could learn and grow. I am very glad to call some of you my friends, and I hope that this friendship will last very long even if our future careers will take place at different countries! Most of all I like to mention Hannes Richter with whom I started my studies from the very beginning and who is actually more like brother to me. Furthermore, I like to thank Claudia Paladini for all the advice that she gave me and the nice social activities (I hope to be more active in future). Mille grazie, resta come sei!

Moreover, I have to thank my family and most of all my mum for patiently tolerating my absence, since I have been very busy with my PhD, and for still supporting me all the time.

I am also very grateful to the family of my dear sweetheart for all the short vacations that I could spend at your place and for all the delicious, home made and home grown food and most of all thank you for your Mudl (a.k.a. Matthias Kronberger). My beloved sunshine, Mudl, there are actually not enough words to thank you! I am very, very thankful for each minute that you spend with me!!! Thank you for all the support in every life situation and thank you for running through the pain of reading and correcting parts of my thesis. You are the one, the best, my everything!

Last but not least, I feel very honoured to have met a great (in more than one sense) person like Piet Reegen. He was not only the developer of the SigSpec software that I have used extensively, he also made our institute a very warm and happy place. Besides all the statistical questions that he always answered immediately and with great joy, he honestly cared a lot about others and always offered a helping hand. I will never forget your passion for coffee, good food, good music, and your sense of humour. Rest in peace dear friend!

Astronomy and Astrophysics
Editor in Chief: C. Bertout

C. Bertout
Observatoire de Paris
61, avenue de l'Observatoire
75014 Paris, France

Tel.: 33 0(1) 43 29 05 41
Fax: 33 0(1) 43 29 05 57
e-mail: aanda.paris@obspm.fr
Web: http://www.aanda.org

merging
Annales d'Astrophysique
Arkiv for Astronomi
Bulletin of the Astronomical Institutes
of the Netherlands
Bulletin Astronomique
Journal des Observateurs
Zeitschrift fur Astrophysik
Bulletin of the Astronomical Institutes
of Czechoslovakia

Paris, October 20, 2011

Reprint Permission

Material:
article by Lorenz et al., 2011, A&A, 532, A78

To be used in:
PhD thesis, Univesität Wien, Austria

Permission granted to:
Denise Lorenz
Universität Wien
Department of Astronomy
1180 Vienna, AUSTRIA
denise.lorenz@univie.ac.at

I hold copyright on the material referred to above, and hereby grant permission for its use as requested herewith. The credit should be given as follows:
Credit: Author, A&A, vol, page, year, reproduced with permission © ESO.

Claude M Bertout.

Claude Bertout
A&A Editor-in-Chief

Sponsored by Argentina, Austria, Belgium, Brazil, Chile, Czech Republic, Denmark, Estonia, Finland, France, Germany, Greece, Hungary, Italy, Netherlands, Poland, Portugal, Slovak Republic, Spain, Sweden, and Switzerland.
Produced and distributed by EDP Sciences for ESO.

Publication List

Refereed publications:

1. Astronomy and Astrophysics, Vol. 532A, p. 78 (2011)
   Long-period variables in NGC 147 and NGC 185
   Lorenz, D., Lebzelter, T., Nowotny, W. et al.

2. Astronomy and Astrophysics, Vol. 515, p. 16 (2010)
   Photometric multi-site campaign on the open cluster NGC 884 I. Detection of the variable stars
   Saesen, S., Carrier, F., Pigulski, ..., Lorenz, D. et al.

3. Astronomische Nachrichten, Vol. 331, p. 1080 (2010)
   Towards ensemble asteroseismology of the young open clusters χ Persei and NGC 6910
   Saesen, S., Pigulski, A., Carrier, ..., Lorenz, D. et al.

4. Communications in Asteroseismology, Vol. 158, p. 179 (2009)
   Asteroseismology of massive stars in the young open cluster NGC 884: a status report
   Saesen, S., Carrier, F., Pigulski, ..., Lorenz, D. et al.

5. The Astrophysical Journal, Vol. 693, p. 564 (2009)
   Whole Earth Telescope Observations of GD 358: A New Look at the Prototype DBV
   Provencal, J. L., Montgomery, M. H., Kanaan, ..., Lorenz, D. et al.

6. Communications in Asteroseismology, Vol.157, p. 315 (2008)
   Asteroseismology in the young open cluster NGC 3293
   Handler, G.,Tuvikene, T., Lorenz, D. et al.

7. Communications in Astroseismology, Vol. 150, p. 191 (2007)
   The ongoing 2005 – 2006 campaign on β Cephei stars in NGC 6910 and χ Persei (NGC 884)
   Pigulski, A., Handler, G., Michalska, G., ..., Lorenz, D. et al.

8. Communications in Astroseismology, Vol. 150, p. 193 (2007)
   Pulsating variables in NGC 3293, the open cluster with the most β Cephei stars known
   Handler, G., Tuvikene, T., Lorenz, D. et al.

9. Monthly Notices of the Royal Astronomical Society, Vol. 365, p. 327 (2006)
   Asteroseismology of the β Cephei star 12 (DD) Lacertae: photometric observations, pulsational frequency analysis and mode identification
   Handler, G., Jerzykiewicz, M., Rodriguez, E., ..., Lorenz, D. et al.

10. Monthly Notices of the Royal Astronomical Society, Vol. 369, p. 171 (2006)
    Photometric studies of three multiperiodic β Cephei stars: CMa, 15 CMa and KZ Mus
    Shobbrook, R. R., Handler, G., Lorenz, D., Mogorosi, D.

11. The Astrophysical Journal, Vol. 646, p. 1230 (2006)
Whole Earth Telescope Observations of the Pulsating Subdwarf B Star PG0014+067
Vuckovic, M., Kawaler, S. D., O'Toole, S., ..., Lorenz, D. et al.

12. Information Bulletin on Variable Stars, Vol. 5651, p. 1. (2005)
A Photometric Null Result in the Search for Pulsations of the Luminous Rapidly Oscillating Ap Star HD 116114
Lorenz, D., Handler, G., Kurtz, D. W.

Other publications:

1. Astrophysics and Space Science Proceedings (2011, in press)
JENAM-S3: Dwarf Galaxies: Keys to Galaxy Formation and Evolution, Sept. 6-10, 2010, Lisbon, Portugal
LPVs as possible distance indicators in NGC 147 and NGC 185
Lorenz, D., Lebzelter, T., Nowotny, W. et al.

2. ASP Conf. Series, Vol. 445, p. 491 (2011)
Why Galaxies Care About AGB Stars II, August 16-20, 2010, Vienna, Austria
Period-Liminosity Relations of LPVs in Nearby Dwarf Galaxies
Lorenz, D., Lebzelter, T., Nowotny, W. et al.

3. EAS Publication Series, Vol. 48, p. 33 (2011)
A Universe of Dwarf Galaxies, June 14-18, 2010, Lyon, France
LPVs in NGC 147 and NGC 185
Lorenz, D., Lebzelter, T., Nowotny, W. et al.

4. Journal of Physics: Conference Series, Vol. 118, p. 12071 (2008)
HELAS IC: Helioseismology, Asteroseismology and MHD Connections, 20-24 August 2007, Göttingen, Germany
Photometric multi-site campaign on massive B stars in the open cluster χ Persei (NGC 884)
Saesen, S., Pigulski, A., Carrier, F., ..., Lorenz, D. et al.

5. ASP Conf. Series, Vol. 349, p. 285 (2006)
Astrophysics of Variable Stars, 5-10 September 2005, Pecs, Hungary
A Calibration of Stellar Parameters for A and F Stars
Lorenz, D., Breger, M., Pamyatnykh, A.

6. Astrophysics and Space Science, Vol. 284, p. 387 (2003)
Asteroseismology Across the HR Diagram: Asteroseismology Workshop, July 1-5 2002, Porto, Portugal
Recent Work of the Delta Scuti Network
Rodler, F., Breger, M., Zima,W., ..., Lorenz, D., Garrido, R.

7. ASP Conference Proceedings, Vol. 259, p. 598 (2002)
   IAU Colloquium 185: Radial and Nonradial Pulsations as Probes of Stellar Physics, 36-31 July, 2001, Leuven, Belgium
   The Delta Scuti Network: Steps Towards Successful Asteroseismology of Delta Scuti Stars
   Zima, W., Breger, M., Bischof, K., ..., Lorenz, D. et al.

Curriculum Vitae

Personal Informations:

Name:	Mag. Lorenz
First name:	Denise
Birth date:	10th of July 1974
Birth place:	Vienna, Austria
Homepage:	http://homepage.univie.ac.at/denise.lorenz/

Education:

1980 - 1993	school (Vienna, Austria)
October 1998	University of Vienna, Austria
March 2007	master degree, Institute of Astronomy, Vienna, Austria
2007-2011	PhD studies, Institute of Astronomy, Vienna, Austria

Employments:

2004	tutor of university course *Advanced practical course in Astronomy*, Vienna, Austria
2005	work on contract basis, Austrian Sience Fund Project P17097-N02, Vienna, Austria
2006	tutor of university course *Beginners practical course in Astronomy*, Vienna, Austria
2007 – 2010	full time position on contract basis, Austrian Science Fund Project P20046-N16, Gaia satellite, Vienna, Austria
2009	tutor of university course *Observing at the vlt*, Vienna, Austria
2011	work on contract basis, Austrian Sience Fund Project P20526-N16 and FFG-Project FA538011, BRITE satellite, Vienna, Austria

Workshops / Conferences / Seminar talks:

July 2002	*Long-Term Photometry of Variables* in Brussels, Belgium
September 2005	*PhD Conference on Astrophysics of Variable Stars* in Pécs, Hungary (talk)
September 2006	member of the LOC for the *Future of Asteroseismology Workshop* in Vienna, Austria
September 2008	member of LOC for *Joint European and National Astronomy Meeting* in Vienna, Austria

September 2009	*Joint Annual Meeting of ÖPG/SPG/OEGAA* in Innsbruck, Austria (poster)
April 2010	OEGAA-Meeting in Graz, Austria (talk)
Juni 2010	*A Universe of Dwarf Galaxies* in Lyon, France (poster)
August 2010	*Why Galxies Care About AGB Stars II* in Vienna, Austria (talk)
September 2010	*Joint European and National Astronomy Meeting* in Lissbon, Portugal (poster)
May 2011	invited talk on *LPVs in NGC147 and NGC185* at Technical University, Vienna, Austria

Gaia-Meetings and Workshops

March 2007	CU7-Meeting, Bologna, Italy
May 2008	CU7-Meeting, Catania, Italy
February 2009	Gaia Database Workshop, ESAC Madrid, Spain
March 2009	Gaia Java Workshop at ISDC Geneva, Swiss
November 2009	CU7-Meeting, Prague, Czech Republic
May 2009	CU7-Meeting, Vienna, Austria
November 2009	CU7-Meeting, Geneva, Swiss
May 2010	CU7-Meeting, Naples, Italy
November 2010	CU7-Meeting, Cambridge, England (UK)

Photometric Observations:

November 2000	one week observing run at Mt. Suhora in Poland, (0.6 m telescope)
February 2002	one week observing run at Piszkestetö in Hungary, (0.5 m telescope)
September 2003	two weeks observing run at Piszkestetö in Hungary, (0.5 m telescope)
June 2004	two weeks observing run at Piszkestetö in Hungary, (0.5 m telescope)
January 2005	two weeks observing run at SAAO in South Africa, (0.5 m telescope)
March 2006	two weeks observing run at SSO in Australia, (1.0 m telescope)
November 2006	two weeks observing run at SAAO in South Africa, (0.5 m telescope)
2003 – 2007	several nights at Institute of Astronomy, north dome, Vienna, Austria , (0.8 m telescope)

Public Outreach:

since Dec. 2005	founder and responsible producer of the Astronomy-Broadcast *SuperNova*, running every second month at the open TV channel *OKTO* since December 2005 until June 2011 32 broadcasts
2005 – 2011	participation in *Astronomy Day*, *Long Night of Science*, *Science Brunch*, *Market of Science*, ... Vienna
October 2007	homepage designer of science youth magazine *SciQ*, Vienna
Juni 2009	school attendance, topic: sun and Astronomy in the TV, Vienna
July 2009, 2010	children university curse *Our sun in a cooking pot*, Vienna
July 2009	Webcast talk about the sun at www.smile2.de
December 2009	*Explorer l'Univers* at the French Institute, Vienna
November 2010	invited talk for amateur astronomers (WAA) on Gaia, Vienna
Nov, Dec 2010	three school attendances, general Astronomy lecture
April 2011	invited talk at *Daughters day* about being an Astronomer, Planetarium Wien, Vienna
August 2011	two talks at the Viennese *Ferienspiel*, Planetarium Wien, Vienna